

Copyright © 1983, by the author(s).
All rights reserved.

Permission to make digital or hard copies of all or part of this work for personal or classroom use is granted without fee provided that copies are not made or distributed for profit or commercial advantage and that copies bear this notice and the full citation on the first page. To copy otherwise, to republish, to post on servers or to redistribute to lists, requires prior specific permission.

CHARACTERIZATION OF PLASMA ETCHED
STRUCTURES IN IC PROCESSING

by

J. L. Reynolds

Copyright © 1983

Memorandum No. UCB/ERL M83/78

June 1983

(over)

CHARACTERIZATION OF
PLASMA ETCHED STRUCTURES
IN I C PROCESSING

- by -

John L. Reynolds

copyright © 1983

Memorandum No. UCB/ERL M83/78

June 1983

ELECTRONICS RESEARCH LABORATORY

College of Engineering
University of California, Berkeley
94720

*... dedicated to
Mom, Dad and Sis
as a token of the education
that they encouraged me to get.*

CHARACTERIZATION OF PLASMA ETCHED STRUCTURES IN IC PROCESSING

John L. Reynolds

Department of Electrical Engineering and Computer Science
University of California
Berkeley, California 94720


Research Advisor

ABSTRACT

Plasma etching has become an essential process in integrated circuit fabrication, yet it remains a complex and not well understood combination of chemistry and physics. A complete model is important in for process control, but it is also very difficult. Toward this goal, three useful experiments that give a better characterization of plasma etching are the measurements of the rf impedance, the dc bias on the substrate electrode, and the emission spectra of the plasma. The plasma is electrically modeled by an equivalent circuit comprised of a resistor in series with sheath resistors and capacitors. The impedance of the plasma is measured experimentally for $CF_4/10\%O_2$, $SF_6/10\%O_2$, $C_2F_6/10\%O_2$, and *Argon* plasmas and values are deduced for these equivalent circuit elements. The plasma resistance increases linearly above a certain pressure, until at high pressures collisions extinguish the plasma. Electrical characterization indicates the importance of ion bombardment and ion energy in the etching process. For the chemical diagnosis of the plasma the Fluorine 703.7 nm intensity is measured with a scanning monochromator. A relative fluorine atom density is calculated by normalizing this line to the 750.4 nm Argon line.

These impedance and density data are used to explain the etching characteristics of cantilever test structures. The factors include surface migration, ion directionality, and the basic isotropic and anisotropic components in plasma

etching. The process simulator program SAMPLE is used to illustrate the various mechanisms that may be expected. Integrated cantilever structures were fabricated by overetching a supporting material beneath a non-eroding mask. This diagnostic structure is used in studies of silicon etching with SF_6/O_2 , CF_4/O_2 , and C_2F_6/O_2 under various powers, pressures and flow rates. Etching components are given as a function of power, pressure and flow-rate and related to the plasma properties introduced earlier.

As an application, some aspects of the interaction among wafer topography and the thin film processes of directional dry etching are presented in experiment and simulation. The anisotropy of dry etching increases the interdependence of processing steps and opens the possibility of creative uses of topographical effects in fabricating devices. The anisotropy also offers greater line width and profile control in pattern transfer in the etching of thin film layers. The loading effect and mask interaction are explored in simulation and experiment, also, in order to help realize this control.

Although a complete understanding of the plasma is a complex problem, a model is proposed which divides plasma processing into two components. The first part seeks to predict the plasma properties from the laboratory controls and system parameters. The second part ties the etching mechanisms and physics to the plasma properties and is independent of the laboratory conditions. Two dimensional characteristic rate equations are presented with terms that reflect the physical characteristics of the plasma. These characteristics are qualitatively related to the impedance and spectroscopic observables.

Table of Contents

Title and copyright.....	i
Dedication.....	ii
Abstract.....	iii
Table of Contents.....	v
Acknowledgements.....	vi
Figure List.....	vii
Chapter One: Introduction.....	1
Historical.....	1
Two Box Model.....	2
Chapter Two: Basic characteristics of plasmas.....	9
Introduction.....	9
Text book model.....	9
Definitions and Background.....	9
Calculations and physics.....	14
Conclusions.....	24
Plasma reactions and surface chemistry.....	25
Classification of characteristics.....	25
Single and double component etching.....	27
Multiple component etching.....	29
Anisotropy considerations.....	31
Plasma reactions.....	33
Impedance models.....	34
Conclusion.....	39
Chapter Three: Experimental Plasma Properties.....	43
Introduction.....	43
Impedance Model.....	43
Plasma Equivalent Circuit.....	43
Analysis via the Matching Network.....	47
Impedance Measurements.....	50
The Sheath Capacitance and Conductance.....	55
Plasma Resistance.....	57
The DC Bias.....	63
Optical Spectroscopy Measurements.....	72
Conclusions.....	63
Chapter Four: Studies of plasma etching mechanisms with cantilever structures.....	63
Introduction.....	63
Computer simulation.....	63
Experiment.....	90
Conclusion.....	93
Chapter 5: Topography Modeling in Dry Etching Processes.....	103
Introduction.....	103
Anisotropic etching at steps.....	104
Step coverage.....	108
Planarization.....	114
Conclusion.....	120
Chapter Six: Profile Determining Mechanisms in Thin Film Layers..	124
Introduction.....	124
The Loading Effect with Fluoro-carbons.....	124
Dependence on power.....	125
Dependence on photo resist.....	127
Computer simulation.....	127
The Loading Effect with Chloro-carbon Additions.....	132

Introduction.....	132
Experimental configuration.....	134
Data and Observations.....	136
Conclusions and discussion.....	151
Chapter Seven: Feasibility of a Macroscopic Plasma Etching Model.	155
Bibliography.....	164
Appendix A: The Plasma Therm PK-12 Plasma Etcher and User Manual....	175
Appendix B: Computer Code for Calculating the Impedance of the Plasma..	196
Appendix C: Tables of data from the PK-12.....	206
Appendix D: Simulation Input for Figures (SPICE and SAMPLE).....	224

ACKNOWLEDGEMENTS

I want to acknowledge the staff and employees of Sandia National Laboratories for funding and furthering my research, particularly Ron Light. The guidance of the professors at Berkeley has been invaluable toward achieving my goals. I wish to thank Ted van Duzer, Bill Oldham, Dennis Hess, Eugene Wong, and Mike Lieberman for their roles. Students at UCB are also exceptional. I wish to acknowledge Reza Kazerounian for his help in processing, Harry Weeks and Sharad Nandgaonkar for adding their genius to the computer, and Dave Haas and Gary Atkinson for their humor and encouragement. Without Kathleen Nichols I would have thrown in the towel before graduating.

My stay in California has been much more than academia and computers. I wish to thank those who have shown Christ's love to me, and particularly to two ministers, Jack Buckley and Bill Kellogg, who are a credit to the word 'minister'. I want to express my gratitude for the support of friends far away, too.

Finally and importantly, I want to acknowledge the guidance, patience and kindness of the person that made my completing this work possible, my research advisor, Andy Neureuther.

—John Reynolds

Figure 1.1
Computer simulation of isotropic etching.

Figure 1.2
Computer simulation of anisotropic etching.

Figure 1.3
Division of the plasma etching model into two problems. The plasma characteristics and how they depend on laboratory conditions. The etching mechanisms and how they depend upon the plasma characteristics.

Figure 2.1
Characteristic frequencies of a radio frequency plasma. High density ionization above the line and low density ionization below the line.

Figure 2.2
Reactor cross section for the Plasma Therm PK-12.

Figure 2.3
Current and voltage characteristic for an rf plasma with the rf voltage superimposed. Initially the electron current is much larger than the ion current.

Figure 2.3B
Current and voltage characteristic for an rf plasma with the rf voltage superimposed. In equilibrium a dc bias forms to match the electron current and the ion current.

Figure 2.4
Current and voltage characteristic for an rf plasma with equal electrode areas.

Figure 2.5
Potential distribution between the electrodes in a parallel plate reactor.

Figure 2.6
Definitions of isotropic etching, directional etching, and the degree of anisotropy.

Figure 2.7
Kushner's multi-component model for plasma etching.¹

Figure 2.8
Koenig-Maisel equivalent circuit model for rf sputtering system.²

¹ M.J. Kushner, "A kinetic study of the plasma etching process: I. A model for etching Si and SiO₂ in C₂F₄/H₂ and C₂F₄/O₂ plasmas," *Journal of Applied Physics*, vol. 53, no. 4, p. 2923, (April 1982).

² H.R. Koenig and L.I. Maisel, "Application of rf discharges to sputtering," *IBM Journal of Research and Development*, vol. 14, no. 3, p. 168, (March 1970).

Figure 2.9

Zarowin's ellipse of ion transport directionality.³

Figure 3.1

Equivalent circuit representation for the plasma in a planar system with equal electrode areas.

Figure 3.2

SPICE transient analysis for the equivalent circuit in Figure 3.1.⁴

Figure 3.3

RF Matching network with two variable capacitors to tune the plasma impedance to the 50 Ω source resistance.

Figure 3.4

The real and imaginary parts of the plasma impedance as a function of pressure at 100, 250 and 400 Watts for 20 sccm Carbon Tetrafluoride and 10% Oxygen.

Figure 3.5

The real and imaginary parts of the plasma impedance as a function of pressure at 100, 250 and 400 Watts for 20 sccm Sulfur Hexafluoride and 10% Oxygen.

Figure 3.6

The real and imaginary parts of the plasma impedance as a function of pressure at 100, 250 and 400 Watts for 20 sccm Hexafluoroethane and 10% Oxygen.

Figure 3.7

The real and imaginary parts of the plasma impedance as a function of pressure at 100, 250 and 400 Watts for 20 sccm Argon.

Figure 3.8

The real and imaginary parts of the plasma impedance as a function of power at 100 mT for 20 sccm Carbon Tetrafluoride with 10% Oxygen.

Figure 3.9

The real and imaginary parts of the plasma impedance as a function of power at 100 mT for 20 sccm Sulfur Hexafluoride with 10% Oxygen.

³ C.B. Zarowin, "Plasma etch anisotropy - Theory and some verifying experiments relating ion transport, ion energy and etch profiles," *Journal of the Electrochemical Society*, vol. 130, no. 5, p. 1144, (May 1983).

⁴ L.W. Nagel, "SPICE2: A computer program to simulate semiconductor circuits," *ERL Memo*, no. ERL M520, Electronics Research Laboratory, University of California, Berkeley, May 1975.

Figure 3.10

The negative DC bias on the substrate versus pressure at 100, 250 and 400 Watts for 20 sccm Carbon Tetrafluoride and 10% Oxygen.

Figure 3.11

The negative DC bias on the substrate versus pressure at 100, 250 and 400 Watts for 20 sccm Sulfur Hexafluoride and 10% Oxygen.

Figure 3.12

The negative DC bias on the substrate versus pressure at 100, 250 and 400 Watts for 20 sccm Hexafluoroethane and 10% Oxygen.

Figure 3.12B

The negative DC bias on the substrate versus pressure at 100, 250 and 400 Watts for 20 sccm Argon.

Figure 3.13

DC bias on substrate electrode versus power at 100 mTorr for Carbon Tetrafluoride and Sulfur Hexafluoride mixed with oxygen.

Figure 3.14

Schematic for measuring emission intensities and optical spectra from the plasma.

Figure 3.15

Fluorine emission intensity at 703.7 nm versus power at 50 mTorr for Carbon Tetrafluoride and Sulfur Hexafluoride mixed with oxygen.

Figure 3.16

Fluorine emission intensity at 703.7 nm versus pressure at 100, 250 and 400 Watts for Carbon Tetrafluoride mixed with oxygen.

Figure 3.17

Fluorine emission intensity at 703.7 nm versus pressure at 100, 250 and 400 Watts Sulfur Hexafluoride mixed with oxygen.

Figure 3.18

Fluorine emission intensity at 703.7 nm versus pressure at 100, 250 and 400 Watts Hexafluoroethane mixed with oxygen.

Figure 3.19

Argon emission intensity at 750.4 nm versus pressure at 100, 250 and 400 Watts.

Figure 3.20

Normalized fluorine emission intensity (703.7:750.4 nm) versus pressure at 100, 250 and 400 Watts for Carbon Tetrafluoride mixed with oxygen.

Figure 3.21

Normalized fluorine emission intensity (703.7:750.4 nm) versus

pressure at 100, 250 and 400 Watts Sulfur Hexafluoride mixed with oxygen.

Figure 3.22

Normalized fluorine emission intensity (703.7:750.4 nm) versus pressure at 100, 250 and 400 Watts Hexafluoroethane mixed with

Figure 4.1

a). Computer simulation of the cantilever structure and b). etching with isotropic and anisotropic components.

Figure 4.2

Computer simulation of the cantilever structure with a degree of anisotropy of 0.40 a). without surface migration and b). with surface migration of characteristic length $0.2 \mu m$.

Figure 4.3

Computer simulation of the cantilever structure using an source distribution angle of 30 degrees and two different spacer thicknesses.

Figure 4.4

Cantilever structure with Ti mask; a). top view, b). profile, c). edge close-up, and d). close-up at polyimide support. Etching conditions - 100 sccm $CF_4/10\%O_2$, 100 Watts at 100 mTorr.

Figure 4.5

Cantilever structure with hardened resist mask matrix for Carbon Tetrafluoride. Powers: o- 100 Watts, +- 250 Watts, & *- 400 Watts. Pressures: o- 50 mTorr, +- 100 mTorr, & *- 200 mTorr. Flowrates: - 5 sccm, o- 20 sccm, & +- 100 sccm.

Figure 4.6

Cantilever structure with hardened resist mask matrix for Sulfur Hexafluoride. Powers: o- 100 Watts, +- 250 Watts, & *- 400 Watts. Pressures: o- 50 mTorr, +- 100 mTorr, & *- 200 mTorr. Flowrates: - 5 sccm, o- 20 sccm, & +- 100 sccm.

Figure 4.7

Cantilever structure with hardened resist mask matrix for Hexafluoroethane. Powers: o- 100 Watts, +- 250 Watts, & *- 400 Watts. Pressures: o- 50 mTorr, +- 100 mTorr, & *- 200 mTorr. Flowrates: - 5 sccm, o- 20 sccm, & +- 100 sccm.

Figure 5.1

Percentage of electrical shorts between parallel lines of poly-silicon versus line spacing.

Figure 5.2

Simulation of residue removal and gate definition using directional

etching and isotropic overetching.

Figure 5.3a

Etch rate ratio of poly-Si to SiO₂ (from reference [5].)

Figure 5.3b

Line-width lost and oxide etched during over etching time to remove residue at a 0.5 micrometer step.

Figure 5.4

Simulation of aluminum deposition in varying window sizes.

Figure 5.5

Profiles of dry etched silicon dioxide using non-reflowed and reflowed (angled) resist masks.

Figure 5.6

Simulation of the dry etching of silicon dioxide followed by aluminum deposition using straight and angled masks.

Figure 5.7

Relative resistance of aluminum across gaps and contact window expansion versus selectivity for two mask angles; a). 90°, non-reflowed and b). 45°, reflowed.

Figure 5.8

Simulation of a multistep process planarizing an edge by successively leaving residue; a). initial profile, a 0.3μm rectangular step, b). profile after the initial deposition /anisotropic etch cycle, c). profile after the second deposition /anisotropic etch cycle, d). profile after the third deposition /anisotropic etch cycle.

Figure 5.9

Simulations of planarization by filling gaps with isotropically deposited material and then anisotropically back etching.

Figure 5.10

Scanning electron micrographes of planarization processes using successive isotropic deposition and anisotropic etching: a). a space and an edge b). an edge c). a 2 micrometer space and d). a 7 micrometer space.

Figure 5.11

Comparison of aluminum application over planarized and non-planarized surfaces.

* D.L. Flamin, D.N.K. Wang, and D. Maydan, "Multiple etchant loading effect in ClF₃ and related mixtures," *Journal of the Electrochemical Society*, vol. 129, no. 12, p. 2755, (December 1982).

Figure 6.1

Poly-silicon profiles etched to an end point in Sulfur Hexafluoride and oxygen. Top left-150 Watts. Top right-250 Watts. Bottom left-350 Watts. Bottom right-450 Watts.

Figure 6.2

Poly-silicon profile just prior to end point etched in $SF_6/10\%O_2$.

Figure 6.3

Computer simulation of a poly-silicon profile etched isotropically at three different times.

Figure 6.4

Computer simulation of a poly-silicon profile etched anisotropically with accelerating rate upon endpoint.

Figure 6.5

Computer simulation of a poly-silicon profile etched anisotropically with an eroding mask at three different times.

Figure 6.6

Micrographes of profiles etched anisotropically under the same conditions with hard-baked photo resist (top) and unbaked photo resist (bottom).

Figure 6.7

Computer simulation of a poly-silicon profile etched anisotropically with surface migration upon endpoint at three different times.

Figure 6.8

Poly-silicon profile etched in 180 sccm CF_4 , 20 sccm O_2 , 3.5 mTorr, 150 Watts. Top - etched to an endpoint. Bottom - over-etched by 50%.

Figure 6.9

Poly-silicon profile etched in 180 sccm CF_4 , 20 sccm O_2 , 3.5 mTorr, 350 Watts. Top - etched to an endpoint. Bottom - over-etched by 50%.

Figure 6.10

Poly-silicon profile etched in 160 sccm CF_4 , 20 sccm CF_3Cl , 20 sccm O_2 , 3.5 mTorr, 150 Watts. Top - etched to an endpoint. Bottom - over-etched by 50%.

Figure 6.11

Poly-silicon profile etched in 180 sccm CF_4 , 20 sccm CF_3Cl , 20 sccm O_2 , 3.5 mTorr, 350 Watts. Top - etched to an endpoint. Bottom - over-etched by 50%.

Figure 6.12

Poly-silicon profile etched in 140 sccm CF_4 , 40 sccm CF_3Cl , 20 sccm O_2 , 3.5 mTorr, 150 Watts. Top - etched to an endpoint. Bottom - over-etched by 50%.

Figure 6.13

Poly-silicon profile etched in 140 sccm CF_4 , 40 sccm CF_3Cl , 20 sccm O_2 , 3.5 mTorr, 350 Watts. Top - etched to an endpoint. Bottom - over-etched by 50%.

Figure 6.14

Silicon nitride profile etched in 180 sccm CF_4 , 20 sccm O_2 , 3.5 mTorr, 150 Watts. Top - etched to an endpoint. Bottom - over-etched by 50%.

Figure 6.15

Silicon nitride profile etched in 180 sccm CF_4 , 20 sccm O_2 , 3.5 mTorr, 350 Watts. Top - etched to an endpoint. Bottom - over-etched by 50%.

Figure 6.16

Silicon nitride profile etched in 180 sccm CF_4 , 20 sccm CF_3Cl , 20 sccm O_2 , 3.5 mTorr, 150 Watts. Top - etched to an endpoint. Bottom - over-etched by 50%.

Figure 6.17

Silicon nitride profile etched in 180 sccm CF_4 , 20 sccm CF_3Cl , 20 sccm O_2 , 3.5 mTorr, 350 Watts. Top - etched to an endpoint. Bottom - over-etched by 50%.

Figure 6.18

Silicon nitride profile etched in 140 sccm CF_4 , 40 sccm CF_3Cl , 20 sccm O_2 , 3.5 mTorr, 150 Watts. Top - etched to an endpoint. Bottom - over-etched by 50%.

Figure 6.19

Silicon nitride profile etched in 140 sccm CF_4 , 40 sccm CF_3Cl , 20 sccm O_2 , 3.5 mTorr, 350 Watts. Top - etched to an endpoint. Bottom - over-etched by 50%.

Figure 7.1

Energy distributions for electrons in CF_4 plasma and CF_4 plasma with oxygen addition.⁶

⁶ J.W. Coburn and E. Kay, "Some chemical aspects of the fluorocarbon plasma etching of silicon and its compounds," *IBM Journal of Research and Development*, vol. 23, no. 1, p. 33, (January 1979).

CHAPTER ONE

1. INTRODUCTION

1.1. Historical

Radio Frequency (rf) generated glow discharge etching has found many uses in semiconductor processing and manufacture. Originally, sputter etching was the completely physical removal of material by energetic charged Ar^+ ions.¹ High power levels were necessary to achieve reasonable etch rates for the types of materials in semiconductor device fabrication. These are impractical because such power densities (greater than 1 Watt/cm^2) result in poor images due to poor material selectivity, surface damage, and significant temperature increases.

This method of pattern transfer can be contrasted to the conventional wet etching techniques² using reactive chemicals. There is far better selectivity and less damage, but there exists a loss in process control due to the continued etching occurring during wafer rinsing and a loss in line width due to mask undercut. Dry process technology advanced to include new applications of the glow discharge³ to plasma assisted etching and reactive ion etching (RIE). A reactive gas is used in the rf glow discharge to etch silicon and compounds at appreciable rates. The chemical reactions and the physical enhancement lead to etch rates over an order of magnitude higher along with a reduction in surface damage and heating effects.

Plasma etching has the advantages of the absence of wet rinses, of profile shape control, and of image size control with the cessation of etching when the rf plasma is extinguished and the reduction of isotropic undercut. These

advantages have been realized in etching poly-silicon, silicon nitride, silicon dioxide, aluminum, photo resist removal (ashing), and most other patterning⁴ in integrated circuit processing. The reduced feature sizes and controlled processing has made VLSI (Very Large Scale Integration) possible, (eg. references[5, 6, 7].), plus the flexibility allows for reactive process designs (eg. references[8, 9].) The capabilities of plasma etching has increased faster than the understanding of the complicated physics and chemistries involved. It is definitely useful to characterize plasma processing to make present capabilities reproducible and also to allow creative extensions into new applications.

1.2. The Two Box Model

This dissertation documents several characteristics of the plasma toward a model of the complete dry etching process from laboratory observables to etched profiles. Figures 1.1 and 1.2 illustrate two extremes in etching using computer simulation¹⁰ of the profile cross-section. The profile in Figure 1 evolves from a pure isotropic rate that is characteristic of wet chemical etching or plasma etching in a barrel reactor^{11, 12} where the sample is shielded from most physical bombardment. The second profile results from totally directional, anisotropic etching. Now dry etched structures range between these two extremes with a variety of additional mechanisms. Chapters Four, Five and Six report various aspects of these mechanisms.

Chapter Four illustrates the mechanisms of surface migration and angularly distributed effects using cantilever structures in experiment and computer simulation. Chapters Five and Six are more applied, describing dry etching effects on common IC (integrated circuit) topographies and in thin film layers, respectively. The emphasis of these chapters is on profile control and shape of the etched structures.

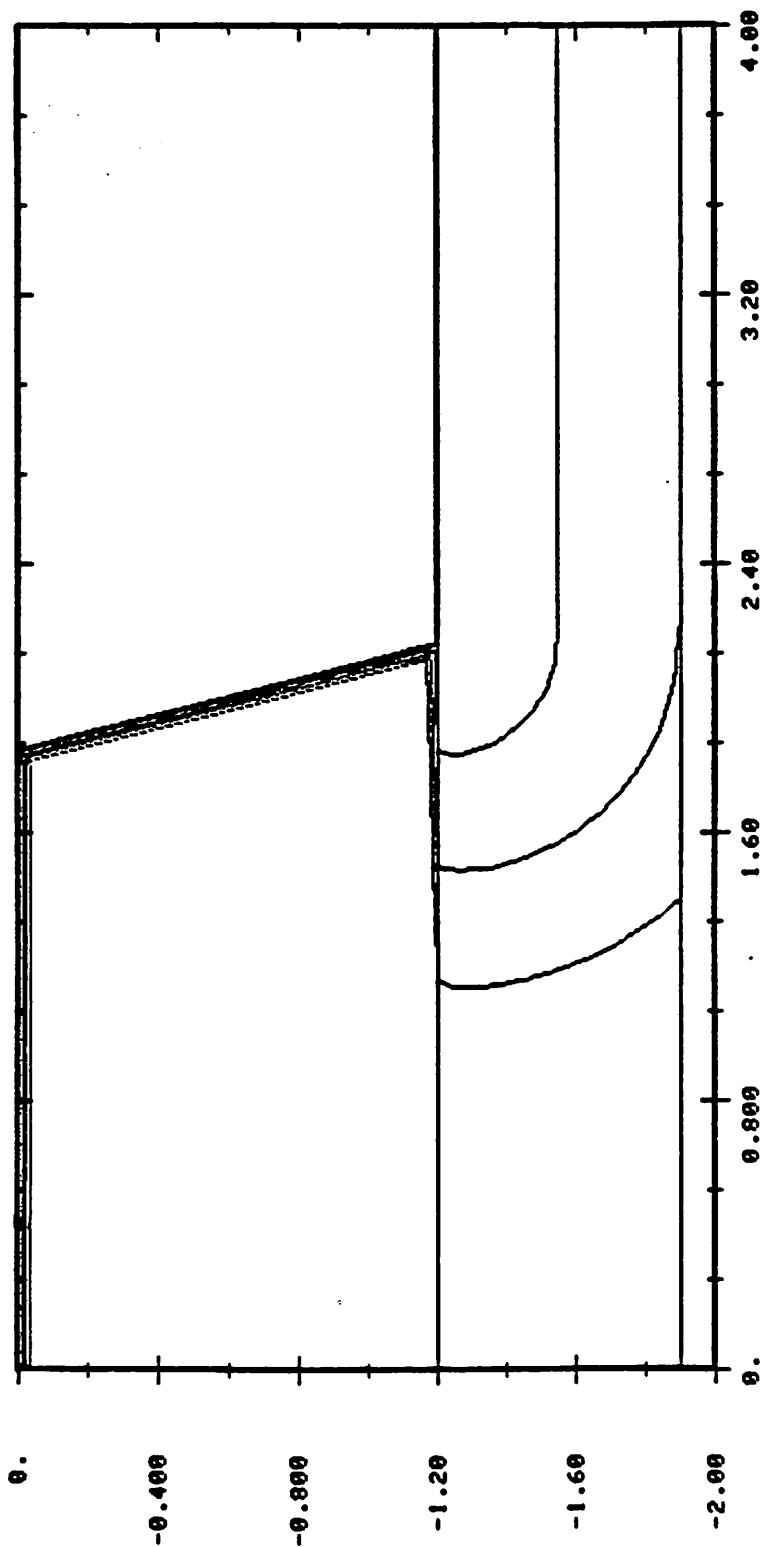


Figure 1.1 Computer simulation of isotropic etching.

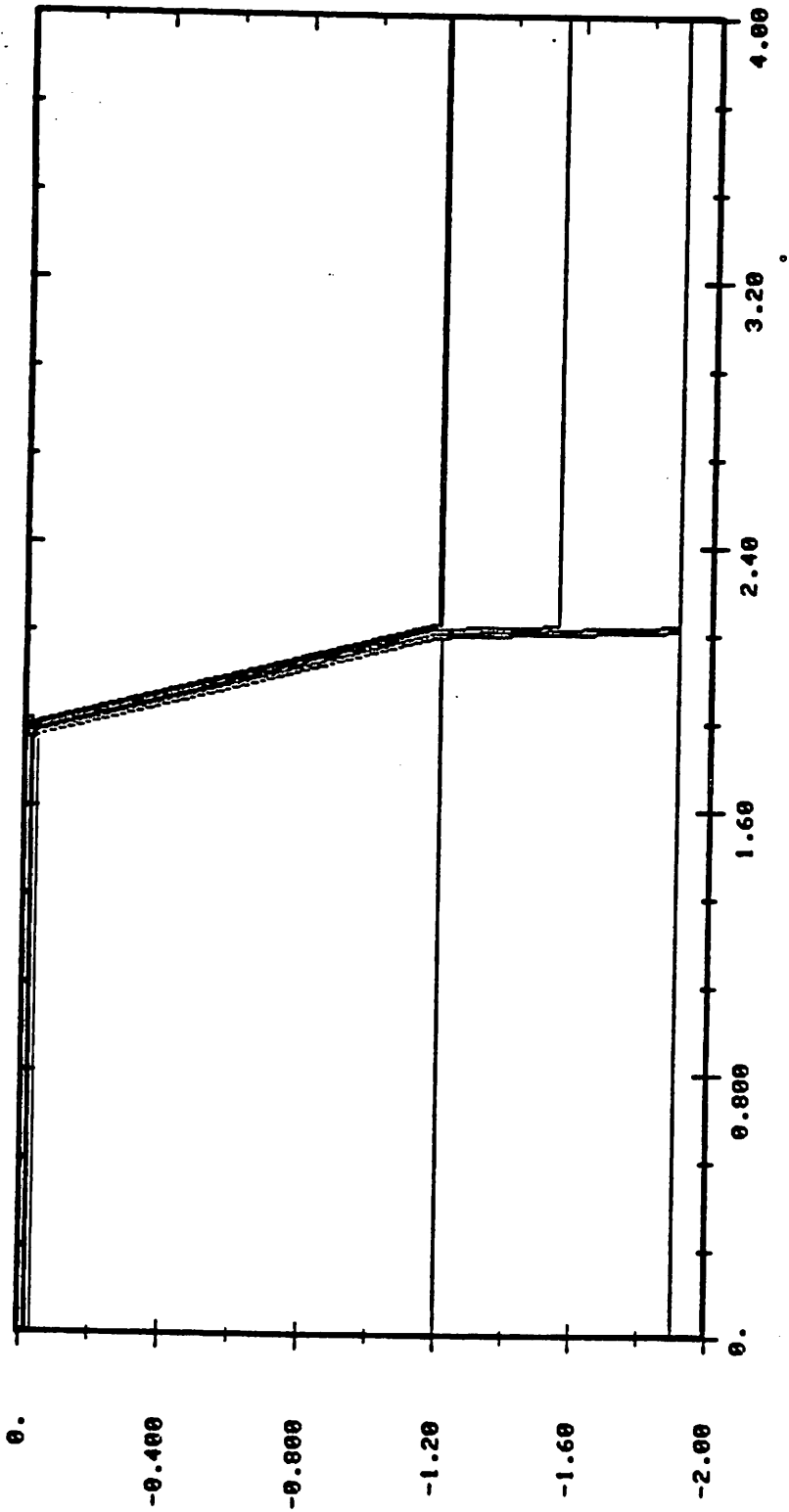


Figure 1.2 Computer simulation of anisotropic etching.

Chapter Two emphasizes the fundamental physics and present understanding of plasma etching. It looks at various aspects of the plasma and how they affect the etching. Chapter Three reports non-intrusive means of experimentally characterizing the plasma through monitoring the impedance, the dc bias, and the optical emission spectra for selected wavelengths.

With these two segments, Chapter Seven proposes a model for plasma etch rates in two dimensions in terms of the plasma characteristics discussed in Chapter Three. It discusses the model in terms of the schematic in Figure 1.3. Laboratory conditions and system parameters are used to predict certain plasma characteristics; say n_i , the ion density, and V_{DC} , the dc bias potential across the sheath. A rate depending on the flux of ions (related to n_i) and their energy (related to V_{DC}) gained in crossing the sheath can be calculated. Chemical species have similar terms for representing their density and transport efficiency to the etching surface. Finally, the appendices describe the plasma etching reactor and computer aids that were used to generate and measure the data presented herein.

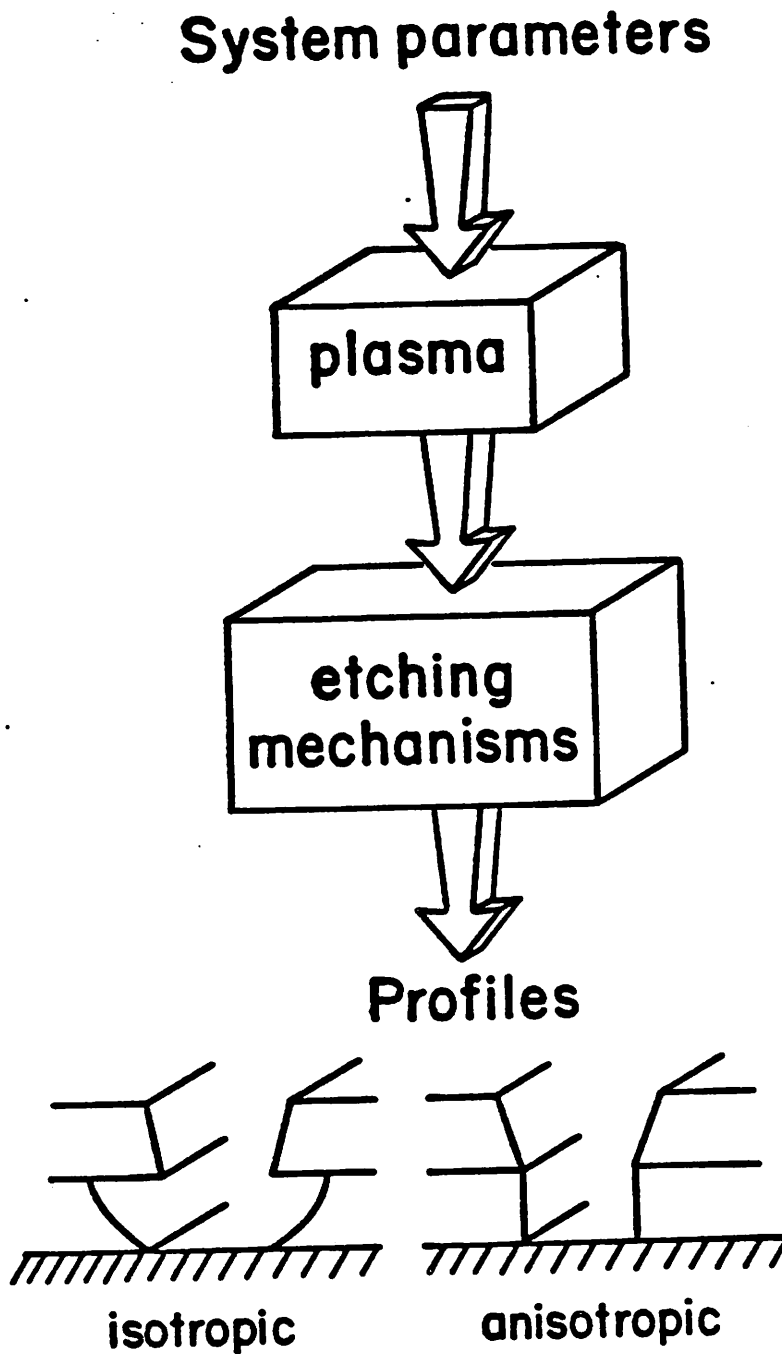


Figure 1.3

Division of the plasma etching model into two problems. The plasma characteristics and how they depend on laboratory conditions. The etching mechanisms and how they depend upon the plasma characteristics.

References

1. S. Somekh, "Introduction to ion and plasma etching," *Journal of Vacuum Science and Technology*, vol. 13, no. 5, p. 1003, (1975).
2. L.T. Romankiw, "Pattern generation in metal films using wet chemical techniques," in *Etching for Pattern Definition*, Electrochemical Society symposium series, (1976).
3. J.A. Bondur, "Dry process technology," *Journal of Vacuum Science and Technology*, vol. 13, no. 5, p. 1023, (May 1976).
4. Maddox and Parker, "Application of reactive plasma to practical microelectric processing systems," *Solid State Technology*, p. 107, (April 1978).
5. L.M. Ephrath, "Reactive ion etching for VLSI," *IEEE-Transactions on Electron Devices*, vol. ED 28, no. 11, p. 1315, (November 1981).
6. K. Hirata, Y. Ozaki, M. Oda, and M. Kimizuka, "Dry etching technology for 1um VLSI fabrication," *IEDM*, p. 405, (December 1980).
7. T. Shibata, K.Hieda, M Sato, M. Konaka, R.L.M. Dang, and H. Zizukai, "An optimally designed process for submicron MOSFETs," in *1981 IEDM Technical Digest*, p. 647, (1981).
8. W.R. Hunter, T.C. Holloway, P.K. Chatterjee, and A.F. Tasch, "New edge-defined vertical etch approaches for submicrometer MOSSFET fabrication," *IEDM*, p. 764, (December 1980).
9. S. Watanabe, "SET - Stepped electrode transistor," in *Semi-conductor Silicon*, p. 992, Electrochemical Society Symposium Series, (1977).
10. W.G. Oldham, A.R. Neureuther, J.L. Reynolds, C.S. Sung, and S.N. Nandgaonkar, "A general simulator for VLSI lithography and etching processes: Part II application to deposition and etching.," *IEEE-Transactions on Electron*

Devices, vol. ED 27, no. 8, (August 1980).

11. P.G.T. van de Ven and P.A. Zijlstra, "A critical comparison of SiF₄/O₂ and CF₄/O₂ as plasma etching gasses," in *Plasma Processing*, ed. R.G. Frieser & C.J. Mogab, Proceedings of the Symposium on Plasma Etching and Deposition, p. 112, The Electrochemical Society, (1981).
12. J.F. Battey, "The effects of geometry on diffusion controlled chemical reaction rates in a plasma," *Journal of the Electrochemical Society*, vol. 124, no. 3, p. 437, (March 1977).

CHAPTER TWO

2. BASIC CHARACTERISTICS OF PLASMAS

2.1. Introduction

Plasmas have been extensively utilized and modeled before interest grew in plasma etching processes. Basic studies of the plasma phenomena give us ways of mathematically describing the plasma with electromagnetic theory, and ways of quantifying the plasma with characteristic lengths, distributions, frequencies, densities and energies. Although these representatives themselves do not predict an etched profile directly, they are useful in setting the ground rules in plasma etching. The second major factor in plasma etching is the plasma chemistry. The surface reactions also greatly influence etch rates and profiles. This section summarizes the textbook knowledge of plasmas relevant to plasma etching and reviews some chemical considerations as well. Several calculations based on these basic models form a foundation for interpreting the experimental observations presented in later chapters.

2.2. Text book model.

2.2.1. Definitions and Background

Wulf Kunkel defines a plasma as "a collection of mobile charged particles that satisfy the condition that collective effects (i.e. due to long range effects) predominate, so each particle affects all others."¹ In order to satisfy the

requirement that long range effects do dominate, the Debye length defined as:

$$\lambda_D = \sqrt{\frac{k_B T_e}{4\pi e^2 n_e}} \approx 740 \sqrt{\frac{T_e (eV)}{n_e (cm^{-3})}} (cm) \quad (2.1)$$

is much smaller than the characteristic lengths as chamber dimensions. The Debye length defines over what range a perturbation decays in a plasma and also sets up the condition of quasi-neutrality ($n_i \approx n_e$) in the plasma body. For the collective effects to dominate the difference in the densities of charged particles $n_i - n_e$, ions and electrons respectively, must be small compared to the amount of charged particles, n_i or n_e .

Another defining characteristic is the plasma frequency, ω_p . This is a measure of the response of charged particles to a disturbance. It is defined as:

$$\omega_{pe} = \sqrt{\frac{4\pi e^2 n_e}{m_e}} \approx 2\pi \cdot 9000 \sqrt{n_e} \frac{rad}{s} \quad (2.2)$$

for electrons and

$$\omega_{pi} = \sqrt{\frac{4\pi e^2 n_i}{M_i}} \approx 2\pi \cdot 200 \sqrt{\frac{n_i}{A_i}} \frac{rad}{s} \quad (2.3)$$

for ions. The plasma frequency depends on mass which gives it an inertial interpretation and distinguishes the behavior of the ions from the electrons in the plasma. If one considers the charged particles coupled as harmonic oscillators, the plasma frequency is the division between frequencies at which disturbances are damped (collective behavior dominates) and frequencies at which the disturbances themselves dominate. When collisions, for example, overcome the collective behavior of charged particles the plasma is extinguished. Here, the collision frequency $2\pi \nu_{ei} \gg \omega_{pe}, \omega_{pi}$

Now compare these two descriptive quantities of the plasma to those characteristic of a plasma etching configuration. There are several reactor configurations; barrel, parallel plate (diode), and triode; made from different

materials; aluminum, anodized aluminum, quartz, stainless steel. For now consider a parallel plate reactor with conducting electrodes. (The primary system used for these studies is described in detail in Appendix A). The chamber is operated at low pressures from 0.001 to 1.0 Torr (0.133-133. Pascal). At these pressures, there are approximately $3.2 \cdot 10^{15}$ particles $-cm^{-3} n_0$
 $= 3.2 \cdot 10^{16} p$ (in Torr @ STP). The degree of ionization is low $\approx 10^{-4}$ so the electron and ion densities are $\sim 10^{11} cm^{-3}$. The electrons being less massive are much more active than the ions and typically have a thermal energy $\approx 2-3eV$.² The massive ions have a temperature close to that of the gas ($\approx 26meV$). Using these estimates, the Debye length follows at $\sim 30\mu m$ which is much smaller than any of the reactor dimensions which are on the order of centimeters.

The plasmas in dry etching are most often powered by high frequency power supplies. The higher frequencies enable a more continuous plasma.³ Electrons oscillating in the radio frequency field and elastically colliding with the gas atoms acquire enough energy to cause ionization of the atoms. The high voltage electrode of the dc discharge for secondary electron generation is not essential to maintain the discharge.⁴ Typical operating frequencies include 5 KHz, 48 MHz, and 13.56 MHz being by far the most common. From the charged particle density above and a typical ion of atomic number $A \approx 50$

$$\omega_{pe} \approx 2\pi \cdot 9000 \sqrt{10^{11}} = 2\pi 2.9 GHz \gg \text{generating frequency} \quad (2.4)$$

and

$$\omega_{pi} \approx 2\pi \cdot 200 \sqrt{\frac{10^{11}}{10}} = 2\pi 9. MHz \approx \text{generating frequency}. \quad (2.5)$$

The massiveness of the ions help in orienting the plasma for etching, but that is discussed in a later section.

Another convenient length that can be calculated from this basic theory is the mean free path of particles in the plasma. First, an electron/neutral

collision cross section, σ_{eo} , is estimated since the charged particles wander around and collide in a sea of neutrals. $\sigma_{eo} \approx 10^{-15} \text{cm}^2$ is approximated as an order of magnitude larger than the atomic cross section.⁵ The mean free path is therefore:

$$\lambda_{mfp} = \frac{1}{\sigma_{eo} n_o} \approx \frac{1}{32p(\text{Torr})} \text{cm}. \quad (2.6)$$

Collisions and scattering act as randomizing effects in the plasma and it is desirable to minimize these for controllable, anisotropic etching. Table I shows how different pressures affect the mean free path and collision frequency.

The collision frequency can be calculated from the thermal velocity,

$$v_e = \sqrt{\frac{2k_B T_e}{m_e}} \approx 6 \cdot 10^7 \sqrt{T_e(\text{eV})} \frac{\text{cm}}{\text{sec}} \approx 10^8 \frac{\text{cm}}{\text{sec}}. \quad (2.7)$$

$$\nu_{eo} = \left(\frac{v_e}{\lambda_{mfp}} \right) = n_o \langle \sigma_{eo} v_e \rangle \approx 2 \cdot 10^9 p(\text{Torr}) \sqrt{T_e(\text{eV})}. \quad (2.8)$$

Note how practically the collision frequency falls between the generator frequency and the electron plasma frequency. Figure 2.1 summarizes these characteristic frequencies graphically.

The plasmas generated for dry etching vary between high and low ion densities depending on the power density and the efficiency of the coupling of the rf power into the discharge. The sparsity of charged particles, about 0.01% of the total, make the ion-electron collision events (ν_{ei}) the most rare. The ion and electron plasma frequencies (f_i and f_e) vary with the ion density of the plasma and differ by their mass difference. For a given pressure, here 50 mTorr, the electron neutral collision frequency is fixed since it depends on the concentration of neutrals. The operating frequency, 13.56 MHz, is fixed by Federal Communication Commission regulations³ as an industrial standard.

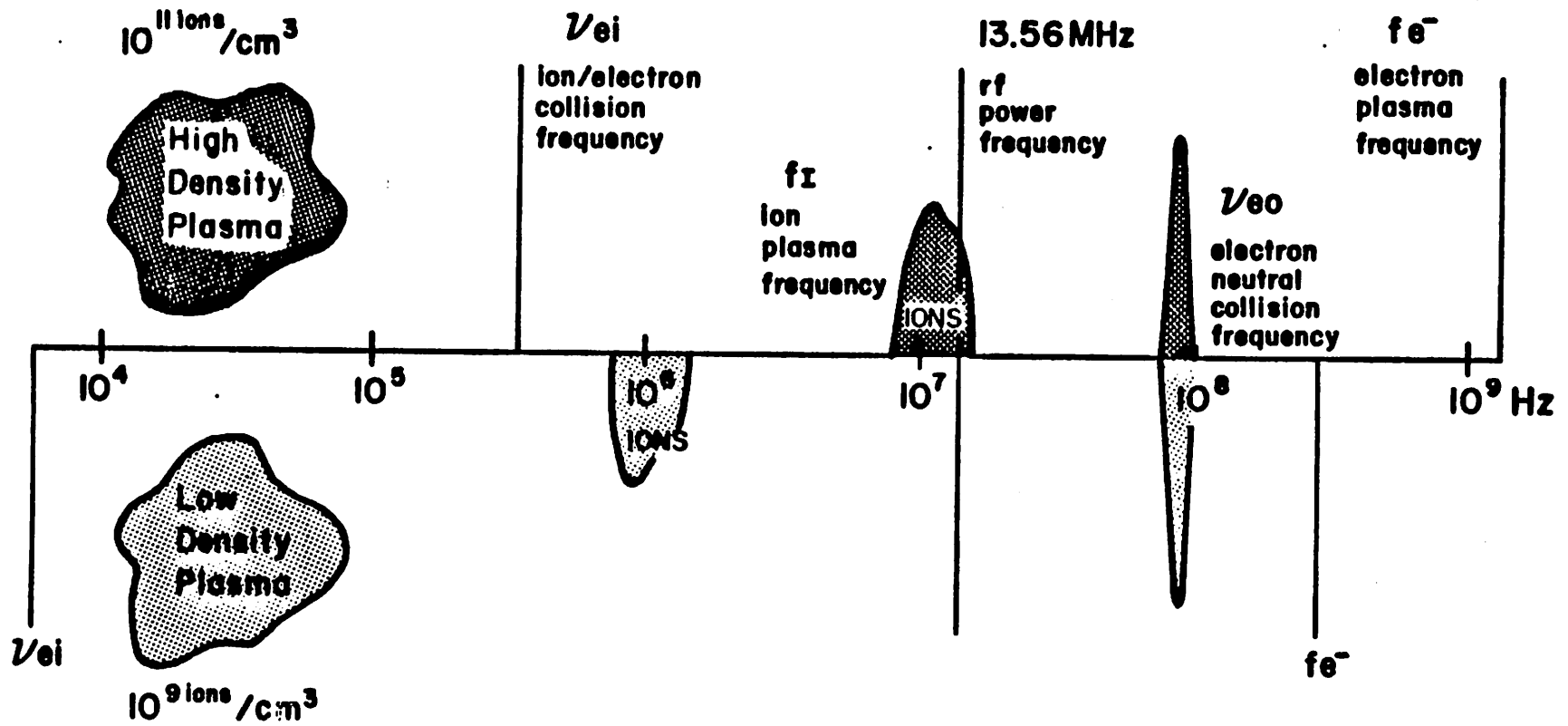


Figure 2.1

Characteristic frequencies of a radio frequency plasma. High density ionization above the line and low density ionization below the line.

Table 2.1

pressure	λ_{mfp}	ν_{eo}
1 mT	31. cm	3.3 MHz
10 mT	3.1 cm	33. MHz
100 mT	0.31 cm	333 MHz
1 Torr	0.31 mm	3.3 GHz

The massive ions cannot move through the plasma as the electrons do, so a different velocity than the thermal velocity is used to characterize their motion.

This is the ion acoustic velocity⁸ given by $u_i = \sqrt{\frac{k_B T_e}{M_i}} \approx 10^6 \sqrt{T_e (eV)} \frac{cm}{s}$

and represents the motion of the ions pulled along behind the mobile electrons.

With the ions moving at this velocity, it is instructive to see what distance they travel in an rf half-cycle.

$$d_{iu} = \frac{u_i}{2f_{rf}} = 0.2mm. \quad (2.9)$$

This distance is small compared to the body of the plasma and suggests that the ions' motion is only detectable at the edges of the plasma. This length and motion depend on the ion mass and they thus vary for different ions in the plasma.

2.2.2. Calculations and physics.

With this background on the plasma, we can continue now to talk about how the text book model represents etching in a parallel plate reactor. A prototypical reactor is shown in Figure 2.2 and discussed at length in Appendix A. The more mobile electrons move about the chamber sensing the rf fields. A typical

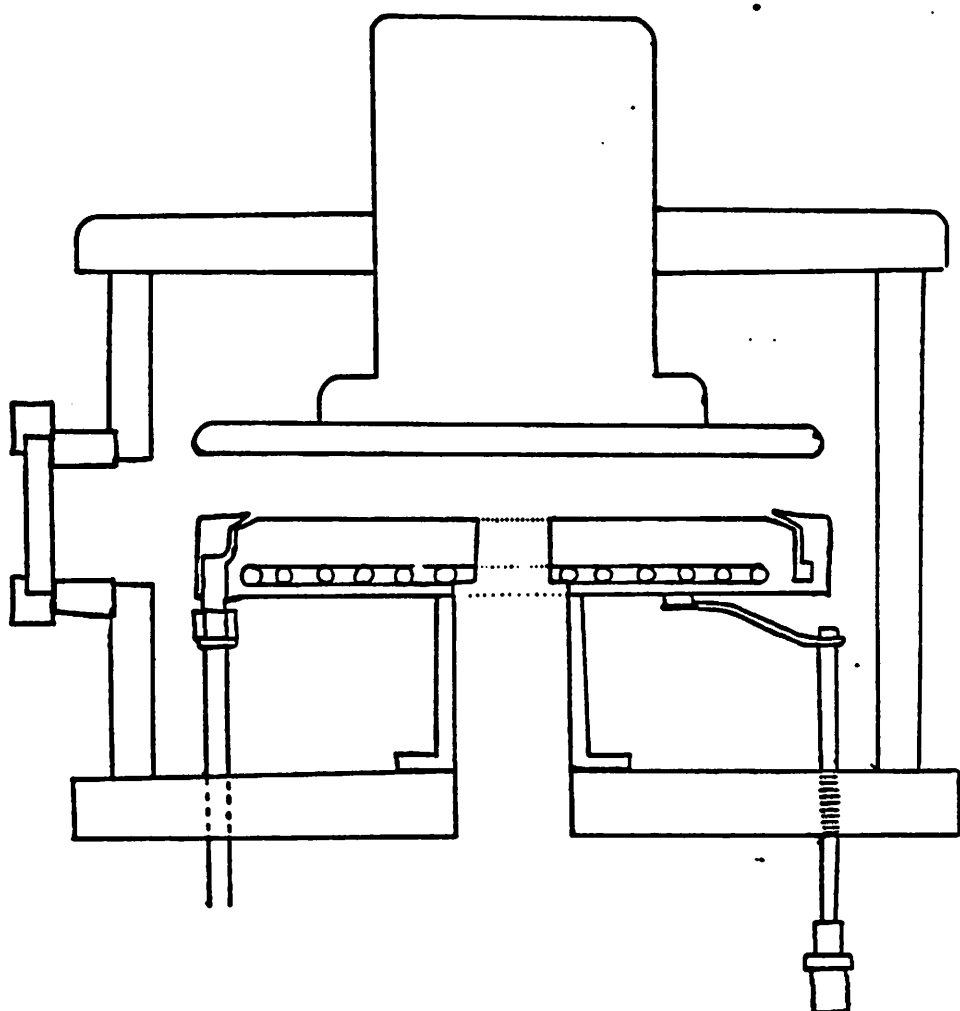


Figure 2.2
Reactor cross section for the Plasma Therm PK-12.

distance is $d_e = \frac{v_e}{2f_{rf}} \sim 4 \text{ cm} \geq \text{reactor dimensions}$. The electrons can reach the chamber walls during one half-cycle. In order that the plasma does not become depleted of electrons and violate quasi-neutrality which would extinguish the plasma, a negative dc bias builds up on the reactor walls in the rf applied field. The plasma then sits at the most positive potential in the chamber and the negative bias acts to balance the flux of ions and electrons exiting the plasma. The transition region between the confined plasma and the negative walls is called the sheath. This sheath is of primary importance since it surrounds the substrates during the etching process. Species generated in the plasma must cross the sheath to initiate etching. Since the mass difference between ions and electrons causes the formation of the sheath, it cannot be modeled as a linear circuit element. At best it is considered a rectifier. For positive voltages a large electron current can flow, but for negative voltages a much smaller mobility limited ion current flows. Figure 2.3 illustrates this I-V characteristic plus the rf voltage superimposed. A massive electron flux can escape the plasma until the dc bias forms to equilibrate the ion and electron currents.

From this diode model of the sheath, the geometrical dependence on the self-bias can be seen. When the area of the powered electrode is small compared to the grounded area in the chamber much rectification occurs at the smaller electrode. The sheath size increases and the dc bias goes more negative as more electrons build up in the smaller area. If the powered electrode is relatively larger, then rectification is small per unit area and the sheath and bias decrease. Figures 2.3b and 2.4 compare these situations schematically. The dc potential dependence on areas can be derived using the Child-Langmuir law.⁴

$$\left(\frac{V_{dc1}}{V_{dc2}} \right) = \left(\frac{A_2}{A_1} \right)^{4/3} \quad (2.10)$$

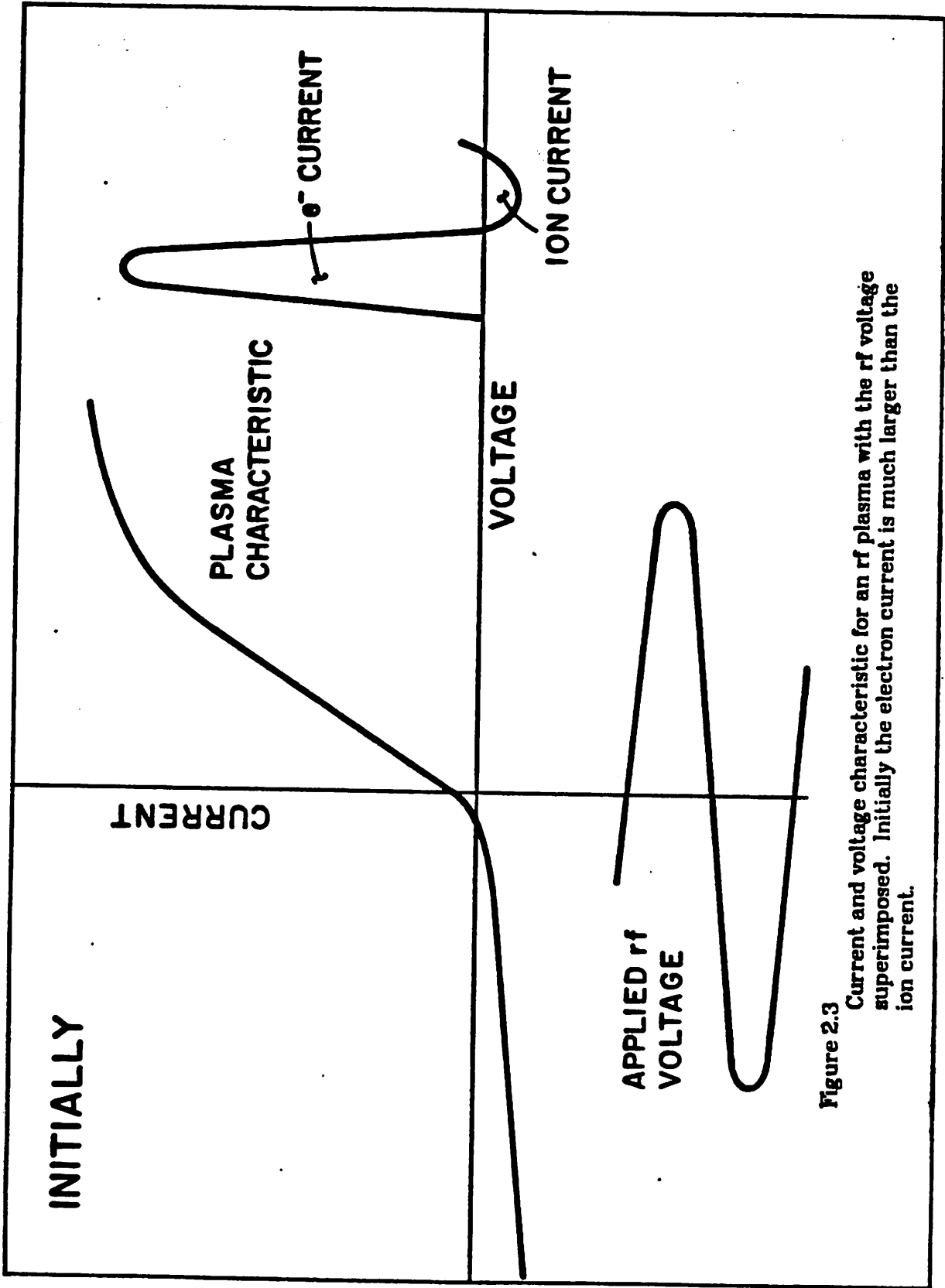
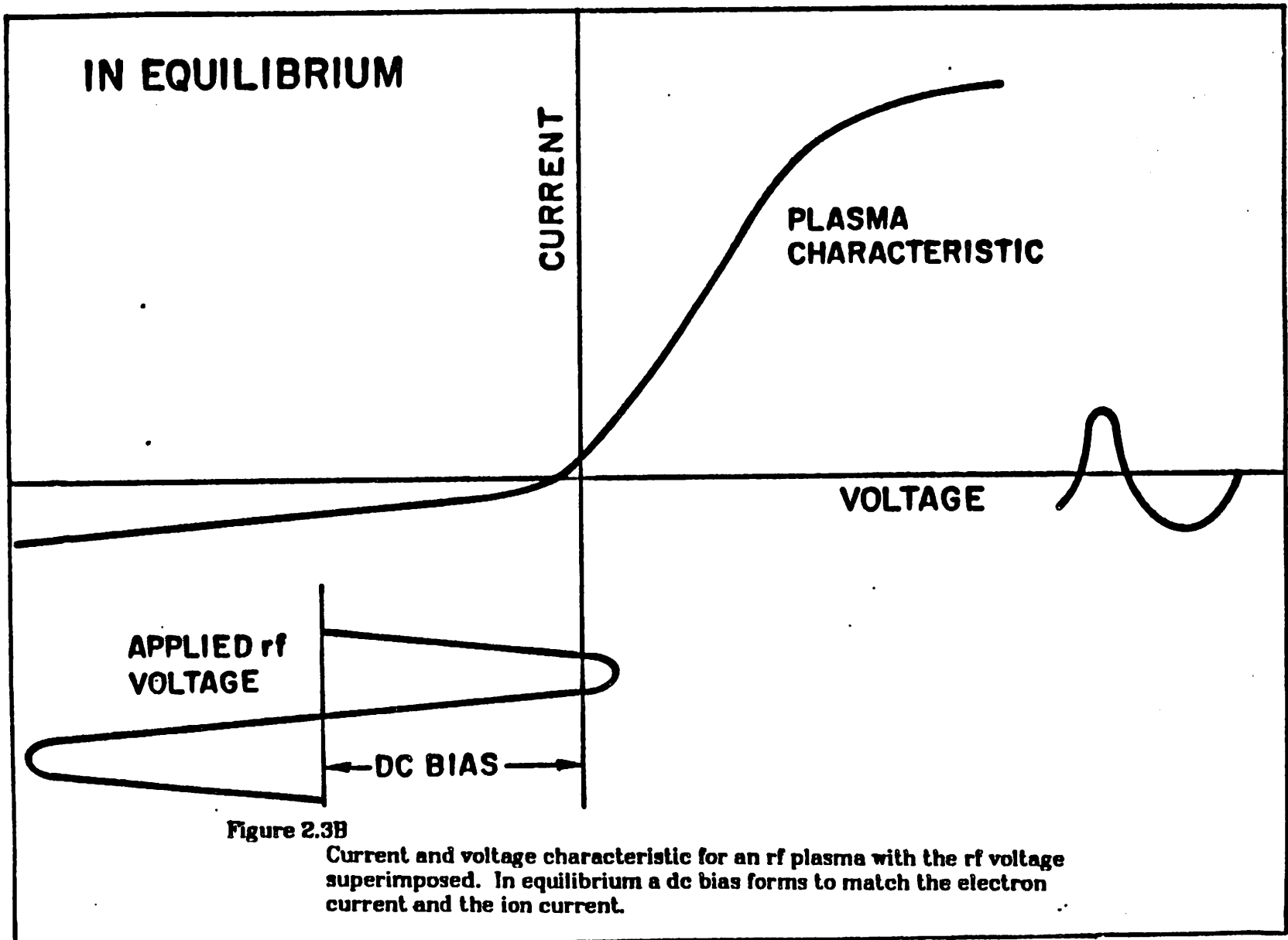


Figure 2.3 Current and voltage characteristic for an rf plasma with the rf voltage superimposed. Initially the electron current is much larger than the ion current.



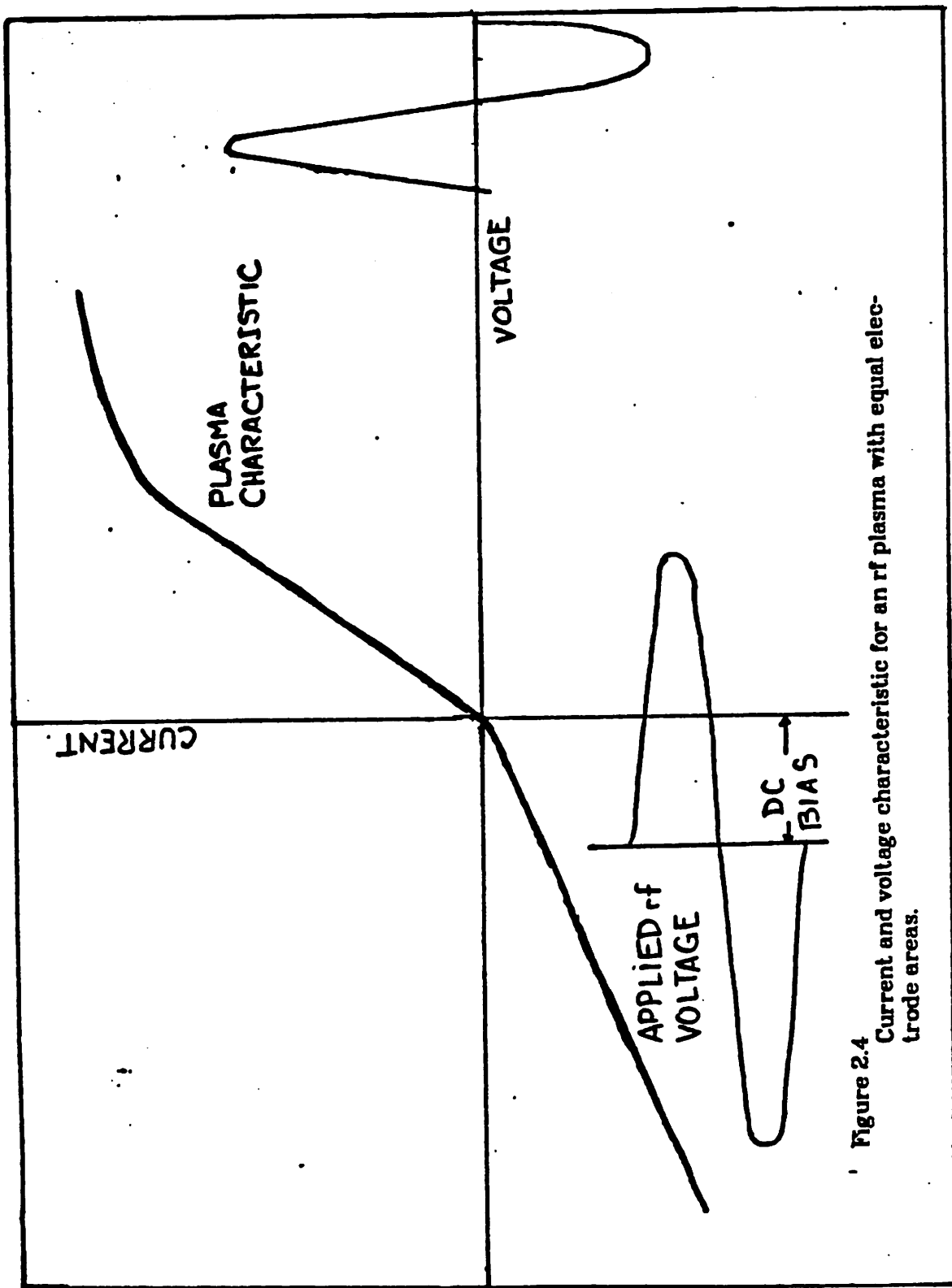


Figure 2.4 Current and voltage characteristic for an rf plasma with equal electrode areas.

Experimentally the dependence is less than the 4th power, ($\approx 1.4^{\text{th}}$ power)⁴ due to collisions in the sheath for which the Child-Langmuir law does not account. Ambipolar diffusion also affects the transport and potential variation.³ Applying the area dependent bias, a hexagonal electrode (hexode) reactor⁷ with the center column powered and the surrounding chamber grounded maximizes the area ratio to increase this dc self-bias for etching wafers attached to the center electrode.

Some of the effects of the reactor design can be accounted for by this model. In reactive ion etching (RIE), the samples sit on the smaller powered electrode and are thus bombarded by higher energy ions hurled across a higher potential. In plasma-assisted etching the potential on the grounded electrode is lower causing less energetic bombardment. Figure 2.5 shows the potential distribution between the electrodes graphically.

From the small half-cycle motion of the ions, u_i , only the edge of the sheath is resourceful in supplying ions into the sheath. The density of ions subject to the Bohm sheath criterion,³ helps to provide information about the ion flux to the surface. The ion current density across the sheath

$$J_i = qn_i e \frac{v_s}{T_e} u_i \quad (2.11)$$

where $e \frac{v_s}{T_e}$ is the reduced ion Bohm factor at the sheath edge with $\frac{V_s}{T_e} \approx \frac{1}{2}$

$$= qn_i e \frac{1}{2} u_i \approx 5. \frac{\text{mAmps}}{\text{cm}^2}$$

For our configuration,

$$J_i = J_i A = 3. \text{Amps} \quad (2.12)$$

which is large but plausible for high power densities. Note this is a strong

VOLTAGE DISTRIBUTION ACROSS THE PLASMA

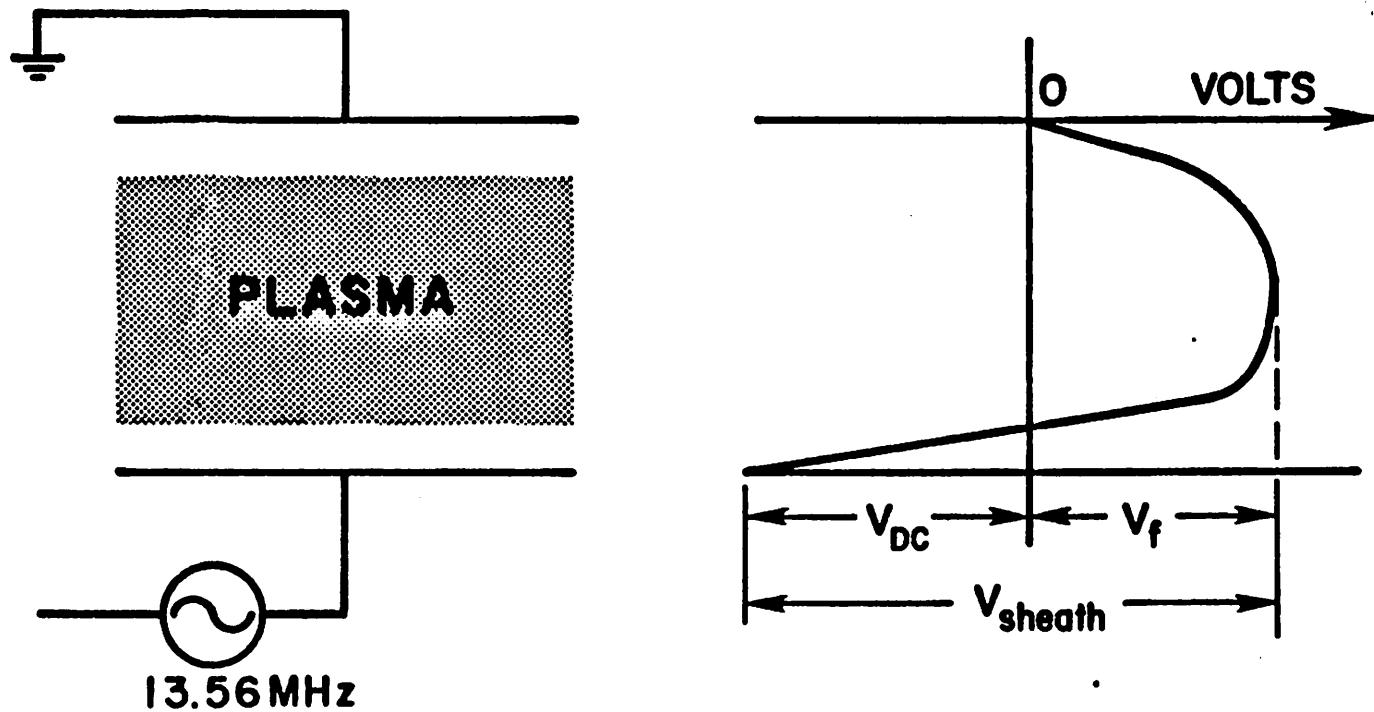


Figure 2.5
Potential distribution between the electrodes in an parallel plate reactor.

function of the ion density which we have only approximated. The ion density does not increase with the number of particles, i.e. the pressure, of the discharge. The ionized fraction, $\frac{n_i}{n_0}$, does not remain constant. Collisions occur in the plasma to produce many non-ionic species. The power is seen to increase the number density of charged particles in the plasma.

To get more quantitative information from this basic theory more details must be known about the sheath than the simple rectification model. The plasma also exhibits conduction and displacement currents which form a large part of the impedance information reported in this thesis. From the equation of motion for electrons in a plasma, equivalent circuit elements can be derived for the terms:

$$m_e \frac{\partial \bar{u}_e}{\partial t} = -q\bar{E}(t) - \nu_{e0} m_e \bar{u}_e \quad (2.13)$$

The first term represents the force due to the applied field and the second, that lost to collisions with neutrals. Linearizing, (which neglects harmonics and the rectification occurrence) gives:

$$m_e i\omega \bar{u}_e = -q\bar{E}(t) - \nu_{e0} m_e \bar{u}_e \quad (2.14)$$

$$\bar{u}_e = \frac{-q}{m_e} \left[\frac{\nu_{e0} + i\omega}{\nu_{e0}^2 + \omega^2} \right] \bar{E}(t) \quad (2.15)$$

The corresponding current is:

$$\bar{j}_e = n_e q \bar{u}_e \frac{n_e q^2}{m_e} \left[\frac{\nu_{e0} + i\omega}{\nu_{e0}^2 + \omega^2} \right] \bar{E}(t) \quad (2.16)$$

$$= [\sigma + i\omega\chi] \bar{E}(t)$$

$$\sigma = \frac{-n_e q^2 \nu_{e0}}{m_e (\nu_{e0}^2 + \omega^2)} \quad \text{and} \quad i\omega\chi = i\omega \frac{-n_e q^2}{m_e (\nu_{e0}^2 + \omega^2)} \quad (2.17)$$

This is the associated conductance and reactance of the electrons. The

reactance is due to the oscillation of electrons at the sheath edge.

A major contribution of this work is impedance characterization of the plasma. With the theory in this form and the geometry of our apparatus, a resistance and capacitance can be calculated and compared to experiment. Using

$$\nu_{eo} = 2. \text{GHz}, \omega = 14. \text{MHz}, n_e = 10^{11} \text{cm}^{-3}, l = 1.7 \text{cm}$$

$$\sigma = 0.022 \frac{\text{cm}}{\Omega} \quad R_{\text{plasma}} = \frac{A}{\sigma l} \approx 180 \Omega \quad (2.18)$$

$$\omega\chi = 0.15 \cdot 10^{-3} \frac{\text{cm}}{\Omega} \quad X_{\text{plasma}} = \frac{\omega\chi A}{l} \approx 5.5 \Omega \quad (2.19)$$

From this we have a reasonable estimate of the resistance of the plasma. It will be shown later that this resistance is within a factor of two of the experimentally measured resistance of the plasma. The electrons, we can conclude are primarily responsible for conduction in the plasma. The estimate for the reactance is far too low though. Concerning the displacement current we must consider other terms than the oscillation of electrons and the displacement current across the sheath must be added in series. Building the impedance model, the oscillation of the electrons can be neglected with respect to the sheath capacitance.

A second method looks at the oscillation of the sheath edge as a contribution to the plasma capacitance. Here the displacement current due to the motion of the sheath edge can be written:

$$j = qn\nu = qn \frac{dx}{dt} = qn \frac{dx}{dV} \frac{dV}{dt} \quad (2.20)$$

where the equivalent capacitance due to the oscillation of the sheath with the voltage is:

$$C^*(V) = qn \frac{dx}{dV} \quad (2.21)$$

The sheath length can be related to the voltage from the Child-Langmuir law.

$$x = \frac{2}{3} \left(\frac{2q \epsilon_0^2}{m_e} \right)^{\frac{1}{4}} \frac{V^{\frac{3}{4}}}{i^{\frac{1}{2}}} \quad (2.22)$$

and taking

$$i = \alpha + \beta V \quad (2.23)$$

$$\frac{dx}{dV} = \frac{2}{3} \left(\frac{2q \epsilon_0^2}{m_e} \right)^{\frac{1}{4}} \left(\frac{\frac{3}{4} V^{-\frac{1}{4}} i + \beta V^{\frac{3}{4}}}{i^{\frac{3}{2}}} \right) \quad (2.24)$$

$$C^*(V) = \frac{2}{3} \left(\frac{2q \epsilon_0^2}{m_e} \right)^{\frac{1}{4}} qn \left(\frac{\frac{3}{4} V^{-\frac{1}{4}} i + \beta V^{\frac{3}{4}}}{i^{\frac{3}{2}}} \right) \quad (2.25)$$

For measurements of i and V in an Argon plasma of 1.0 A and 27 V respectively $C^*(V) \approx 3.0 \mu F$ which is still a much smaller impedance than that measured in the lab (cf Section 3.2).

Finally, just considering the sheath as a parallel plate capacitance with air as a dielectric yields:

$$C = \frac{\epsilon_0 A}{l_{sh}} = \frac{(8.85 \cdot 10^{-14} \frac{F}{cm})(613 cm^2)}{2. mm} \approx 270 pF \quad (2.26)$$

$$X = \frac{1}{\omega C} \approx 45 \Omega \quad (2.27)$$

This is much closer to the measured values and effectively explains the reactance of the plasma. Because the sheath dielectric and the oscillation of the charge particles at the edge are in series this smaller capacitance dominates.

2.2.3. Conclusions

Text book models are helpful in characterizing the plasma and helping to unify its descriptions. Ion fluxes and potential distributions follow well from the classical knowledge. The simple theory explains the roles and distinguishing

features of ions and electrons. The density of the charged particles in the plasma does not increase as the number of particles (the pressure) is increased. Subtle effects as the motion of electrons in the rf field and the oscillation at the sheath edge do not contribute significantly to the characteristic reactance of the plasma. The collection of charged particles will not always dominate the process, although they greatly enhance the chemical process. In the next section, we shall add the experience and theories on plasma chemistry which also directly affect the profile of the etched surfaces.

2.3. Plasma reactions and surface chemistry.

2.3.1. Classification of characteristics

The plasma has been described in terms of its physical properties. When applied to etching, the plasma must be characterized in terms of its effects on the etched surface, such as rates, anisotropy, selectivity, and loading effects. The physical properties can rarely be associated with these effects directly. For example, in ion milling a sputtering rate in atoms removed per incident ion and material parameters can be converted directly into an etch rate. In dry etching, however, the gasses used and the species generated in the plasma form much more complicated relations between plasma properties and etched profiles.

A plasma etching process is classified as anisotropic if material is removed more quickly in the direction normal to the surface of the wafer. Figure 2.6 defines isotropic and anisotropic etching and the degree of anisotropy for non-eroding masks. For fine, sub-micrometer patterning, anisotropic etching is desirable. For removal of entire layers and patterning large features, isotropic techniques suffice and are often desirable for various reasons. Anisotropy is the

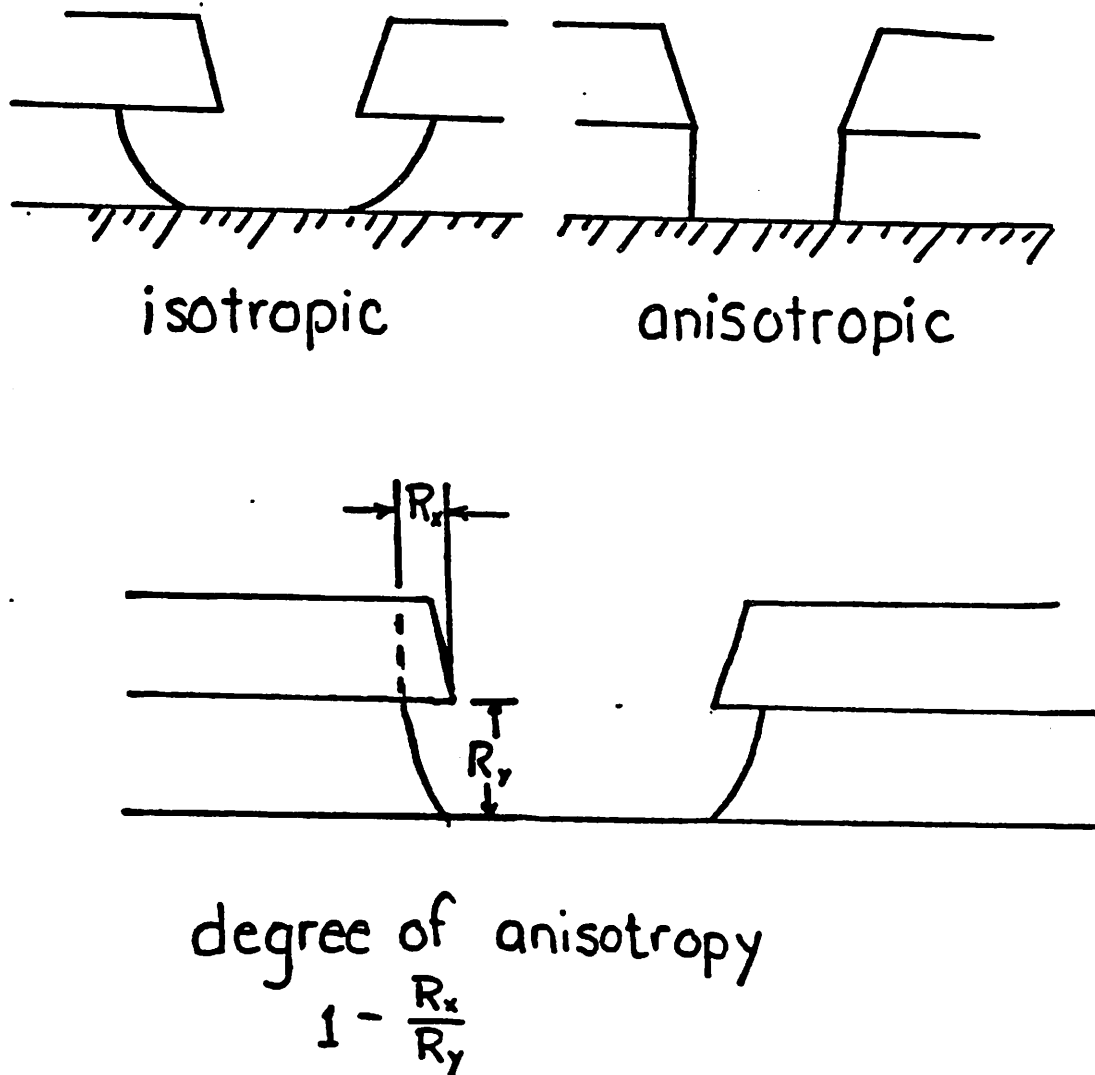


Figure 2.8

Definitions of isotropic etching, directional etching, and the degree of anisotropy.

main consideration in profile control and there are several theories of mechanisms that the plasma etching techniques institute. Selectivity, the preferential etching of one material relative to another reveals some information about the plasma process also. Different materials are susceptible to different mechanisms and species. Certain plasma techniques exhibit a loading effect which indicate that transport and reactant supply dominate the etching process.

Exposing a silicon or silicon dioxide (SiO_2) surface to ion radiation in a fluorine gas ambient produces material removal at a rate many times quicker than the chemical etching of fluorine or the ion sputtering alone.⁸ The enhancement of etching several times over the sum of the constituents indicate the interrelation between physics and chemistry instigated by the plasma. The etching rate cannot be explained directly by one or the other alone. This is especially true in fluorinated plasmas where a large number of reactive neutrals etch with great enhancement from ionic species.

2.3.2. Single and double component etching

Fluorine and chlorine are the two most commonly used etchants of silicon and its compounds. This section summarizes the research that characterizes their etching roles. Fluorine atoms etch Si and SiO_2 with an Arrhenius behavior with respect to substrate temperature. Flamm and colleagues⁹ have titrated the fluorine atoms from an F_2 plasma and determined the rates to be:

$$R_{\text{Si}} = 2.91 \pm .02 \cdot 10^{-12} n_F T^{\frac{1}{2}} e^{-\frac{E_{\text{Si}}}{k_B T}} \quad (2.28)$$

$$R_{\text{SiO}_2} = 6.14 \pm .49 \cdot 10^{-13} n_F T^{\frac{1}{2}} e^{-\frac{E_{\text{SiO}_2}}{k_B T}} \quad (2.29)$$

where the activation energies are

$$E_{\text{Si}} = 0.108 \text{ eV} \quad (2.30)$$

$$E_{SiO_2} = 0.183 \text{ eV and} \quad (2.31)$$

$$n_F = \text{density of F atoms in cm}^{-3}. \quad (2.32)$$

The free fluorine atoms readily remove silicon at room temperature with out ion bombardment where they etch SiO_2 slowly. This accounts for much of the etching and almost all of the undercut in fluorine based gas systems. Calculating a fluorine gas density for an isotropic silicon etch rate of $0.1 \frac{\mu m}{min}$ at $333^\circ C$ in our reactor (described in Appendix A) $n_F \approx 10^{14} cm^{-3}$ which implies a partial F pressure of $3.2 \cdot 10^{16} \cdot n_F \approx 25 mT$ which is a reasonable percentage for these operating pressures.

The common fluorine generating plasmas, such as CF_4 and SF_6 with oxygen, produce fluorocarbon radicals and sulfur containing films that complicate the etching process. ClF_3 liberates F atoms in the plasma without other complex constituents. In addition, etching Cl atoms are released that can be compared to fluorine atoms. Flamm, Wang and Maydan¹⁰ have used ClF_3 and Cl_2 mixtures to provide controlled loading and anisotropy information for etching silicon. This work sets a basis for multiple etchant effects in plasmas. Beginning with a mass balance for each etching species, a steady state concentration C_i can be calculated. The etch rate with m wafers present in the reactor is then: $R_m = \sum k_{w_i} C_i$ where k_{w_i} is the rate of loss of species i from etching the substrates. This can be formed into the expression:

$$\frac{R_o}{R_m} = \frac{\sum_{j=1}^N \Phi_j}{\sum_{j=1}^N \frac{\Phi_j}{1+N\Phi_j}} \quad (2.33)$$

which has the usual loading expression form

$$\frac{R_o}{R_m} = 1 + kA \quad (2.34)$$

Where,

R_o = the loaded rate

m = number of substrates present

ϕ_j = ratio of species i consumed by etching that lost by recombination.

ϕ_i can be interpreted as the slope of the loading effect curve for component i .

Applied to the CF_3 and Cl_2 mixture¹⁰ this becomes:

$$\begin{aligned} \frac{R_o}{R_m} &= \frac{\phi_F + \phi_{Cl}}{\frac{\phi_F}{1+m\phi_F} + \frac{\phi_{Cl}}{1+m\phi_{Cl}}} & (2.35) \\ &= \frac{1 + \phi_{Cl,F}}{\frac{1}{1+m\phi_F} + \frac{\phi_{Cl,F}}{1+m\phi_{Cl}}} \\ &= \frac{1 + 0.16}{\frac{1}{1+m \cdot 2.19} + \frac{0.16}{1+0.0}} \quad \text{by curve fitting.} \end{aligned}$$

With these two etching components, this seems reasonable with $\phi_{Cl} = 0$. (no loading effect) and $\phi_{Cl,F} = 0.16$ (the chlorine etch rate is ~ 0.16 that of the fluorine in an unloaded reactor). With different gasses ion bombardment and/or surface inhibition contribute to the etching with other components considered.

2.3.3. Multiple component etching.

Using computer simulation, Mark Kushner^{12, 13} considers quantitatively the electron impact events, ion chemistry, neutral gas phase reactions, diffusion, space charge effects, adsorption and desorption. Figure 2.7 illustrates the actual model of the etching process. Neutral and charged radicals that are produced in the plasma body diffuse by concentration gradient or space-charge enhanced diffusion to the substrate surface. A fraction γ adsorbs and the rest

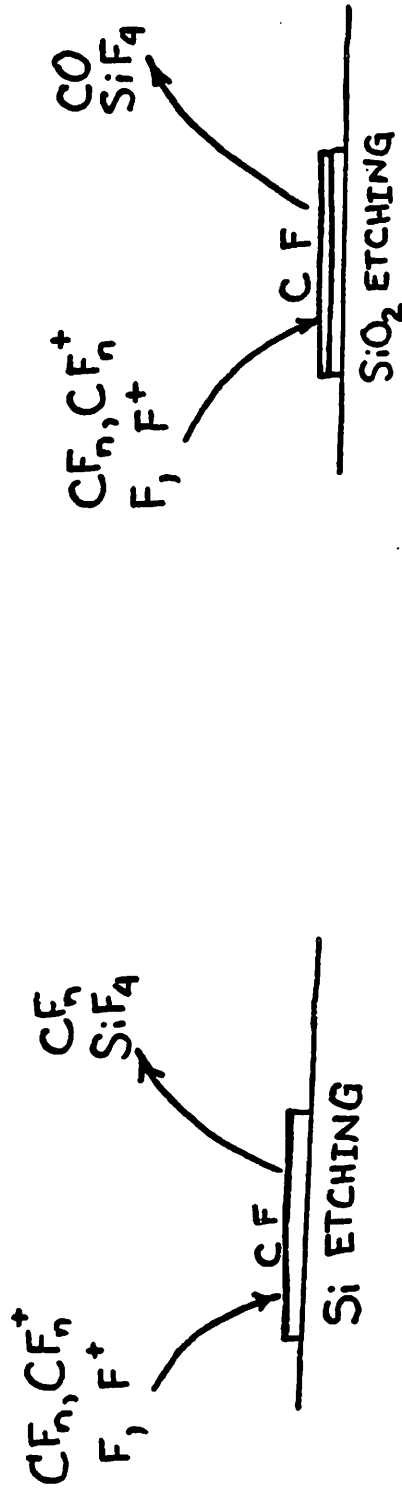


Figure 2.7 Kushner's multi-component model for plasma etching.

M.J. Kushner, "A kinetic study of the plasma etching process: I. A model for etching Si and SiO₂ in CnFm/H₂ and CnFm/O₂ plasmas," *Journal of Applied Physics*, vol. 53, no. 4, p. 2823, (April 1982).

return to the plasma. Ambipolar diffusion³ is used to represent the transport mechanism. The rate can then be written in terms of diffusion coefficients, D_i

$$R_s = \frac{M_s h \gamma}{2 \rho_s \Gamma^2} \left[\sum_{j=1}^N [X_i] D_i \right] \quad (2.36)$$

Where,

ρ_s = atomic density of substrate s

M_s = atomic mass of substrate s

Γ = reactor diffusion length

$[X_i]$ = concentration of species i

h = chamber height

This method shows good agreement with selective etching of Si and SiO_2 . The etching is found to be a sensitive function of the O_2 and H_2 fractionated in the plasma. By keeping track of dozens of species in the plasma Kushner has demonstrated the importance of additives (O_2 & H_2) to fluorocarbon plasmas. Although his research says little about the etched profiles, it exhibits the trends in charged particle and neutral densities on the plasma as a function of concentrations.

2.3.4. Anisotropy considerations.

In the common systems ion bombardment and other species complicate the etching process beyond that of simple component etching. The side walls under the mask are often unexposed to the ion bombardment and etch according to the F density which depends on the chemistry. Even the isotropic, unexposed etching rates are not a linear function of the fluorine atoms present. The gas molecules used have produced various amounts of F, but also produce different recombinants to hinder etching. The process depends on three steps occurring; 1) the etching species adsorbs on the surface, 2) it reacts with the

surface, and 3) the resulting compound desorbs. The chemistry of the other species can help or hinder and ion radiation may help any or all of these steps. Ion bombardment accelerates directional etching and this may occur in two ways proposed by Coburn and Flamm.

Flamm favors the view¹⁴ that ion bombardment damages several monolayers of Si and these broken bonds are halogenated faster than an undamaged silicon surface. Ion bombardment enhances the slow breaking of Si-Si bonds underlying a chemisorbed layer causing material removal to proceed more rapidly in the vertical direction, producing anisotropy. In systems where the etching is slow (Fluorinated gasses etching SiO_2 and chlorine plasmas etching undoped Si) almost total isotropy can be achieved.

Coburn and colleagues believe the role of ion bombardment accelerates the product formation step.¹⁵ The clean surface of Si readily adsorbs F atoms from the gas phase. Ion bombardment helps to create and clear the absorbed products, resulting in etching in the direction of the ion flux where Si is cleared and products form the fastest. The application of both these mechanisms result in similar profiles and explain the anisotropy equally well.

Other contaminants and products formed in the plasma can adsorb on the surfaces⁸ and may hinder etching. On sidewalls where ion radiation is ineffective in removing these products, two things can happen. In some systems, such as with Cl atoms, these "recombinant" species combine with the etchant atoms suppressing etching. In the second situation, these products can form etching barriers, such as polymer films, thus halting etching.

2.3.5. Plasma reactions

Flamm offers a model ordering the reactivity to predict the dominant etchants as a function of gas compositions.¹⁴

$e^- + \text{Halocarbon} \rightarrow \text{Saturated species} + \text{Unsaturated species} + \text{atoms}$

$\text{Reactive atoms/molecules} + \text{Unsaturates} \rightarrow \text{saturates}$

$\text{Atoms} + \text{surfaces} \rightarrow \text{Chemisorbed layer of volatile products}$

$\text{Unsaturates} + \text{Surfaces} (+ \text{Initiating radicals}) \rightarrow \text{Films}$

The reactivity of atoms and molecules are ordered in these saturation reactions.

$F \sim O > Cl > Br$

$F_2 > Cl_2 > Br_2$

Additions to the plasma alter the balance of these atoms/molecules and unsaturates producing different results. For example, adding O_2 to CF_4 plasmas removes CF_x radicals, preventing them from recombining¹⁶ and initiating polymers. This increases the F radical concentrations leading to enhanced etching all around. Other additions, such as O_2 to CF_3Br ^{16,17} tend to increase the Br concentrations relative to O_2 and F concentrations which leads to more directional etching.

Ignoring the mechanistic details but dwelling on the additives, Coburn gives a *pseudo black-box* approach¹⁸ where F and C must be conserved. The significance of the F-to-C ratio was originally noted by Heinecke¹⁹ to qualitatively describe the chemistry of the plasma. The extent to which F and C are present determines the etching and polymerization chemistries. Using the CF_4/O_2 example again, active carbon is oxidized into relatively unreactive CO and CO_2 ²⁰ increasing $\frac{F}{C}$ and the fluorine etching mechanisms and hindering polymer initiation. Hydrogen additions decrease $\frac{F}{C}$ by consuming F to form HF.

Here, fluorine is not available to form volatile SiF_4 and CF_4 from Si and carbon, and enhances the selectivity of SiO_2 to Si.²¹ Surface inhibitors and their mechanisms are neglected in summarizing C and F conservation in the effluent gas.

$$Q(\text{SiF}_4) = \frac{1}{2}Q(\text{C}_2\text{F}_6) - \frac{1}{2}Q(\text{F}_2) + \frac{1}{2}Q(\text{COF}_2) - \frac{1}{4}Q(\text{HF}) + Q(\text{CO}) + Q(\text{CO}_2)$$

where the Q's are the number of molecules per second and silicon removal is associated with $Q(\text{SiF}_4)$. This expression demonstrates both Si: SiO_2 selectivity and loading effects.

2.4. Impedance models

The modeling of the plasma discharge as circuit elements is a major part of this work. Authors at IBM⁴ developed an equivalent circuit model to describe the internal voltages in the operation of rf discharges during sputtering. The representative network is shown in Figure 2.8. This configuration is used to derive the relation between the dc self biases and the electrode areas. They first concluded that the applied rf voltage is divided between the dark spaces at the powered and ground electrodes. The plasma rectifies the rf voltage creating a dc voltage. The total dc bias equals one-half the rf peak to peak voltage. The relative electrode areas control this dc bias, on which the energies of incident ions primarily depend.

Keller and Pennebaker²² have generalized that the impedance network of Fig. 2.8 can predict the velocity and the effects of scattering of ions across the sheath. Their work gives much insight into the electrical phenomena underlying the impedance model in sputtering systems. From a sinusoidal voltage

$$V = V_{dc} + V_{rf} \sin(2\pi f_{rf} t) \quad (2.37)$$

and a Maxwell Boltzmann distribution for electrons the average current density

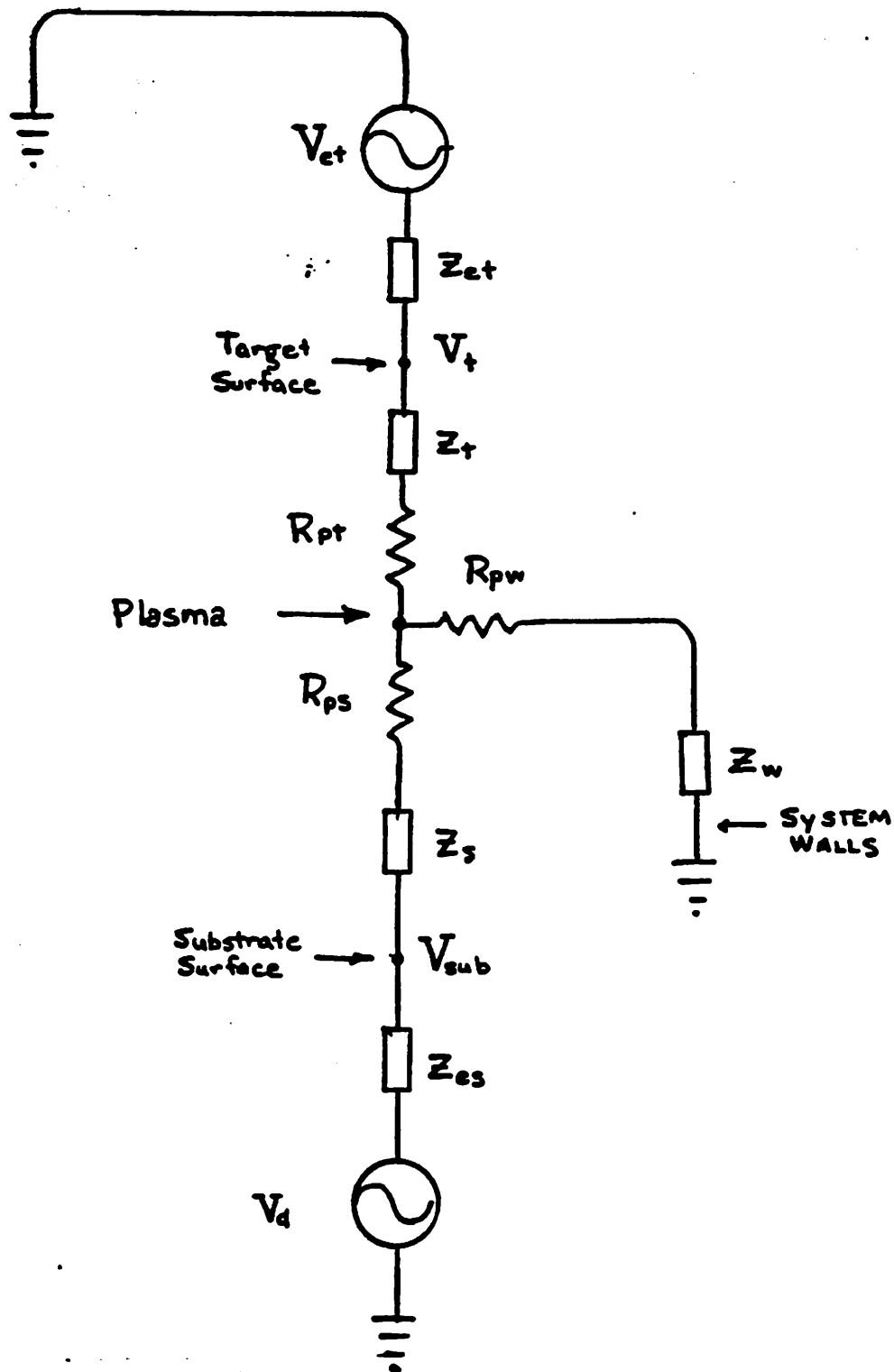


Figure 2.8

Koenig-Maisel equivalent circuit model for rf sputtering system.²

² H.R. Koenig and L.I. Mahel, "Application of rf discharges to sputtering." *IBM Journal of Research and Development*, vol. 14, no. 3, p. 168, (March 1970).

through the sheath is

$$\langle J \rangle = \langle J_{sat} e^{qV/k_B T_e} \rangle = J_{sat} e^{\frac{qV_{dc}}{k_B T_e}} I_0\left(\frac{qV_{rf}}{k_B T_e}\right) \quad (2.38)$$

where I_0 is the zeroth-order modified Bessel function. The effect of the rf voltage on the dc self-bias can be calculated:

$$\begin{aligned} V_{dc} &= \frac{k_B T_e}{q} \ln I_0\left(\frac{qV_{rf}}{k_B T_e}\right) \quad (2.39) \\ &\approx -V_{rf} + \left(\frac{k_B T_e}{2q}\right) \ln\left(\frac{2\pi q V_{rf}}{k_B T_e}\right) \approx -V_{rf} \end{aligned}$$

for $qV_{rf} \gg k_B T_e$.

This result, $V_{dc} \approx -V_{rf}$, has been independently measured by Tsui²³ giving the easily measured V_{dc} usefulness in characterizing the plasma and credence to the rectification model due to different masses, $M_i \gg m_e$.

The measured dc bias, V_{dc} , is related to the plasma floating potential, V_f , and the voltage across the sheath, V_{sh} , by $V_{dc} = V_f - V_{sh}$. The floating potential of the plasma is fixed by the electron temperature, so for constant T_e , the dc bias is indicative of the voltage across the sheath. The sheath impedance and ion current density then follow from the voltage across the sheath. This theory then estimates the ion bombardment at the target in rf sputtering.

Observation of these sheath parameters then leads to conclusions on the influence of scattering and ionization in the glow discharge sheath.²² At low pressures the ion transport obeys the Child-Langmuir Law. At intermediate (.100-1 Torr), the transport becomes mobility-limited. Finally, at high pressures (100T), the transport and sheath thickness reach an ionization limit where power dissipated in the sheath evidences a parallel sheath resistance. Here the energy is lost to secondary electron emission at the substrate and ion collisions in the sheath.

The estimated ion bombardment at the target can be used to calculate a sputtering rate and material back scatter which can then be used to approximate a deposition rate. Although this theory says little about etching, especially profiles, the concepts developed in the rf equivalent circuit network are applicable to rf etching systems.

A simple equivalent circuit model has been applied to the plasma in dry etching to explain the electric fields present in the process.²⁴ The electric field developed across the sheath is related to the rf power and current density through the plasma ($E \cdot J = P_{rf}$). A theory of etching anisotropy²⁵ is then proposed based on the ions' drift velocity from the electric field and the ions' thermal velocity.

Zarowin's model particularly applies to etching processes dominated by ion transport. It assumes that the plasma generates a constant flux of reactive ions. The etching capabilities of these ions are then 'partitioned' as lateral and vertical rates, R_x and R_y , respectively. The lateral etching arises from the random thermal scattering of the impinging ions and the vertical from acceleration in the E-field. The degree of isotropy, $\delta = \frac{R_x}{R_y}$, is theorized to follow a $\frac{\sqrt{P_{rf}}}{p}$ $\propto \frac{J_{rf}}{p}$ dependence. The horizontal etch component depends upon the pressure due to the scattering of ions' velocity vectors in a sheath of neutrals. The power and rf current dictate the directional, vertical etching. Figure 2.9 best summarizes the etching distribution as an ellipse²⁵ where the major axis is the directional etching component and the minor axis is the lateral, undercutting component. Zarowin²⁵ has produced several experimental studies which demonstrate the proposed dependence on the rf power and pressures for chlorine gas etchants.

SCHEMATIC OF ION TRANSPORT DIRECTIONALITY ($\rho^2(\alpha)$)

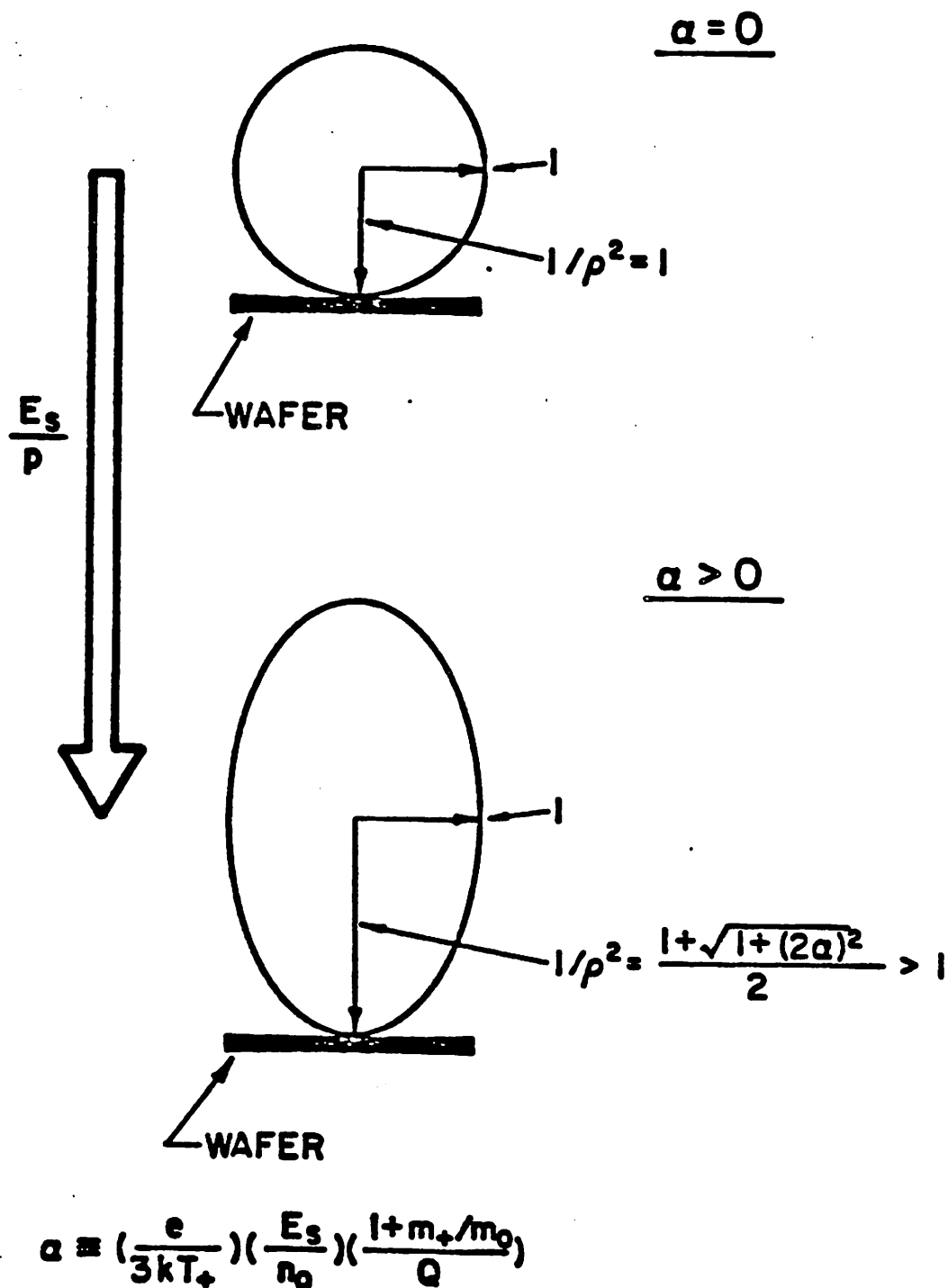


Figure 2.9
Zarowin's ellipse of ion transport directionality.

C.B. Zarowin, "Plasma etch anisotropy - Theory and some verifying experiments relating ion transport, ion energy and etch profiles," *Journal of the Electrochemical Society*, vol. 130, no. 5, p. 1144, (May 1983).

In general, however, this model is restrictive to the cases where all the etching can be attributed to the ions. The lateral isotropic component arises from scattering during its travel across a sheath full of nonreactive neutrals. The local lateral etching is associated with the random thermal velocity developed from collisions through a density of particles $n_0 (= 3.2 \cdot 10^{16} p)$ of mass M_0 in the sheath. The relative vertical etching is related to the momentum gained in the electric field developed in the sheath ($E \propto J_{rf} \propto \sqrt{P_{rf}}$). The model qualifies the physics of etching with ionized species, but neglects the background isotropic etching (different from ionic lateral etching) that is common in the faster, more selective fluorine-based plasma etchants. A plasma perceived as more than just a source for ions initiating etching is needed to make a complete model for plasma etching.

2.5. Conclusion

Several models have been presented illuminating different aspects of dry etching. The more chemical models based on mass balance and chemical species present show trends in etch rates and also in selectivities. Physical and electrical models exhibit the voltage distribution and predict the ion energy and velocity distribution in rf sputtering situations. A model has also been presented to explain the etch anisotropy due to ion transport in terms of the independent variables of power and pressure. These models work with restrictions that do not allow diagnosis of the plasma in general. The next chapter contributes an impedance electrical model and an actinometric characterization to diagnose the plasma in general. Chapters Six and Seven then further interpret these models in terms of the etched profiles.

References

1. Wulf Kunkel, *142A notes*, Introduction to plasma physics, UC Berkeley course, (Winter 1980).
2. Ch. Steinbruechel, "Langmuir probe measurements on CHF₃ and CF₄ plasmas: The role of ions in the reactive sputter etching of SiO₂ and Si," *Journal of the Electrochemical Society*, vol. 130, no. 3, p. 648, (March 1983).
3. Brian Chapman, in *Glow discharge processes - - sputtering and plasma deposition*, Wiley-Interscience, (1980).
4. H.R. Koenig and L.I. Maisel, "Application of rf discharges to sputtering," *IBM Journal of Research and Development*, vol. 14, no. 3, p. 168, (March 1970).
5. S.C. Brown, *Basic Data of Plasma Physics*, MIT press, (1959).
6. Frances F. Chen, *Introduction to Plasma Physics*, Plenum Press, New York, (1974).
7. F.D. Egitto, D.N.K. Wang, and D. Maydan, "Ion-assisted plasma etching of silicon-oxides in a multifacet system," *Solid State Technology*, p. 71, (December 1981).
8. H.F. Winters and J.W. Coburn, "The etching of silicon with XeF₂ vapor," *Applied Physics Letters*, vol. 34, no. 1, p. 70, (January 1979).
9. D.L. Flamm, C.J. Mogab, and R. Sklaver, "The reaction of fluorine atoms with silicon," *Journal of Applied Physics*, vol. 50, p. 624, (February 1979).
10. D.L. Flamm, D.N.K. Wang, and D. Maydan, "Multiple etchant loading effect in ClF₃ and related mixtures," *Journal of the Electrochemical Society*, vol. 129, no. 12, p. 2755, (December 1982).
11. C.J. Mogab, "The loading effect in plasma etching," *Journal of the Electrochemical Society*, p. 1262, (August 1977).

12. M.J. Kushner, "A kinetic study of the plasma etching process: I. A model for etching Si and SiO₂ in CnFm/H₂ and CnFm/O₂ plasmas," *Journal of Applied Physics*, vol. 53, no. 4, p. 2923, (April 1982).
13. M.J. Kushner, "A kinetic study of the plasma etching process: II. Electrical properties in an rf plasma reactor," *Journal of Applied Physics*, vol. 53, no. 4, p. 2939, (April 1982).
14. D.L. Flamm and V.M. Donnelly, "The design of plasma etchants," *Plasma Chemistry and Plasma processing*, vol. 1, no. 4, p. 317, (1981).
15. Gerlach, *Surface Science*, (1981).
16. C.J. Mogab and H.J. Levinstein, "Anisotropic plasma etching of polysilicon," *Journal of Vacuum Science and Technology*, vol. 17, no. 3, p. 721, (May/June 1980).
17. D.L. Flamm, "Mechanisms of etchant production and the role of oxidants in CF₃Cl, CF₃Br and related plasma etching gasses," in *Plasma Processing*, ed. R.G. Frieser & C.J. Mogab, Proceedings of the Symposium on Plasma Etching and Deposition, p. 55, The Electrochemical Society, (1981).
18. H.F. Winters, J.W. Coburn, and E.Kay, "Plasma etching - A 'pseudo-black-box' approach," *Journal of Applied Physics*, vol. 48, no. 12, p. 4973, (December 1977).
19. R. Heinecke, "Plasma reactor design for selective etching of SiO₂ on Si," *Solid State Technology*, vol. 19, p. 1039, (1976).
20. G. Smolinsky and D.L. Flamm, "The plasma oxidation of CF₄ in a tubular-alumina fast-flow reactor," *Journal of Applied Physics*, vol. 50, no. 7, p. 4982, (July 1979).
21. E.A. Truesdale and G. Smolinsky, "The effect of added Hydrogen on the rf discharge chemistry of CF₄, CF₃H, C₂F₆," *Journal of Applied Physics*, vol.

- 50, no. 11, p. 8594, (November 1979).
22. J.H. Keller and W.B. Pennebaker, "Electrical properties of sputtering systems," *IBM Journal of Research and Development*, vol. 23, no. 1, p. 3, (January 1979).
 23. R.T.C. Tsui, "Calculation of ion bombarding energy and its distribution in rf sputtering," *Physics Review*, vol. 168, no. 1, p. 107, (April 5, 1968).
 24. C.B. Zarowin, "Control of plasma etch profiles with plasma sheath electric field and rf power density," *Journal of the Electrochemical Society*, vol. 129, no. 11, p. 2541, (November 1982).
 25. C.B. Zarowin, "Plasma etch anisotropy - Theory and some verifying experiments relating ion transport, ion energy and etch profiles," *Journal of the Electrochemical Society*, vol. 130, no. 5, p. 1144, (May 1983).

CHAPTER THREE

3. EXPERIMENTAL PLASMA PROPERTIES

3.1. Introduction

In order to get a better handle on the plasma properties that span the effects between laboratory settings and etched profiles we investigate three non-intrusive methods of diagnosing the plasma. The first measures values and trends to circuit elements that model the plasma. The dc bias is monitored to add additional electrical characterization. Finally, the relative density of fluorine atoms in the plasma is estimated from optical emission spectra. These diagnostics provide a basis from which we can derive a consistent model of what is occurring in dry etching.

3.2. Impedance Model

3.2.1. Plasma Equivalent Circuit

In Section 2.3, an equivalent network from the literature was used to exhibit properties of an rf sputtering system. Figure 3.1 illustrates the working equivalent circuit model used to characterize the plasma and deduce experimental results from the parallel plate system we considered. It contains parallel conductance and capacitance to represent the sheaths in series with a resistor for the plasma body. An inductor may also be included in parallel to the resistor to represent an inertia term for the electrons crossing the plasma, but here it is neglected at

Equivalent circuit model for the plasma

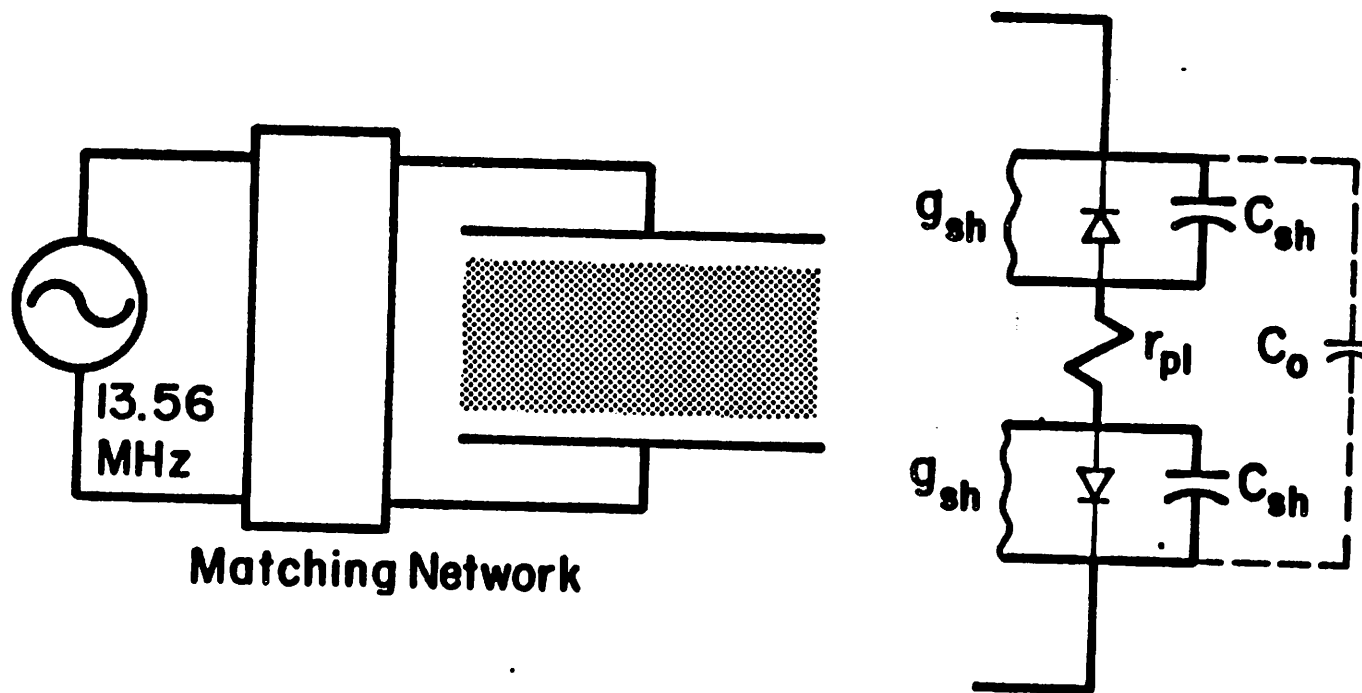


Figure 3.1
Equivalent circuit representation for the plasma in a planar system with equal electrode areas.

13.56 MHz where the electrons respond suitably fast.

Ideal diodes at the sheath lattice stand for the physics of rectification from the difference in ion and electron masses. Although these diodes play an important role in the physics of the sheath, they have been neglected in the overall linear plasma impedance model. Figure 3.2 shows the effect of the non-linearity which is neglected. Basically, it is assumed in the linear model that both current and voltage are sinusoidal with the current following the voltage due to the capacitive effects.

A small chamber capacitor, C_o , is also neglected for its high impedance relative to the impedance of the glow discharge.

The parallel capacitors, C_{sh} , represent the space charge area of the sheath. Essentially, it is a parallel plate capacitor with air as the dielectric, the plasma as the positively charged electrode, and the chamber electrode as the negative plate. The conductance, g_{sh} , allows for power dissipation in the sheath from an ion flux impinging upon the surface. Since electrons are repelled in the sheath, these elements account only for ion displacement and conduction current in later calculations. The geometry of air plasma system (cf. Appendix A) has similar grounded and powered electrode areas. The sheath circuit elements are therefore assumed to be identical.

The series resistor modeling the plasma body is of particular importance. Usually, the plasma body is extremely conductive, where there is no electric field and electrons oscillate with the applied frequency, causing ionizing events. For this case, this resistance would be negligible, but in some regions of operation the resistance becomes non-negligible, changing the characteristics of the plasma and thus the etching. In this model, electrons carry the current through the plasma and this impedance, τ_{pl} , characterizes their behavior.

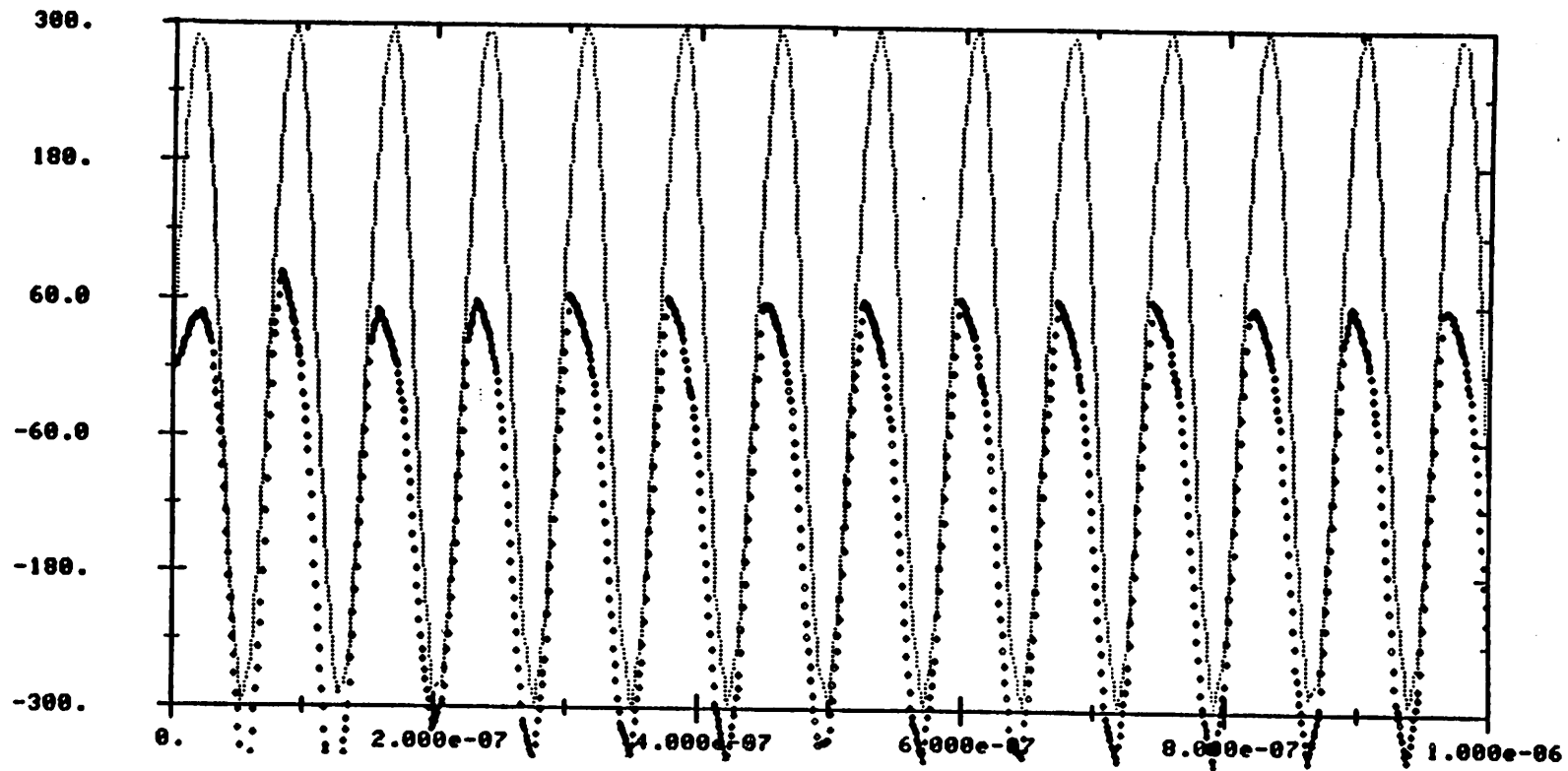


Figure 3.2

SPICE transient analysis for the equivalent circuit in Figure 3.1.⁴

⁴ L.W. Nagel, "SPICE2: A computer program to simulate semiconductor circuits," *ERL Memo*, no. ERL M520, Electronics Research Laboratory, University of California, Berkeley, May 1975.

Writing the entire expression for the plasma impedance

$$Z_{\text{plasma}} = R + iX = \frac{2}{g_{sh} + i\omega C_{sh}} + r_{pl} \quad (3.1)$$

$$R = \text{real}[Z_{\text{plasma}}] = r_{pl} + \frac{2g_{sh}}{g_{sh}^2 + \omega^2 C_{sh}^2} \quad (3.2)$$

$$X = \text{imag}[Z_{\text{plasma}}] = -\omega \frac{2C_{sh}}{g_{sh}^2 + \omega^2 C_{sh}^2} \quad (3.3)$$

note that only the real part depends on r_{pl} and variation of R without accompanying variation in X tends to indicate the relative variation in resistance of the plasma body.

The physical values of these parameters are determined by analyzing the response of the automatic matching network.

3.2.2. Analysis via the Matching Network

On the Plasma Therm PK-12 an automatic matching network tunes to make the plasma look like a 50Ω load to match the source resistance of the rf generator. The tuning network, Figure 3.3, consists of two variable capacitors: one series, called input or tuning; and one parallel, called loading; and a series inductor of $1 \mu H$. The series inductor/capacitor pair looks like a variable inductor ranging between $.14 \mu H$ and $1.0 \mu H$ ($11.7-85.0 \Omega$ at 13.56 MHz) and C_p scales the real part of the plasma impedance to 50Ω . The impedance of the matching network is then 50Ω less than the complex conjugate of the plasma impedance.

The variable capacitors are attached to servo-motors which adjust the number of capacitor turns (1-20) to produce a matched network. The parallel capacitor varies between 7 and 500pF almost linearly and the series capacitor for 20-1000pF by the following equations:

$$C_p = 500pF \left(1 - \frac{t_n}{20.0}\right) \quad 0 < t_n < 19.0 \quad (3.4)$$

Describing the plasma impedance from the matching network

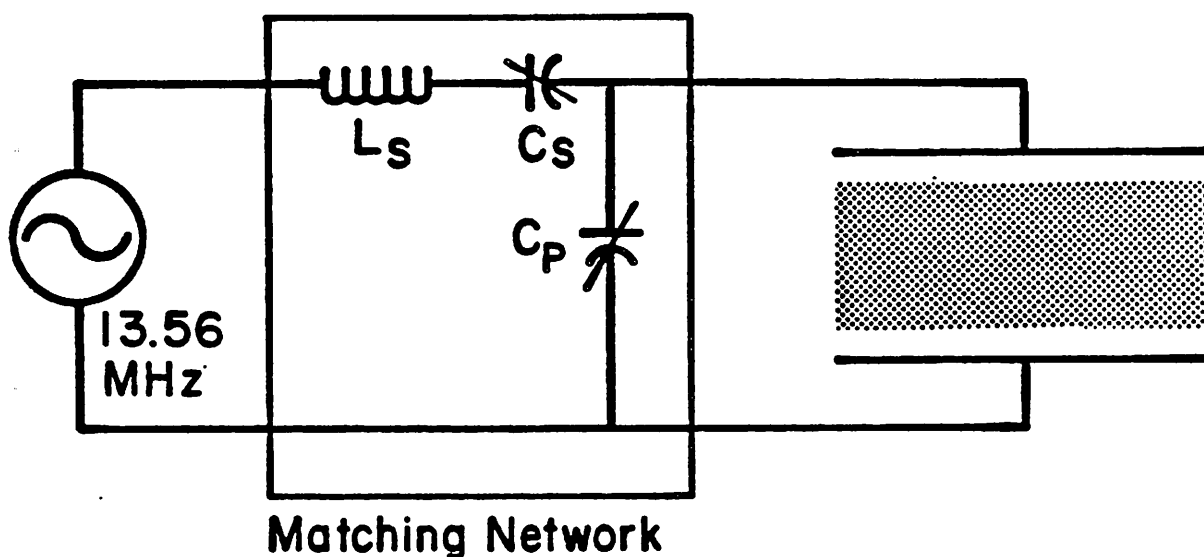


Figure 3.3

RF Matching network with two variable capacitors to tune the plasma impedance to the 50Ω source resistance.

$$\begin{aligned}
&= 7.0pF \quad t_n > 19.0 \\
C_s &= 1000pF \left(1 - \frac{t_n}{14.2}\right) \quad 0 < t_n < 13.0 \\
&= 98.5pF \left(1 - \frac{t_n}{20.3}\right) \quad 13 < t_n < 20.0
\end{aligned} \tag{3.5}$$

where t_n is the number of turns indicated by the servo-motor. (These equations are derived from the IIT Jennings specification sheets and are incorporated into a C and FORTRAN computer program included in Appendix B.)

Describing the plasma impedances in terms of the matching network elements, it follows that:

$$R - iX = i\omega L + \frac{1}{i\omega C_s} + \frac{R_s}{1 + i\omega R_s C_p} \tag{3.6}$$

$$R = \frac{R_s}{1 + \omega^2 (R_s C_p)^2} \tag{3.7}$$

$$X = -\omega L + \frac{1}{\omega C_s} + \frac{\omega R_s^2 C_p}{1 + \omega^2 (R_s C_p)^2} \tag{3.8}$$

Here it is important to note that the real part of the plasma depends only on the parallel capacitor and that it indeed shows the largest variation in tuning. Note, R is necessarily less than $R_s = 50\Omega$ for the network to be matched. Under those conditions, usually higher pressure, where the matching network is unable to make C_p small enough to eliminate the reflected power, a second method is used to calculate the real part of the plasma impedance. Here, assuming that the series capacitor is able to match the conjugate imaginary part, the resistance can be calculated from the ratio of the reflected to the incident power.

$$\frac{P_{refl}}{P_{inc}} = \frac{(R_s - R)^2}{(R_s + R)^2} \tag{3.9}$$

$$R = R_s \frac{\left(1 + \sqrt{\frac{P_{refl}}{P_{inc}}}\right)}{\left(1 - \sqrt{\frac{P_{refl}}{P_{inc}}}\right)} \tag{3.10}$$

In this case, the efficiency of the rf generator drops below 50% and power is wasted in the generator. Experimentally, the measurements rise continuously across $R=49.7\Omega$ where the system goes out of tune, which adds validity to both the measurements.

3.2.3. Impedance Measurements

With these computations, the curves in Figures 3.4-3.7 illustrate how the plasma impedance varies with pressure for three different powers in sulfur hexafluoride, carbon tetrafluoride, hexafluoroethane, and argon. A discussion of these curves follows in Section 3.2.4.

The measurement process started with a sealed chamber pumped to the base pressure by the combination of roughing pump and roots blower. A nitrogen plasma followed by a high powered oxygen plasma was used to out gas and clean the system. The base gas and oxygen mixture was then ignited and allowed to stabilize for approximately a quarter of an hour. For a given power, 100 Watts, the turns on the matching network capacitors were recorded along with the intensity of the fluorine emission line. The intensity of the Argon actinometer was taken separately, during a similar, later procedure. For the pressure range from base to 250 mTorr the matching network and intensity values were taken at 25 mTorr intervals by throttling the 4 inch blower butterfly valve.. Above this range, to 1 Torr or the plasma extinguishing, recordings were written every 100 mTorr. Above a certain pressure the matching network was no longer able to zero the reflected power. Above this point the forward and reflected power were set manually, in order that their difference be the operating power and then recorded. The variation in pressure was similarly recorded for 250 and 400 Watts input power.

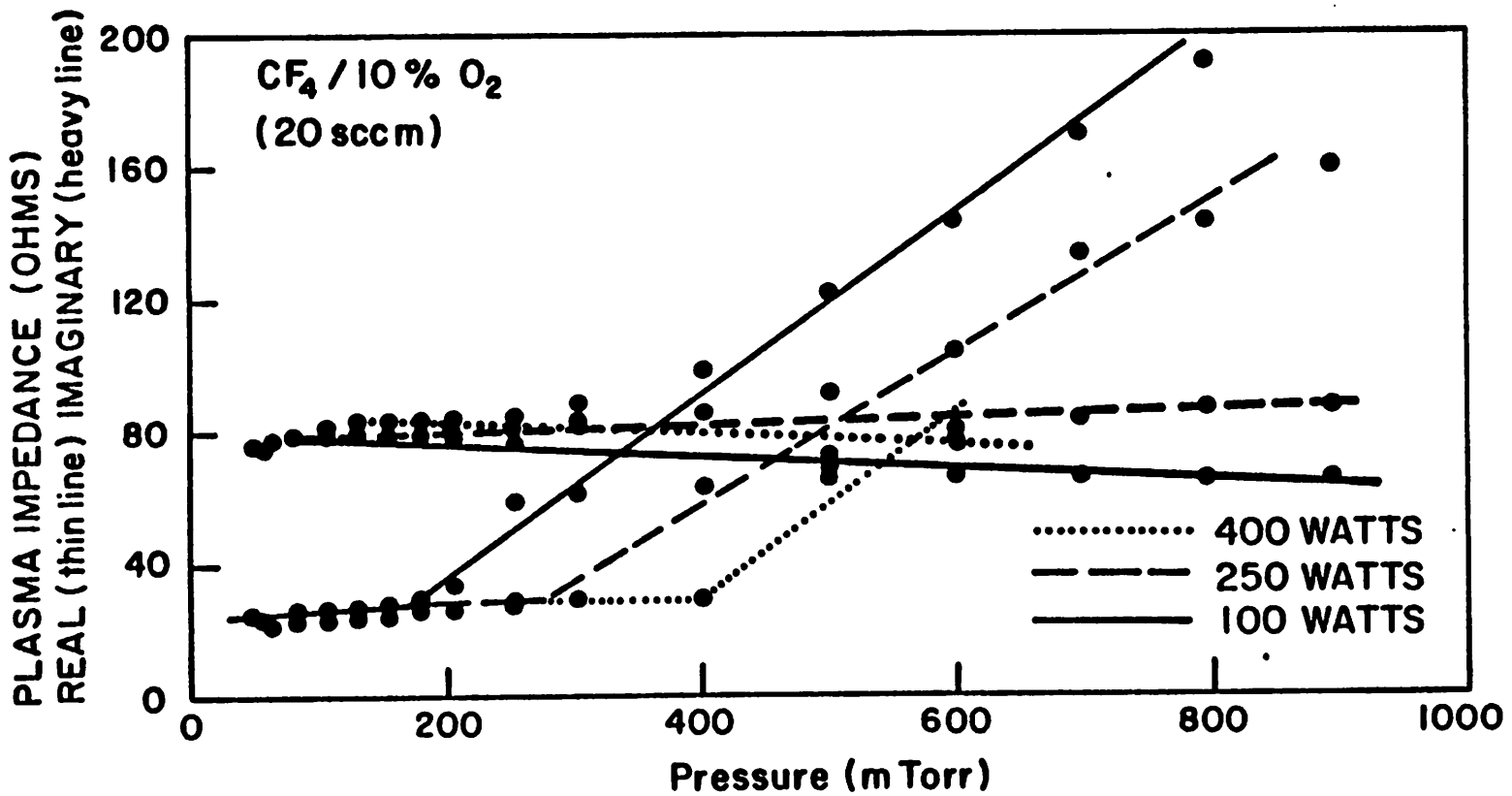


Figure 3.4

The real and imaginary parts of the plasma impedance as a function of pressure at 100, 250 and 400 Watts for 20 sccm Carbon Tetrafluoride and 10% Oxygen.

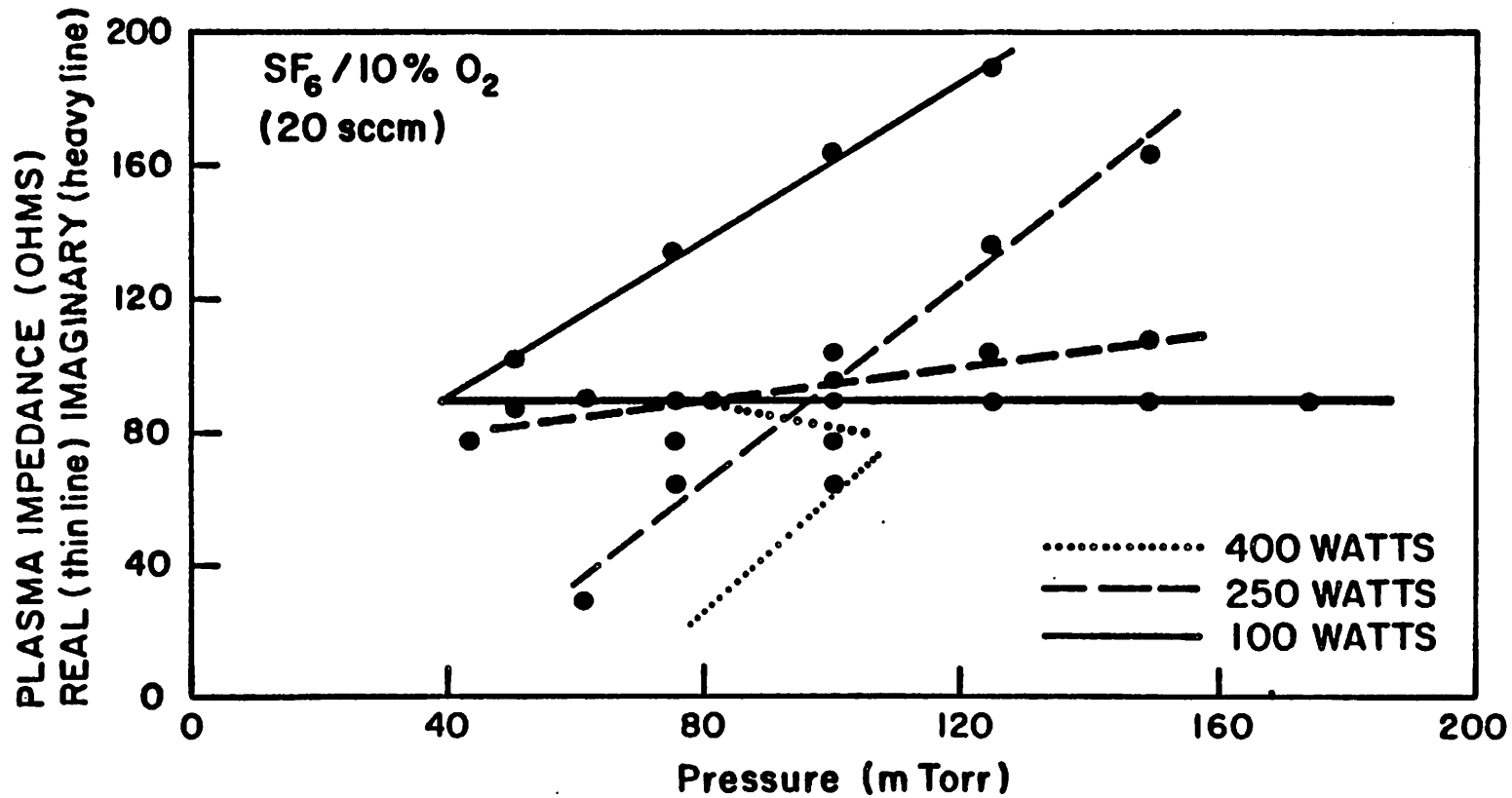


Figure 3.5

The real and imaginary parts of the plasma impedance as a function of pressure at 100, 250 and 400 Watts for 20 sccm Sulfur Hexafluoride and 10% Oxygen.

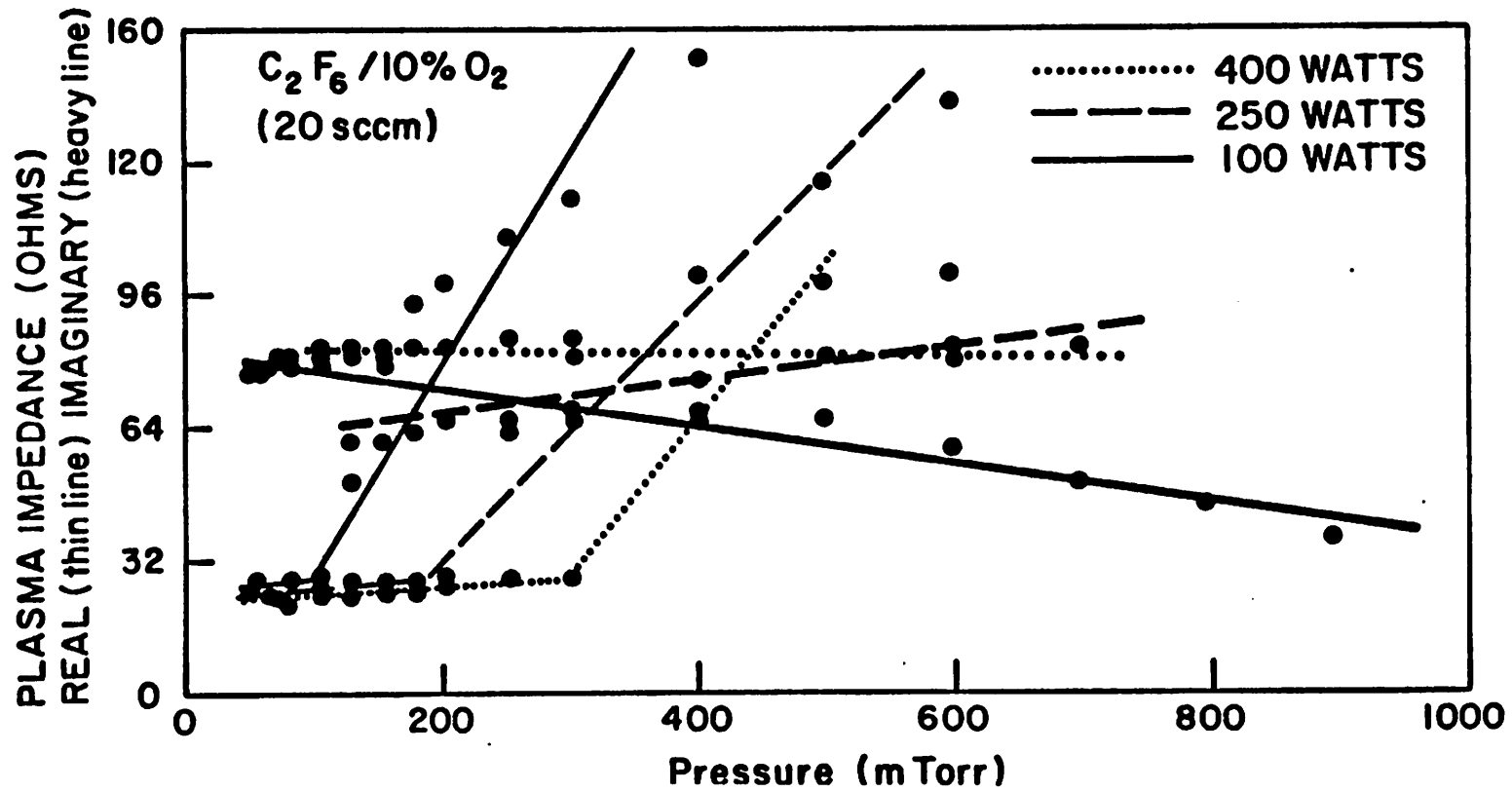


Figure 3.8

The real and imaginary parts of the plasma impedance as a function of pressure at 100, 250 and 400 Watts for 20 sccm Hexafluoroethane and 10% Oxygen.

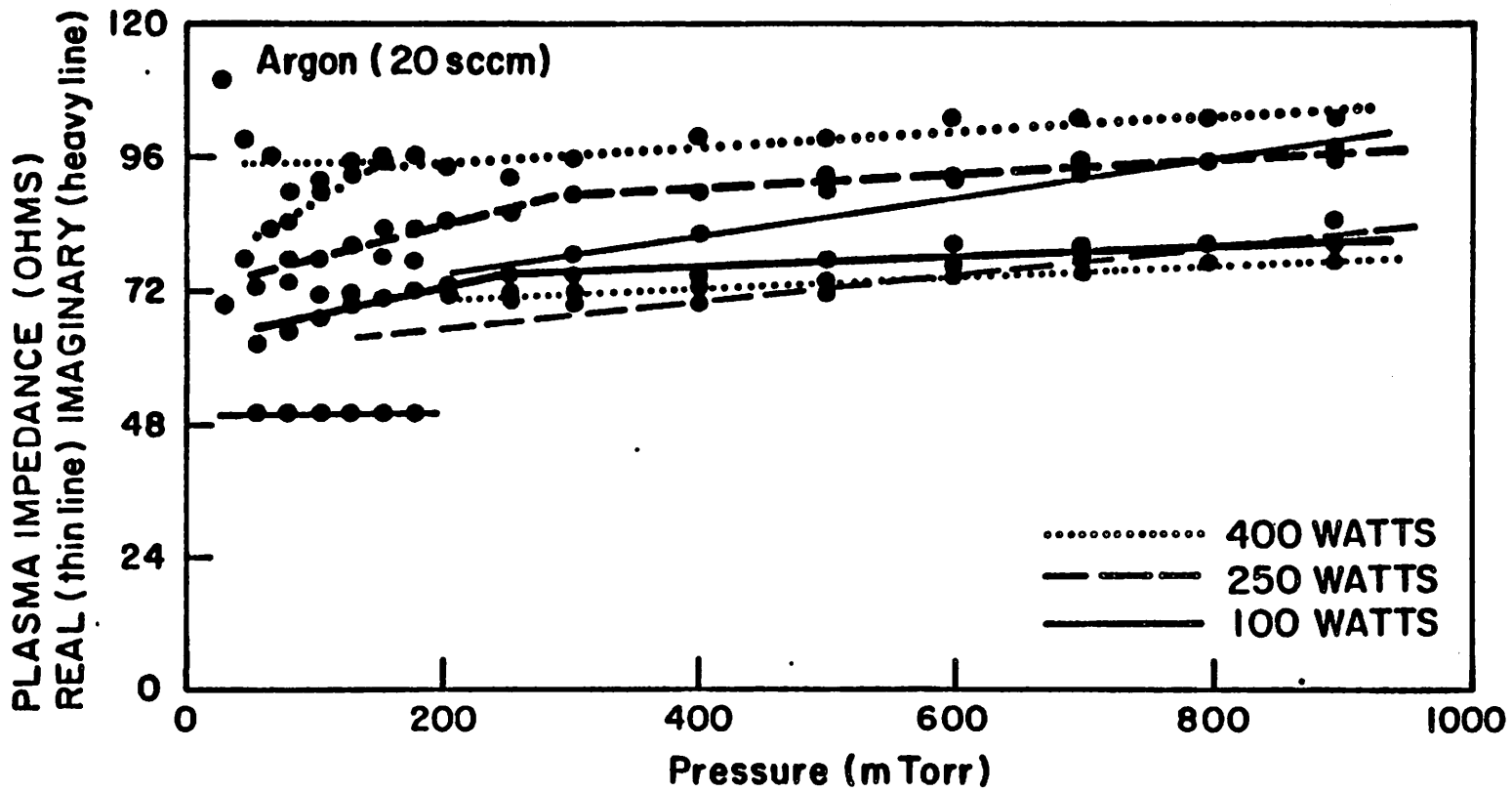


Figure 3.7

The real and imaginary parts of the plasma impedance as a function of pressure at 100, 250 and 400 Watts for 20 sccm Argon.

A computer program calculated the values of the tuning capacitors and associated discharge impedance elements. This program and all the data appear in Appendix B of this report.

3.2.4. Interpretation of Measurements

3.2.4.1. The Sheath Capacitance and Conductance

From the imaginary part of the plasma impedance and a non-collisional, highly-conductive real part at low pressures, the values in Table 3.1 are curve-fit to the parallel conductance and capacitance used to represent the sheath impedance. These values remain virtually constant through out the pressure range investigated. The values for the capacitance are indicative of a parallel plate capacitor with air as a dielectric and sheath thickness for plate separation. That is, $C_{sh} \approx \frac{\epsilon_0 A}{t_{sheath}}$, where $t_{sheath} \approx 2.7mm$. The larger capacitances of sheath boundary oscillation are obscured in series with the small capacitance. The constancy of the sheath capacitance indicates that there is insignificant scatter and ionization in the sheath for the pressure range investigated. Ionization or increased scattering within the sheath would tend to make these capacitances increase.

The conductance of the sheath appears larger than usually expected. This term stands for the power dissipated by ions crossing the sheath and colliding with the surface. An average (of sorts) of the ion density in the sheath can be calculated from this conductance. For ions at $333^\circ K$ at 50 mTorr, the collision rate is

$$\nu_{io} = \frac{v_{Ti}}{\lambda_{mfp}} = \frac{10^5 \frac{cm}{s}}{15.cm} \approx 7.KHz \quad (3.11)$$

Table 3.1

Values of the plasma impedance elements			
gas mixture	g_{sheath} $1/\Omega$	C_{sheath} $n \text{ Farads}$	τ_{plasma} $p > p_{27\Omega}$
$SF_6/10\%O_2$	$\frac{1}{160}$	0.24	$1.5p + 11.$
$CF_4/10\%O_2$	$\frac{1}{140}$	0.30	$.24p - 1.8$
$C_2F_8/10\%O_2$	$\frac{1}{150}$	0.30	$.40p + 10.$
Argon	$\frac{1}{80}$	0.16	0.0

$$g_{sh} = \frac{A}{t_{sh}} \sigma_{sh} = \frac{A}{t_{sh}} \left(\frac{q^2 n_i}{M_+ v_{io}} \right) \quad (3.12)$$

$$n_i = \frac{g_{sh} t_{sh} v_{io} M_+}{A q^2} \approx 5 \cdot \frac{10^{10}}{\text{cm}^3} \quad (3.13)$$

This is approximately one-half the density which the plasma is estimated to have, which agrees quite well with the Bohm sheath criterion.¹ From the estimated density of ions in the sheath, two different currents can be evaluated, the ion thermal current and the drift current due to the electric field across the sheath.

$$i_{T_i} \approx n_i q A v_{T_i} \approx 50 \text{ mA} \quad (3.14)$$

$$i_{drift_i} \approx n_i q A v_{drift_i} \approx 1.2 \text{ A} \quad (3.15)$$

$$\text{where } v_{drift_i} \approx \frac{q V_{sh}}{t_{sh}} \frac{t_{sh}}{M_+} v_{io} \approx 2.5 \cdot 10^8 \frac{\text{cm}}{\text{s}}$$

for $V = 200 \text{ Volts}$ and $t_{sh} = 0.2 \text{ cm}$.

The value for the electric field drift current is closer to those currents measured in the chamber. Also, it dwarfs the thermal current designating the collimated, accelerated ions to be the primary cause for anisotropic etching with very little deviation to allow for lateral ionic etching. The lateral etching in this operating system can be attributed to non-ionized reactive particles superimposed behind the accelerated ions described here. This situation differs from chlorine etching and etching without oxygen where the dispersion of ions initiates the lateral etching.²

3.2.4.2. Plasma Resistance

In most laboratory plasmas, the plasma glow itself is highly conductive. Unimpeded, an electron could travel $\frac{v_{Te}}{2f_{rf}} \approx 4 \text{ cm}$ in an rf half-cycle. Collisions in the plasma, which are the main source of ionization, reduce this length further to $\frac{v_{Te}}{\nu_{eo}} \approx .7 \text{ cm}$ at 50 mTorr. At this low pressure, the electrons still can carry a lot of current, so that the resistance of the plasma body is negligible compared to sheath impedance. Increasing the pressure increases the number of collisions, which is evident from the resistance, r_{pl} , and the real part of the plasma impedance, when the collision frequency exceeds the electron plasma frequency. In the extreme, the electrons are unable to gain enough energy between collisions to produce ionization and the plasma extinguishes. In the intermediate collisional plasma though, the properties in dry etching change considerably. A larger voltage appears across the plasma, changing the potential distribution and the ion energies. This voltage subtracts from the sheath bias voltage which will diminish the amount of energy that ions can gain crossing the sheath. More importantly, there is more power dissipated in the plasma, changing the quantities of species generated there.

In Figures 3.4, 5, and 6, the real part of the plasma resistance is seen to increase linearly above a certain pressure, called $p_{27\Omega}$. The sheath contributes approximately 27 Ohms to the real part of the impedance when the plasma resistance is negligible. This value is special to the fluorinated gasses in this system and about half for Argon. This increase can be attributed to the rise in the plasma resistance, r_p , as the imaginary part remains relatively constant. The increase in collisions with an increase in the number density of particles explains the linearity. Tables 3.2 and 3.3 summarize the least squares fit information for two different electrode spacings and three different powers. ρ , the correlation coefficient, assigns a closeness to a linear fit by its proximity to unity. $p_{27\Omega}$ labels the pressure which gives $R=27\Omega$, the minimum real part of the impedance. b is the y-intercept and decreases with increasing power and m is the slope of the R versus p line for $p > p_{27\Omega}$.

Table 3.2 - Dependence on pressure

Electrodes at 1.9 cm

<i>SF₆/10%O₂</i>				
power (Watt)	$m \frac{\Omega}{mT}$	$b \Omega$	ρ	$p_{27\Omega} mT$
100	1.55	11.1	.982	10.3
250	1.48	-52.4	.990	53.7
400	1.91	-127.	--	80.7
$p_{27\Omega} = 0.235 P - 10.4 mT (\rho=0.991)$				

These values showed no variation when the gas flow rates were varied from 5 to

<i>CF₄/10%O₂</i>				
power (Watt)	$m \frac{\Omega}{mT}$	$b \Omega$	ρ	$P_{270} mT$
100	.245	-1.84	.991	118.
250	.214	-25.3	.987	245.
400	.252	-68.6	.975	380.
$P_{270} = 0.873 P + 29.3 mT (\rho=0.9998)$				

<i>C₂F₆/10%O₂</i>				
power (Watt)	$m \frac{\Omega}{mT}$	$b \Omega$	ρ	$P_{270} mT$
100	.407	9.84	.897	42.3
250	.266	-13.0	.980	150.
400	.282	-52.6	.951	283.
$P_{270} = 0.802 P - 42.2 mT (\rho=0.998)$				

100 sccm. The flow rate does not affect the electrical properties or even the optical emission spectra for fluorine. The residence time does depend on flow rate and therefore loading effect and degree of anisotropy depend upon it.

Decreasing the spacing between the powered and grounded electrodes increases

Table 3.3 - Dependence on pressure

Electrodes at 2.5 cm

<i>SF₆/10%O₂</i>				
power (Watt)	$m \frac{\Omega}{mT}$	b Ω	ρ	$P_{270} mT$
100	1.47	-30.4	.999	39.0
250	1.20	-62.0	.978	74.4
400	1.16	-86.0	---	101.
$P_{270} = 0.207 P - 19.8 mT (\rho=0.997)$				

<i>CF₄/10%O₂</i>				
power (Watt)	$m \frac{\Omega}{mT}$	b Ω	ρ	$P_{270} mT$
100	.221	-20.0	.997	213.
250	.142	-28.6	.977	382.
400	.0953	-20.4	.981	499.
$P_{270} = 0.950 P + 127. mT (\rho=0.994)$				

the onset of a resistive plasma. The more closely spaced electrodes provide a better opportunity for loss of carriers to the chamber plates. This action is also seen to increase the degree of anisotropy slightly.

From the slope m , the ratio of the electron velocity to the electron density can be estimated. The resistance, which is proportional to the collision frequency, is also proportional to the neutral density and thus the pressure. Assuming that electrons carry the current through the plasma, it follows that

$$\begin{aligned} R_{pl} &= \rho_{pl} \frac{L}{A} = \frac{L m_e v_{eo}}{A n_e q^2} & (3.16) \\ &= \frac{L m_e}{A q^2 n_e} v_{Te} \sigma_{eo} n_o \\ &= \frac{L m_e}{A q^2 n_e} v_{Te} \sigma_{eo} 3.2 \cdot 10^{13} p (\text{mTorr}) \end{aligned}$$

Therefore, the slope

$$m = \frac{3.2 \cdot 10^{13} m_e \sigma_{eo}}{q^2} \frac{L}{A} \frac{v_e}{n_e} \quad (3.17)$$

All of the symbols in this equation have known values so that ratio $\frac{v_{Te}}{n_e}$ can be calculated. Table 3.4 encapsulates the slopes of the lines extracted from the R vs. p curves and the estimates of $\frac{v_{Te}}{n_e}$ and the density of electrons (and ions) in the plasma, assuming an electron temperature of 2eV.

The densities of and and electrons are higher than those normally encountered in laboratory discharges. Typically $10^9 \frac{\text{ions}}{\text{cm}^3}$ would be expected.^{3,4} The power densities used in the system for these data range from 0.1 to 0.5 $\frac{\text{Watts}}{\text{cm}^3}$ and are efficiently coupled into the plasma at these electrode spacings.

Increasing the power applied to the plasma increases the pressure at which the plasma begins to become resistive. This may be due to two reasons.

Estimates for electrode spacing of 1.9 cm			
gas	power (Watts)	n_e/n_p (cm ⁴ /s)	n_e ($T_e = 2eV$)
$SF_6/10\%O_2$	100	$8.4 \cdot 10^{-4}$	$1.0 \cdot 10^{11}$
(20 sccm)	250	$8.0 \cdot 10^{-4}$	$1.1 \cdot 10^{11}$
400	$10.3 \cdot 10^{-4}$	$.82 \cdot 10^{11}$	
pressure at 50 mTorr			
gas	power (Watts)	n_e/n_p (cm ⁴ /s)	n_e ($T_e = 2eV$)
$SF_6/10\%O_2$	100	$1.3 \cdot 10^{-4}$	$6.4 \cdot 10^{11}$
(20 sccm)	250	$1.2 \cdot 10^{-4}$	$7.3 \cdot 10^{11}$
400	$1.4 \cdot 10^{-4}$	$6.2 \cdot 10^{11}$	
Estimates for electrode spacing of 2.5 cm			
gas	power (Watts)	n_e/n_p (cm ⁴ /s)	n_e ($T_e = 2eV$)
$SF_6/10\%O_2$	100	$7.9 \cdot 10^{-4}$	$1.1 \cdot 10^{11}$
(20 sccm)	250	$6.5 \cdot 10^{-4}$	$1.3 \cdot 10^{11}$
400	$6.3 \cdot 10^{-4}$	$1.4 \cdot 10^{11}$	
Estimates for electrode spacing of 2.5 cm			
gas	power (Watts)	n_e/n_p (cm ⁴ /s)	n_e ($T_e = 2eV$)
$CF_4/10\%O_2$	100	$1.2 \cdot 10^{-4}$	$1.1 \cdot 10^{11}$
(20 sccm)	250	$7.7 \cdot 10^{-4}$	$1.1 \cdot 10^{11}$
400	$5.1 \cdot 10^{-4}$	$16. \cdot 10^{11}$	

Table 3.4

First, the added power could increase the electron temperature so that the electrons move faster and therefore more freely and farther between collisions. The second and most probable reason is that the number density of the electrons increases, increasing the conductivity. The latter alternative is consistent with the calculations from the slopes in Table 3.4 and also agrees with published results from Langmuir probe studies.⁵ Figures 3.8 and 3.9 show explicitly the power dependence of the impedance of CF_4 and SF_6 with oxygen. CF_4 has a small increase in electron density over the range, but SF_6 exhibits a great increase in n_e as evident from the large resistance drop. For a pressure of 100 mTorr, the powers above 350 Watts produce enough carriers to make the plasma conductive. The electron temperature remains constant with power while the density increases.

The pressure at which the plasma becomes collisional reveals the dominant physics in some cases. In sulfur hexafluoride, the operating points for the diagnostic etched structures straddle the breaks due to pressure. In this case, the etching depends on many mechanisms in a complicated fashion, as shown in Chapter Four.

The use of CF_4 , however, whose break pressures fall above the operating conditions, show linear and monotonic dependence on the etching parameter. Chemistry dominates the etching process in Freon-116 so that little is certain from the electrical characteristics.

3.3. The DC Bias

The second source of information extracted from the plasma comes from monitoring the dc bias. These data are obtained through a low pass filter added to the input to the matching network. A series inductor and parallel capacitor remove the rf components and isolate the dc average that accumulates on the

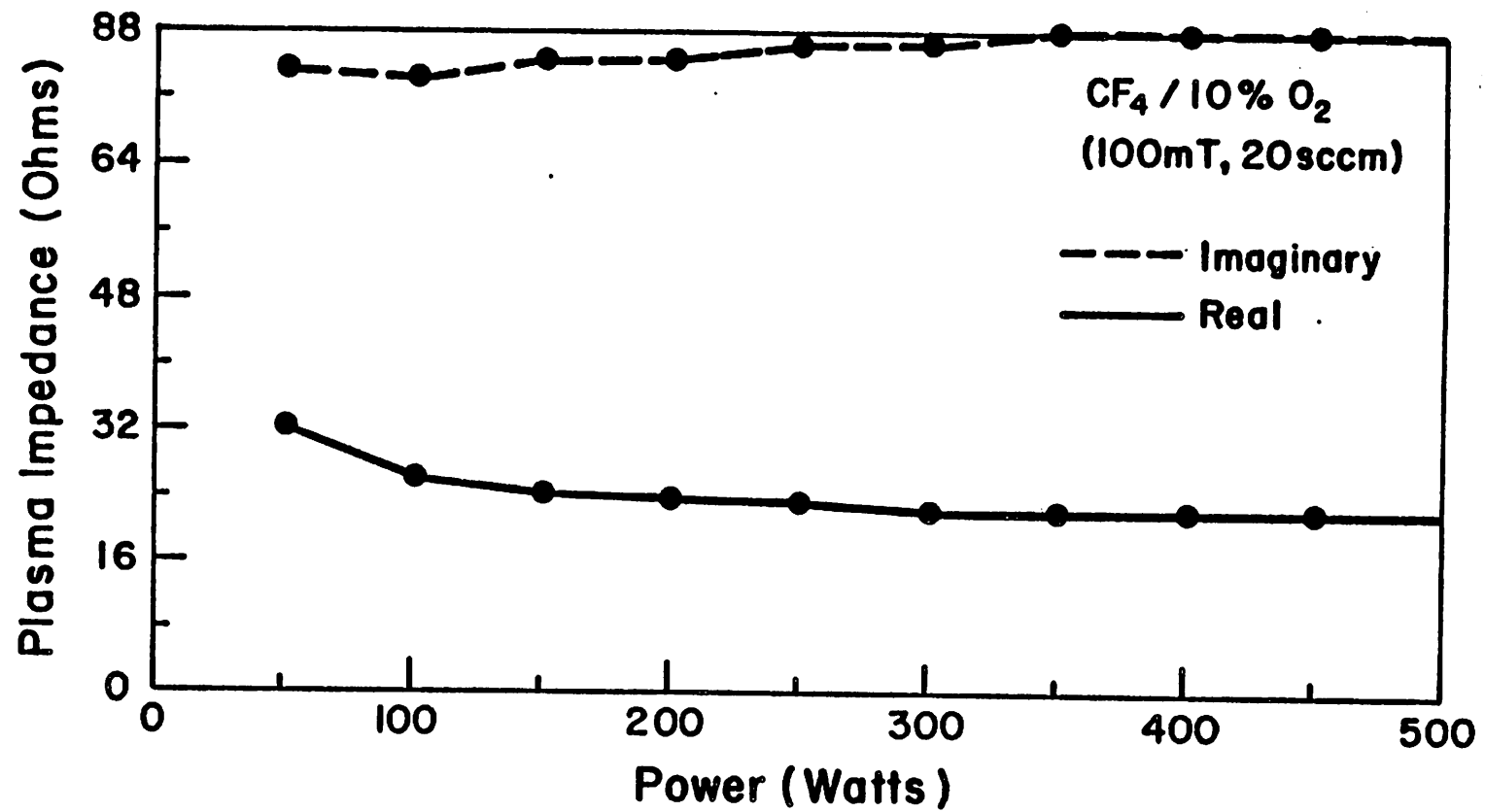


Figure 3.8

The real and imaginary parts of the plasma impedance as a function of power at 100 mT for 20 sccm Carbon Tetrafluoride with 10% Oxygen.

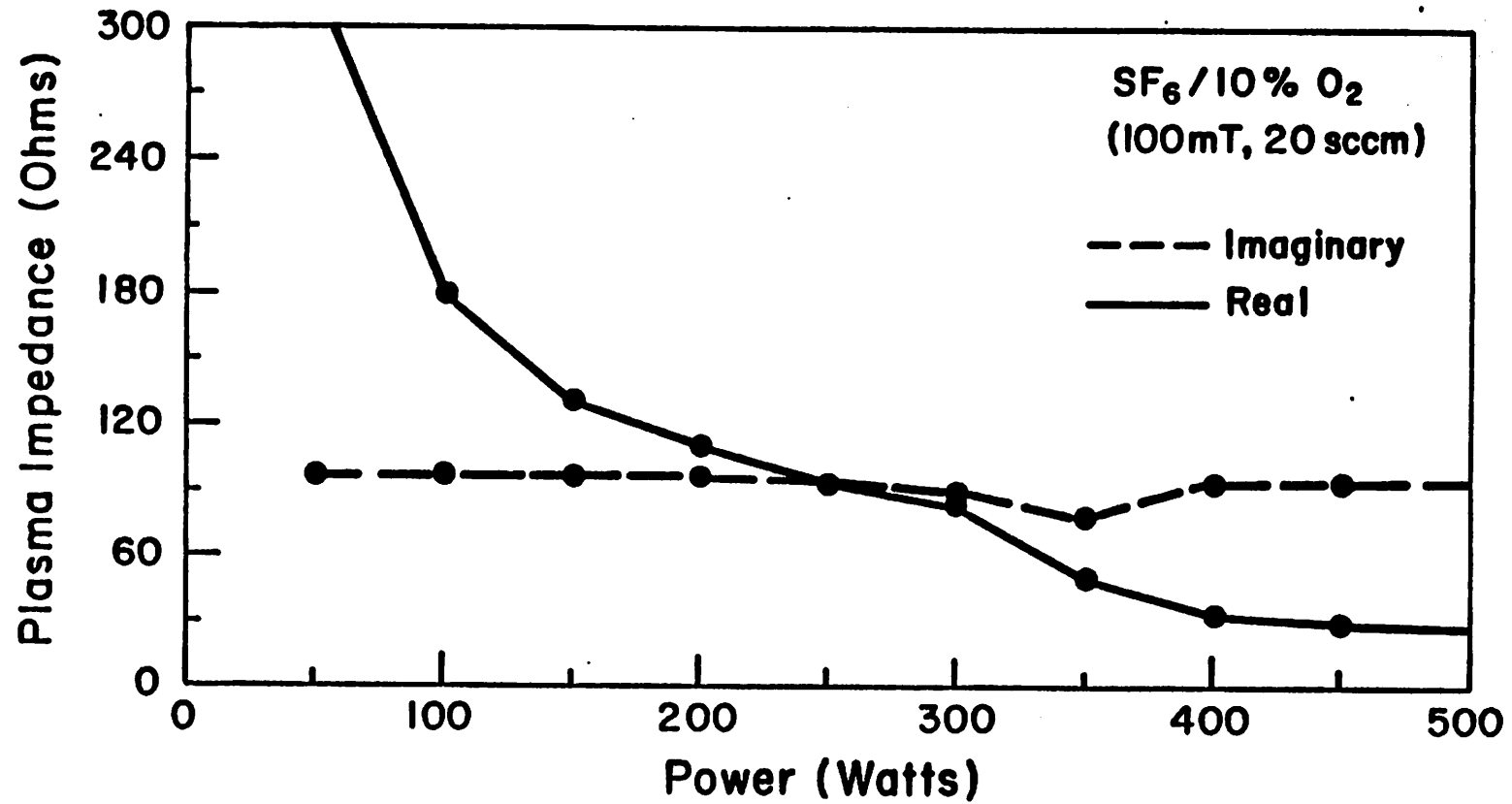


Figure 3.9

The real and imaginary parts of the plasma impedance as a function of power at 100 mT for 20 sccm Sulfur Hexafluoride with 10% Oxygen.

powered electrodes (cf. Figure 2.5). The schematic of this circuit appears in Appendix A. Equation 2.39 expresses this dc bias as the voltage across the sheath less the floating potential, $V_{dc} = V_f - V_{fl}$. The electron temperature fixes the floating potential. In the last section, we estimated this to be constant. Therefore, the dc bias is indicative of the accelerating voltage that the ions experience in crossing the sheath.

This potential has a very strong pressure dependence evident in Figures 3.10, 11 and 12. This dependence suggests a mobility limited situation for ions crossing the sheath. The anisotropy in etching does not show this same dependence. Etching with fluorinated gasses, the mechanisms are more complex than just ion transport across an electric field because of the more complicated chemistries.

Inspecting this dc bias as a function of power in Figure 3.13, CF_4 mixed with oxygen shows a square root dc voltage dependence with applied power. SF_6 , however, which has a collisional, resistive plasma at low powers, does not experience an increasingly negative bias until above 250 watts. Because there are not many carriers (electrons) generated in the plasma or because of their attachment to positive ions escaping the plasma below a power of 250 watts, a significant amount of the voltage appears across the plasma instead of across the sheath. A least squares fit shows that at 50 mTorr

$$DC_{CF_4} = 92.85 - 18.9\sqrt{P_{rf}} \quad (3.18)$$

$$DC_{SF_6} = 462.5 - 29.5\sqrt{P_{rf}} \quad P_{rf} > 250 \text{ Watts.} \quad (3.19)$$

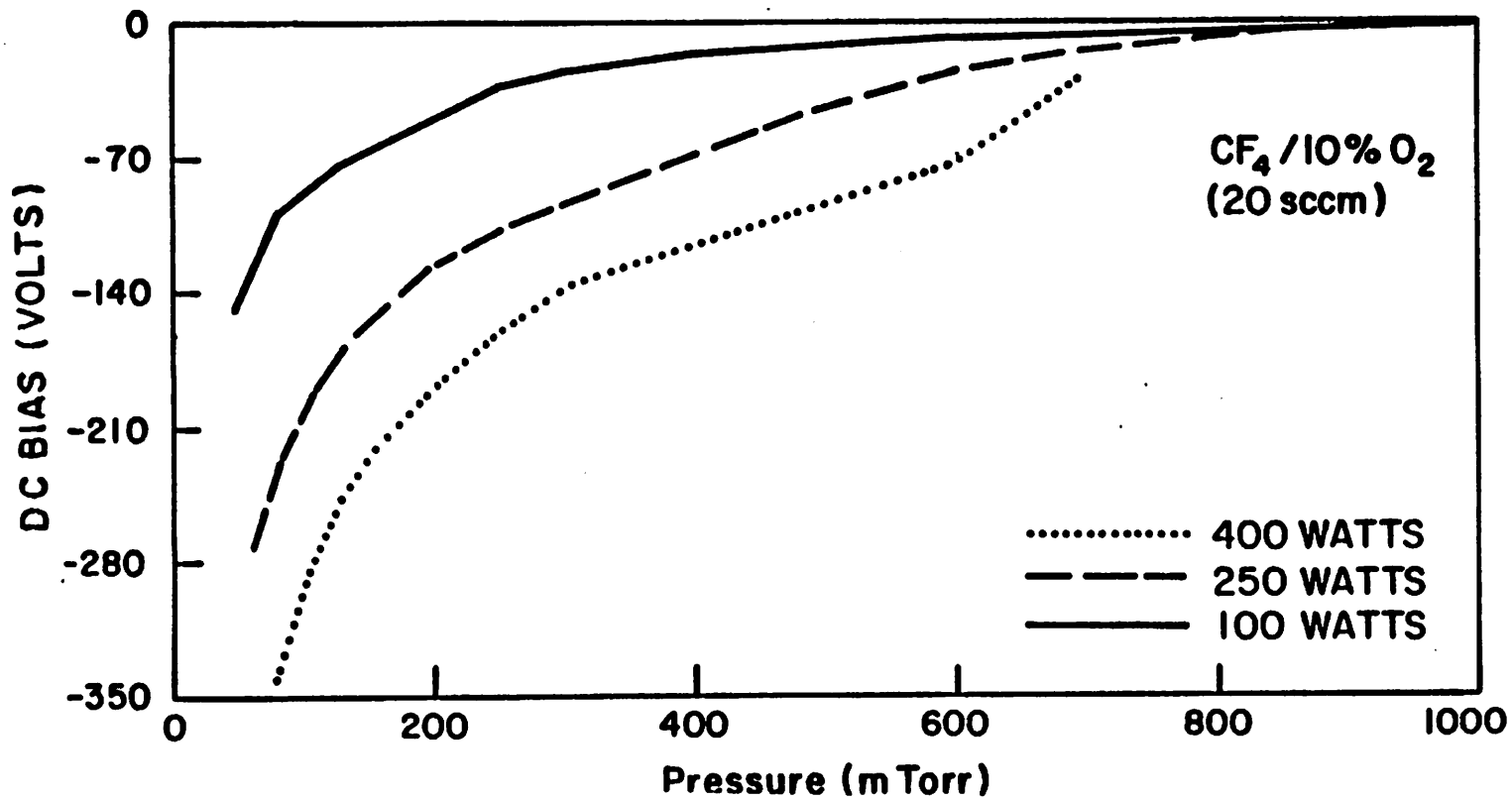


Figure 3.10

The negative DC bias on the substrate versus pressure at 100, 250 and 400 Watts for 20 sccm Carbon Tetrafluoride and 10% Oxygen.

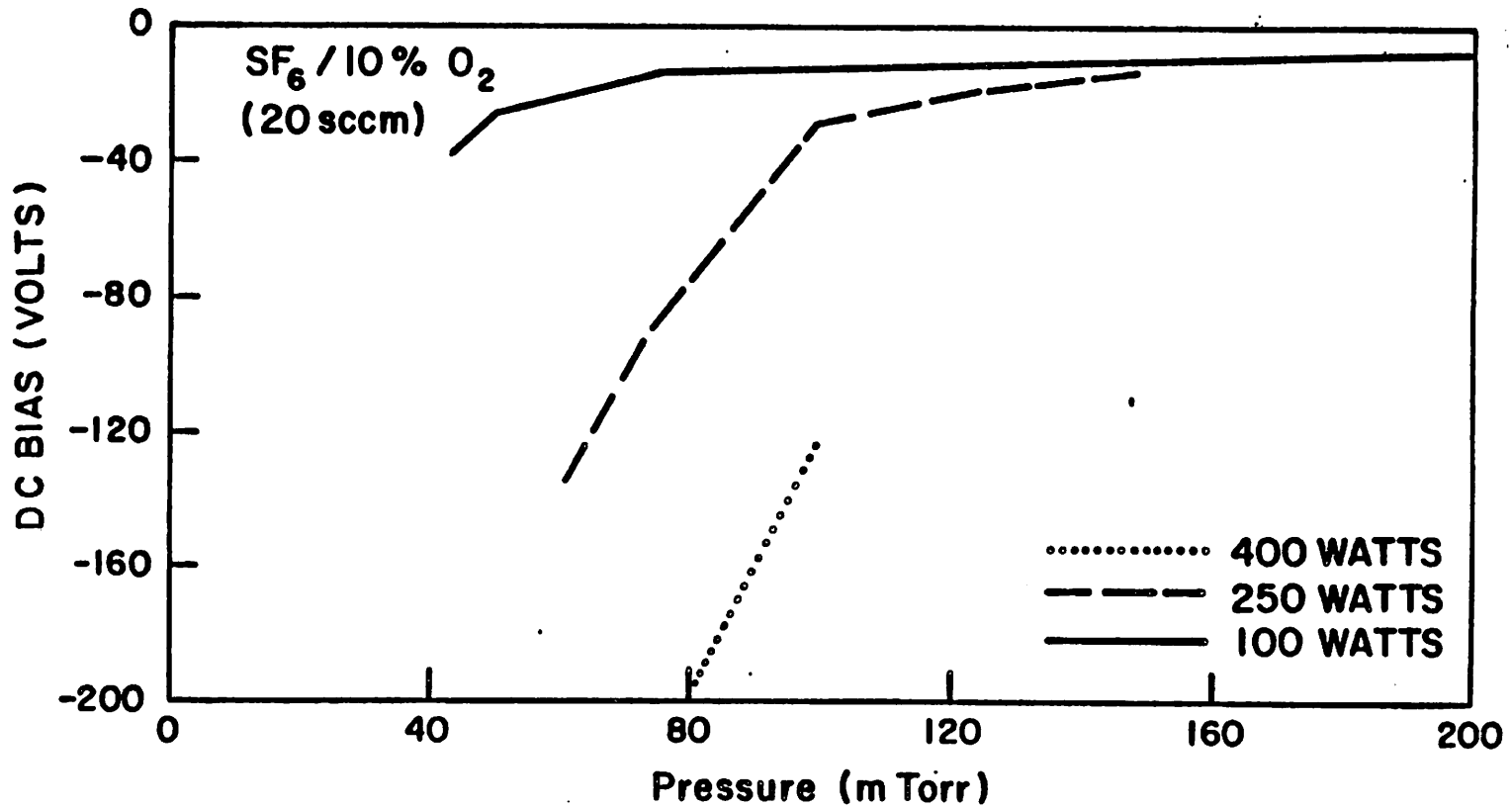


Figure 3.11

The negative DC bias on the substrate versus pressure at 100, 250 and 400 Watts for 20 sccm Sulfur Hexafluoride and 10% Oxygen.

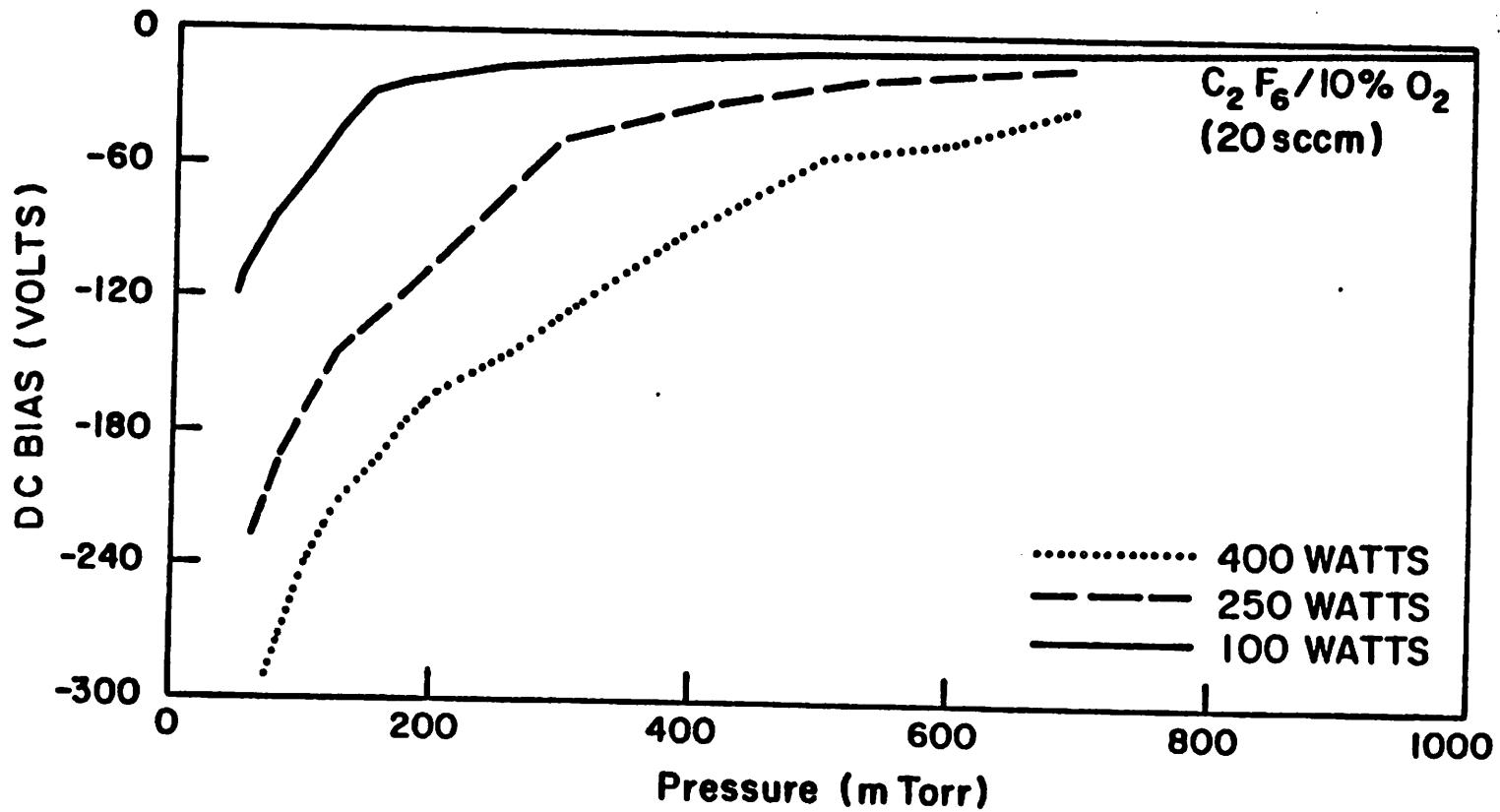


Figure 3.12

The negative DC bias on the substrate versus pressure at 100, 250 and 400 Watts for 20 sccm Hexafluoroethane and 10% Oxygen.

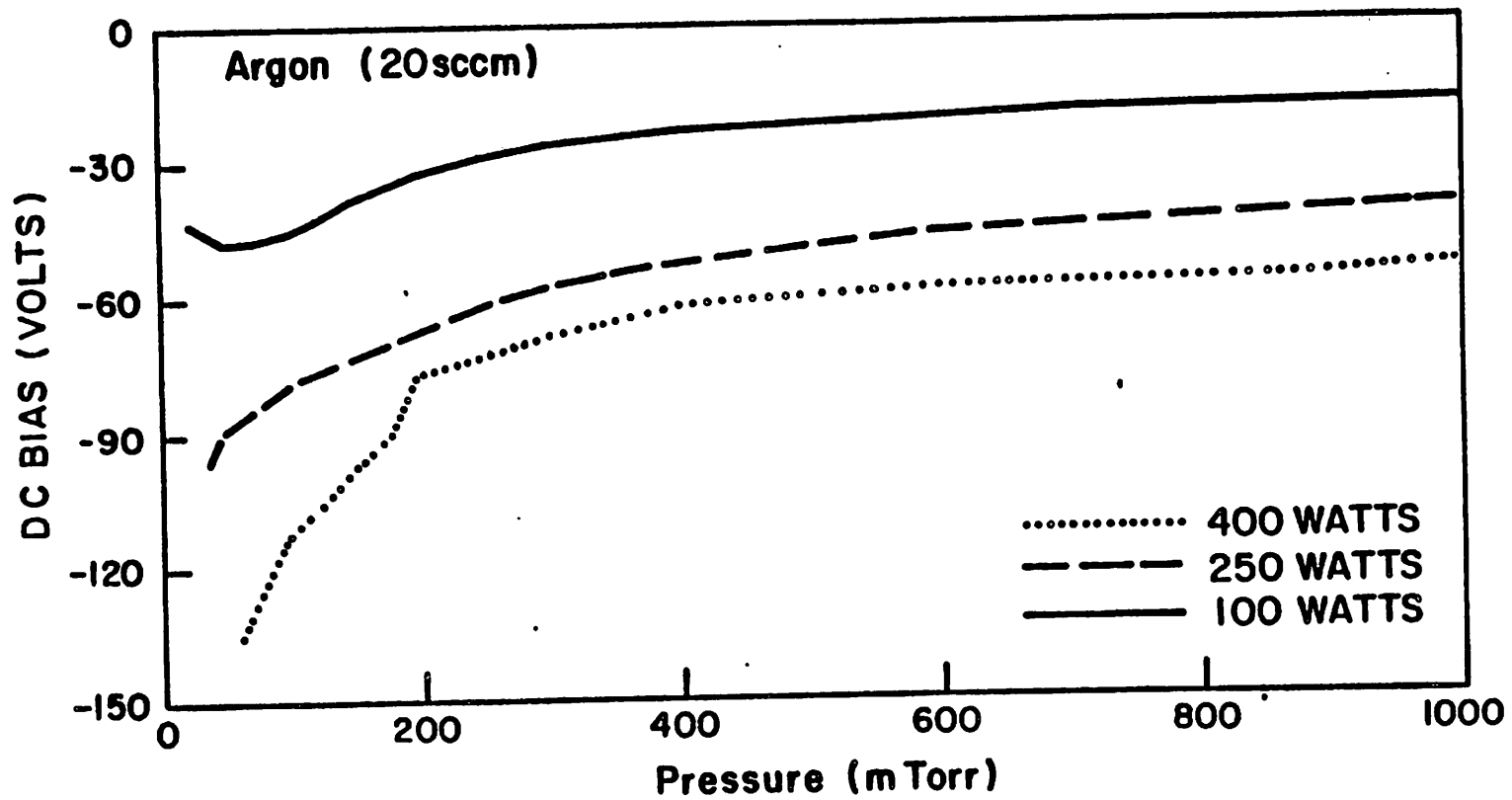


Figure 3.12B
 The negative DC bias on the substrate versus pressure at 100, 250 and 400 Watts for 20 sccm Argon.

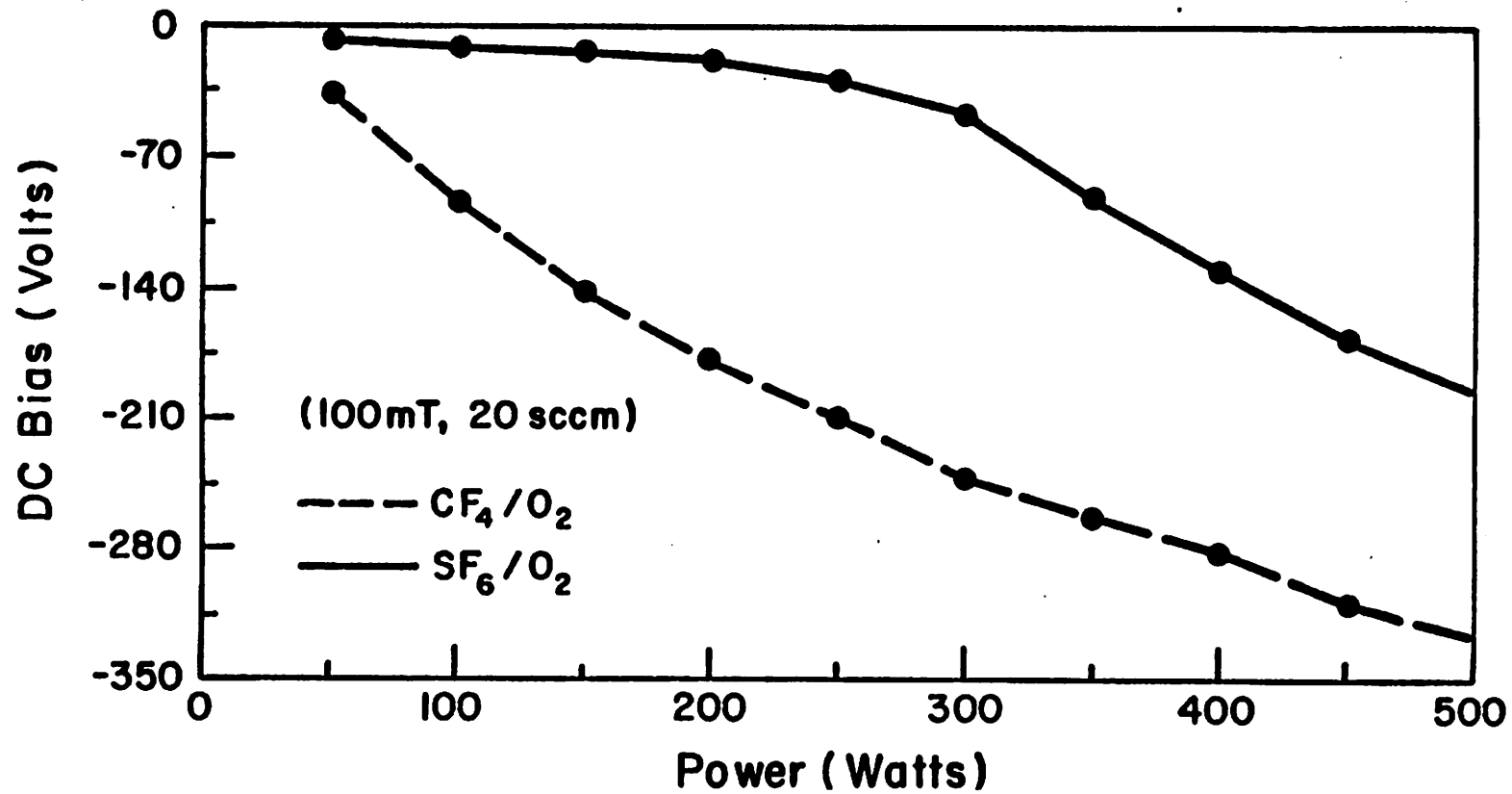


Figure 3.13
 DC bias on substrate electrode versus power at 100 mTorr for Carbon Tetrafluoride and Sulfur Hexafluoride mixed with oxygen.

3.4. Optical Spectroscopy Measurements

The final non-intrusive method of characterizing the plasma involves more the chemical nature of the discharge than it does the electrical and physical properties. The relative density of fluorine atoms can be measured by monitoring the intensity of emission lines with a scanning monochromator. The essentials of the apparatus are portrayed in Figure 3.14. The device can measure the relative intensities of wavelengths ranging between 200 to 900 nanometers.

The first observation using the monochromator determines the intensity of the plasma, for a fixed line (703.7nm), versus power. Figure 3.15 shows this dependence for sulfur hexafluoride and carbon tetrafluoride. Both intensities are fairly linear, with power as would be expected. This test confirms that the plasma remains between the electrodes for these conditions and does not lose power to discharges elsewhere in the chamber. It often occurs for this system, especially at large electrode spacings and at high pressures, that the plasma escapes from between the electrodes.

Figures 3.16-18 graph the dependence of the intensity of the fluorine 703.7 nm line versus pressure. This line has a strong intensity above the background and is often used for end point detection. By itself, this information is only qualitative from run to run. By normalizing the intensity of this line to that of the argon 750.4 nm line, more quantitative information can be obtained. The process of actinometry is defined in ⁶ and gives some clues to the relative density of free fluorine in the glow discharge. The presence of free fluorine in the plasma is not a strict function of the fluorinated source gas. The chemistry involved in dissociation of complex molecules make the presence of F unpredictable. Results show that the silicon etch rate is not strictly proportional to the F intensity also.⁷ Thus, if the excited state responsible for the noble gas optical emission matches closely the energy of the level responsible for excitation of the

MEASUREMENT SCHEME OF RELATIVE INTENSITIES FROM THE PLASMA

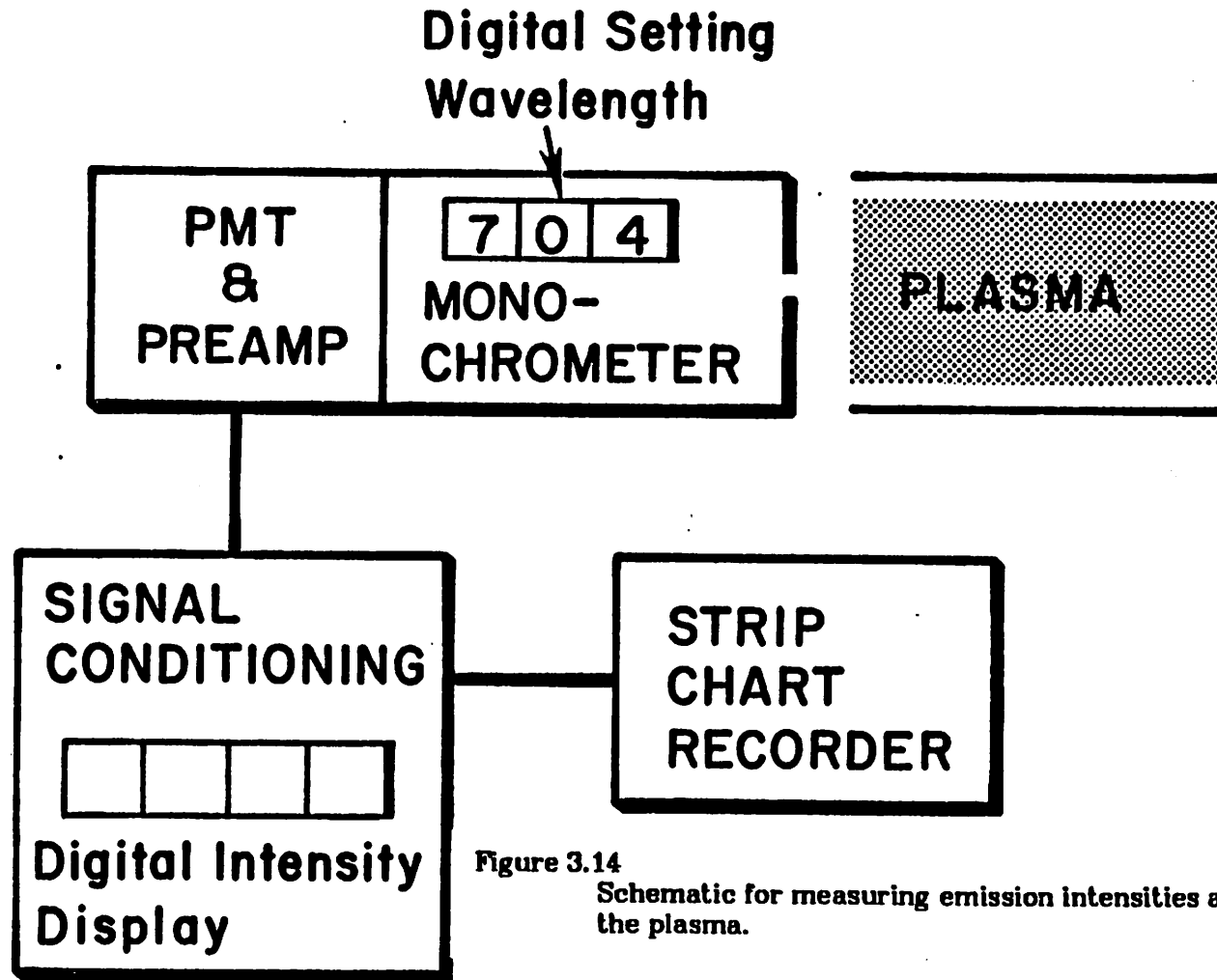


Figure 3.14
Schematic for measuring emission intensities and optical spectra from the plasma.

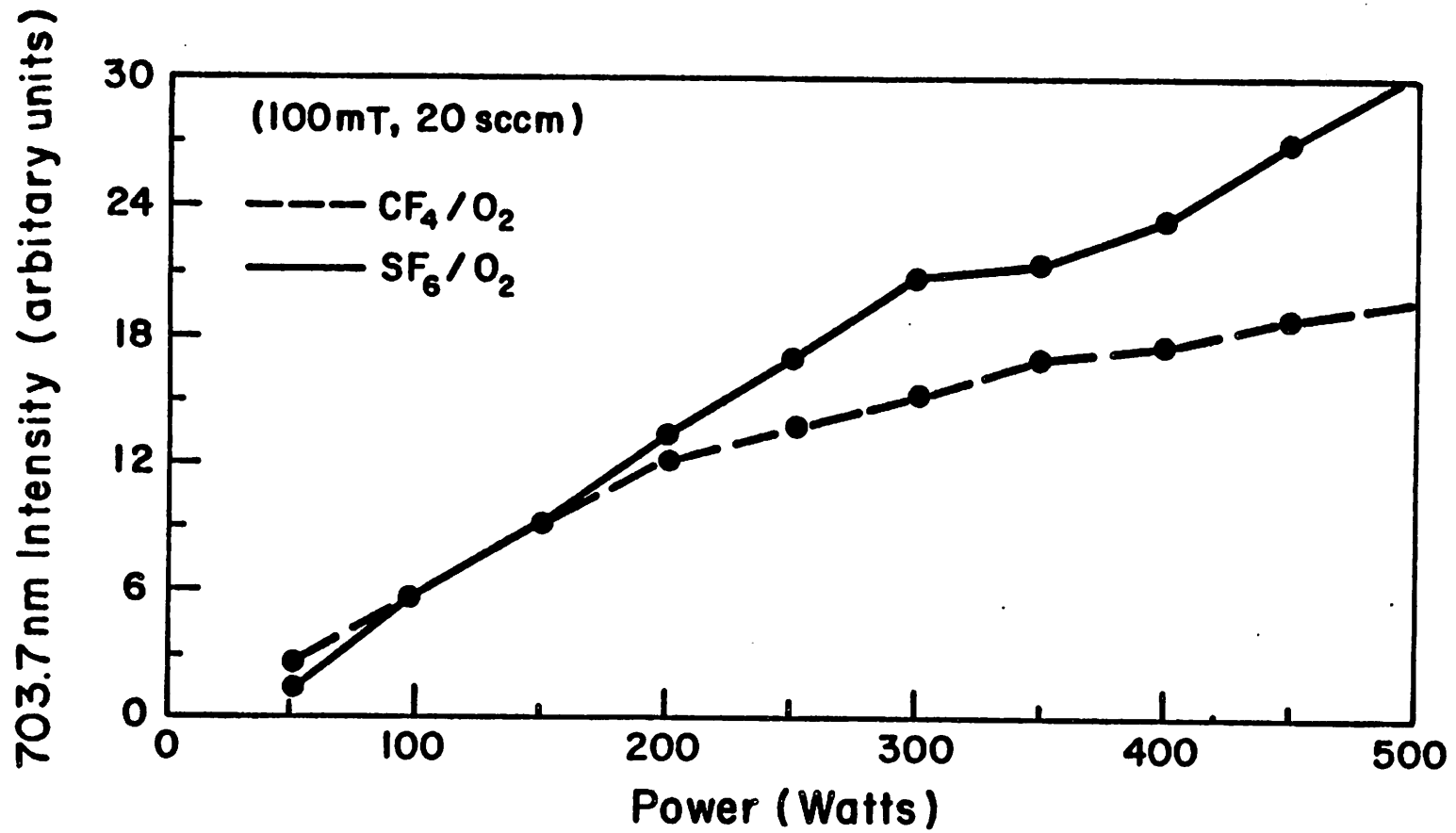


Figure 3.15
Fluorine emission intensity at 703.7 nm versus power at 50 mTorr for
Carbon Tetrafluoride and Sulfur Hexafluoride mixed with oxygen.

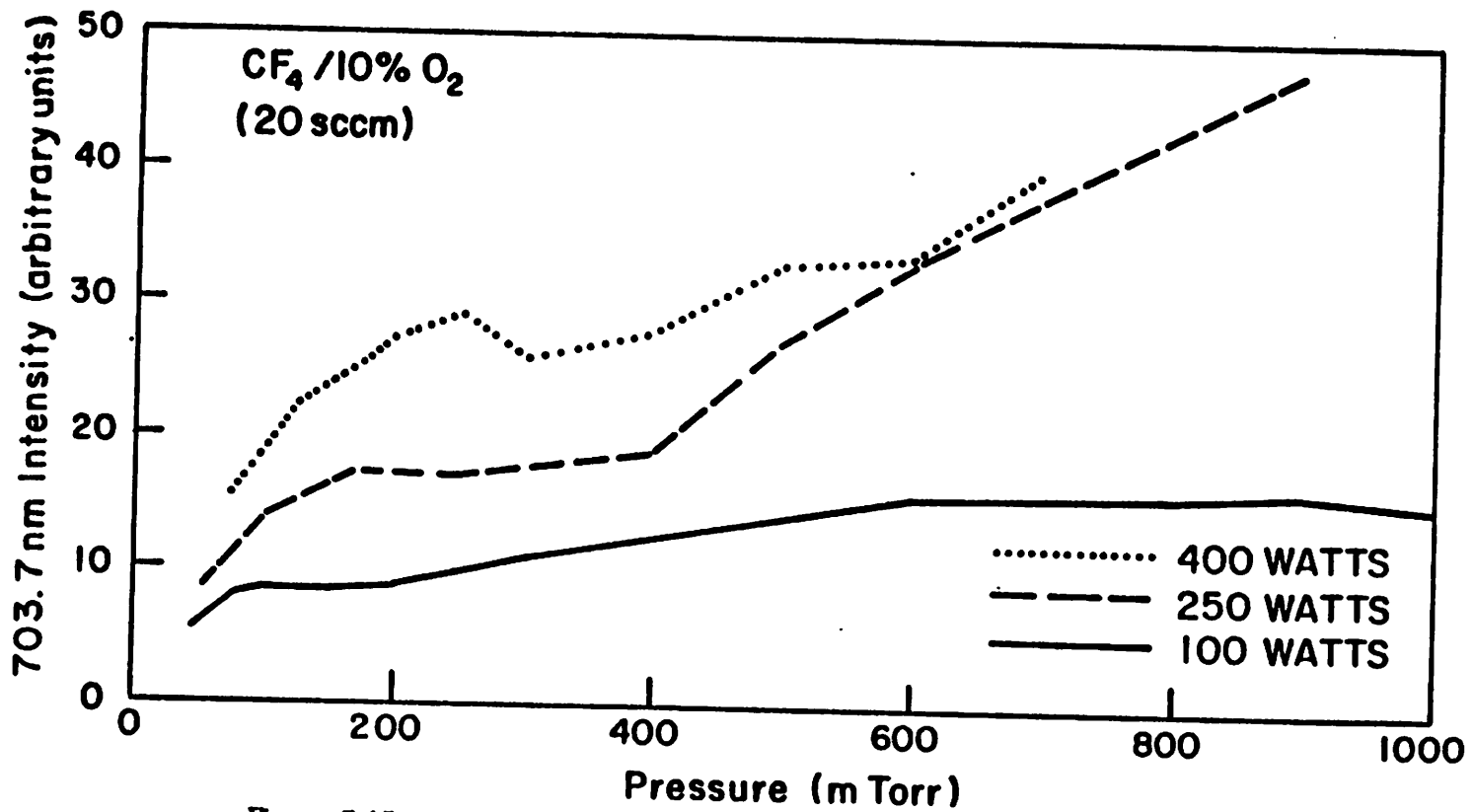


Figure 3.18

Fluorine emission intensity at 703.7 nm versus pressure at 100, 250 and 400 Watts for Carbon Tetrafluoride mixed with oxygen.

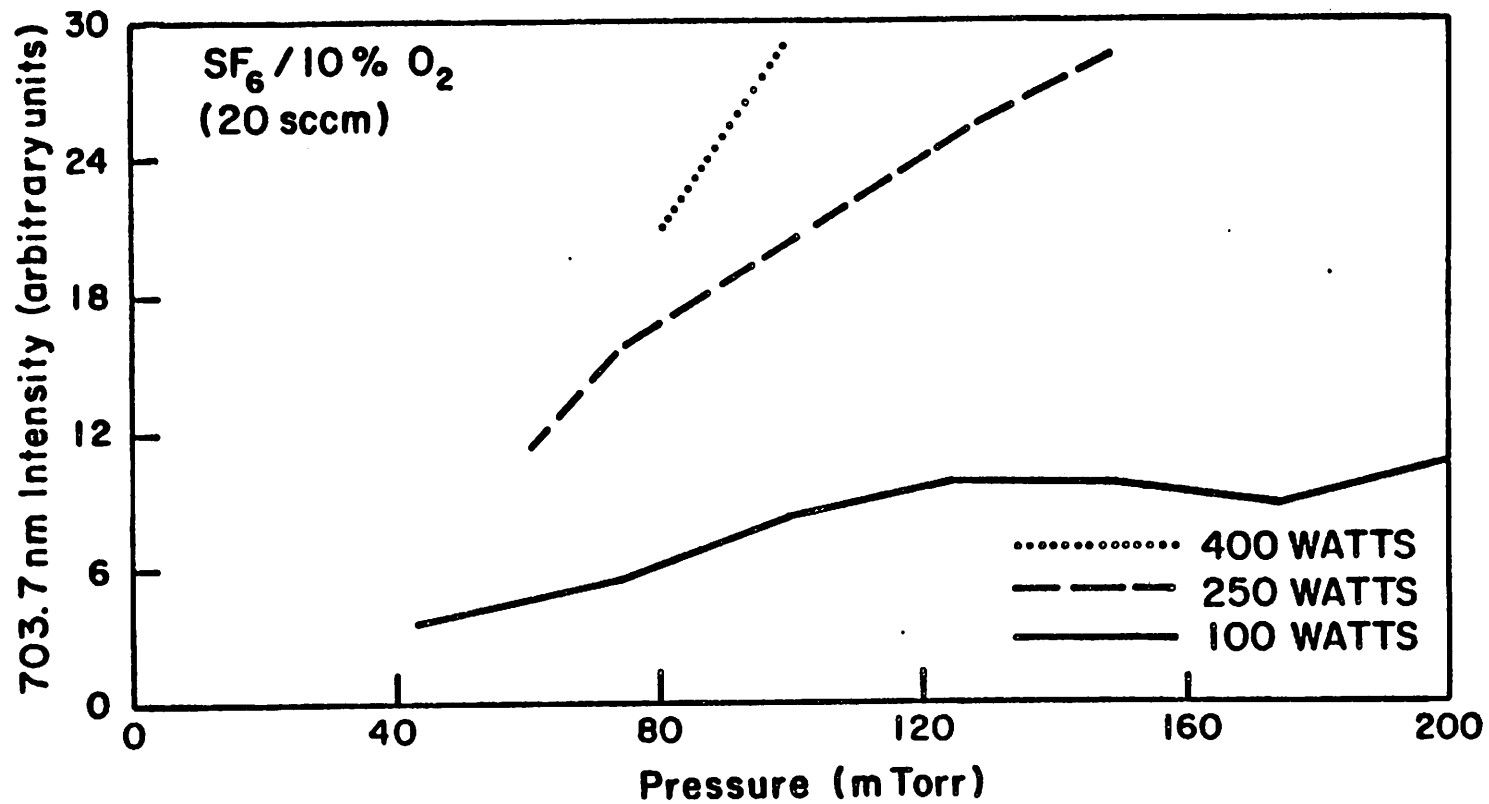


Figure 3.17
 Fluorine emission intensity at 703.7 nm versus pressure at 100, 250 and 400 Watts Sulfur Hexafluoride mixed with oxygen.

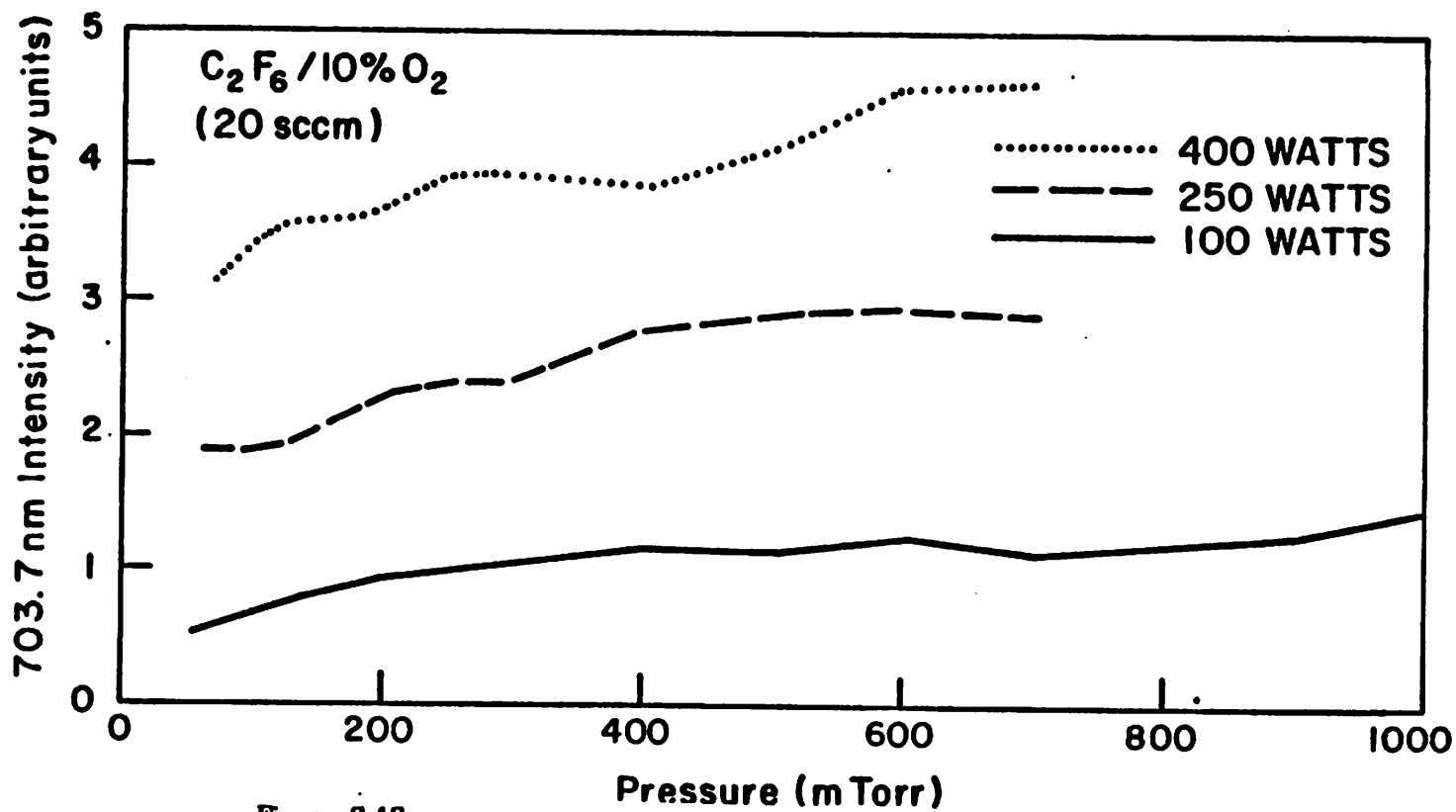


Figure 3.18
 Fluorine emission intensity at 703.7 nm versus pressure at 100, 250 and 400 Watts Hexafluoroethane mixed with oxygen.

reactive species, then the excitation efficiencies of these levels have similar dependences on the plasma parameters. By monitoring both noble gas and reactive plasma gas intensities, the reactive particle density is determined by normalizing its emission intensity with that of the noble gas.

Essentially, the process can be interpreted as follows: the density of species q is related to the optical-emission intensity I_q by $I_q = k_q n_q \eta_q$ where n_q is the density of species q in the ground state, η_q is the excitation efficiency of the discharge to excite q from ground to electronically excited emitting state and k_q is a proportionality constant independent of discharge parameters. Combining these expressions for fluorine and argon, the relative reactive density can be determined as

$$\frac{n_F}{n_{Ar}} \propto \frac{I_F}{I_{Ar}} \quad (3.20)$$

from just the emission intensities. The density of argon, n_{Ar} , is known because argon is a noble gas which does not participate significantly in the plasma chemistry.

Figure 3.19 shows the 750.4 nm line as it varies with pressure. Figures 3.20-22 demonstrate the normalized dependence of the fluorine intensity on pressure. The curves for all three of the gasses exhibit a linear dependence on pressure. The relative density in sulfur hexafluoride tapers off for low powers as the plasma is extinguished. It is informative in the etching process to compare the power dependence of the relative density of fluorine. As shown by Flamm,⁸ the fluorine spontaneously etches silicon. The intensity of the fluorine line may not correlate to the etching mechanisms, but the density does. In SF_6/O_2 and C_2F_6/O_2 plasmas, the amount of fluorine generated in the glow strongly depends on power. As demonstrated in Chapter Six, this free fluorine also participates in the total and isotropic etch rates. In Freon-14 and oxygen, however, the

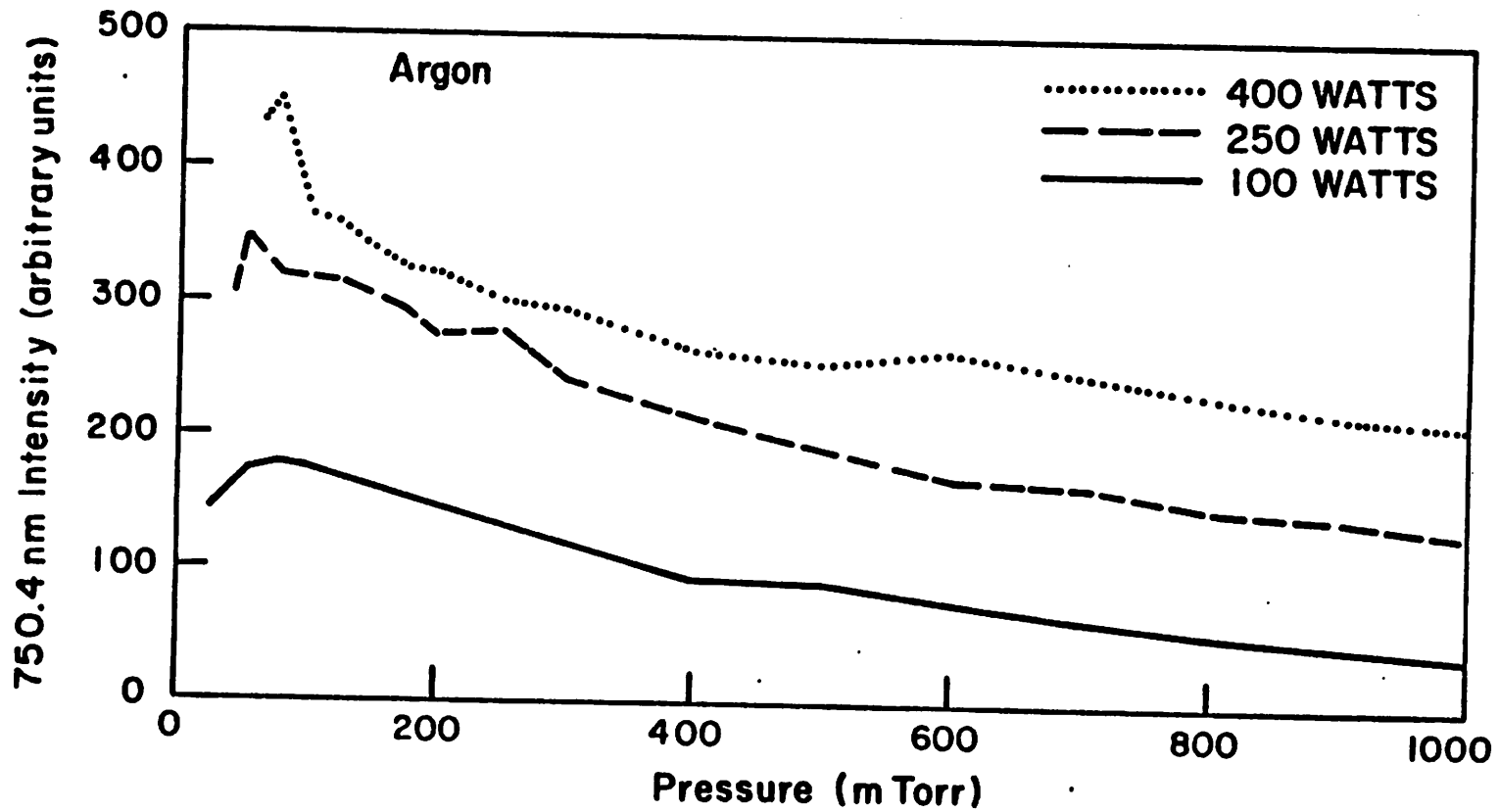


Figure 3.19
Argon emission intensity at 750.4 nm versus pressure at 100, 250 and 400 Watts.

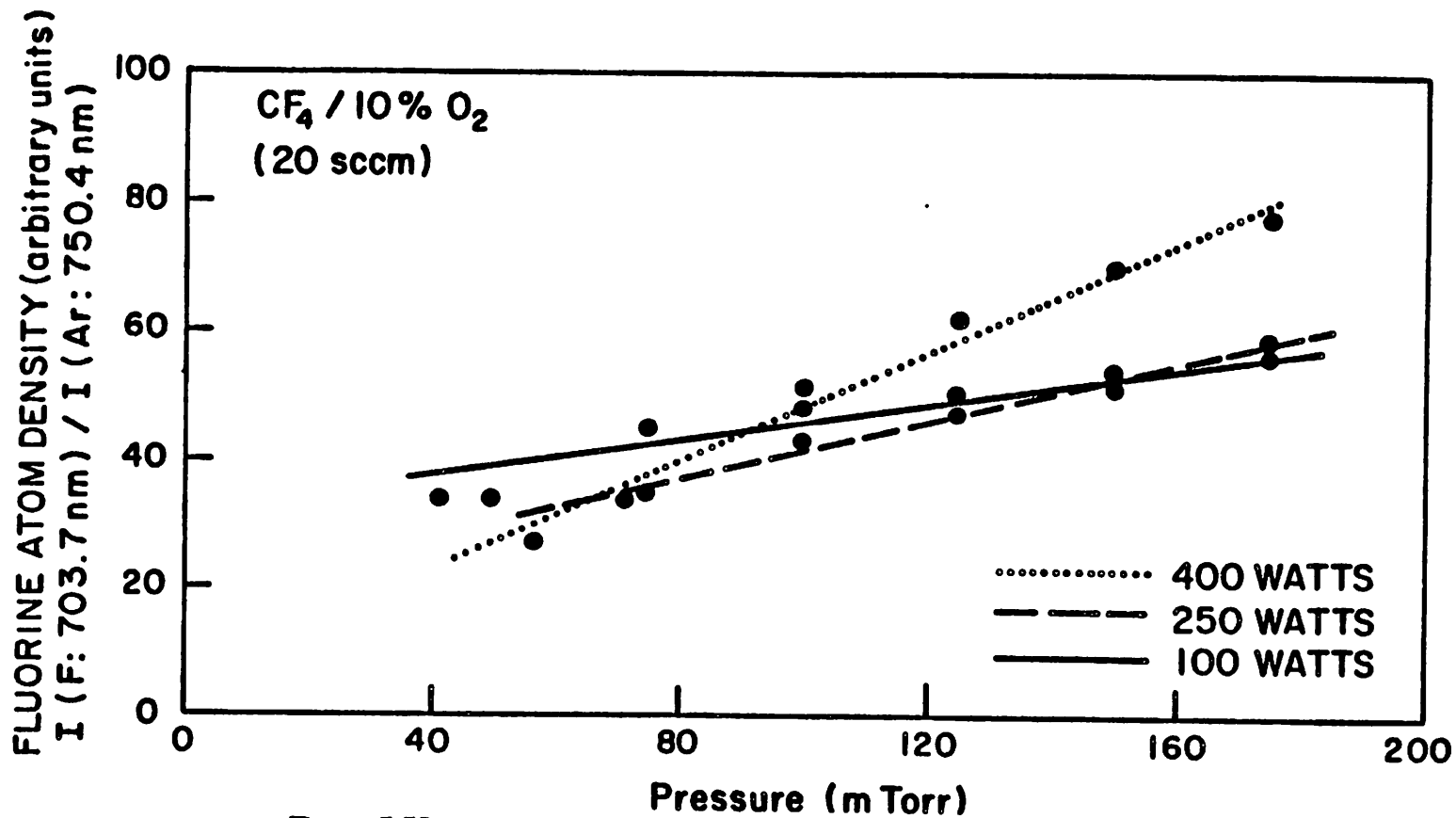


Figure 3.20

Normalized fluorine emission intensity (703.7:750.4 nm) versus pressure at 100, 250 and 400 Watts for Carbon Tetrafluoride mixed with oxygen.

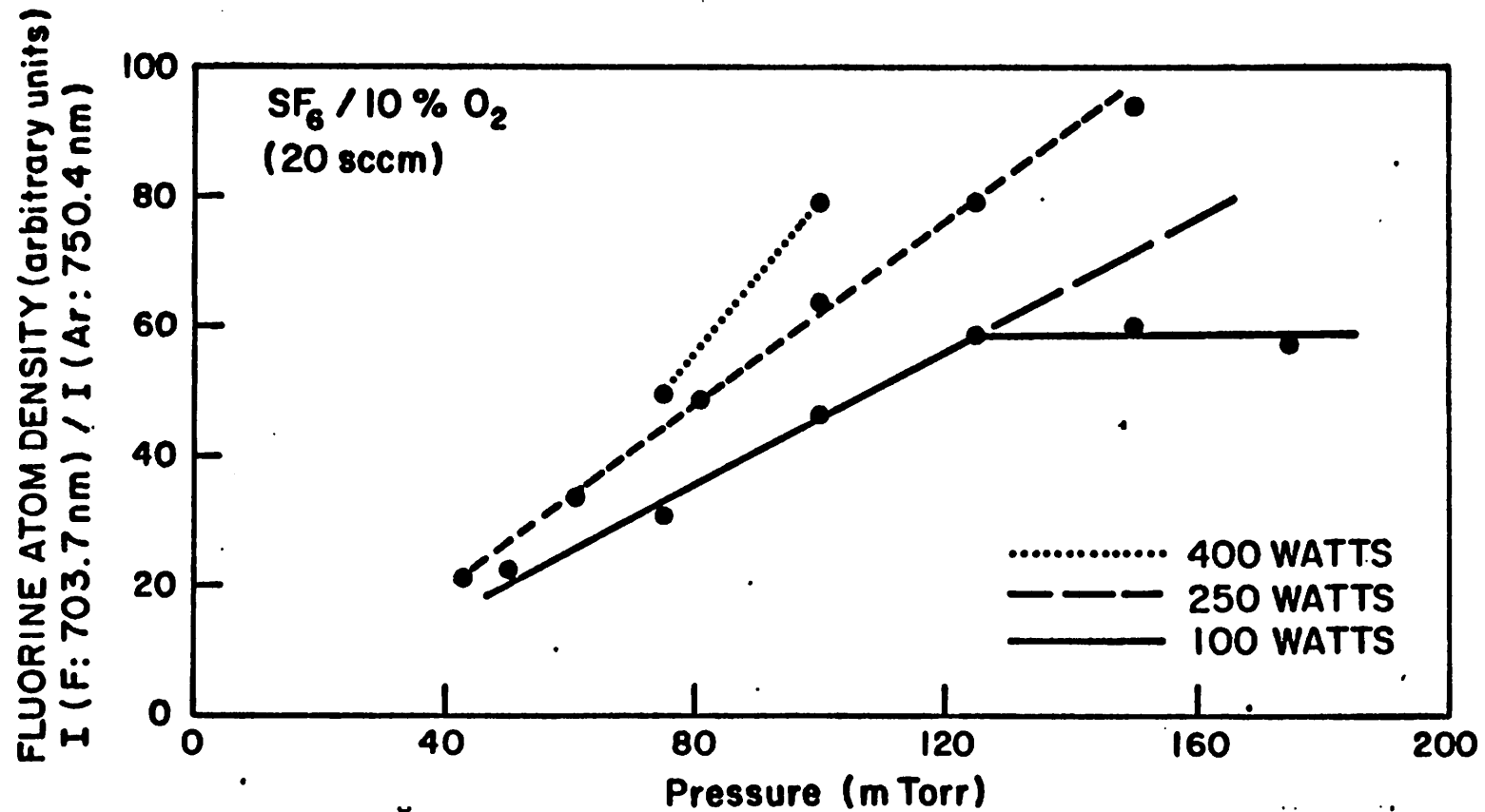


Figure 3.21
 Normalized fluorine emission intensity (703.7:750.4 nm) versus pressure at 100, 250 and 400 Watts Sulfur Hexafluoride mixed with oxygen.

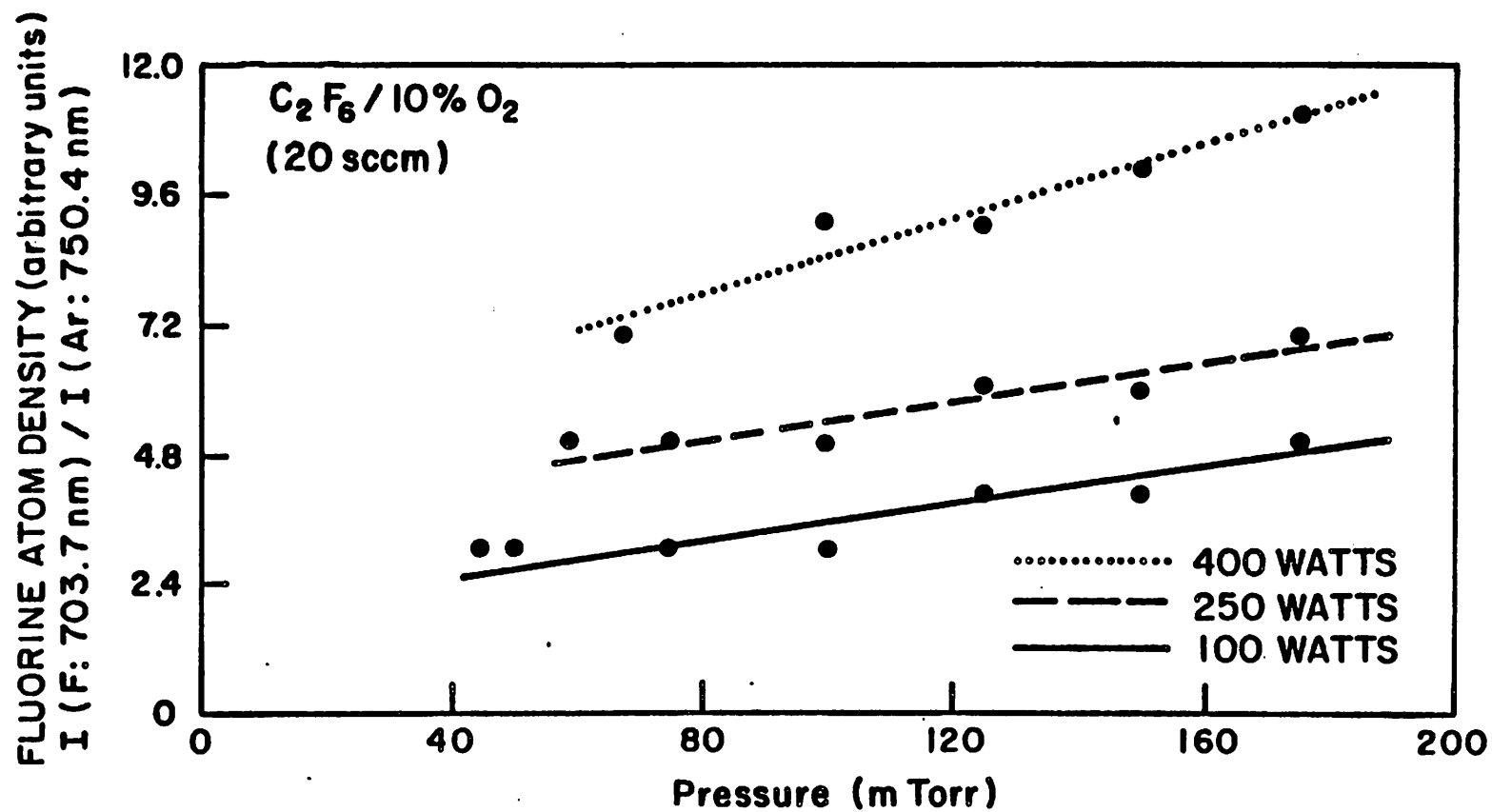


Figure 3.22

Normalized fluorine emission intensity (703.7:750.4 nm) versus pressure at 100, 250 and 400 Watts Hexafluoroethane mixed with oxygen.

additional power does not generate more free fluorine and the etch rates depend linearly on power without the additional chemical etching.

3.5. Conclusions

From non-intrusive means of characterizing the plasma, a fairly consistent view of etching features can be based on these direct observables.

Modeling the plasma electrically as a parallel capacitance and conductance, in series with a resistor demonstrates the dependence of the model circuit elements of the plasma on power and pressure. The value of the parallel capacitance suggests a displacement current of a parallel plate capacitor, the sheath, with a free space dielectric. Its constancy indicates the absence of scatter and ionization in the sheath. The value of the conductance agrees with the number density of ions calculated entering the sheath and also tells that the flux is primarily a well-collimated, drift beam through the sheath potential. The resistance in the plasma itself varies the most dramatically, taxing the matching network equipment. It increases linearly with pressure above a certain break pressure suggesting a collisional plasma above that pressure. This break pressure increases with power as more carriers, n_e , are generated. From the slope of pressure curve the ratio of the electron velocity to the electron density, $\frac{v_e}{n_e}$ are calculated and summarized in Table 3.2. These values agree with the text book theory for laboratory plasmas. As the plasma resistance changes the potential distributions and power dissipated in the glow varies, changing the characteristics of the etching mechanisms.

Observation of the dc self-bias created at the substrate electrode along with these electrical characteristics helps to determine the voltage distribution. From the modeled impedance elements the electron temperature appears to be constant, fixing the plasma floating potential. The dc self bias should then vary

as the voltage across the sheath. For Freon-14 the dc voltage follows the expected square-root of power dependence. For SF_6 the same dependence is observed at high powers where the number of carriers reduce the potential drop across the plasma. This voltage then is indicative of the sheath and rf peak-to-peak voltage which figure into the ion transport mechanisms in reactive ion etching.

Turning to the chemistry involved in plasma etching the relative change in density of fluorine radicals generated in the plasma is estimated from the optical emission intensities. Reactive fluorine atoms chemically etch silicon spontaneously and isotropically. The concentration of F increases linearly with pressure as does the isotropic component in CF_4 and oxygen. This amount depends heavily on power in both SF_6 and C_2F_6 etch gasses. In C_2F_6 the etching appears to be a competition between polymerization and the F available to remove it. Carbon tetrafluoride, which does not have a strong F dependence on power, demonstrates etching components depending linearly on power.

References

1. Brian Chapman, in *Glow discharge processes - - sputtering and plasma deposition*, p. 66, Wiley-Interscience, (1980).
2. C.B. Zarowin, "Plasma etch anisotropy -- Theory and some verifying experiments relating ion transport, ion energy and etch profiles," *Journal of the Electrochemical Society*, vol. 130, no. 5, p. 1144, (May 1983).
3. M.J. Kushner, "A kinetic study of the plasma etching process: I. A model for etching Si and SiO₂ in CnFm/H₂ and CnFm/O₂ plasmas," *Journal of Applied Physics*, vol. 53, no. 4, p. 2923, (April 1982).
4. Wulf B. Kunkel, *Plasma physics in theory and application*, McGraw-Hill, (1986).
5. Ch. Steinbruechel, "Langmuir probe measurements on CHF₃ and CF₄ plasmas: The role of ions in the reactive sputter etching of SiO₂ and Si," *Journal of the Electrochemical Society*, vol. 130, no. 3, p. 648, (March 1983).
6. J.W. Coburn and M.Chen, "Optical emission spectroscopy of reactive plasmas: a method for correlating emission intensities to reactive particle density.," *Journal of Applied Physics*, vol. 51, no. 6, p. 3134, (June 1980).
7. C.J. Mogab, "The loading effect in plasma etching," *Journal of the Electrochemical Society*, p. 1262, (August 1977).
8. D.A. Danner, D.L. Flamm, and J.A. Mucha, "Downstream Atomic Monitoring for absolute etch-rate determination," *Journal of the Electrochemical Society*, vol. 130, no. 4, p. 905, (April 1983).

CHAPTER FOUR

4. STUDIES OF PLASMA ETCHING MECHANISMS WITH CANTILEVER STRUCTURES

4.1. Introduction

In this chapter, cantilevered structures are used to explore the relative importance of factors such as surface migration, ion directionality, and the basic isotropic and anisotropic components in plasma etching. Computer simulation is used to illustrate the various mechanisms that may be expected. Integrated cantilever structures were fabricated by overetching a supporting material (polyimide or SiO_2) beneath a non-eroding mask (titanium or hardened resist). This diagnostic structure is used in studies of silicon etching with SF_6/O_2 , CF_4/O_2 , and C_2F_6/O_2 under various powers, pressures and flow rates. Etching components are given as a function of power, pressure and flow-rate and related to the plasma properties introduced in the previous chapter.

A thorough understanding of etching mechanisms is necessary for evaluating profile shape and line-width loss in dry etching. The etched profile can be a complicated function of many possible etching mechanisms. To a first order, a simple isotropic component and an anisotropic component perpendicular to the wafer due to ion bombardment suffice. However, the transport of ions¹ and the angle of arrival of ions may also be important. In certain cases migration along the surface also occurs.^{2,3}

Cantilever structures can be used as a tool for exploring and controlling these mechanisms. A silicon wafer and a spacer have been used as a cantilever

to observe the etching of silicon exposed and unexposed to a plasma. Also, three layer structures have been used to achieve tapered profiles in oxide etching.^{4,5} In this paper, computer simulation of etching with cantilever structures is used to relate characteristic profile shapes to various etching mechanisms. The diagnostic profile shape technique is then used to evaluate the mechanisms in etching silicon with fluorinated gasses. The simulation is carried out by generalizing the etching routines in the program, for Simulation And Modeling of Profiles in Lithography and Etching (SAMPLE⁶).

The use of a cantilever structure gives a more complex masking structure which illustrates the effects of the various components. It is convenient for diagnostic purposes as the isotropic and anisotropic components can be read directly and checked against profile wall angles for consistency. The cantilever structure also gives an extra degree of freedom, that is mask height above the substrate, which helps separate mechanisms such as angular ion effects and surface migration which depend upon the existing profile.

The ultimate goal of applying the cantilever diagnostic structure to etching of silicon in fluorinated gasses is the mapping out of the dependence of the etch rate components on plasma parameters. To do this cantilever structures were first fabricated from hardened resist on undercut silicon dioxide and titanium supported on polyimide. A catalog of etching profiles is then made and interpreted for mechanisms and rate parameters. Although the rates components are found to be a complicated function of operating conditions a consistent prediction of the profile features can be made.

4.2. Computer simulation.

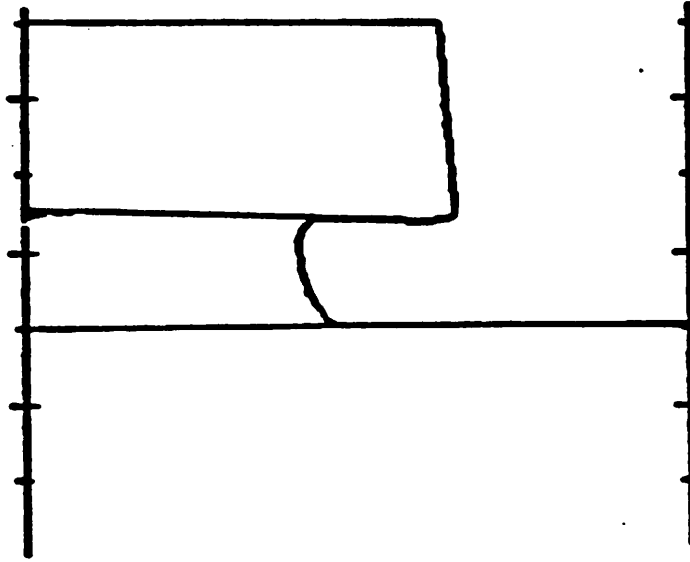
The SAMPLE computer program is used to illustrate the effects of various etching mechanisms on cantilever structures. The plasma etching routines in SAMPLE were generalized for this purpose. Figure 4.1 introduces the cantilever structure and gives a simple example of etching using two components in the computer simulation. This is a two dimensional cross-section as it would appear in a scanning electron micrograph (SEM). Here an anisotropic component three times larger than the isotropic component is used. The five different lines in the graph show the etching progression at five different equally spaced times. This corresponds to the degree of anisotropy,

$$A = \frac{Rate_{anisotropic}}{Rate_{total}} = \frac{Rate_{anisotropic}}{Rate_{isotropic} + Rate_{anisotropic}} = 0.75 \quad (4.1)$$

The anisotropy ratio can be seen directly in the cantilever profile cross-section as the ratio of the height of the step formed by the overhanging structure to the total etched depth. The extreme cases are, $A=1$ is totally directional and $A=0$ where the etching proceeds isotropically as in wet-chemical etching. Note that the isotropic etching under the mask forms a flat horizontal plateau. Etching with these two components produces a side wall angle of the step equal to $\tan^{-1} \frac{Rate_{aniso}}{Rate_{iso}}$ which can be used as a self consistency check. As the isotropic component dominates the step angle decreases from 90° .

Figure 4.2 introduces an additional effect of surface migration compared to etching with two components. Surface migration is modeled by the addition of a lateral etching component found by taking a fraction of the direct incident flux and convolving with a Gaussian diffusion function. In Figure 4.2, the anisotropy ratio is 0.40 which is fairly isotropic. In Figure 4.2a, no migration is assumed. The side wall angle is characteristic of etching with two components. The shaded horizontal edge proceeds downward horizontally. In Figure 4.2b a

Cantilever Structure



Etching with isotropic vertical components

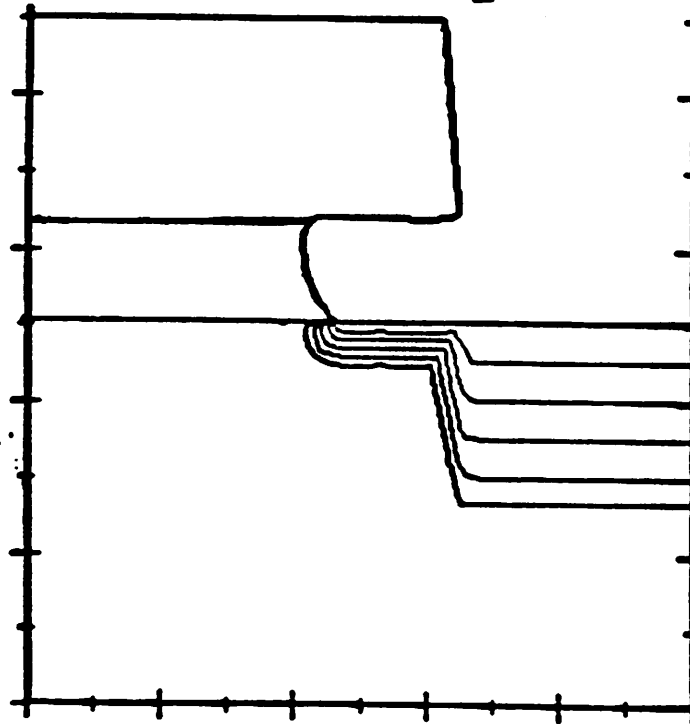


Figure 4.1

a). Computer simulation of the cantilever structure and b). etching with isotropic and anisotropic components.

surface migration with a diffusion length of 2.0 micrometers is added. This initially horizontal shaded region begins to slope downward toward the mask edge as the process proceeds. The profile tends to round more and shifts laterally. Migration can most easily be detected by the sloping of the shadowed region.

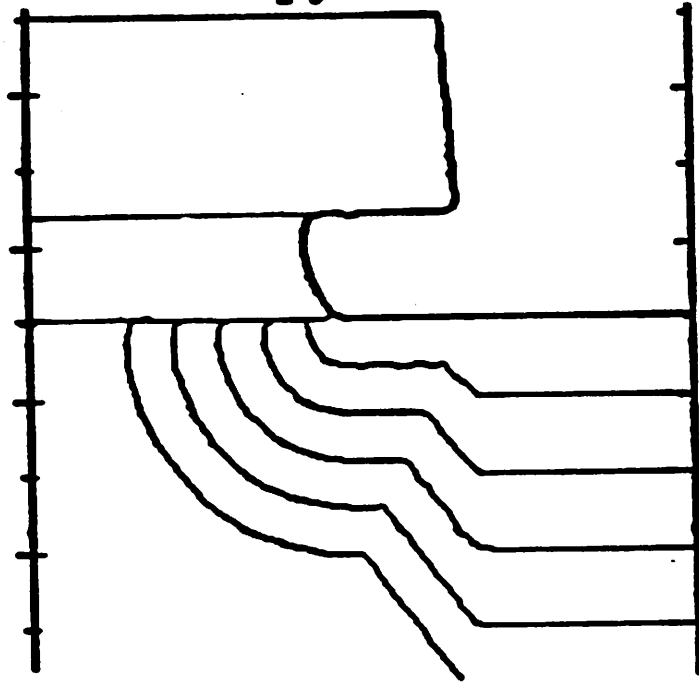
Figure 4.3 illustrates another mechanism of the angular incidence of ions. The etching is done completely with ions and the undercut is caused by ions arriving an angular distribution. The spacer thickness determines the slope of the vertical section of the profile and the size of the edge motion. The higher the mask edge above the etched surface, the lower the slope and the more the edge extends beneath the elevated mask. Figure 4.3 shows the simulation for two different mask heights for a cone of incidence of 30° . The amount of taper can be changed in reactive sputter etching using this technique.⁵

4.3. Experiment

The cantilever diagnostic technique is applied to study silicon etching with fluorinated gasses. The cantilever test structure contains three layers-- the Si substrate to be etched, an intermediate supporting layer, and a non-eroding mask. In choosing the materials, each has its own selective etchant. For the initial studies of etching silicon, the supporting layer was polyimide. Its thickness was controlled by the spin speed of application. After curing, a $0.2 \mu\text{m}$ layer of Ti is evaporated and patterned using an $\text{H}_2\text{O}_2:\text{HF}$ wet etch. Prolonged exposure in an oxygen plasma then undercuts the polyimide and oxidizes the titanium. For etching with a Sulfur Hexafluoride (SF_6) plasma, the titanium erodes too quickly. A high temperature resist, McDermid 74, was applied above $1.0 \mu\text{m}$ of thermal oxide. The resist was patterned with standard photolithographic techniques and hard baked at 120°C for 90 minutes. The silicon dioxide layer is then overetched in a buffered HF solution.

Etching with 2 components

anisotropy ratio = .40



Etching with surface migration

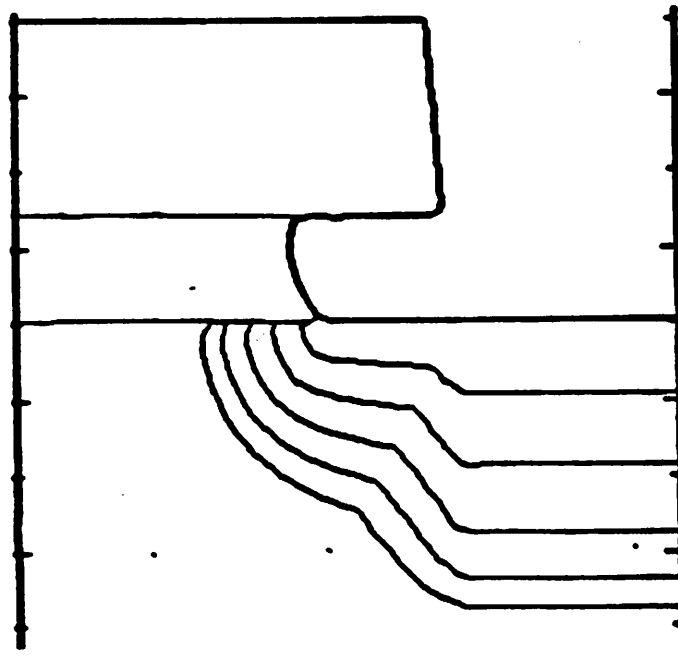


Figure 4.2

Computer simulation of the cantilever structure with a degree of anisotropy of 0.40 a). without surface migration and b). with surface migration of characteristic length $0.2 \mu m$.

Etching with an angular distribution

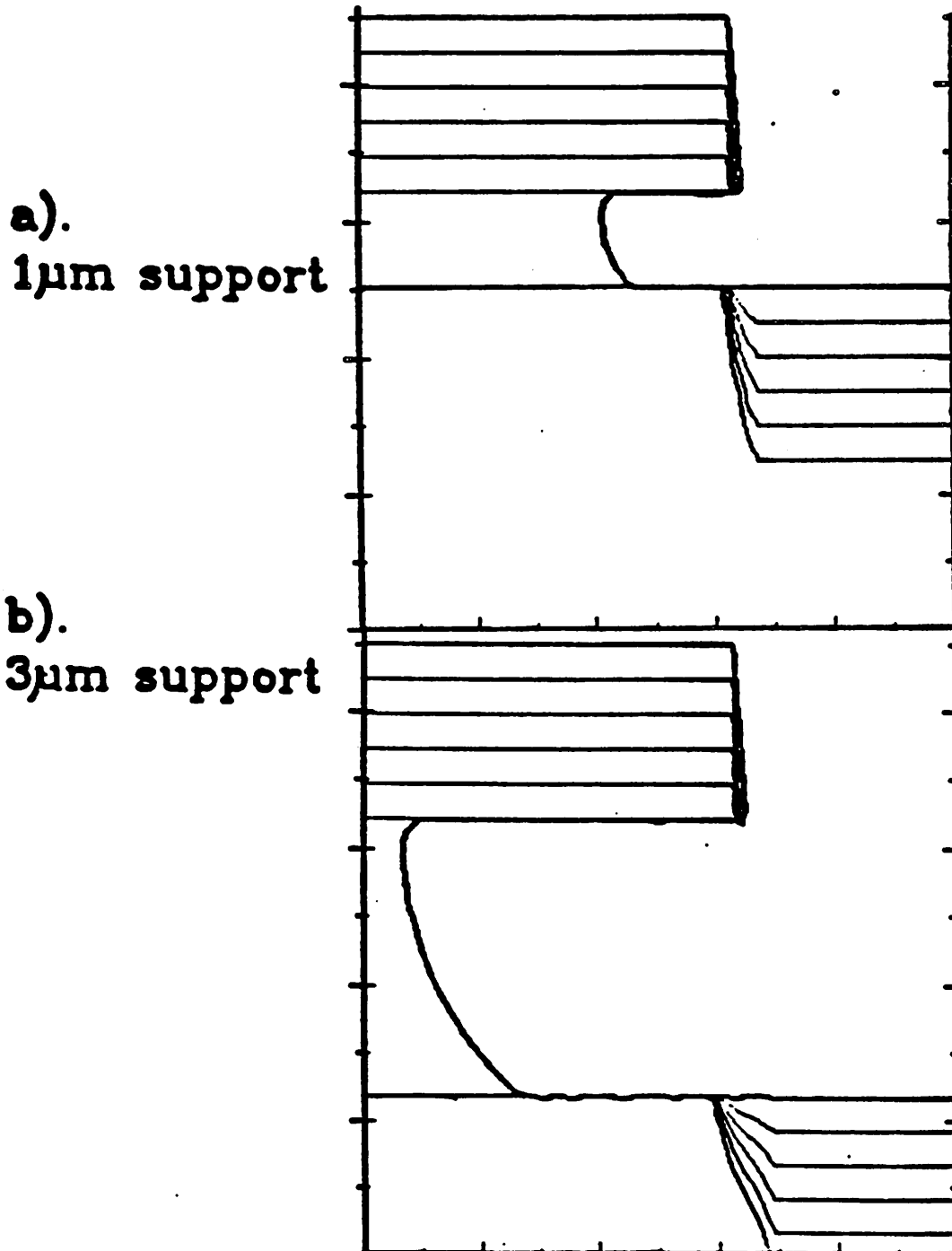


Figure 4.3

Computer simulation of the cantilever structure using an source distribution angle of 30 degrees and two different spacer thicknesses.

The samples were etched in the Plasma Therm PK-12 parallel plate reactor (described in Appendix A). Figure 4.4 shows the resulting etched profiles using Carbon Tetrafluoride and Oxygen ($CF_4/10\%O_2$) with the Ti/polyimide structure. Figure 4.4a is a low magnification SEM of the edge of the titanium mask from the top. The second figure details the edge profile. There is great enhancement of etching at the edge of the Ti even though it is not in contact with the silicon surface. Figure 4.4c shows the distinctive vertical component at the mask edge. The etched edge aligns well with the mask edge presenting no evidence of surface migration or an angular distribution effect. In fact, the raggedness in the patterned Ti transfers into the Si substrate. Figure 4.4d illustrates the isotropic component under the mask which is about one-tenth that of the total rate. The unexposed profile is quite flat and circularly undercut at the polyimide showing no migration or angularly distributed effects. Thus the profiles are explainable on the basis of simple isotropic and anisotropic components.

A matrix of experiments was done to explore the effect of different process parameters on the isotropic and anisotropic rates. Samples were etched in $CF_4/10\%O_2$, $C_2F_6/10\%O_2$, and $SF_6/10\%O_2$ plasmas. The power was set to 100, 250 and 400 Watts, ($0.16, 0.41, 0.65 \frac{\text{Watts}}{\text{cm}^2}$, respectively); the pressure to 50, 100, and 200 mTorr; and the flow rate to 5, 20 and 100 sccm. Hardened resist masks and silicon dioxide spacers were used. All samples were etched for 5 minutes. The micrographes in Figures 4.5 - 4.7 depict the resulting profiles for the different gasses.

The most reproducible and fastest etching gas is Sulfur Hexafluoride mixed with Oxygen. The cantilever structures with oxide and resist are photographed in Figure 4.5. In this case the isotropic component swamps out the anisotropic etching in the 5 minute etch time. But as in simulation the knee still occurs as characteristic of the structure and the two etching components.

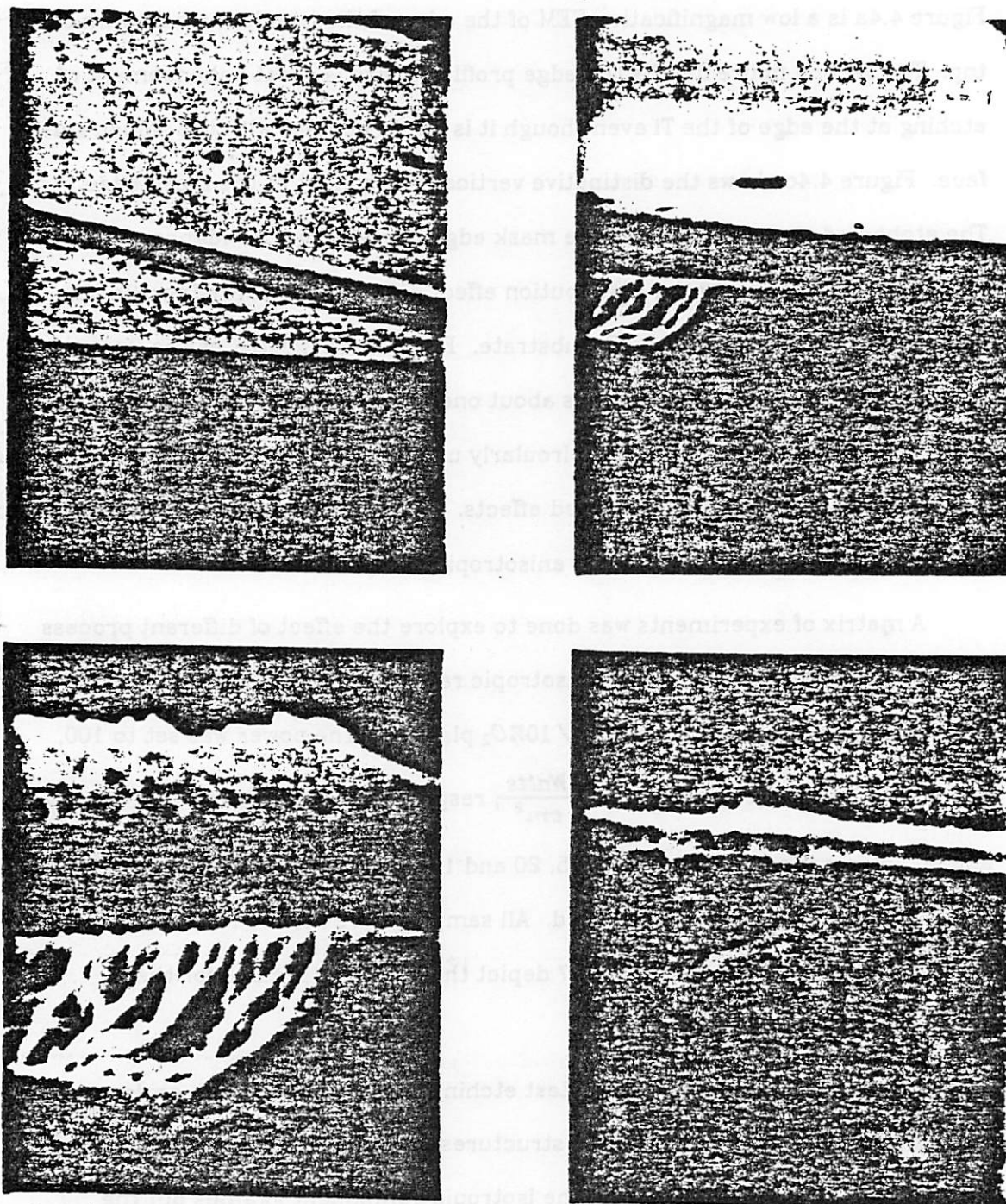


Figure 4.4

Cantilever structure with Ti mask; a). top view, b). profile, c). edge close-up, and d). close-up at polyimide support. Etching conditions - 100 sccm $CF_4/10\%O_2$, 100 Watts at 100 mTorr.

The next set, Figure 4.6, shows the same matrix etched in $CF_4/10\%O_2$. The total etching diminishes greatly. For this gas all the etch rates and components scale linearly with power. The isotropic component increases linearly with pressure. The profiles can be modeled using an isotropic and anisotropic component, with no angular dependence or migratory effects. These last two matrices indicate that the plasma acts as a source for etching species that must be considered in addition to its ion transport properties.

The final gas mixture used to etch the silicon is $C_2F_6/10\%O_2$. This gas demonstrates an extremely low etch rate with very anisotropic results. Figure 4.7 shows how etching competes with inhibition. In the unexposed areas there is no ion enhancement and no etching. The etching conditions which have long residence times, which are attributed to polymer precursor formation⁷ show the least etching. Increasing the power, as in the lower two SEMs in Figure 4.7, increases the etch rates and also the isotropic components. The added power generates etching species in the plasma in order to more successfully compete with the inhibitors. Looking at the profiles alone, the enhanced etching occurs only at the mask edge where there is no undercutting due to a distribution of incoming ions.

Tables 4.1, 4.2 and 4.3 summarize the matrix of results and the isotropic and anisotropic components that can be used to characterize these etching experiments. The best correlation of the degree of anisotropy occurs with the residence time of the species in the plasma. The residence time is defined as the pressure multiplied by a volume constant divided by the flow rate. The etching mechanisms likely depend on the amounts of different fluorinated species generated in the plasma. Those species that enhance the total etch rate the unexposed etch rate require a longer residence time. The degree of anisotropy comes closer to 1.00 for those conditions that either produce fewer of these

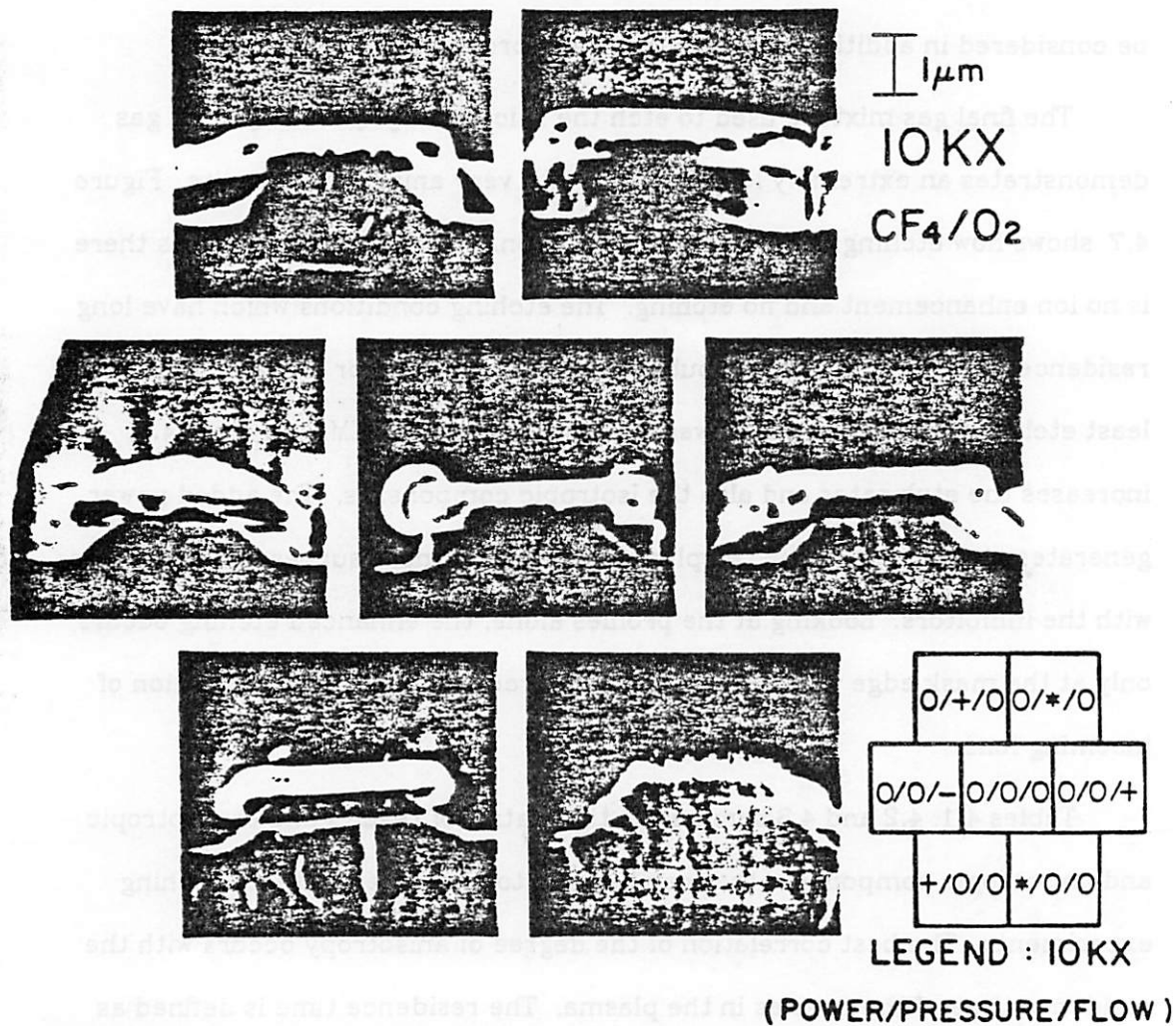


Figure 4.5

Cantilever structure with hardened resist mask matrix for Carbon Tetrafluoride. Powers: 0- 100 Watts, +- 250 Watts, & *- 400 Watts. Pressures: 0- 50 mTorr, +- 100 mTorr, & *- 200 mTorr. Flowrates: - 5 sccm, 0- 20 sccm, & +- 100 sccm.

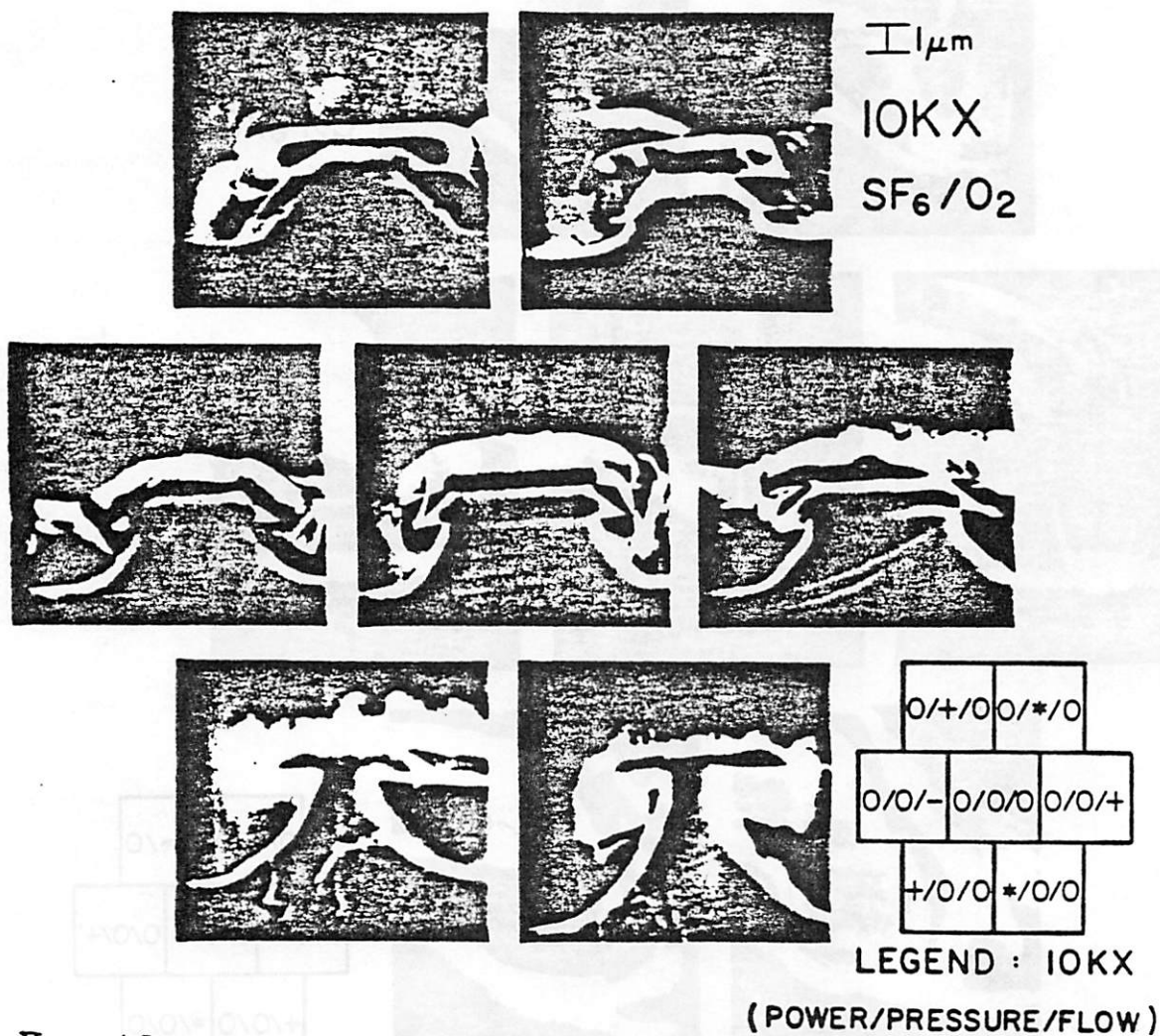


Figure 4.8

Cantilever structure with hardened resist mask matrix for Sulfur Hexafluoride. Powers: 0- 100 Watts, +- 250 Watts, & *- 400 Watts. Pressures: 0- 50 mTorr, +- 100 mTorr, & *- 200 mTorr. Flowrates: - 5 sccm, 0- 20 sccm, & +- 100 sccm.

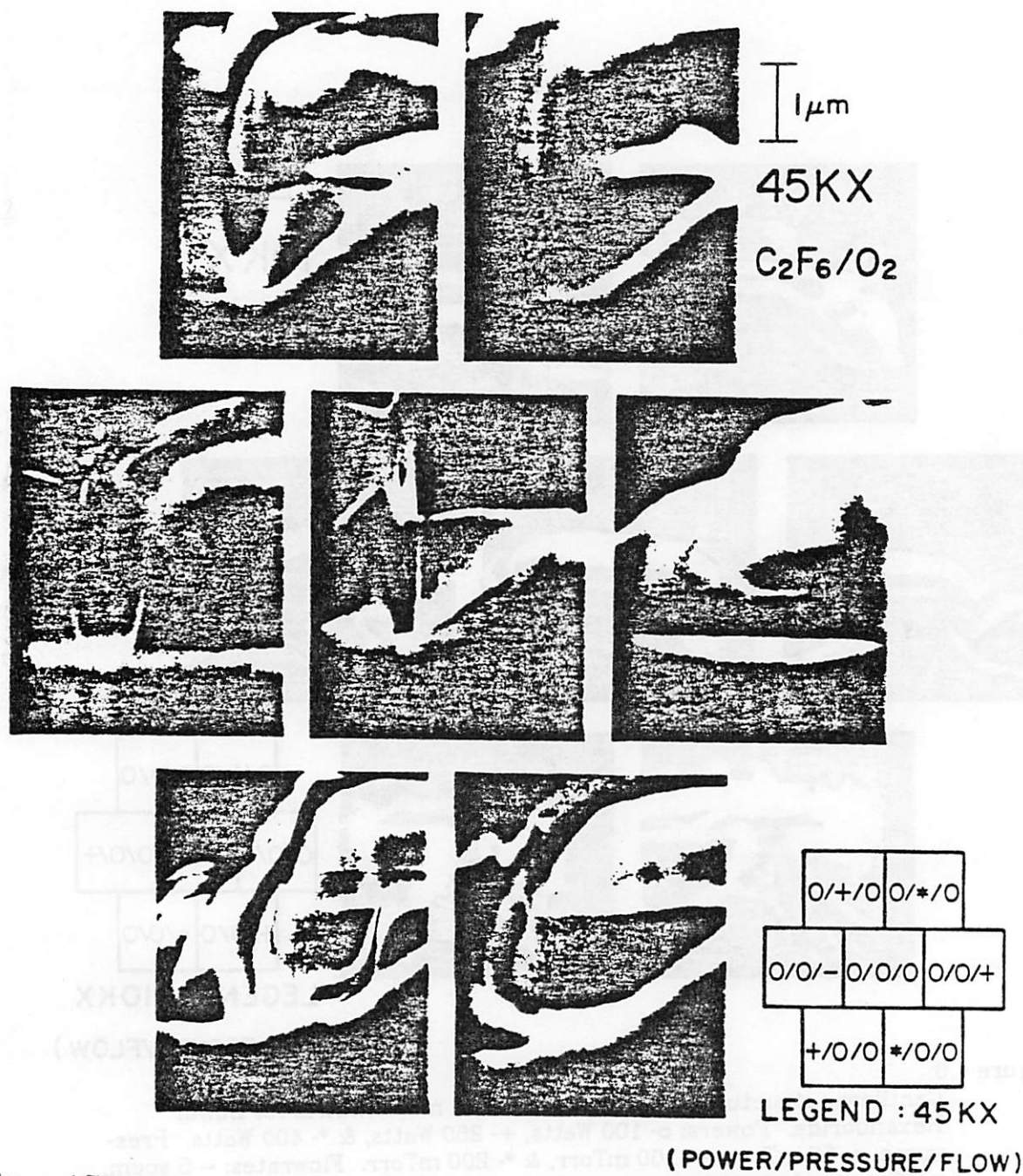


Figure 4.7

Cantilever structure with hardened resist mask matrix for Hexafluoroethane. Powers: 0- 100 Watts, +- 250 Watts, & *- 400 Watts. Pressures: 0- 50 mTorr, +- 100 mTorr, & *- 200 mTorr. Flowrates: - 5 sccm, 0- 20 sccm, & +- 100 sccm.

Table 4.1: $CF_4/10\%O_2$

power (Watts)	pressure (mT)	flow (sccm)	iso rate	vert rate	total ($\mu\text{m}/\text{m}$)	anisotropy ratio
100.0	50.0	20.0	0.034	0.020	0.054	0.37
100.0	50.0	5.0	0.038	0.016	0.054	0.30
100.0	78.0	100.0	0.034	0.020	0.054	0.37
100.0	100.0	20.0	0.076	0.018	0.094	0.19
100.0	200.0	20.0	0.110	0.036	0.146	0.24
250.0	50.0	20.0	0.070	0.064	0.134	0.48
400.0	55.0	20.0	0.110	0.120	0.230	0.50

fluorinated species or more of the competing inhibitor.

4.4. Conclusion.

Cantilever structures offer several advantages in the control and exploration of plasma etching mechanisms. They show etching characteristics in an exposed and unexposed region in addition to profile dependent mechanisms such as surface migration and an angular distribution to incoming ions. Computer simulation was used initially to identify the profile effects for the various mechanisms. These simulations establish that surface migration would result in a sloped profile underneath the overhanging mask. Angular ion effects would round the corner and shift the toe of the edge into unmasked regions. Only

Table 4.2: $SF_6/10\%O_2$						
power (Watts)	pressure (mT)	flow (sccm)	iso rate	vert rate	total ($\mu\text{m}/\text{m}$)	anisotropy ratio
100.0	50.0	20.0	0.244	0.202	0.446	0.45
100.0	50.0	5.0	0.230	0.172	0.400	0.43
100.0	85.0	100.0	0.148	0.346	0.490	0.71
100.0	100.0	20.0	0.066	0.166	0.232	0.72
100.0	200.0	20.0	0.109	0.078	0.188	0.42
250.0	56.0	20.0	0.480	0.460	0.940	0.49
400.0	72.0	20.0	0.846	0.484	1.33	0.36

simple isotropic etching combined with anisotropic etching give horizontal profiles in the unexposed region and sidewall angles related to the anisotropic and isotropic etch rate components.

Two types of cantilever test structures were fabricated to investigate Si etching in fluorinated gasses. These were a titanium mask supported by polyimide, and a hardened resist mask over undercut silicon dioxide. The resulting etched silicon profiles showed horizontal profiles in the unexposed regions and sidewall angles related by $\tan^{-1} \frac{\text{Rate}_{\text{aniso}}}{\text{Rate}_{\text{iso}}}$. Thus only the effects of an isotropic and an anisotropic components were found. Sulfur hexafluoride with oxygen etches at the highest rate with the total rate increasing linearly with power and the isotropic component decreasing with flow-rate. In CF_4/O_2 all rate

Table 4.3: $C_2F_8/10\%O_2$						
power (Watts)	pressure (mT)	flow (sccm)	iso rate	vert rate	total ($\mu\text{m}/\text{m}$)	anisotropy ratio
100.0	50.0	20.0	0.000	0.022	0.022	1.00
100.0	50.0	5.0	0.000	0.000	0.000	---
100.0	75.0	100.0	0.000	0.017	0.017	1.00
100.0	100.0	20.0	0.000	0.038	0.038	1.00
100.0	200.0	20.0	0.000	0.008	0.008	1.00
250.0	59.0	20.0	0.013	0.038	0.051	0.74
400.0	68.0	20.0	0.051	0.046	0.097	0.48

components scale linearly with power and the isotropic component is linear with pressure. C_2F_8/O_2 shows the lowest rate, yet the most anisotropic etching. It suggests competition between polymerizing and etch species produced in the plasma. In all cases, the relative amount of isotropic etching depends on the production of etching species in the plasma.

References

1. C.B. Zarowin, "Plasma etch anisotropy – Theory and some verifying experiments relating ion transport, ion energy and etch profiles," *Journal of the Electrochemical Society*, vol. 130, no. 5, p. 1144, (May 1983).
2. T.M. Mayer and J.H. McConville, "Line-width control in anisotropic plasma etching of polycrystalline Si," *IEDM Technical Digest*, p. 44, (December 1979).
3. A.C. Adams and C.D. Capio, "Edge profiles in plasma etching of polycrystalline silicon," *Journal of the Electrochemical Society*, vol. 128, no. 2, p. 366, (February 1981).
4. Jung Lin, "Via etch in metallization," *Internal Technical Report 82-6*, Integrated Circuit Processing Laboratory, Hewlett Packard, (December 1982).
5. L.B. Rothman, J.L. Mauer IV, G.C. Schwartz, and J.S. Logan, "Process for forming tapered vias in SiO₂ by reactive ion etching," in *Plasma Processing*, ed. R.G. Frieser & C.J. Mogab, Proceedings of the Symposium on Plasma Etching and Deposition, p. 193, The Electrochemical Society, (1981).
6. W.G. Oldham, A.R. Neureuther, J.L. Reynolds, C.S. Sung, and S.N. Nandgaonkar, "A general simulator for VLSI lithography and etching processes: Part II application to deposition and etching.," *IEEE-Transactions on Electron Devices*, vol. ED 27, no. 8, (August 1980).
7. G. Smolinsky and D.L. Flamm, "The plasma oxidation of CF₄ in a tubular-alumina fast-flow reactor," *Journal of Applied Physics*, vol. 50, no. 7, p. 4982, (July 1979).

CHAPTER FIVE

5. TOPOGRAPHY MODELING IN DRY ETCHING PROCESSES

5.1. Introduction

Some aspects of the interaction among wafer topography and the thin film processes of directional dry etching and deposition are presented in experiment and simulation. The anisotropy of dry etching, which has helped make VLSI possible, increases the interdependence of processing steps and opens the possibility of creative uses of topographical effects in fabricating devices. Examples illustrate the importance of these effects and the basic mechanisms involved. Simulation is particularly well suited for systematically examining the trade-offs among processing steps. Design graphs characterize the effect of anisotropy on line-width loss and oxide removal in poly-silicon gate etching, and on thin film resistance in tapered oxide etching. Guidelines for planarization by isotropic deposition and anisotropic etching are suggested. Comparisons with experiments show that the reported planarizing effect is better than expected.

5.2. I. Introduction

The advent of dry etching and new deposition techniques helps make possible the reduced size and increased complexity in integrated circuit devices. The directionality of dry etching allows feature sizes in devices down to 1 micrometer.^{1,2} and provides a flexible medium for creative processing solutions to device performance problems.^{3,4} Novel deposition techniques contribute to higher

packing densities.^{5, 6, 7} Simulation^{8, 9, 10} is useful in characterizing and optimizing the individual deposition and etching processing steps. This paper extends simulation to several new topography control techniques and explains several situations which involve optimization of the interaction between processing steps.

The interaction between process steps is important in anisotropic dry etching. Simple directional etching forms steep, fine patterns which lead to poor coverage in the subsequent deposition of thin films. When followed by deposition and a second directional etch a residue remains in the vicinity of the abrupt topographic steps. This unetched residue can lead to detrimental effects such as electrical shorts, when it is a conductor, but when it is an insulator, it also serves to planarize the topography and can be used in a creative manner as a temporary ion implantation mask.³ Many of these topography creation and interaction problems can be effectively characterized through simulation. The process simulator SAMPLE (Simulation And Modeling of Profiles in Lithography and Etching)⁹ models the time evolution of an etched line-edge profile. The program uses weighted rate components and topographical information to produce a two dimensional line graph. This paper uses SAMPLE and scanning electron micrographs (SEMs) of laboratory test structures to study these wafer topography issues.

5.3. Anisotropic etching at steps.

Figure 5.1 illustrates how the underlying topography in a double level polycrystalline silicon process affects the percentage of electrical shorts in the second level poly-silicon lines. In Figure 5.1a a thermally oxidized insulating layer produces a topography undesirable due to its indented structure at the base. After anisotropic etching of the second level of poly-silicon the indentation remains

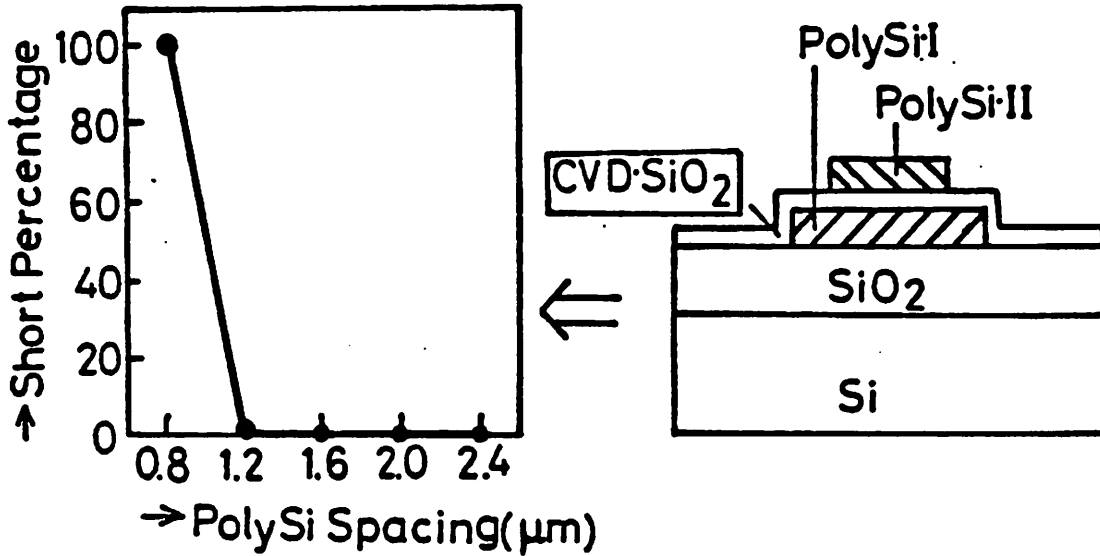
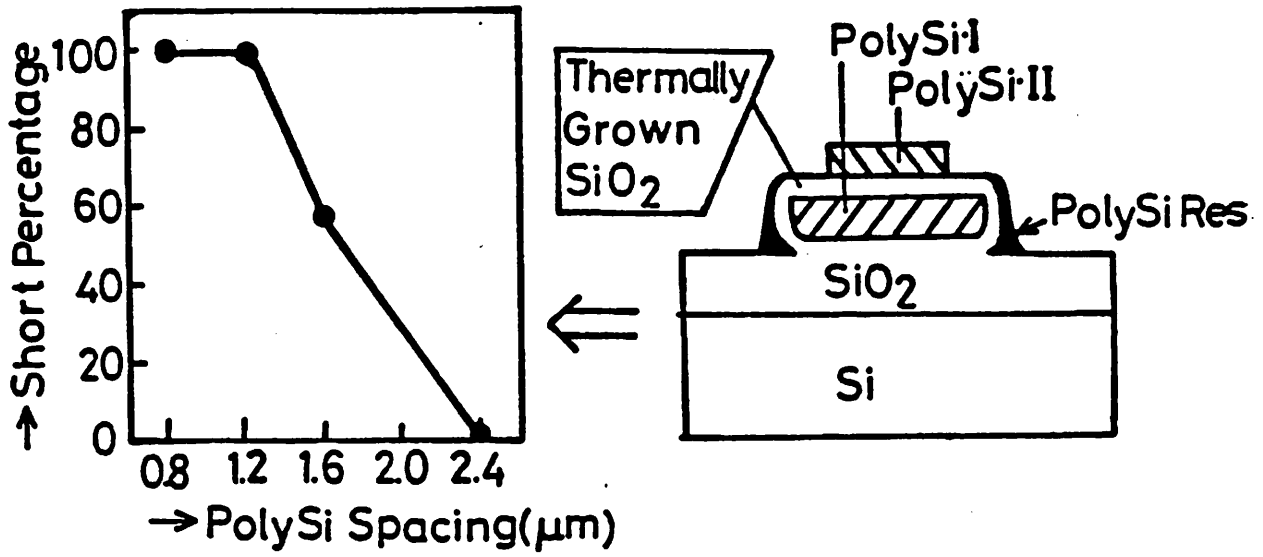
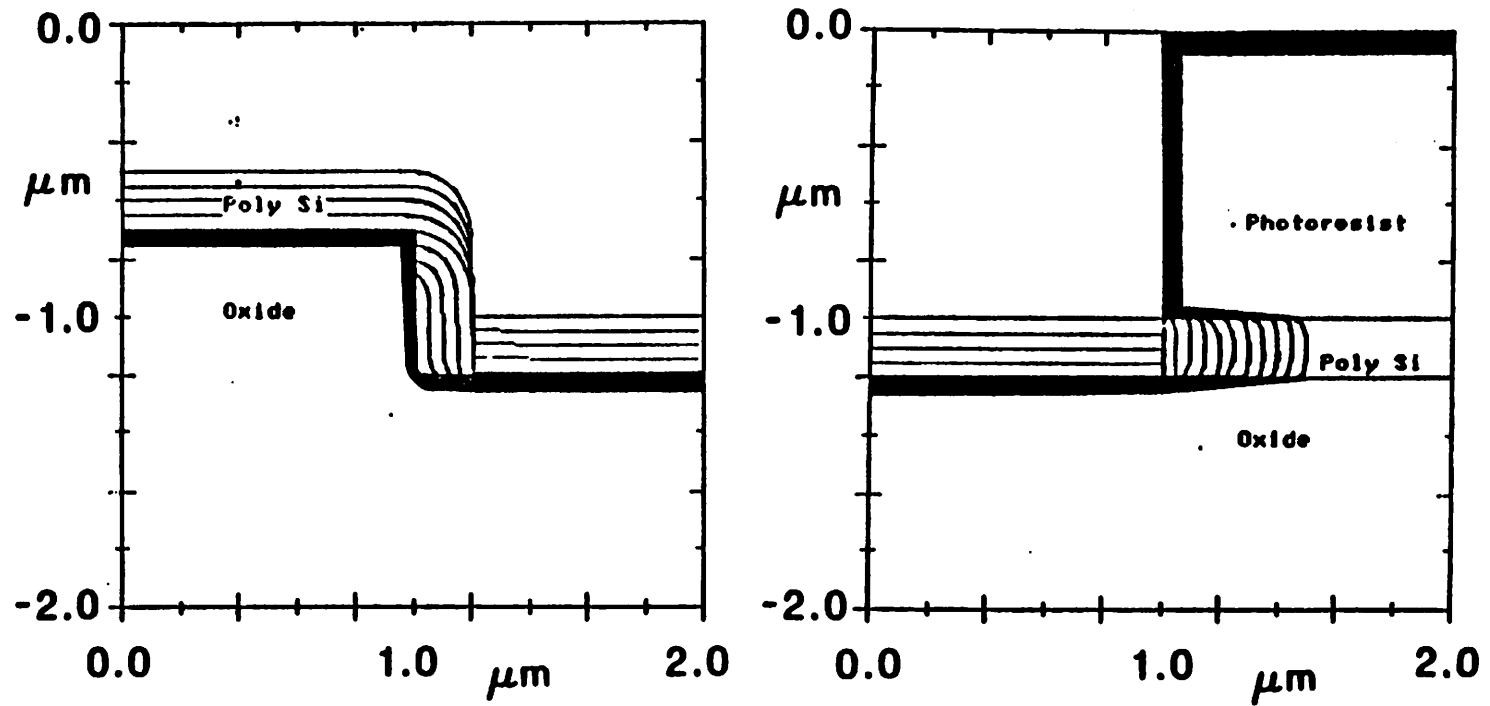


Fig.1 Short Percentage of PolySi in DoubleLevel PolySi Structures

full of unetched poly-silicon. The residue causes the electrical shorts in parallel lines of a second layer of silicon. The percentage of shorts increases rapidly for parallel lines separated by less than 2 micrometers because the filaments can form continuous bridges at this close spacing. Changing the method of applying the insulator provides a more suitable topography for the dry etching of the second conductor level. As shown in the second part of Figure 5.1, silicon dioxide chemically vapor deposited (CVD) at a high temperature makes a better step without indentation. In this case the percentage of shorts in the second level of poly-silicon lines is almost zero above 1 micrometer spacing.

A problem related to the unetched residue at steps also occurs in patterning the first level of poly-silicon. The gate electrode material is undercut while the residue is being etched as shown in the simulation of Figure 5.2. Here the overlying layer is etched directionally to an end point and the residue is then removed by introducing an isotropic component during over etching. Simultaneously in the gate mask region, the isotropic overetching undercuts the line as on the right in Figure 5.2. The line-width lost depends on the residue thickness and the amount of isotropy in the second etching step. In addition to this undercutting problem, the underlying film, such as the gate oxide, is also attacked during the over etching residue removal process.

An alternative to this double step process is the use of a mixture etching in which a directional and an isotropic components are used throughout a single step. With this mixed process the undercutting can be reduced but the residue thickness remains larger and longer over etching is required. Unfortunately, the anisotropic conditions which reduce the line-width loss have lower selectivity (etch rate ratio) between the poly-silicon and the oxide underneath. Anisotropy thus results in more oxide thickness loss. An example of the relationship between the etch rate ratio of poly-silicon to oxide and anisotropy is shown in



**Fig.2 Simulation Of Anisotropic Etching
Followed By Isotropic Etching.**

Figure 5.3a (from reference 11). The etching selectivity is drastically reduced as the anisotropic ratio increases to the more directional extreme.

The relationship between selectivity and anisotropy can be used to explore the basic trade-off between line-width loss and underlying oxide thickness loss. The graph in Figure 5.3b compares the poly-silicon line-width loss and the oxide etched during the over etching process as a function of anisotropy. The assumed step height is 0.5 micrometers and the deposited thickness of poly-silicon is 200 nanometers. The broken curve corresponds to a single step etching process where a mixture of isotropic and directional components are used throughout. The solid curve corresponds to a two step etching process where the first step uses directional etching to an end-point, then uses a mixture etching during the overetch time. In both processes, the line-width loss is large in the isotropic region, while the oxide attacked is large in the anisotropic region. To compare the two processes, the oxide gets etched more in the two step process because of the need for a longer over-etching time. However, the poly-silicon line-width loss is less in the double step process. These curves aid as design guides for determining the optimal etching conditions. A process can be chosen depending upon how much line-width or oxide loss can be tolerated. For instance, if the maximum allowable poly-silicon undercut and oxide etched are $0.2 \mu\text{m}$ and 30 nm respectively, the etching condition would fall into the 0 to 40% anisotropy ratio for two step processing. In this case a good single step process cannot be found due to its large line-width loss.

5.4. Step coverage.

Another topography problem is depositional film coverage of dry etched steps. The directional dry etching provides good line-width control and tight layout tolerances, but it results in profiles with steep edges and high aspect ratios

1981 ECS Fall Meeting

Daniel L.Flamm, David N.K.Wang, Dan Maydan
(Bell Lab.)

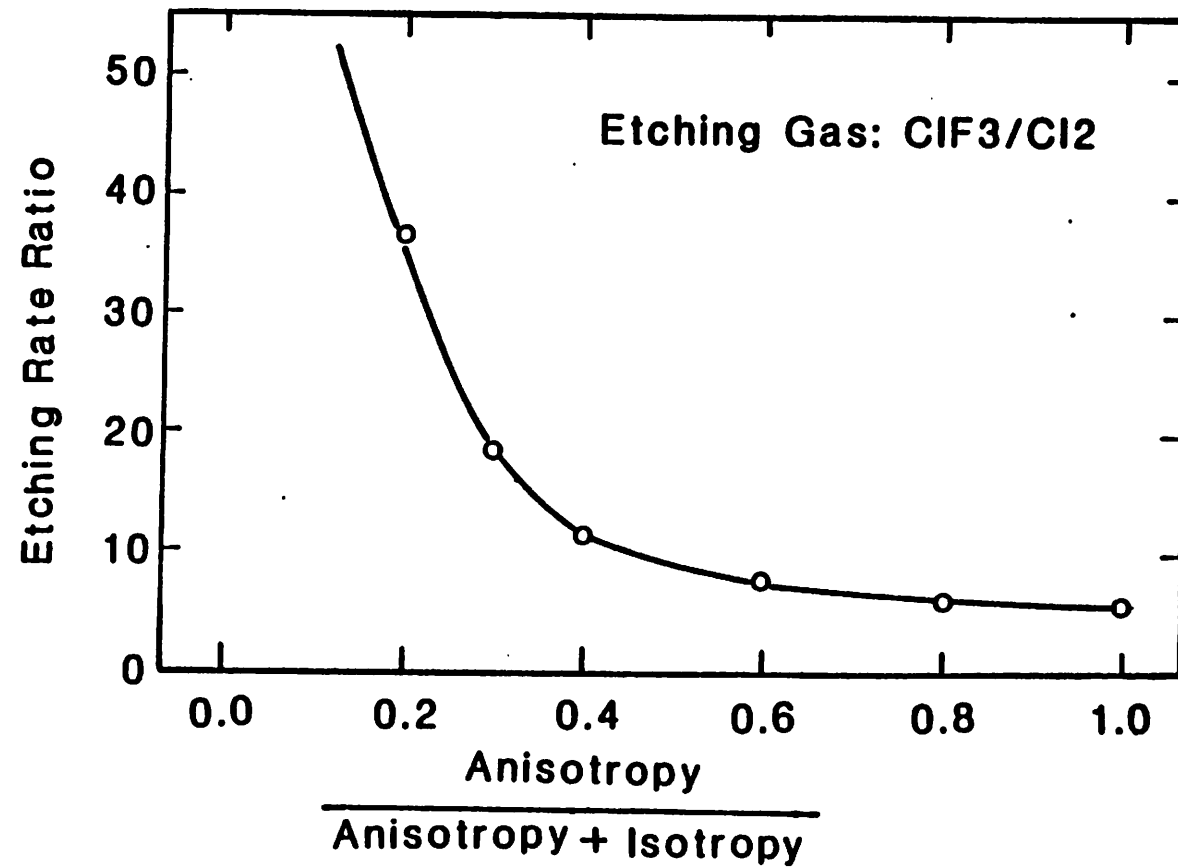


Fig.3a. Etching Rate Ratio of Poly-Si and SiO₂

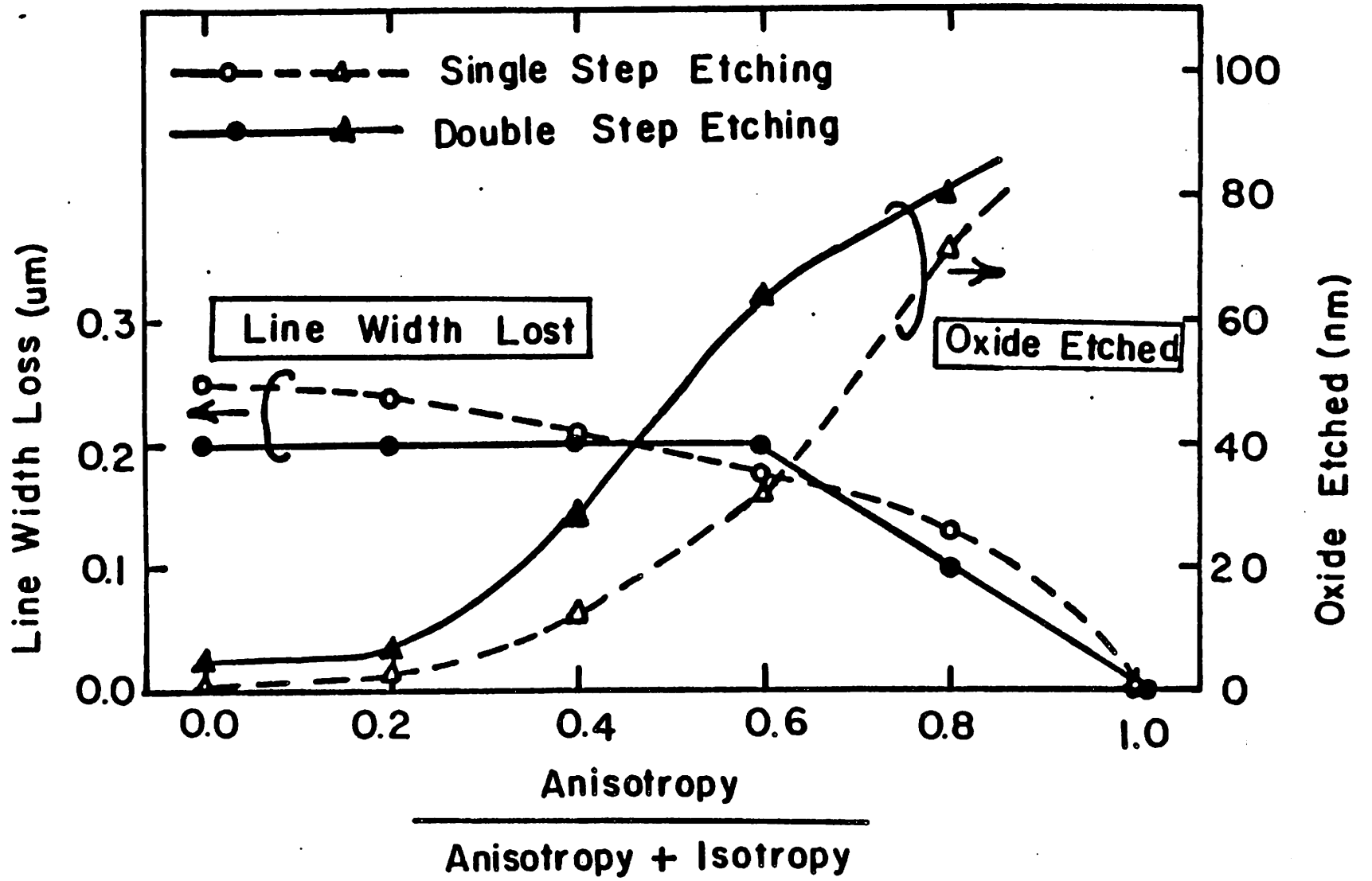


Fig. 3b

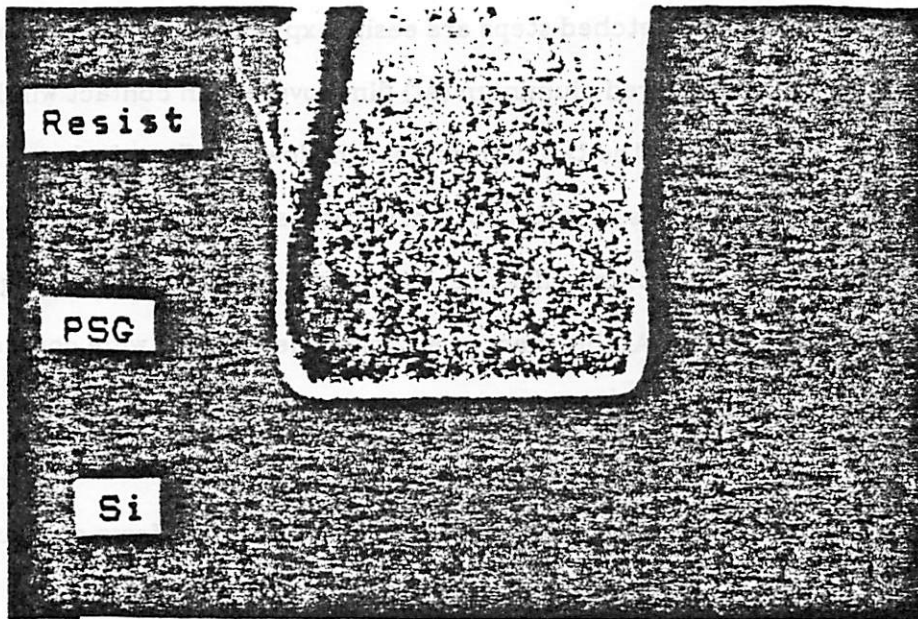


Figure 5.5
Profiles of dry etched silicon dioxide using non-reflow and reflow
(angled) resist masks.

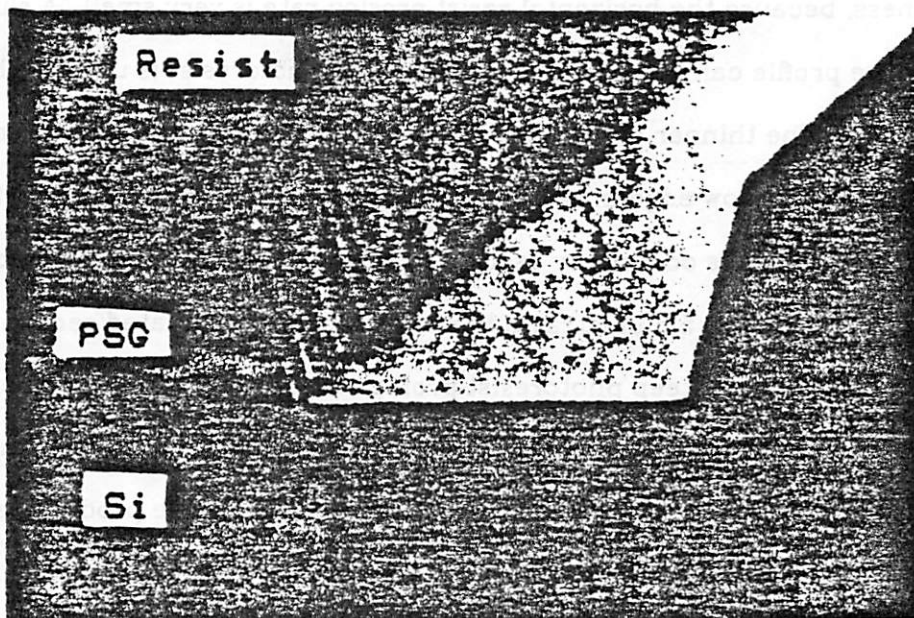


Figure 5.5
Profiles of dry etched silicon dioxide using non-reflow and reflow
(angled) resist masks.

which cause poor coverage when thin films are later deposited. The trade-offs in depositing over dry-etched steps are easily explored using simulation. Figure 5.4 shows the sputtered aluminum (Al) film coverage in contact windows and narrow gaps. Due to the two dimensional shadowing effect during Al deposition¹¹ the aluminum thickness at the bottom corner is much less than the nominal thickness. The shadowing effect becomes more pronounced as the gap dimension is reduced, The Al thickness in a 1 micrometer (μm) wide contact with 1 μm tall vertical walls is only 10% of that of the deposited film thickness. Even though dry etching would allow reduction to submicron size contact holes, the conventional deposition techniques could not be used to form contact electrodes.

To improve the aluminum coverage of steps with conventional sputter deposition, the contact hole may be tapered.¹² A sloped edge provides good coverage, but unnecessarily gradual slopes reduce the tight layout tolerance. Therefore a compromise in slope and coverage is desirable. Figure 5.5^{13, 14} demonstrates how that photoresist erosion during the etching process can be utilized to give a sloped edge profile. When the photoresist with a steep edge is used as an etching mask in conventional etching steps, the contact window reflects the steepness, because the horizontal resist erosion rate is very small. A slightly tapered edge profile can be obtained when tapered photoresist is used as the etching mask. The thinner edge of the mask erodes away transferring a slope to the contact window edge in the etching process. Post baking the resist after development is commonly used to taper the resist edge, as in the bottom of Figure 5.5. Figure 5.6 illustrates the corresponding simulated sequential processing steps. The steep photoresist profile coupled with the vertical etching makes a steep profile that it is difficult for the aluminum to cover. The tapered photoresist with some lateral expansion of the contact hole produces a slightly

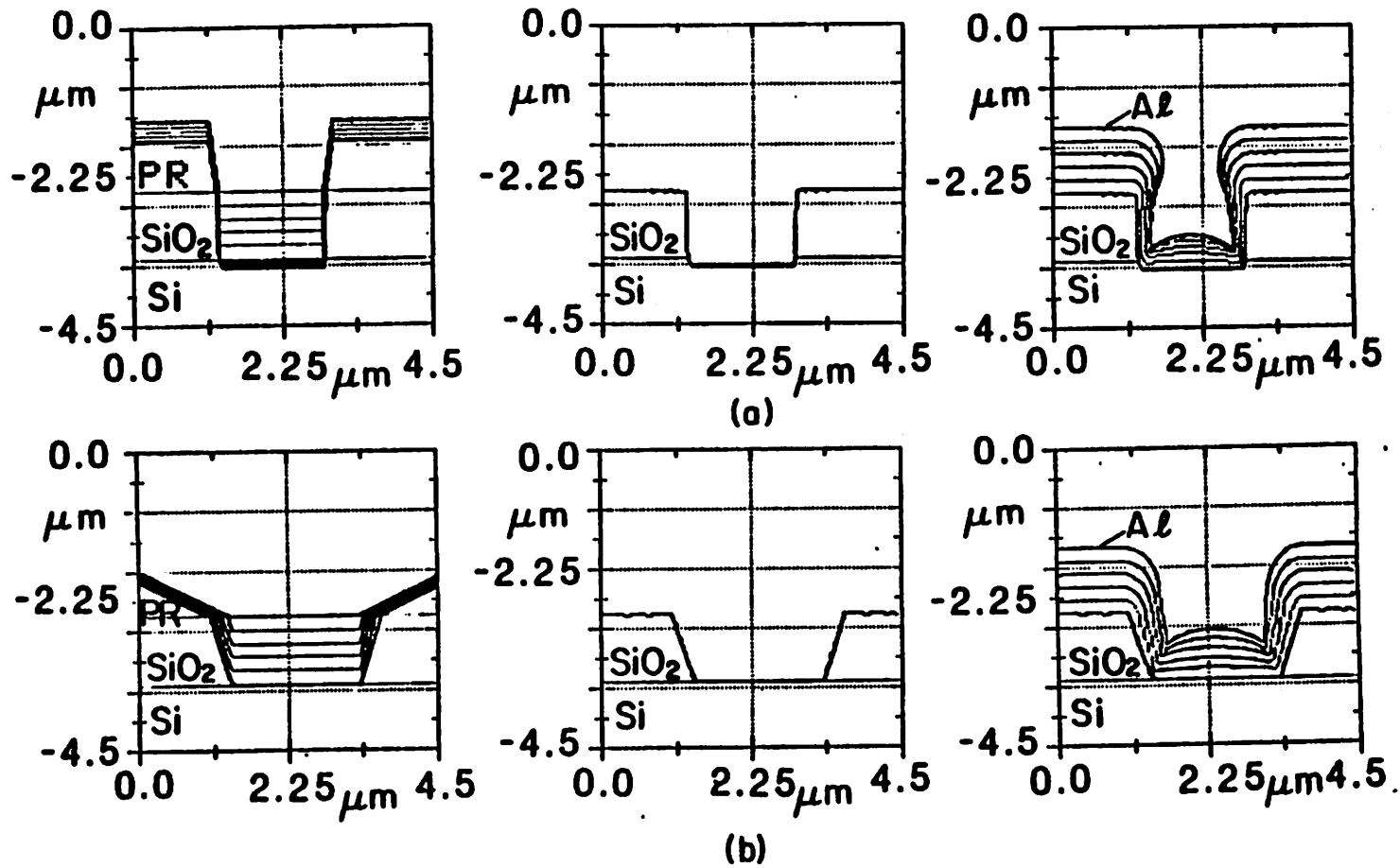


Fig.6 Simulation of Contact Hole Reactive Ion Etching Followed by Al Deposition

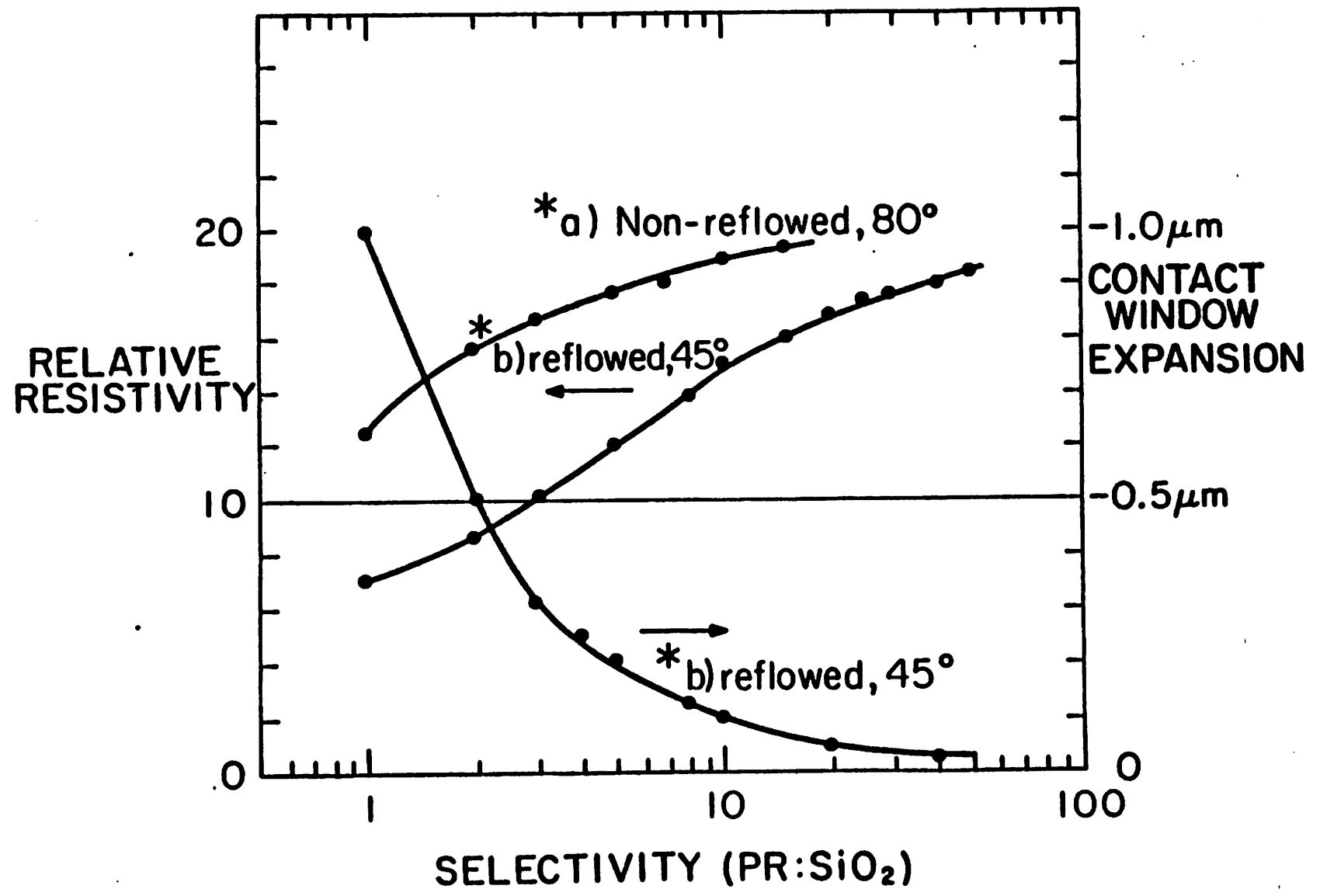
sloped edge that provides better step coverage.

The effect of the resist to oxide selectivity on the resulting contact hole size and on the depositional film resistivity can be characterized. A photo-resist mask with an initial side wall taper angle that is etched anisotropically produces a tapered opening in the silicon dioxide layer. The oxide sidewall angle depends on the initial resist profile angle and the etch selectivity between the resist and the oxide. The taper in the oxide results in an expansion of the contact hole size, though. This is shown in figure 7 for non-reflow resist of 80° and reflow resist of 45° as a function of selectivity. The oxide taper angle also affects the subsequent metal coverage. The relative resistivity of the metal line crossing the gap is used to specify the quality of the deposited line. A relationship between resistance and sidewall taper has been generated for a $1\ \mu\text{m}$ gap in a $1\ \mu\text{m}$ thickness of oxide with $1\ \mu\text{m}$ of sputtered Al in reference 12. This relation between angle and resistance is used for the relative resistance versus selectivity plotted in Figure 5.7. The graph shows how the combination of reflow angle and selectivity can be chosen for the trade-off between resistance and contact window expansion. An oxide side wall angle of about 60° is a reasonable compromise for sputter deposition without bias. For reflow resist, initially tapered to 45° a process with 2:1 oxide selectivity achieves the 60° oxide side wall angle. The use of reflow produced a profile of 63° in Figure 5.5, while without reflow the side wall angle was steeper than 85° .

5.5. Planarization.

Now we examine the constructive use of dry etching in planarizing nonuniform surfaces. If a residue is left at steps intentionally, it can be used to ease step coverage in later processing steps. One example is to deposit a thick oxide by chemical vapor deposition at high temperature or at low pressures to obtain a

Figure 5.7
 Relative resistance of aluminum across gaps and contact window expansion versus selectivity for two mask angles; a), 80°, non-reflowed and b). 45°, reflowed.



completely isotropic covering of the nonuniform topography. This deposited oxide is then etched back anisotropically to leave a rounded residue at every vertical step. Several isotropic deposition / anisotropic etch steps will leave a larger and larger amount of residue at the concave edge giving a gradual slope to the edge as shown in the simulation in Figure 5.8. This residue is the basis for the lowly-doped-drain and offset gate technologies.³

If, however, the deposited oxide film thickness exceeds one-half the gap spacing, as in Figure 5.9, the oxide fills the gap and also tends to planarize the surface. The nonplanar dip remaining in the oxide surface decreases as the ratio of thickness to gap width is increased. From simulation the oxide surface dip in a $2\ \mu\text{m}$ gap with $2\ \mu\text{m}$ of deposited and etched oxide amounts to only $0.1\ \mu\text{m}$. This eliminates the problem of sputtering over narrow, deep channels as compared later in Figure 5.11.

Figure 5.10 illustrates experimentally the isotropic deposition / anisotropic etching method for several test structures. Gaps were directionally etched in silicon. A thin layer of oxide was grown before deposition for later under-etching to distinguish between the layers. Then a layer of (chemical vapor deposition) CVD poly-silicon was deposited and etched anisotropically in a Sulfur Hexafluoride and Oxygen mixture ($SF_6/10\%O_2$). After dry etching each layer of the polysilicon a new distinguishing layer of oxide was grown. This process was repeated several times. The back etching of these thin oxide layers reveals the history of the surface shape at various steps.^{13,5} The first two micrographs show that isotropically deposition followed by anisotropic etching preferentially leaves a smoothing residue at step edges. These correspond well to the simulation in Figure 5.8. The third photo demonstrates how a narrow ($2\ \mu\text{m}$) gap is planarized by filling with CVD material and etching. The final photo in Figure 5.10 shows that the same effect occurs in a wider $7\ \mu\text{m}$ space. This structure has the dip

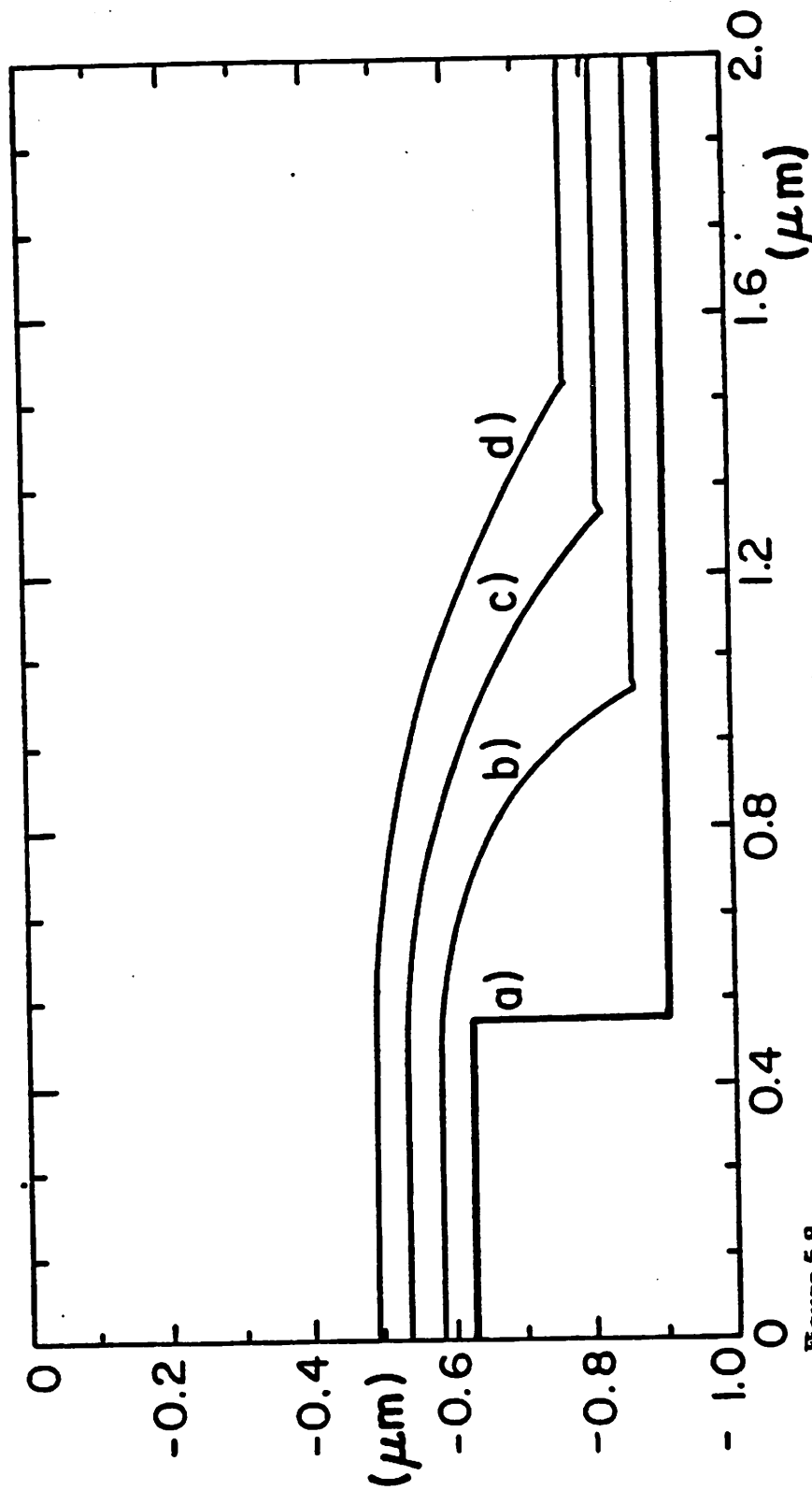


Figure 5.8

Simulation of a multistep process planarizing an edge by successively leaving residue; a) initial profile, a $0.3\mu\text{m}$ rectangular step, b) profile after the initial deposition /anisotropic etch cycle, c) profile after the second deposition /anisotropic etch cycle, d) profile after the third deposition /anisotropic etch cycle.

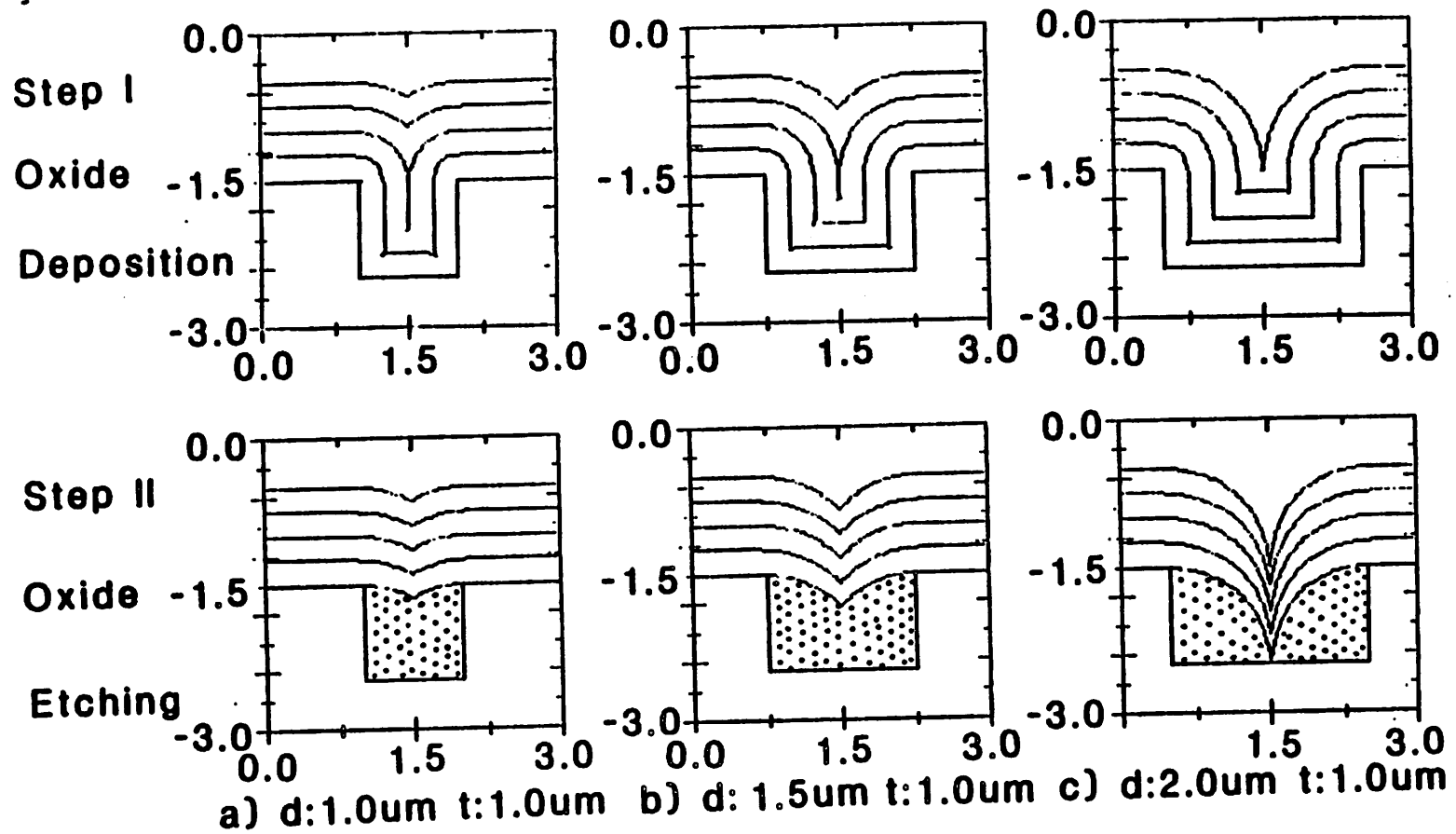


Figure 5.9

Simulations of planarization by filling gaps with isotropically deposited material and then anisotropically back etching.

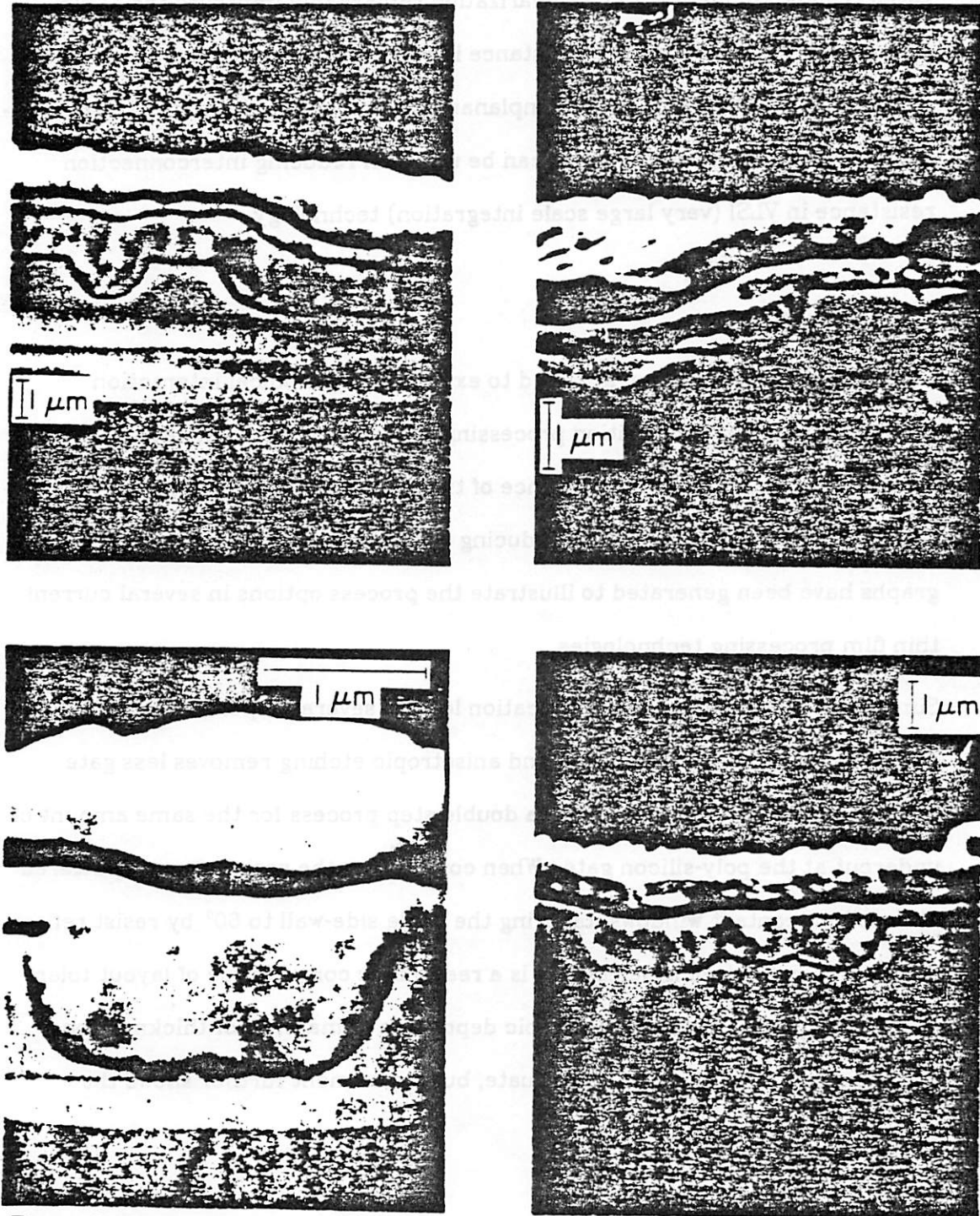


Figure 5.10

Scanning electron micrographes of planarization processes using successive isotropic deposition and anisotropic etching: a). a space and an edge b). an edge c). a 2 micrometer space and d). a 7 micrometer space.

predicted by simulation in Figure 5.9, but shows experimentally that the planarization effect is greater than expected.

Finally, the simulated aluminum deposition across the top of planarized structures is shown in Figure 5.11. Planarization remarkably improves the Al film coverage. The aluminum line resistance is estimated to be almost one order of magnitude less than that of the nonplanarized structure. Therefore, the planarization process for gaps and steps can be useful in reducing interconnection resistance in VLSI (very large scale integration) technology.

5.6. Conclusion.

Experiment and simulation are used to explore topographical interaction between etching and deposition processing steps. Experimental data are included to document the importance of these process interactions and to illustrate the physical mechanisms producing the topographic effects. Design graphs have been generated to illustrate the process options in several current thin film processing technologies.

Simulation and experimental verification lead to several important conclusions. A single step mixture of isotropic and anisotropic etching removes less gate oxide while removing residue than a double step process for the same amount of undercut at the poly-silicon gate. When considering the resistance of sputtered Al lines into contact windows, tapering the oxide side-wall to 60° by resist reflow and appropriate etching selectivity is a reasonable compromise of layout tolerances. For planarization, an isotropic deposition of material of thickness one-half the narrow gap widths is adequate, but experiment further shows the smoothing is better than expected.

a) Without Planarization Process



b) With Planarization Process

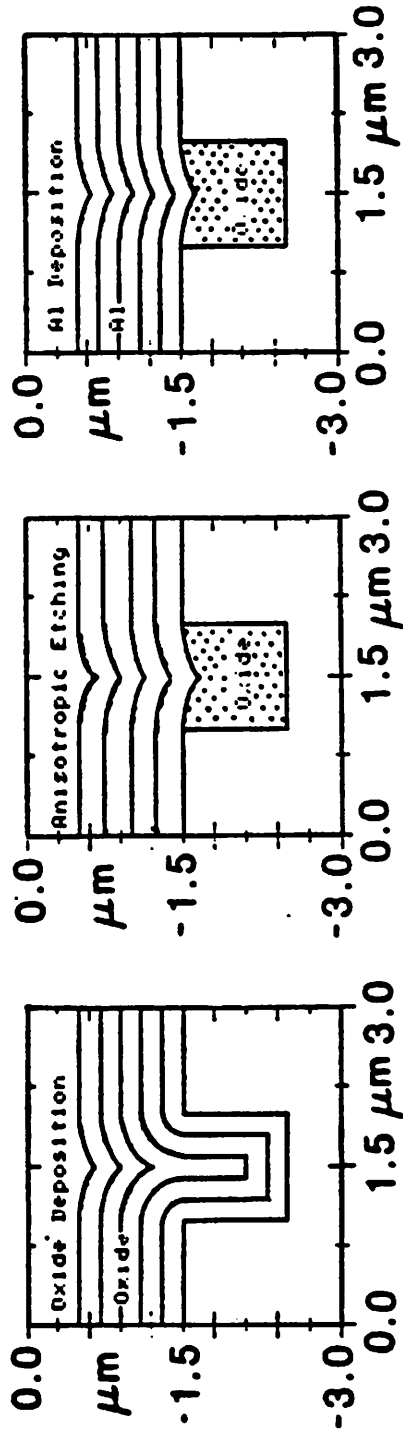


Fig. 11 Simulation of planarization process and Al step coverage

References

1. L.M. Ephrath, "Reactive ion etching for VLSI," *IEEE-Transactions on Electron Devices*, vol. ED 28, no. 11, p. 1315, (November 1981).
2. T. Shibata, K.Hieda, M Sato, M. Konaka, R.L.M. Dang, and H. Zizukai, "An optimally designed process for submicron MOSFETs," in *1981 IEDM Technical Digest*, p. 647, (1981).
3. S. Ogura, P.T. Tsang, W.W. Walker, D.L. Critchlow, and J.F. Shepard, "Elimination of Hot Electron Gate Current by the Lightly Doped Drain-Source Structure," in *1981 IEDM Technical Digest*, December 1981.
4. W.R. Hunter, T.C. Holloway, P.K. Chatterjee, and A.F. Tasch, "New edge-defined vertical etch approaches for submicrometer MOSSFET fabrication," *IEDM*, p. 764, (December 1980).
5. C.Y. Ting, V.J. Vivalda, and H.G. Schaefer, "Study of Planarized Sputter-Deposited SiO₂," *Journal of Vacuum Science and Technology*, vol. 15, no. 3, p. 1105, (May/June 1978).
6. Y. Homma, A. Yajima, and S. Harada, "Feature Size Limit Analysis of Lift-Off Metalization Technology," in *1981 IEDM Technical Digest*, p. 570, (December 1981).
7. T. Batchelder, "Simple Metal Lift-Off Process for 1 Micron AL/5% Cu Lines," *Solid State Technology*, vol. 25, no. 2, p. 111, (February, 1982).
8. I.A. Blech, D.B. Fraser, and S.E. Hasyko, "Optimization of Al Step Coverage Through Computer Simulation and Scanning Electron Microscopy," *Journal of Vacuum Science and Technology*, vol. 15, no. 1, p. 13019, (1978).
9. W.G. Oldham, A.R. Neureuther, J.L. Reynolds, C.S. Sung, and S.N. Nandgaonkar, "A general simulator for VLSI lithography and etching processes: Part II application to deposition and etching," *IEEE-Transactions on Electron*

- Devices*, vol. ED 27, no. 8, (August 1980).
10. A.R. Neureuther, C.H. Ting, and C.Y.Liu, "Application of line-edge profile simulation to thin film deposition processes," *IEEE-Transactions on Electron Devices*, vol. ED-27, no. 8, p. 1449, (August 1980).
 11. I.A. Blech, "Evaporated Film Profiles Over Steps in Substrates," *Thin Solid Films*, vol. 6, p. 113, (1970).
 12. N.S. Viswanathan, "Simulation of Plasma Etched Lithographic Structures," *Journal of Vacuum Science and Technology*, vol. 16, no. 2, p. 388, (Mar/Apr 1979).
 13. Mr. Kiyuji Ikeda and Mr. Yoshifumi, *SEM photographs courtesy of Hitachi Corporation*.
 14. Y. Sakai, J.L. Reynolds, and A.R. Neureuther, "Topology simulation for dry etching," *Proceedings of the Electrochemical Society*, no. Abstract 144, (May 1982, Montreal).
 15. N.Rovedo., in *Master's Report, University of California.*, Electronics Research Laboratory, Berkeley, (1979).

CHAPTER SIX

6. PROFILE DETERMINING MECHANISMS IN THIN FILM LAYERS.

6.1. Introduction

Plasma etching offers greater line width and profile control in pattern transfer for integrated circuits. Realizing these advantages in practice requires a careful characterization of the phenomena which limit the process. Previous chapters have introduced the effects of surface migration^{1,2}, angular effects^{3,4}, plus the basic anisotropy and isotropy. These effects were studied in bulk silicon in Chapter Four. Chapter Five then extended the anisotropic etching models to topologies common in IC fabrication. We now turn to the mechanisms in etching of thin film layers, particularly loading and mask interaction effects in etching polycrystalline silicon (poly-si) and silicon nitride layers on etch resistant silicon dioxide.

6.2. The Loading Effect in Fluoro-carbons.

6.2.1. Introduction

In a planar system using fluorinated gasses, the etch rate tends to increase inversely proportional to the area of silicon that is exposed^{5,6}. This results in an accelerated etch rate near the end of the etching process, particularly with any overetch time. This overetching begins when the slowly etching substrate has been reached, and there is only a small amount of poly-Si exposed

at the sidewalls. The accelerated rate causes significant undercutting similar to that found in isotropic barrel configurations.

This section investigates profile control and overetch time sensitivity for various operating conditions. The experimental system is a planar plasma etcher described in reference ⁷ using 90 sccm SF_6 mixed with 10 sccm oxygen to etch the poly-silicon.

6.2.2. Dependence on power

Figure 6.1 illustrates the variation in profiles for wafers etched to an endpoint in the range of powers from 150 Watts to 450 Watts. The following trends occur. There is more poly-Si undercut and less photoresist erosion as the power increases. This observation coupled with the micrograph in Figure 6.2, taken as the surface begins to clear indicates that the lateral etching occurs primarily at the end of the process. Note that higher power and similarly higher etch rate conditions lead to more lateral rate acceleration and thus more pronounced undercut.

The photoresist degradation primarily depends on the duration of exposure to the plasma. The lower powers which take longer to etch show much more resist erosion, much less undercut and more sloped side walls.

The etch rate acceleration ratio, $\frac{R_{os}}{R_o}$ is defined as the over etch rate after endpoint, R_{os} , normalized to the initial rate, R_o . Due to the accelerated rate under high etching conditions, the sensitivity to time and etch uniformity worsens. This situation can be contrasted with the slow, low etch rate conditions where resist erosion dominates the lateral etch rate which remains constant. At 450 watts the sensitivity is 1.23 during the overetch time, while at 150 watts the sensitivity remains at 1.00.

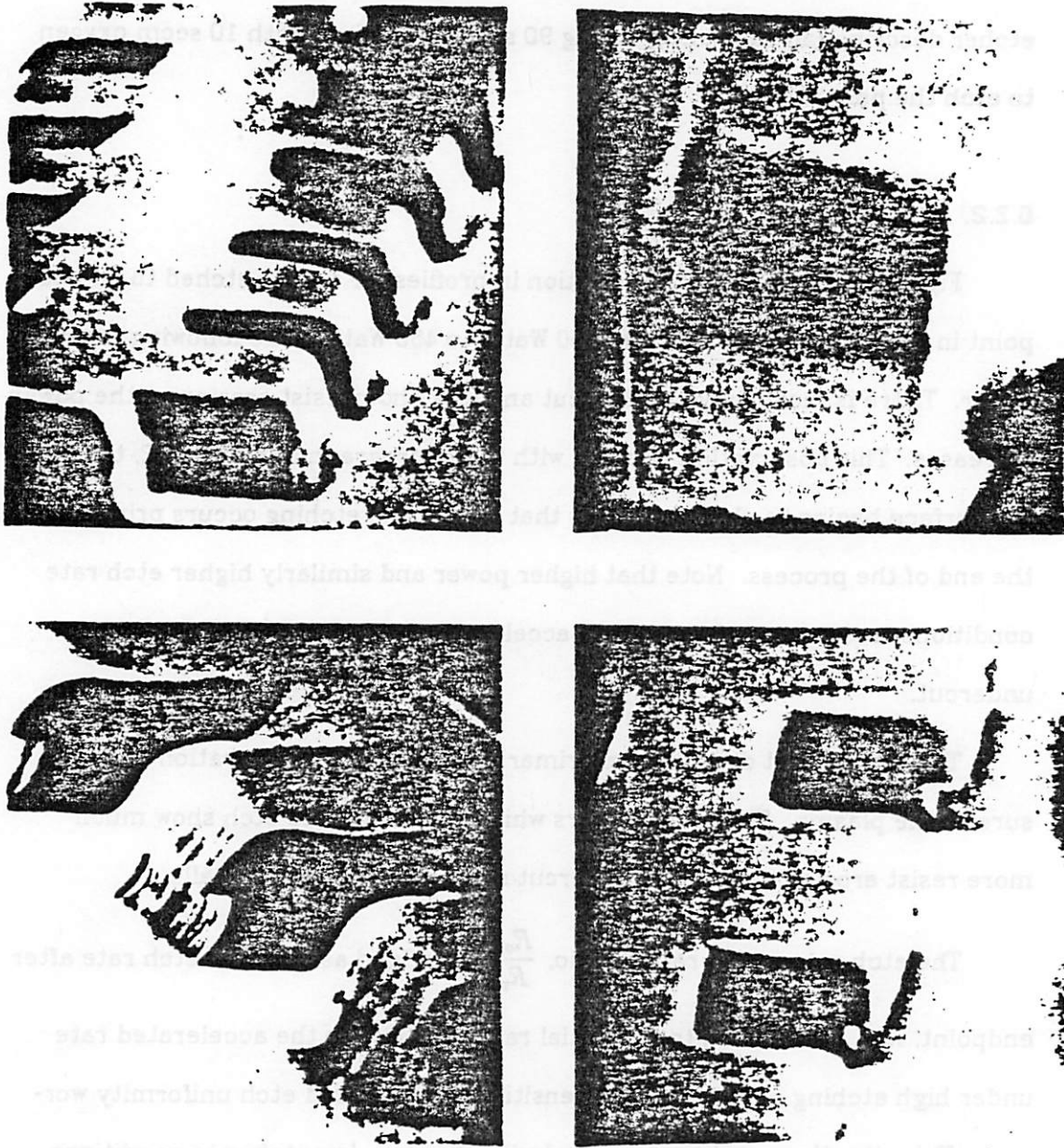


Figure 8.1
 Poly-silicon profiles etched to an end point in Sulfur Hexafluoride and oxygen. Top left-150 Watts. Top right-250 Watts. Bottom left-350 Watts. Bottom right-450 Watts.

Another aspect to lower etch rate conditions is sloped sidewalls. The etch rate ratio between mask and substrate determines sidewall slope. The more a mask erodes, the more tapered the patterned layer evolves. Thus etch rate conditions where the erosion rate is near the lateral etch rate lead to tapered sidewalls.

6.2.3. Dependence on photo resist

Under the same etching conditions, 20 sccm Sulfur Hexafluoride and 10% Oxygen at 50 mTorr and 0.18 Watts/cm², Figure 6.3 illustrates the effect that the resist mask has on the etched profile. The top profile results from a vertical AZ1350J photo resist profile that was not hard baked. The profile remains vertical with no later erosion or undercut. This soft resist does sputter and redeposit leaving a residue on the etching surface. At the edge where not as much resist reaches the etching is not as inhibited. Below the resist is hard baked and flows to a tapered angled. The thinner edge etches during etching leaving a sloped silicon profile. The hardened resist though demonstrates no resputtering to produce trenches on slower etching. Both redeposition and erosion of the resist are variables in structuring with etching as well as the conditions.

6.2.4. Computer simulation.

Computer simulation can be used to study the time evolution of the profiles in detail. The program for Simulation And Modeling of Profiles in Lithography and Etching (SAMPLE, ⁹) accepts weighted rates to produce two dimensional profiles in time. In Figures 6.4, 6.5 and 6.6, three types of processes are modeled. The first simply demonstrates normal isotropic etching with a constant lateral and normal etch rate. This can be compared to the second case involving an accelerated rate due to the loading effect in the final stages of

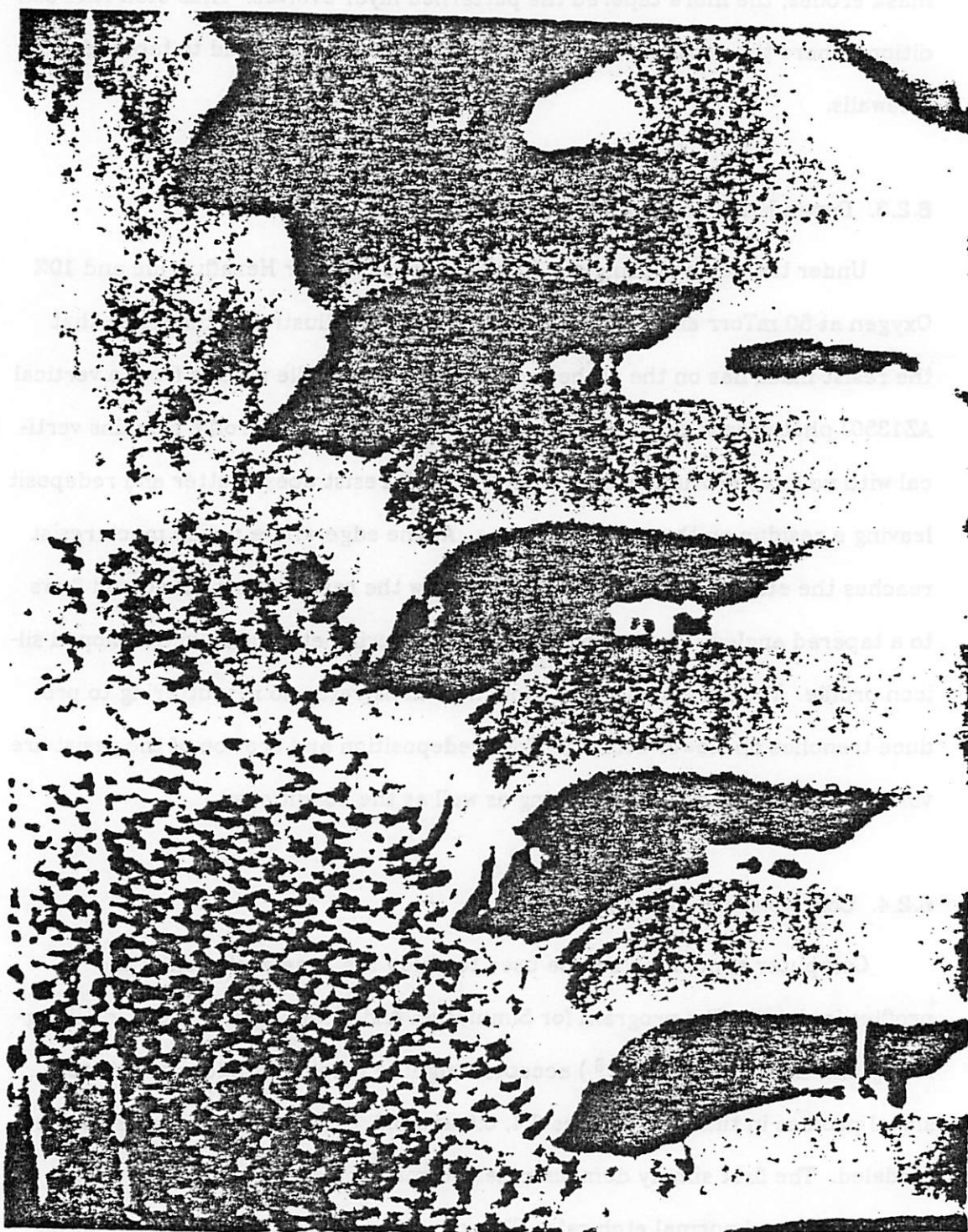


Figure 8.2
Poly-silicon profile just prior to end point etched in $SF_6/10\%O_2$.

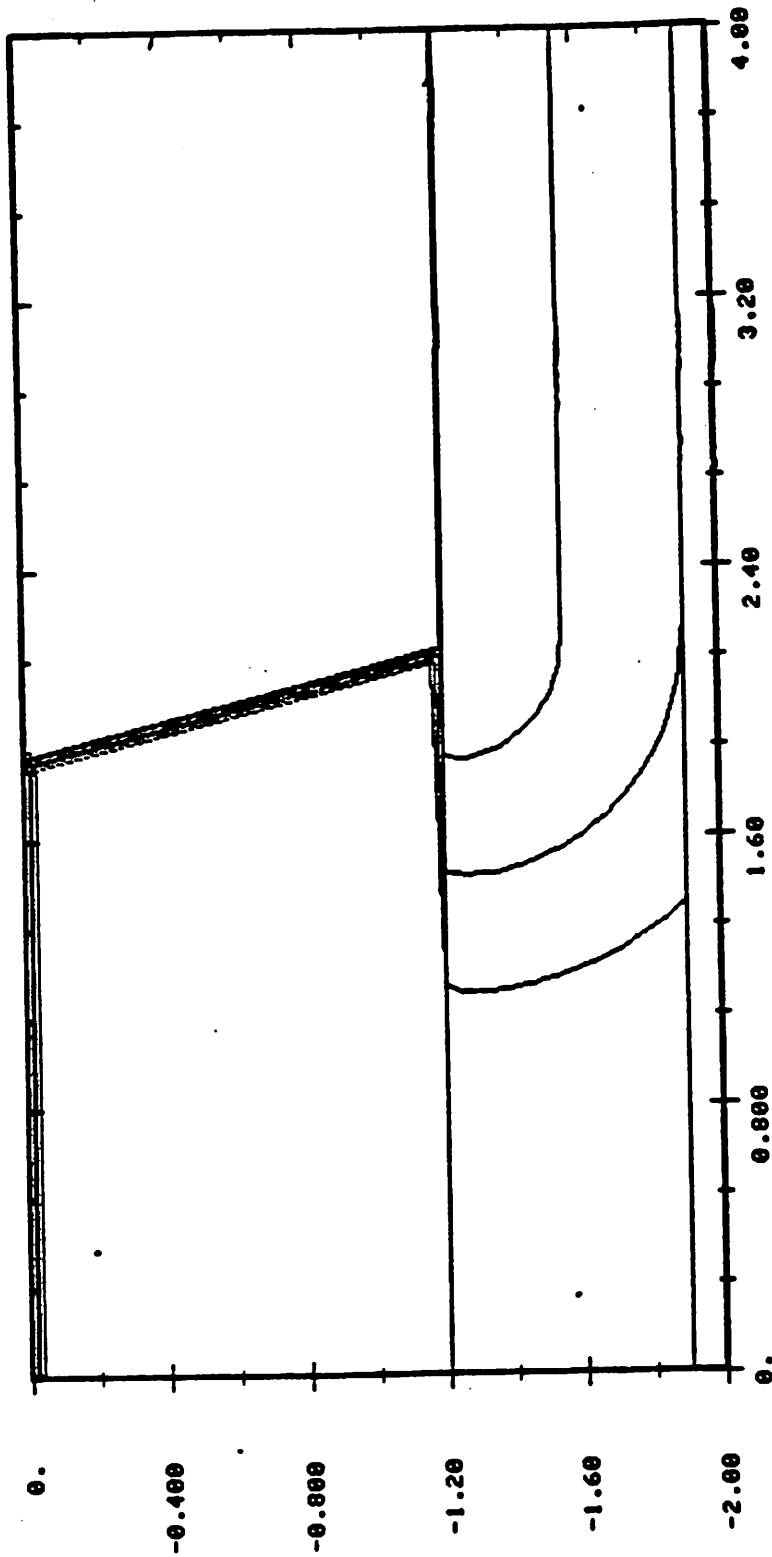


Figure 8.3
Computer simulation of a poly-silicon profile etched isotropically at
three different times.

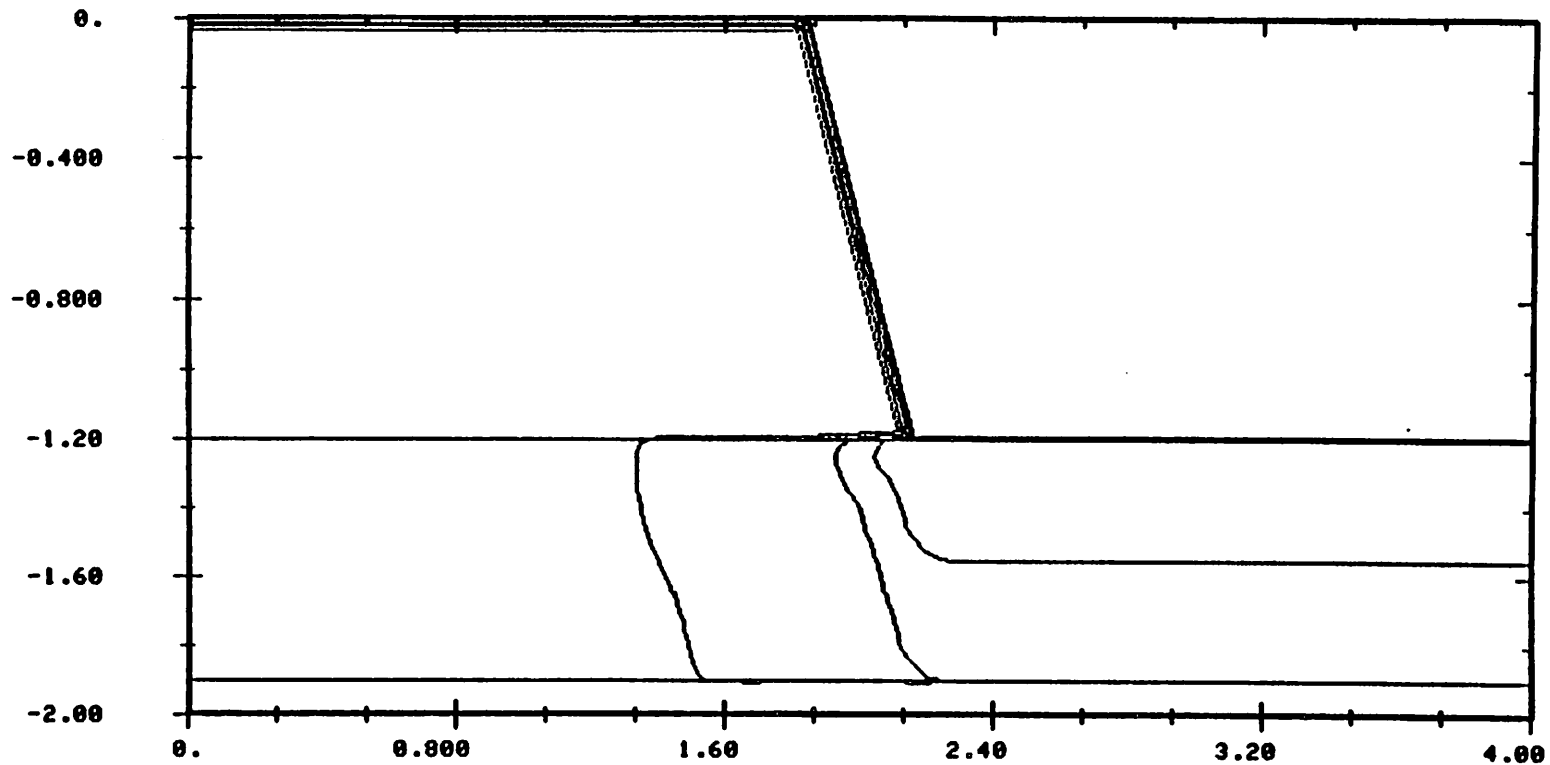


Figure 6.4
Computer simulation of a poly-silicon profile etched anisotropically
with accelerating rate upon endpoint.

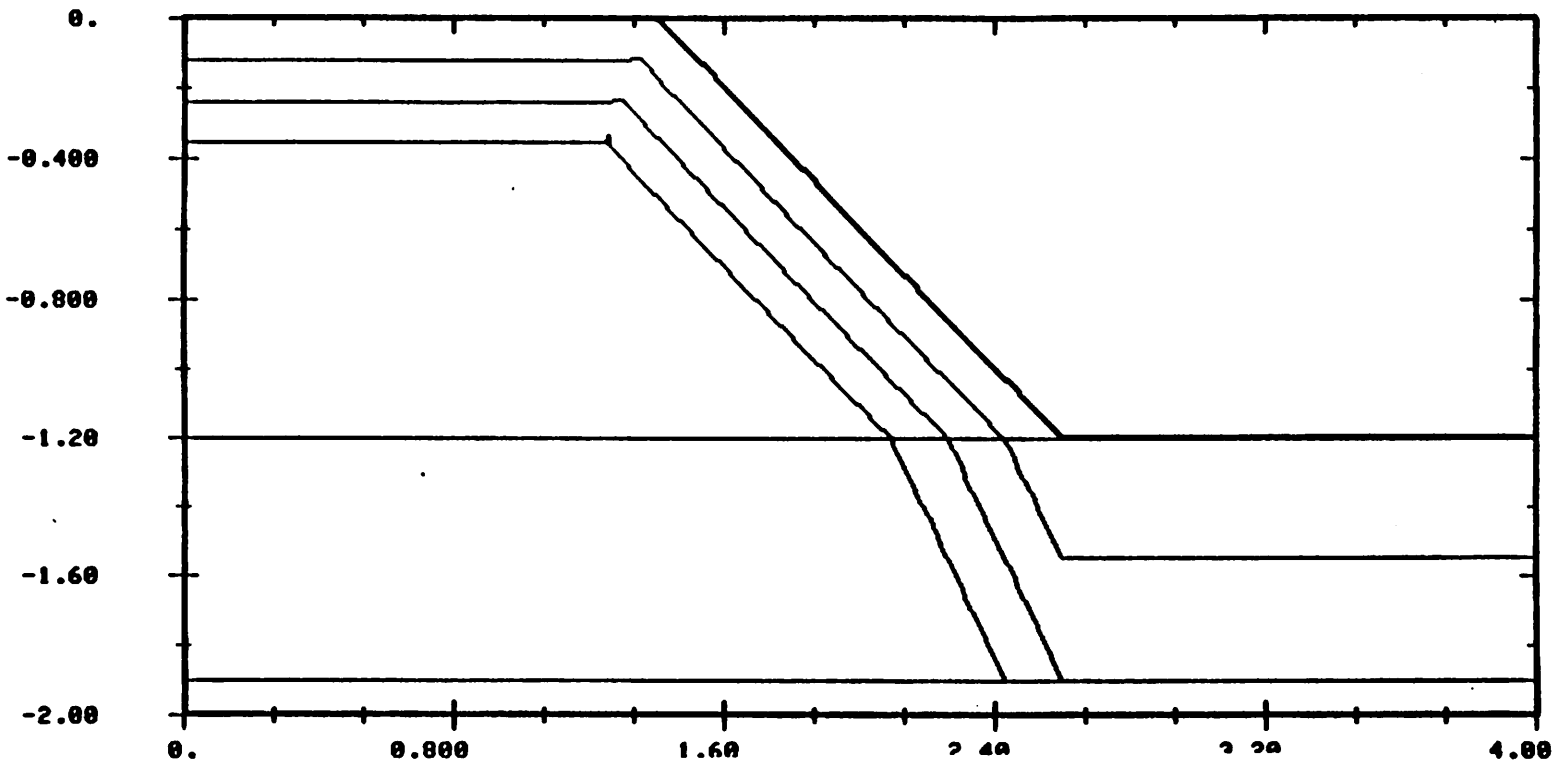


Figure 6.5

Computer simulation of a poly-silicon profile etched anisotropically with an eroding mask at three different times.

etching. Both cases result in equivalent amounts of undercut for an over etch time of 50%. There is no real advantage to etching with fluorine-based gasses with this over etch acceleration. The third simulation illustrates the lower etch rate conditions with no undercut and photoresist erosion. The profile is less sensitive to overetch time when there is less accelerated rates due to loading effects. By proper control of the relative mask erosion to poly-silicon etch rate the profile can be predictably transferred.

A fourth case to be compared to the accelerated etching is illustrated in Figure 6.7. Here, once the non-etching substrate is reached reactive species can migrate along the substrate and cause preferential etching at the interface. This is commonly found with chlorine based etching of doped poly-silicon. The mechanism depends on the interface which causes an even more anisotropic, positive undercut compared to simple accelerated etching.

6.3. The Loading Effect with Chloro-carbon Additions.

6.3.1. Introduction

This section details the behavior of the plasma etching of poly-silicon and silicon nitride with various gas mixtures of CF_4 and CF_3Cl . The intent is to investigate the effect of added Cl atoms on the etched profile and its evolution during overetch. Fluorine based gasses have been shown to demonstrate accelerated etching and a loading effect at the end of the etch cycle due to the disappearance of the bulk of the silicon. Chloro-carbons, however, demonstrate little or no side etching, or loading effects⁵. Chlorine based gasses are also known to cause re-entrant profiles when etching polysilicon^{2, 1}. Both of these mechanisms can be attributed to the ionic initiation of chlorine etching rather than the transport limitations of fluorine atom etching. Section 6.3.2 describes the

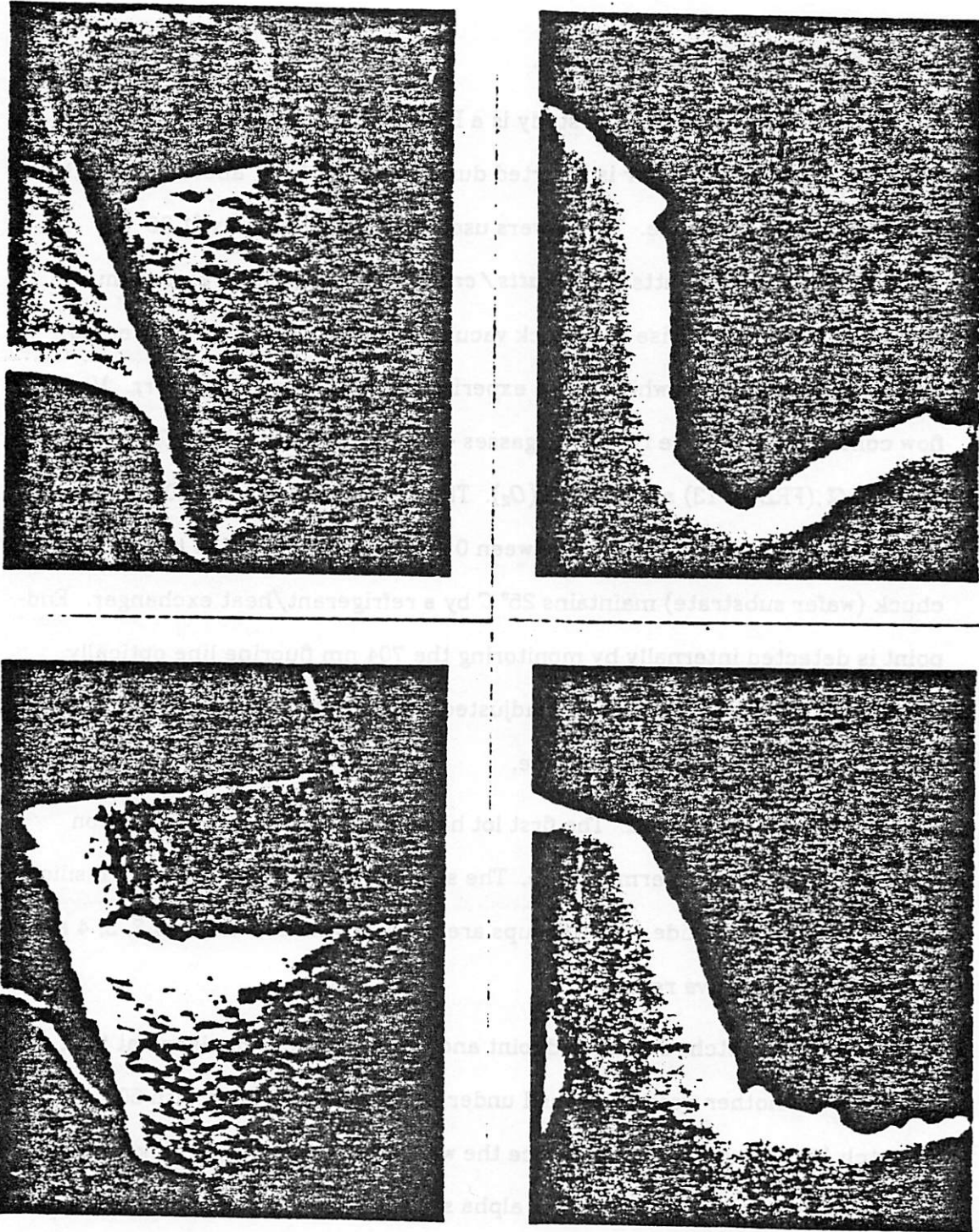


Figure 6.8 Micrographes of profiles etched anisotropically under the same conditions with hard-baked photo resist (top) and unbaked photo resist (bottom).

plasma reactor and the test wafers which differ from those in Appendix A. Sections 6.3.3 and 6.3.4 summarize and discuss the mechanisms.

6.3.2. Experimental configuration.

The plasma etcher used in this study is a Branson IPC Sigma-80 cassette to cassette system. The wafer is inverted during etching 1.75" above the 4" 13.56 MHz rf powered electrode. The powers used here are 150 Watts (1.85 Watts/cm²) and 350 Watts (4.32 Watts/cm²). The chamber pressure must exceed 2.5 Torr, otherwise the chuck vacuum may not support the inverted wafer. The pressure at which these experiments were done is 3.5 Torr. Mass flow controllers regulate the three gasses – Carbon tetrafluoride (CF₄, FREON-14), CF₃Cl (FREON-13) and oxygen (O₂). The total flow is kept at 200 sccm and the CF₃Cl concentration varied between 0 and 40 sccm (0-20% of total). The chuck (wafer substrate) maintains 25° C by a refrigerant/heat exchanger. Endpoint is detected internally by monitoring the 704 nm fluorine line optically. The gain of the endpoint system is adjusted according to the selectivity between the poly or nitride to the thick oxide.

Two sets of wafers are used. The first lot has 0.41 μm of LP-CVD polysilicon above a thick 0.3 μm thermal oxide. The second has 0.293 μm of LP-CVD silicon nitride above thick oxide. Both groups are masked with fine lines of 2, 3, 4 and 5 μm in AZ1470 positive resist.

The wafer is first etched to an endpoint and the plasma extinguished at that point. Then another wafer is etched under the same conditions with 50% overetch (1.5 X endpoint time). Once the wafers are etched the thicknesses are measured physically on the DekTak alpha step to insure that they had etched to completion. Many nitride wafers were not endpointed accurately and the rates are also determined from these measurements. Other information is taken

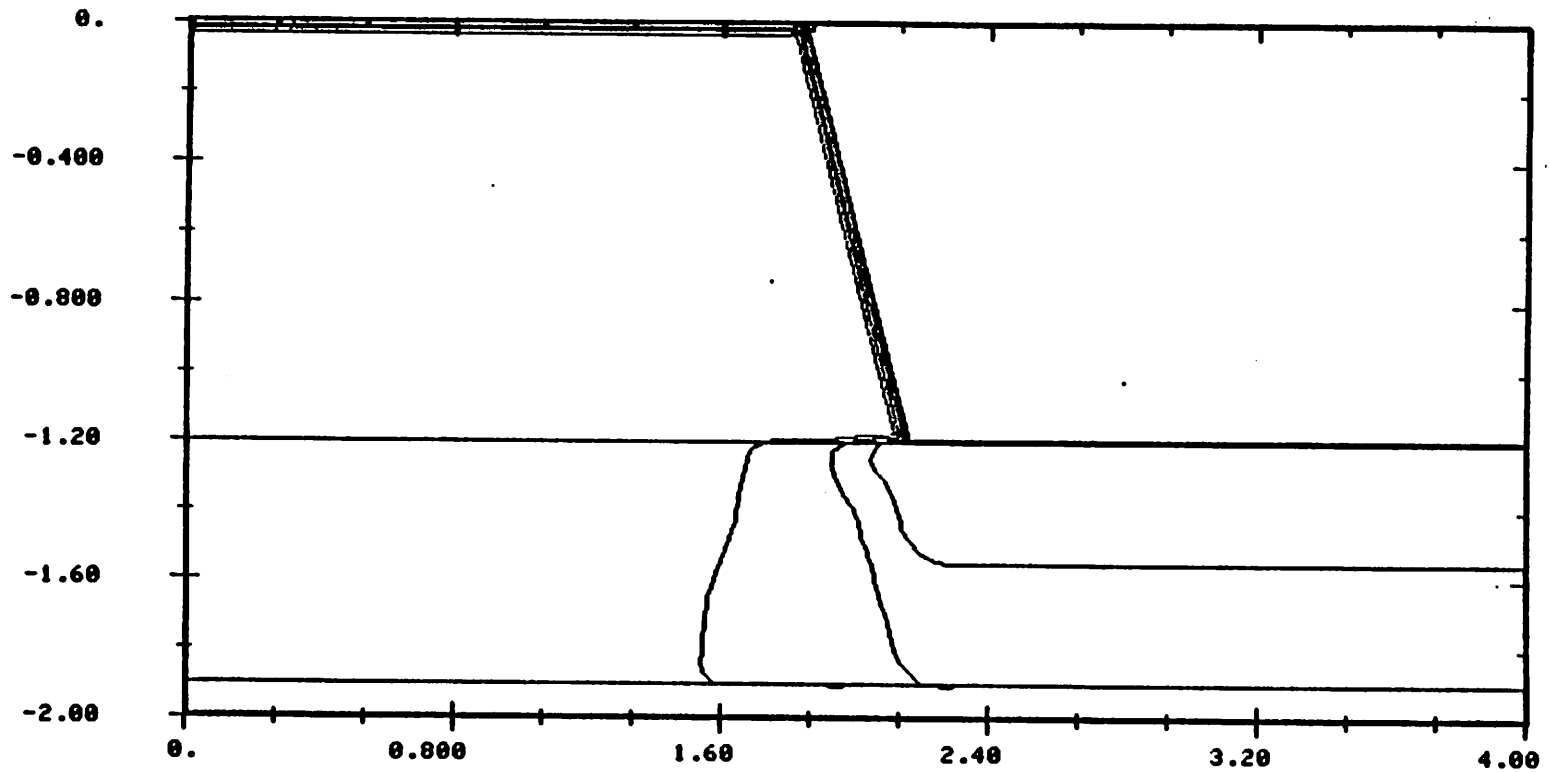


Figure 6.7
Computer simulation of a poly-silicon profile etched anisotropically
with surface migration upon endpoint at three different times.

from scanning electron micrographes taken from die from the center of the wafers. The $5\ \mu\text{m}$ lines are consistently used for photographes. The center of the wafers is used where the etch rate is the highest.

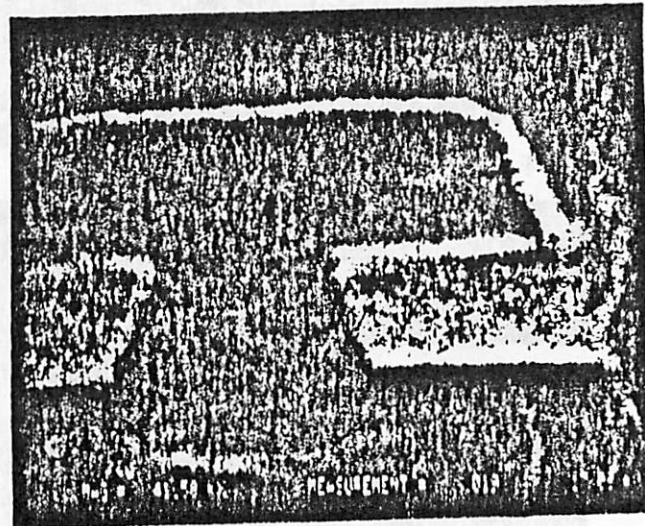
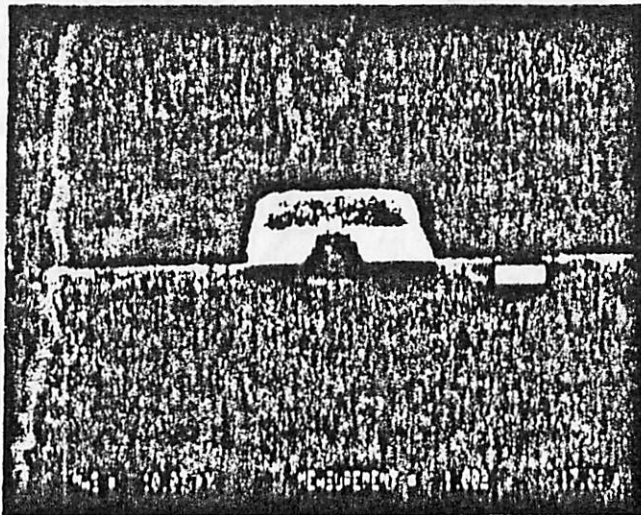
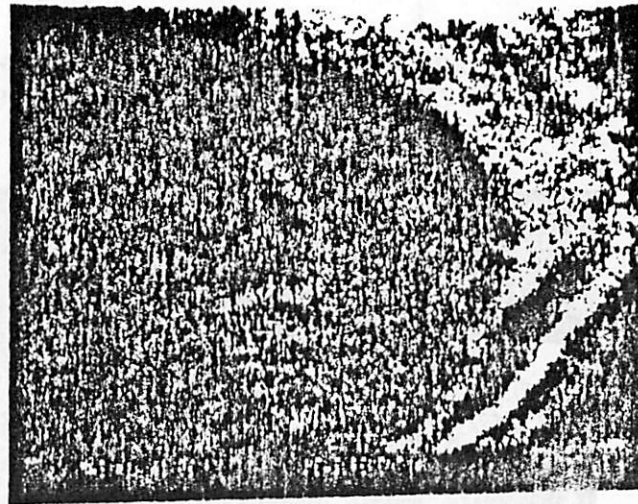
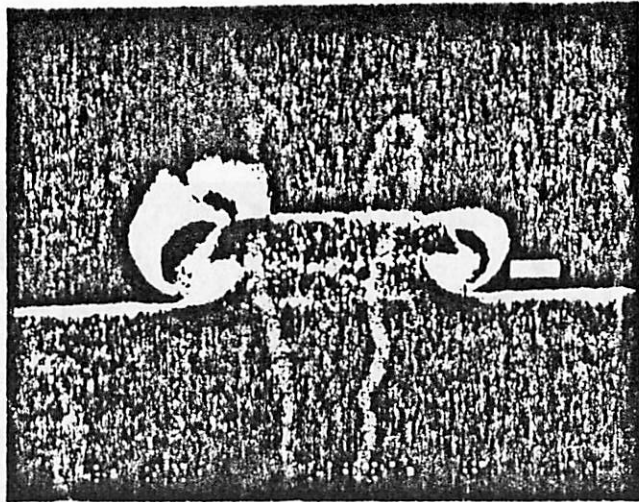
6.3.3. Data and Observations

Table 6.1 summarizes the etch rates and profile characteristics at the various operating points for the micrographes of the following dozen Figures. "Loss" is the amount of material removed laterally. It is the mask undercut in the case of the polysilicon samples. For the nitride samples, the lateral etch rate (\leftarrow -rate) best represents the photoresist erosion rate from $4.0\ \mu\text{m}$ (with the resist patterning bias included). Rates are determined by dividing the etched distance (for lateral) and thickness (for directional) by the etch time.

For the poly-silicon samples the total and lateral etch rates increase with both power and CF_3Cl content. The etched profiles in Figures 6.8-6.13 would result from including an isotropic, lateral component. There is no re-entrant angles found in the SEM's which would indicate surface migration or positive undercut. The accelerated over etch rate is suppressed completely with more Cl atoms present, but the degree of anisotropy is still less than without them.

The nitride always etches totally anisotropically. The actual line width loss, due to the photoresist erosion, remains approximately constant no matter the CF_3Cl concentration, although the total rate increases and photoresist suffers degradation. A taper or a foot in their profile can be accounted for by the photoresist erosion decelerating during the process. The poly-silicon to nitride etch rate ratio (ERR) increases from 1.5 to 2.5 with increasing CF_3Cl concentrations.

The photoresist (AZ 1470) rounds off, but does not shrink in line-width while etching the poly. At high Cl concentrations and high powers the



Sandia National Laboratories

Figure 8.8

Poly-silicon profile etched in 180 sccm CF_4 , 20 sccm O_2 , 3.5 mTorr, 150 Watts. Top - etched to an endpoint. Bottom - over-etched by 50%.

$CF_4/10\%O_2$
150 W
3.5 T

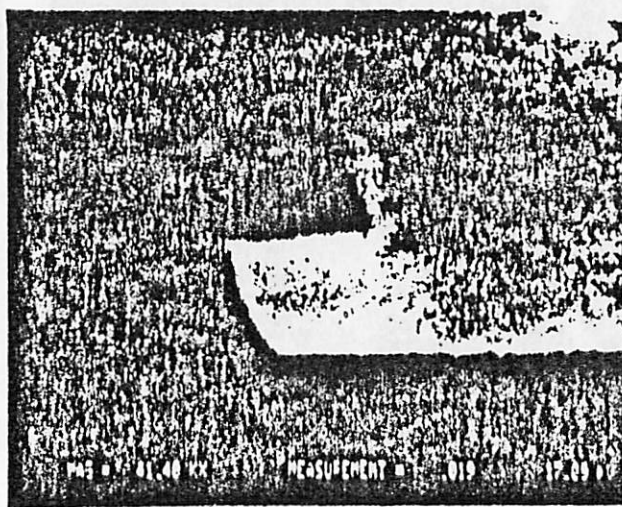
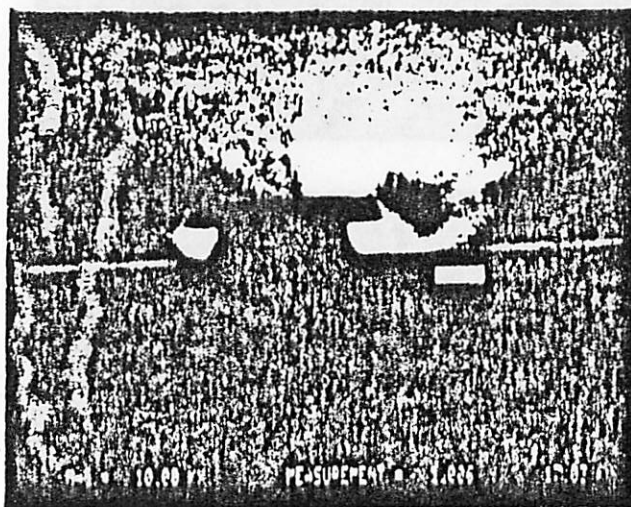
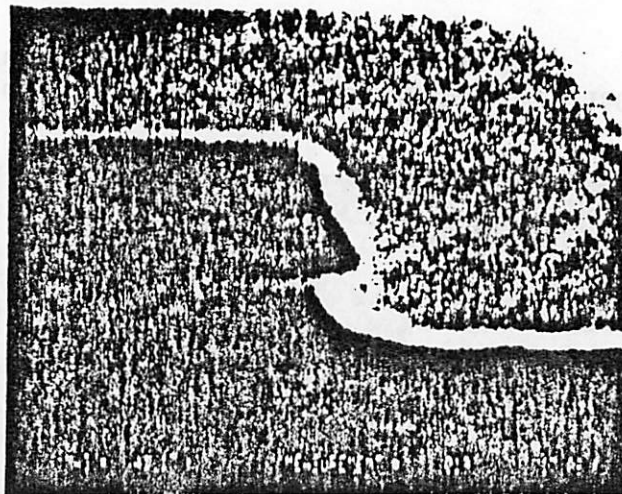
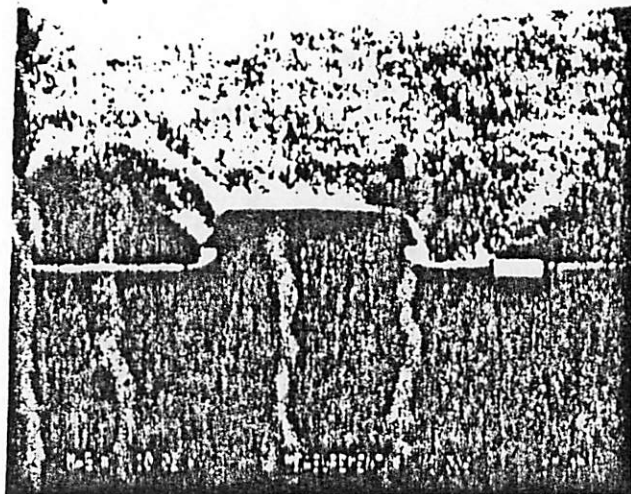
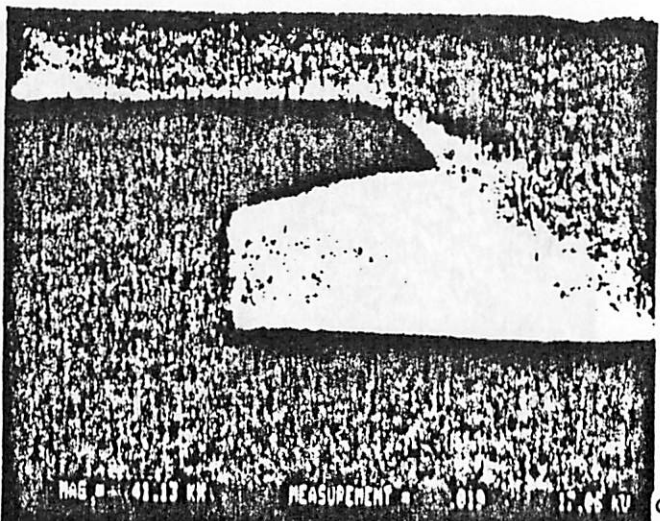
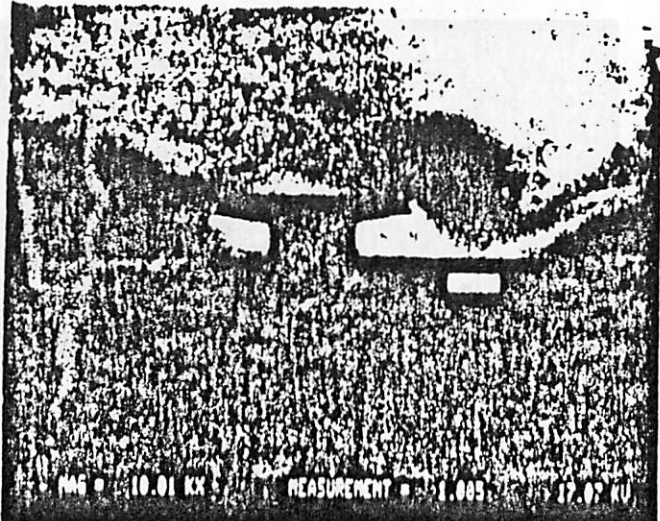
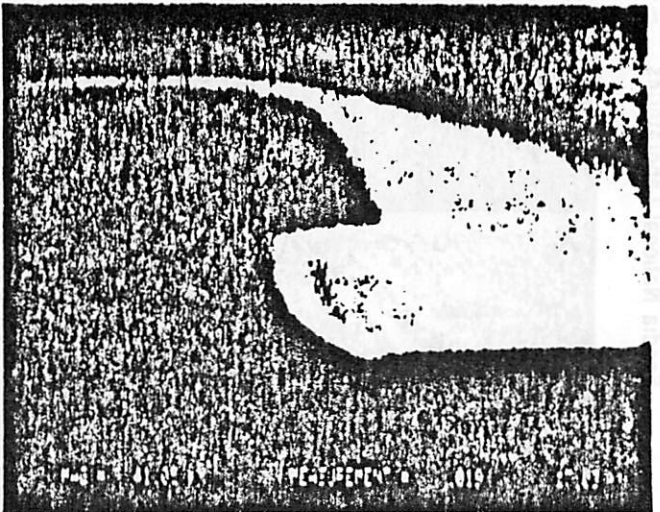
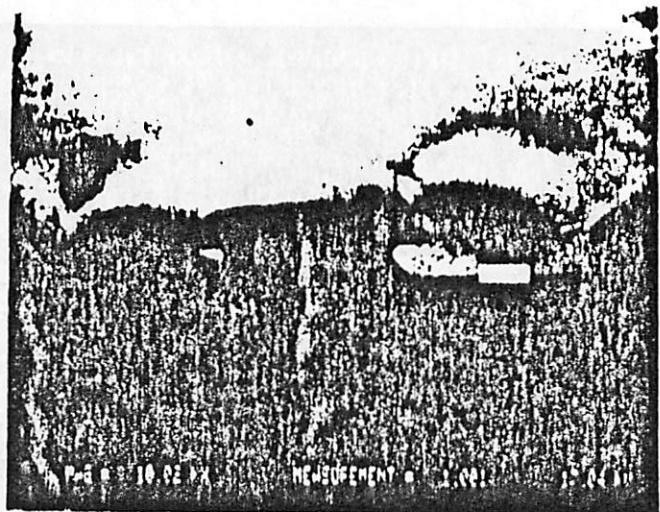


Figure 6.9

Poly-silicon profile etched in 180 sccm CF_4 , 20 sccm O_2 , 3.5 mTorr, 350 Watts. Top - etched to an endpoint. Bottom - over-etched by 50%.

$CF_4/10\%O_2$
350W
3.5 T.

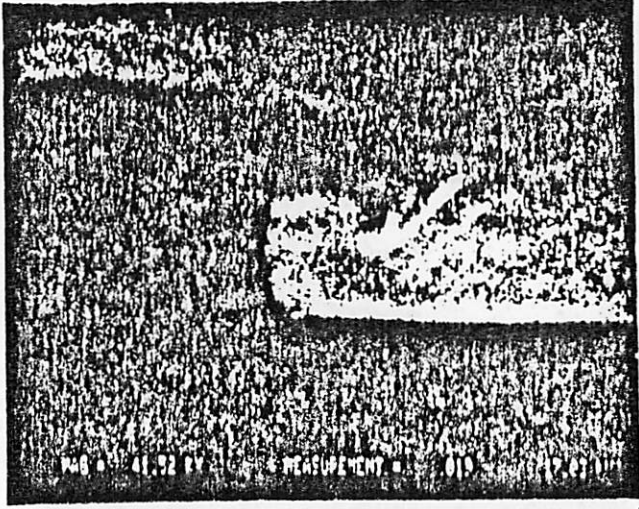
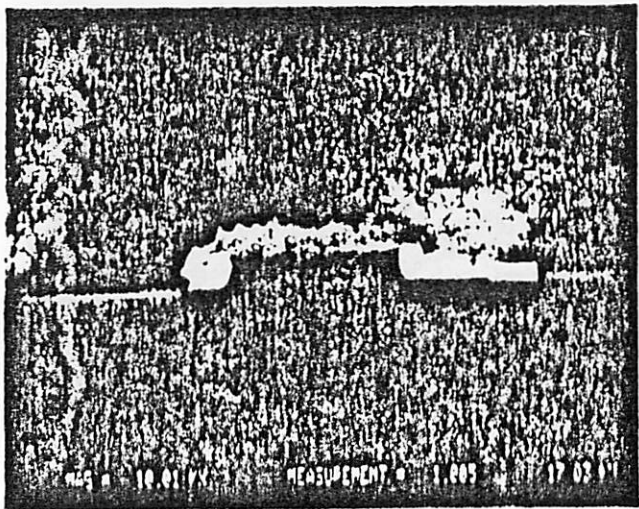
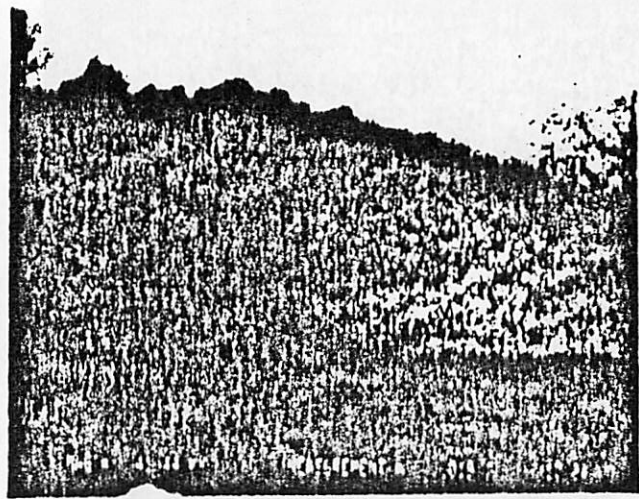
Sandia National Laboratories



Sandia National Laboratories

CF_4 , 10% $CFCl$
10% O_2
150W, 3.5 T

Figure 6.10
 Poly-silicon profile etched in 160 sccm CF_4 , 20 sccm CF_3Cl , 20 sccm O_2 , 3.5 mTorr, 150 Watts. Top - etched to an endpoint. Bottom - over-etched by 50%.



Sandia National Laboratories

Figure 8.11
 Poly-silicon profile etched in 160 sccm CF_4 , 20 sccm CF_3Cl , 20 sccm O_2 , 3.5 mTorr, 350 Watts. Top - etched to an endpoint. Bottom - over-etched by 50%.

$CF_4/10\%CF_3Cl$
 10% O_2
 350W, 3.5T

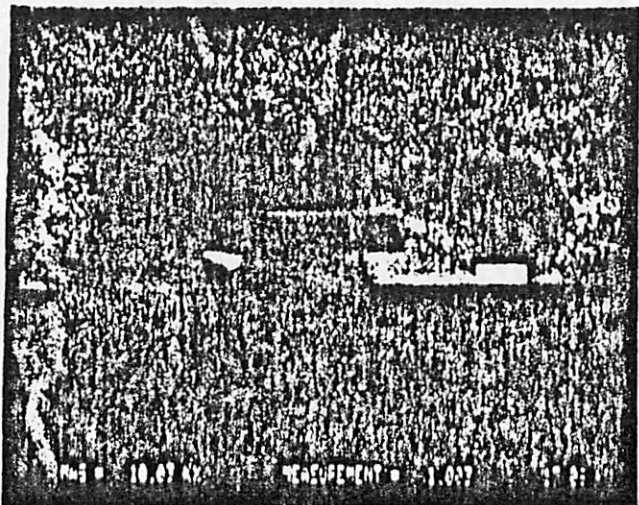
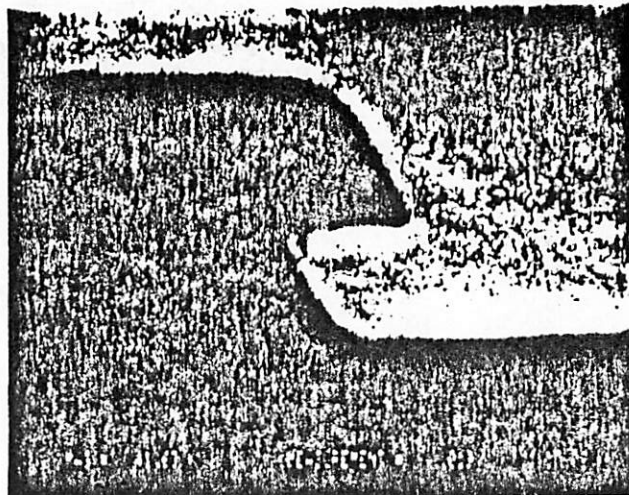
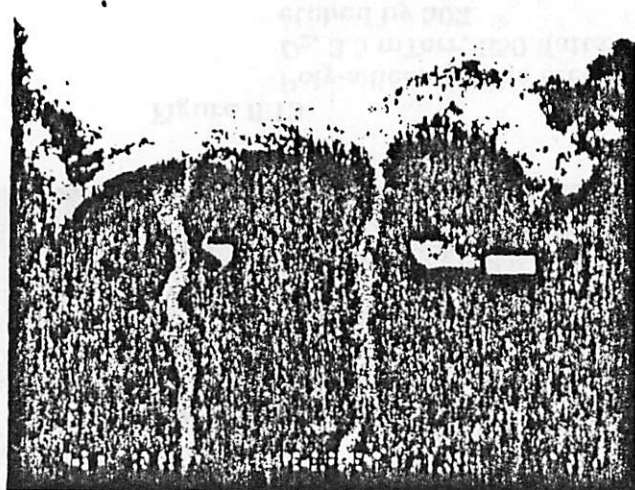
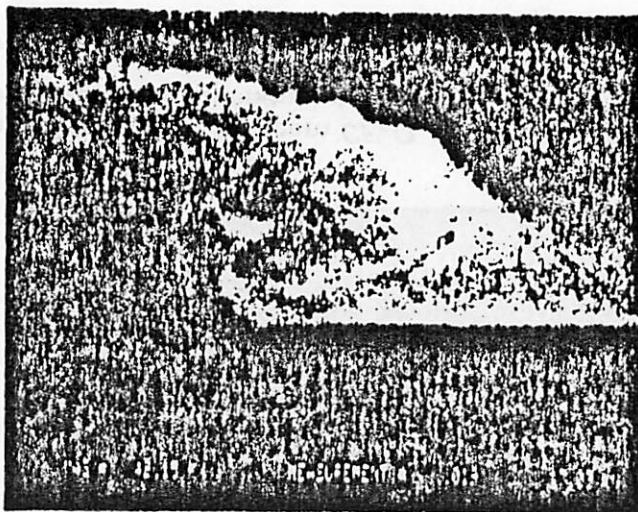
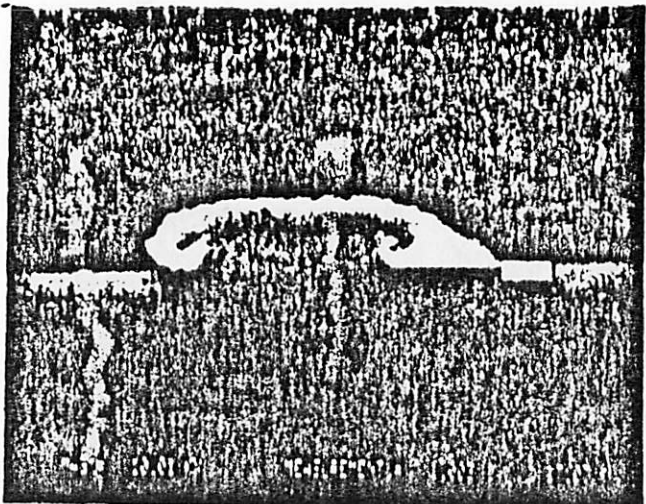


Figure 8.12

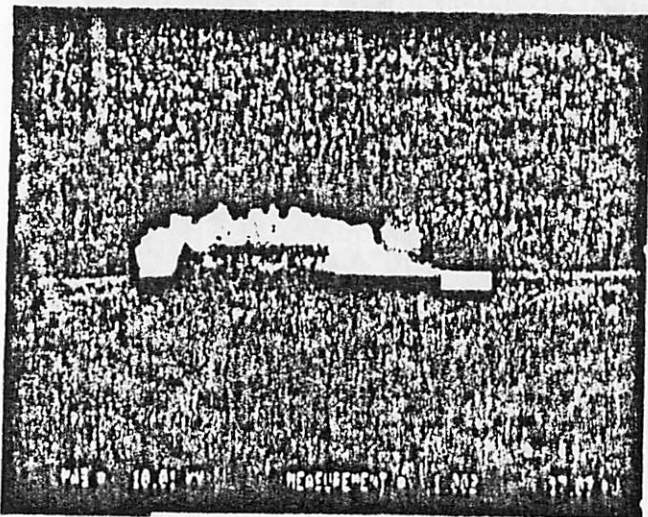
Poly-silicon profile etched in 140 sccm CF_4 , 40 sccm CF_3Cl , 20 sccm O_2 , 3.5 mTorr, 150 Watts. Top - etched to an endpoint. Bottom - over-etched by 50%.

$CF_4/20\%CF_3Cl$
10% O_2
150W, 3.5T

Sandia National Laboratories



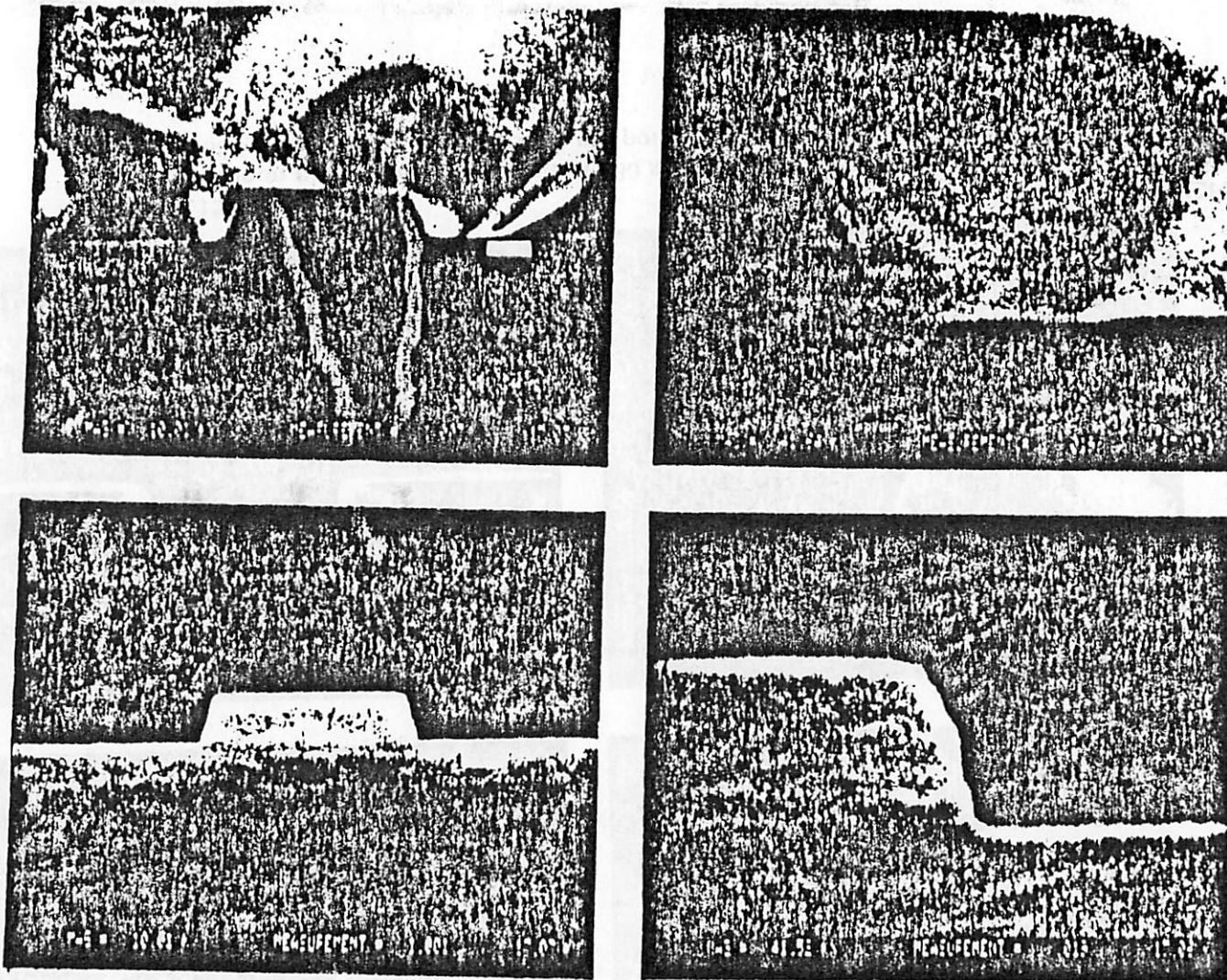
E4613A #34 5um inner 7/82



Sandia National Laboratories
Albuquerque, New Mexico 87185

$CF_4/20\%CF_3Cl$
 $10\%O_2$
3.5T

Figure 8.13
Poly-silicon profile etched in 140 sccm CF_4 , 40 sccm CF_3Cl , 20 sccm O_2 , 3.5 mTorr, 350 Watts. Top - etched to an endpoint. Bottom - over-etched by 50%.

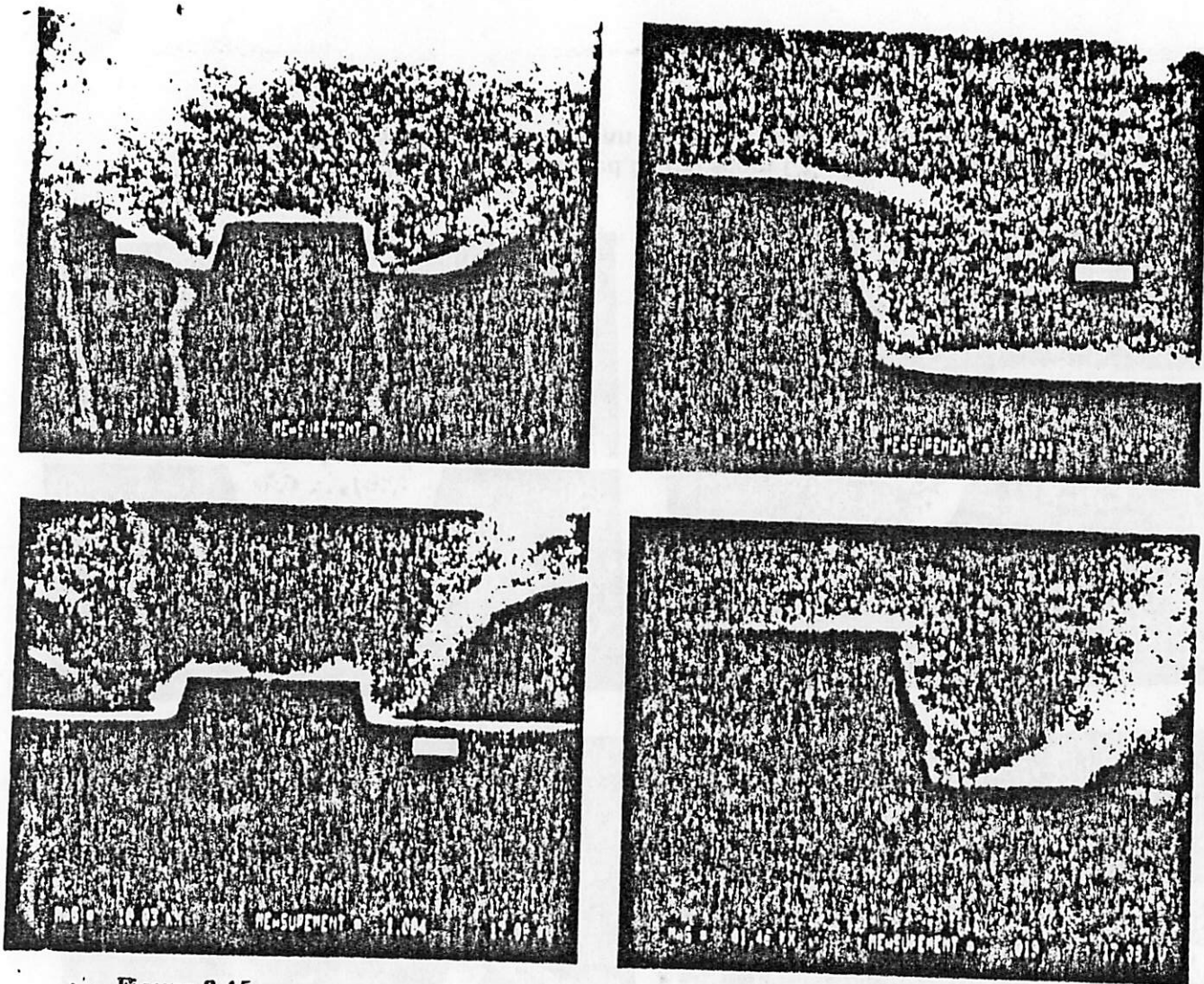


Sandia National Laboratories

Figure 6.14

Silicon nitride profile etched in 180 sccm CF_4 , 20 sccm O_2 , 3.5 mTorr, 150 Watts. Top - etched to an endpoint. Bottom - over-etched by 50%.

$CF_4/10\%O_2$
150W
35T



Sandia National Laboratories

Figure 8.15
 Silicon nitride profile etched in 180 sccm CF_4 , 20 sccm O_2 , 3.5 mTorr,
 350 Watts. Top - etched to an endpoint. Bottom - over-etched by 50%.

$CF_4/10\%O_2$
 350W
 3.5 T.

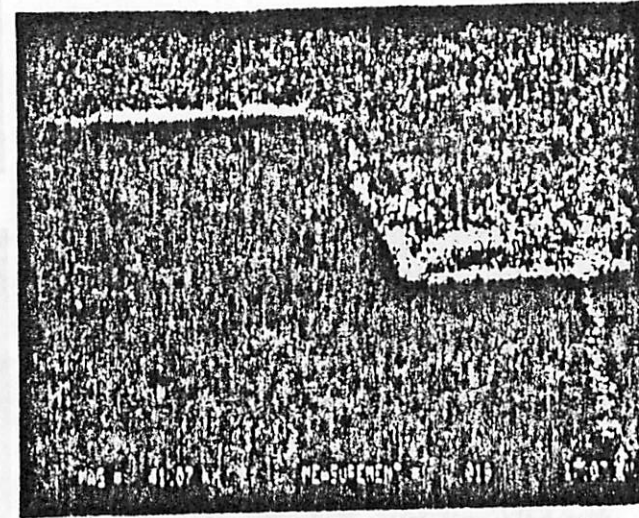
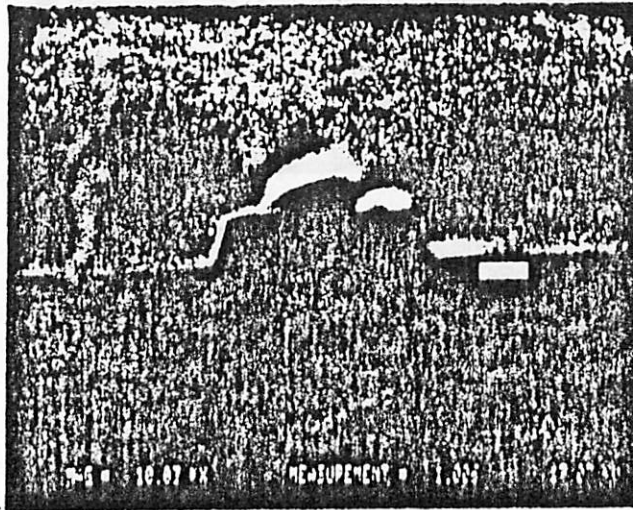
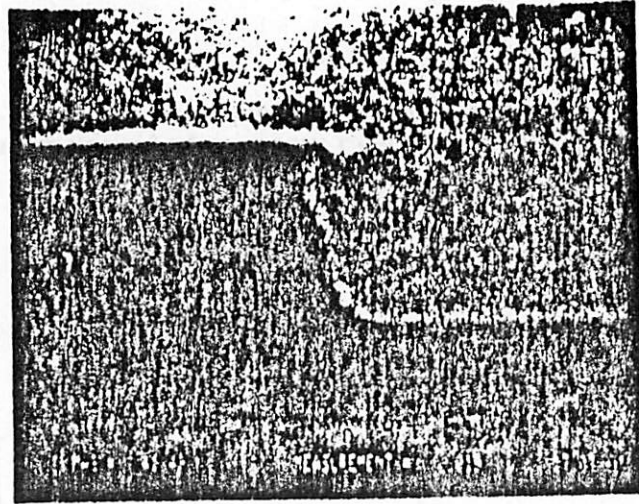
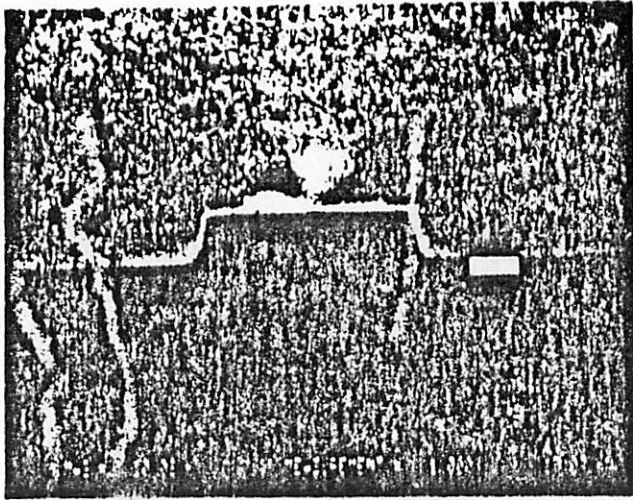
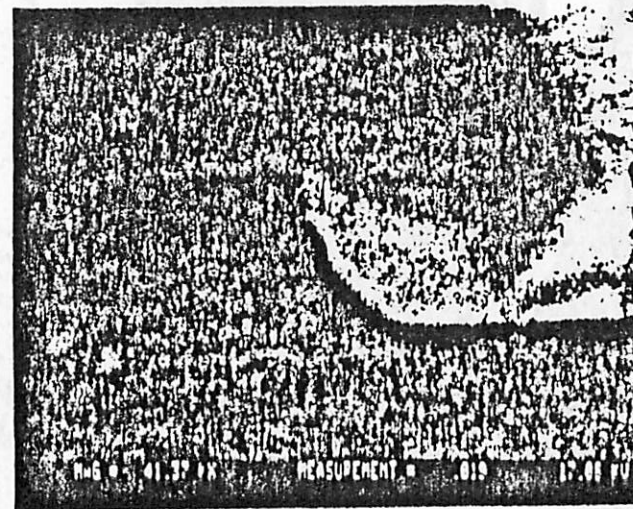
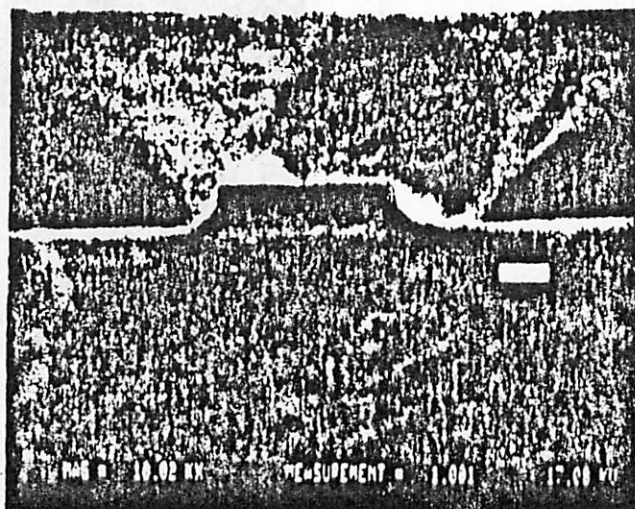
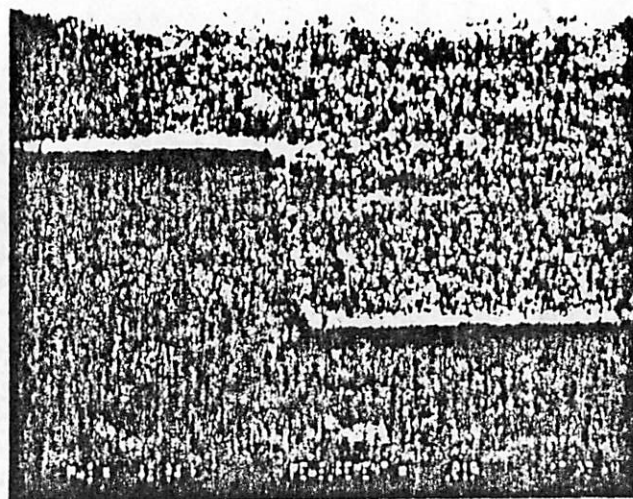
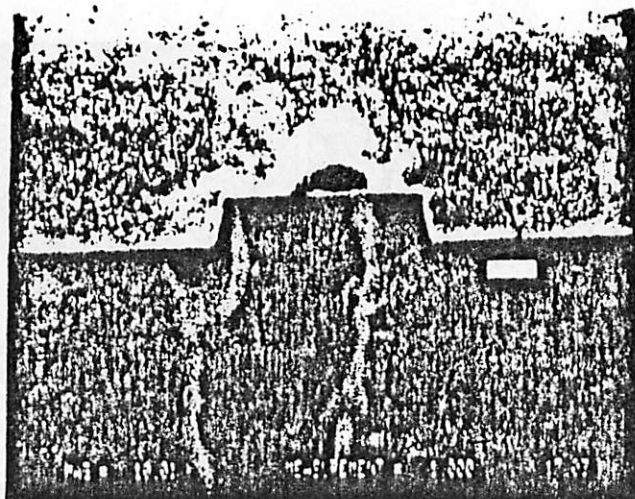


Figure 8.16

Silicon nitride profile etched in 180 sccm CF_4 , 20 sccm CF_3Cl , 20 sccm O_2 , 3.5 mTorr, 150 Watts. Top - etched to an endpoint. Bottom - over-etched by 50%.

Sandia National Laboratories

$CF_4/10\%CF_3Cl$
 $10\%O_2$
150W, 3.5T



Sandia National Laboratories

$CF_4/20\%CF_3Cl$
 $10\%O_2$
 150w, 3.5T

Figure 6.18

Silicon nitride profile etched in 140 sccm CF_4 , 40 sccm CF_3Cl , 20 sccm O_2 , 3.5 mTorr, 150 Watts. Top - etched to an endpoint. Bottom - over-etched by 50%.

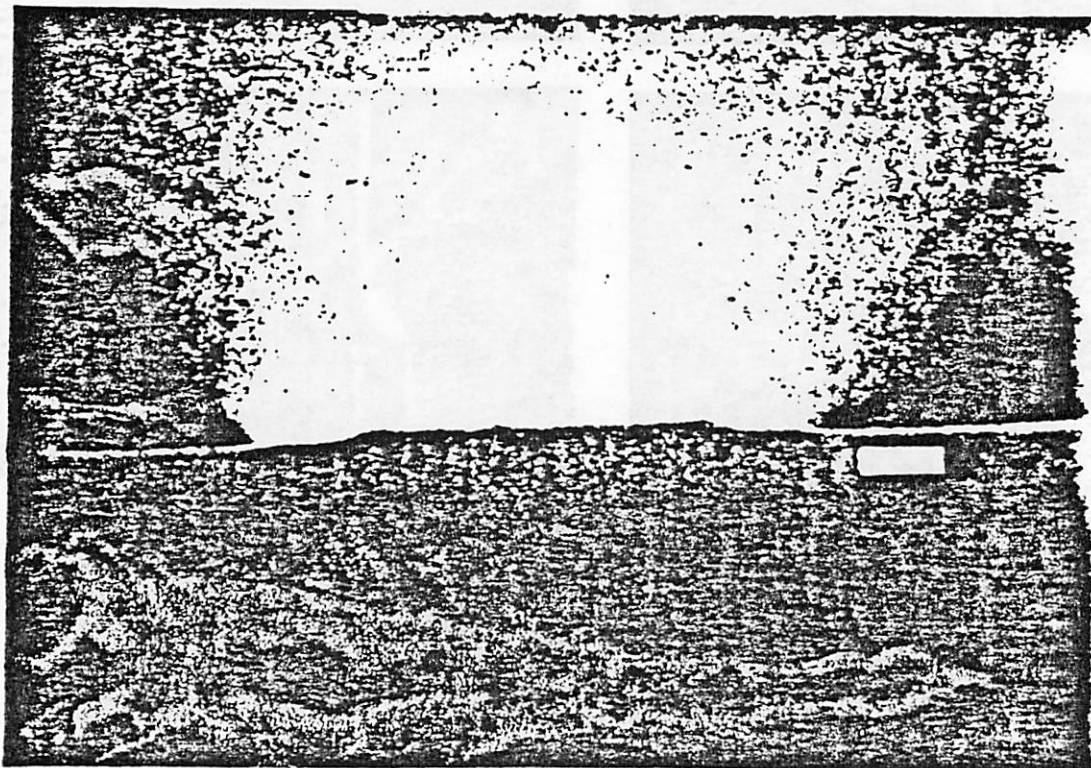
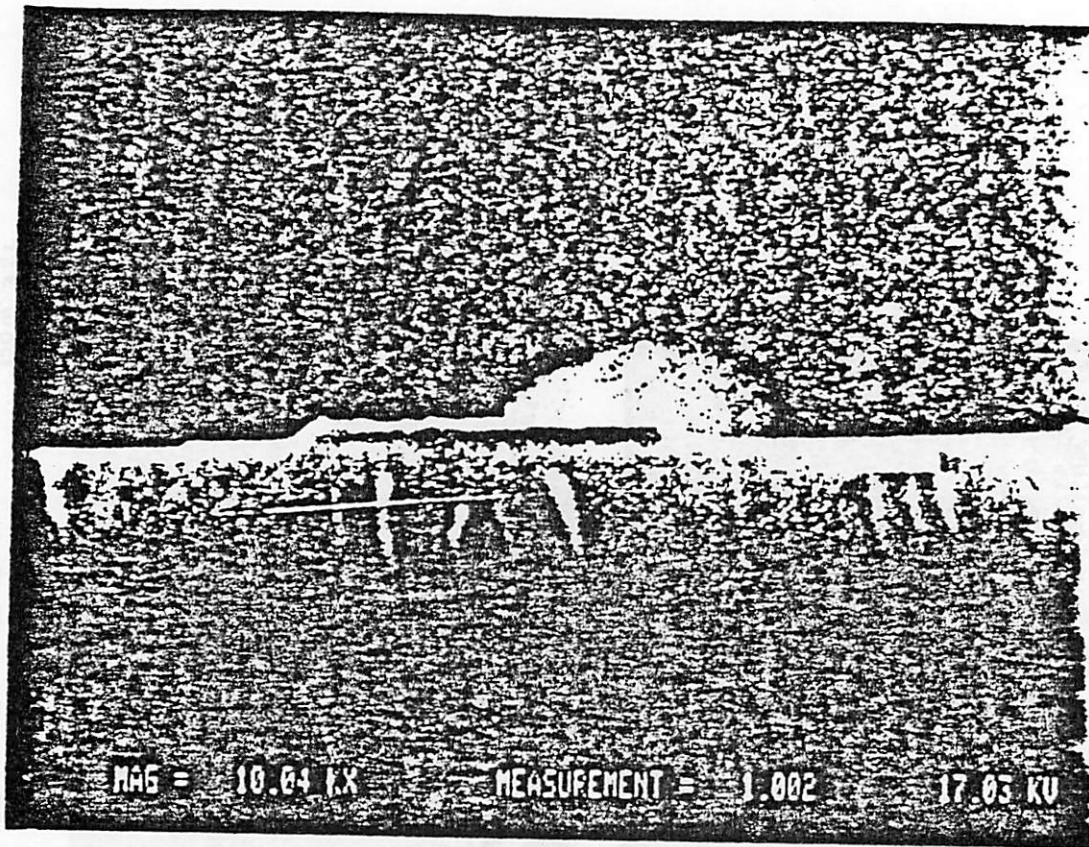


Figure 6.19

Silicon nitride profile etched in 140 sccm CF_4 , 40 sccm CF_3Cl , 20 sccm O_2 , 3.5 mTorr, 350 Watts. Top - etched to an endpoint. Bottom - over-etched by 50%.

Table 8.1 - Etch information for poly-si								
200 sccm gas mixture / CF_4 / CF_3Cl / 20sccm O_2								
pressure 3.5 Torr								
%- CF_3Cl of total	power (Watts)	over etch	undercut (μm)	←rate ($\mu m/m$)	→rate ($\mu m/m$)	time (sec)	accel ratio	aniso ratio
0%	150	-	.237	.198	.342	72	3.85	0.42
0%	150	50%	.694	.782		108		
0%	350	-	.117	.190	.350	37	3.27	0.46
0%	350	50%	.438	.621		68		
10%	150	-	.334	.254	.311	79	1.06	0.18
10%	150	50%	.702	.269		161		
10%	350	-	~.298	~.483	.665	37	0.95	0.27
10%	350	50%	~.321	~.457		40		
20%	150	-	.364	.352	.397	62	0.80	0.11
20%	150	50%	.482	.283		67		
20%	350	-	~.376	~.610	.665	37	0.79	0.08
20%	350	50%	~.4-.53	.48-.84		48		

photoresist is significantly damaged. It appears pitted and fluffed on the poly samples and it is removed completely in the longer etch time for nitride. In the cases where some photoresist remains on the nitride it is sharp, yet eroded laterally and in thickness.

When the just etched are compared to the 50% over etched polysilicon samples a difference in the lateral etching rate can be calculated. For the wafers etched in CF_4 and O_2 alone, the lateral rate accelerates around 400%.

Table 6.2 – Etch information for Si_3N_4							
200 sccm gas mixture / CF_4 / CF_3Cl / 20sccm O_2							
pressure 3.5 Torr							
%- CF_3Cl of total	power (Watts)	over etch	loss (μm)	←rate ($\mu m/min$)	↓rate ($\mu m/min$)	time (sec)	ERR (poly:nit)
0%	150	-	.320	.234	.214	82	1.6
0%	150	50%	.500	.258		116	
0%	350	-	.147	.166	.328	53	1.6
0%	350	50%	.572	.505	.318	68	
10%	150	-	.176	.235	.177	45	1.1
10%	150	50%	.412	.180		137	1.8
10%	350	-	.692	.670	.284	62	2.3
10%	350	50%	.647	.669	.303	58	
20%	150	-	.147	.238	.161	37	2.5
20%	150	50%	.588	.243		145	
20%	350	-	.706	.770	.320	55	2.1
20%	350	50%	.618	.529		70	

This is in response to the polysilicon area diminishing by a factor of 2.1. For those gas mixtures containing CF_3Cl the lateral rate remains constant or even decreases to 80-90% of the original side etching.

6.3.4. Conclusions and discussion.

From the etch rate information we can conclude that the addition of CF_3Cl makes the plasma more effective in removing poly-silicon both normally and laterally. Also the addition of the chloro-carbon suppresses completely the loading effect during the over etch of the silicon layer. The chlorinated additions are not inhibited by transport to and from the surface as the fluorinated species. Also the chlorine atoms may be more efficient in removing carbon from the surface that also hinders the etching of poly-silicon. No re-entrant angles are evident from the profiles. Surface migration is not a dominant mechanism in the etching of poly-silicon for these amounts of chlorine atoms in the plasma.

The silicon nitride etches completely anisotropically. All aspects of the profiles are determined by the erosion of the masking layer. The photoresist erodes much more quickly in the chlorinated plasmas at high powers, in spite of the cooled substrate. Its erosion also shows a time dependence as evidenced by the foot at the bottom of the nitride lines. Also the selectivity between the poly-silicon and nitride increases with CF_3Cl additions. The more easily ionized Chlorine atoms are thus able to deposit more energy at the surface damaging the resist and removing the nitride more effectively.

The addition of chloro-carbons is effective in avoiding the accelerated etching during the over etch time, even under high etch rate conditions. However, they do not diminish the lateral etching of poly-silicon layers. The damaging of the photoresist makes it a bad choice for reproducibility at higher powers.

References

1. A.C. Adams and C.D. Capiro, "Edge profiles in plasma etching of polycrystalline silicon," *Journal of the Electrochemical Society*, vol. 128, no. 2, p. 366, (February 1981).
2. T.M. Mayer and J.H. McConville, "Line-width control in anisotropic plasma etching of polycrystalline Si," *IEDM Technical Digest*, p. 44, (December 1979).
3. C.B. Zarowin, "Plasma etch anisotropy - Theory and some verifying experiments relating ion transport, ion energy and etch profiles," *Journal of the Electrochemical Society*, vol. 130, no. 5, p. 1144, (May 1983).
4. L.B. Rothman, J.L. Mauer IV, G.C. Schwartz, and J.S. Logan, "Process for forming tapered vias in SiO₂ by reactive ion etching," in *Plasma Processing*, ed. R.G. Frieser & C.J. Mogab, Proceedings of the Symposium on Plasma Etching and Deposition, p. 193, The Electrochemical Society, (1981).
5. D.L. Flamm, D.N.K. Wang, and D. Maydan, "Multiple etchant loading effect in ClF₃ and related mixtures," *Journal of the Electrochemical Society*, vol. 129, no. 12, p. 2755, (December 1982).
6. C.J. Mogab, "The loading effect in plasma etching," *Journal of the Electrochemical Society*, p. 1262, (August 1977).
7. J.L. Vossen, "Glow discharge phenomena in plasma etching and plasma deposition," *Journal of the Electrochemical Society*, vol. 126, no. 2, p. 319, (February 1979).
8. K. Jinno and S. Inomata, *Study of plasma etching reactions and photoresist performance in CF₄-O₂ plasmas*, Translation provided by IPC, (1978).

9. W.G. Oldham, A.R. Neureuther, J.L. Reynolds, C.S. Sung, and S.N. Nandgaonkar, "A general simulator for VLSI lithography and etching processes: Part II application to deposition and etching." *IEEE-Transactions on Electron Devices*, vol. ED 27, no. 8, (August 1980).

CHAPTER SEVEN

7. FEASIBILITY OF A MACROSCOPIC PLASMA ETCHING MODEL Feasibility of a Macroscopic Plasma Etching Model

The purpose of a plasma etching model is to predict etched profiles from independent controllable laboratory conditions; that is, from switches and dials, and reproducing them with certainty. A universal model would serve as an instructive tool, as well as save time in developing and tailoring a dry etching process. The controls most desired to completely specify a process are: power, pressure, temperature, flow rate, etching gasses, etched materials, and reactor configuration. The initial work in dry etching introduced limits and trends depending on these conditions. For example, a barrel reactor configuration is expected to etch polycrystalline silicon isotropically. Early trends ran the continuum between this type of chemical process and physical sputtering. General ideas of chemical reactions and ion energy arise from gasses, power, and pressure. The types of profiles and reactor configurations increased far faster than the physical modeling. Plasma etching became an empirical science.

Working backwards, as the observed etching phenomena and profiles expanded, several mechanisms were introduced to explain them. Physics and chemistry were readily tied to these mechanisms. For example, silicon dioxide etches appreciably only in the presence of ion bombardment^{1, 1}. The etching chemistry is necessarily physically enhanced, therefore, there is little undercut where there is no ion bombardment in these systems. In the case of polysilicon etched in chlorinated gasses, a negative undercut profile develops². This is

attributed to migratory ions and reactive species at the interface. Damaged and doped materials etch more quickly in some gasses³ and these trends can be mapped onto the material properties. With the mechanisms linked to plausible physical situations, we are still left with the original question; "How are these physics related quantitatively to a limited number of laboratory controllables?"

The answer is "with great difficulty and in a stepwise manner. The reactors and gasses used in dry etching complicate the situation. The source gasses for the etching species introduce a large number of new and different components. Additives, such as hydrogen and oxygen⁴, which are used to facilitate etching, alter plasma properties⁵ along with rate enhancement.

This present work seeks to divide the problem into two components. The second one ties the etching mechanisms and physics to the plasma properties. The first predicts the plasma properties from the system parameters. The purpose is to make the second half of the model independent from the first half in order that all geometries and minutiae of the operating system need not be specified. The representation is not completely quantitative, but it aims toward that end, especially for a system similar to the one described in Appendix A.

The second block of the model is described first assuming we know certain plasma parameters. The etching rates likely depend on the plasma species in the general chemical form of a concentration multiplied by a reaction rate exponential and efficiency. This can be written for the isotropic, anisotropic and inhibiting rates as follows.

$$R_{anis} \propto \sum_{j=0}^J n_{ij} f_j \exp\left(-\frac{qV_0}{k_B T_0}\right) \exp\left(-\frac{E_{xj} - E_{ij}}{k_B T_0}\right) \quad (7.1)$$

$$R_{iso} \propto \sum_{k=0}^K n_k f_k \exp\left(-\frac{E_{xk} - E_{ik}}{k_B T_0}\right) \quad (7.2)$$

$$R_{inhib} \propto -\sum_{p=0}^P f_p n_p \quad (7.3)$$

\vec{R}_{anis} is necessarily a vector quantity to reckon the transport of the ions in the electric field. n_j is the density of ions of species j produced in the plasma. J is the total number of types of ionic species in the plasma, so $\sum_{j=0}^J n_j = n_0$. The term $\exp^{-\frac{qV_0}{k_B T_0}}$ represents the attenuation of the number of ions entering the sheath according to the Bohm sheath criteria^{6,7}. The value $qV_0 = \frac{1}{2}k_B T_0$ works theoretically and experimentally for the rf plasmas used in etching. The unit vector, \hat{r}_j contains the ion direction information from both the electric field and scatter in the sheath. The chemical reaction term, $\exp^{-\frac{E_{xj} - E_{ij}}{k_B T_0}}$, is common to both the isotropic and anisotropic terms. E_{xk} represents the activation energy of material x with species k . This contains the Arrhenius behavior with the substrate temperature, T_0 , making it important to know the dependence of this temperature on the conditions also. The ion energy of species j reduces the activation energy to remove material by an amount E_{ij} in the bombarded regions. This reduction would disappear in unexposed regions. n_k is the concentration of neutral etching species k in the plasma and f_k , the transport efficiency to the surface. f_k encapsulates much information pertinent to transport and therefore contains the loading effect and residence time characteristics. Again a summation over the K different species is used for generality. The inhibitor rate R_{inhib} subtracts from the above two etch rates. For simplicity it is modeled as a group of polymer precursors, n_p , generated in the plasma multiplied by their delivery efficiency f_p which would depend on transport properties and residence times. Note that all these rates are proportionalities with constants dependent on the reactor geometries that would be characterized in the first stage of the model.

The plasma characteristics that are investigated to give insight into these parameters for the Plasma Therm PK-12 system are the dc bias, the plasma impedance, and the relative intensity (δn_F) of the 703.7 nm F emission line. From an analysis of the plasma impedance, an equivalent circuit can be hypothesized and the values and trends of these components tell of the properties of the charged particles, n_i and n_e . The values of sheath components suggest that properties of the charged species in the sheath. a large sheath conductance indicates a large directed ion flux compared to the thermal flux. This observation concludes that the ionic component of etching is well collimated and directed and that \vec{r}_j is normal to the surface. The constancy of the sheath capacitance allows us to neglect ionization and ion scatter in the sheath and the types of profiles that would be associated with that, also. The addition of oxygen affects this directed etching. For carbon tetrafluoride alone the electron flux has a large energy distribution. Adding oxygen peaks this distribution as shown in Figure 7.18 . The resistance of the plasma body itself helps to estimate the density of charged particles n_e and their thermal velocity (thus T_e) generated in the plasma. A large resistance implies a larger voltage across the plasma and also a more collisional, less reactive plasma. The more charged particles generated and entering the sheath produce a large directional etch rate. The dc bias is representative of the voltage across the sheath if the electron temperature is assumed constant. The energy of the ions traversing the sheath are affected by its magnitude and the anisotropic component reflects this increase through the parameter E_i . As the dc bias diminishes, the ions in the sheath become mobility-limited and E_i decreases.

The characteristics mentioned thus far are electrical and physical components and give no insight into the isotropic component that dominates the fluorine etching of silicon. Free fluorine atoms are claimed responsible for the

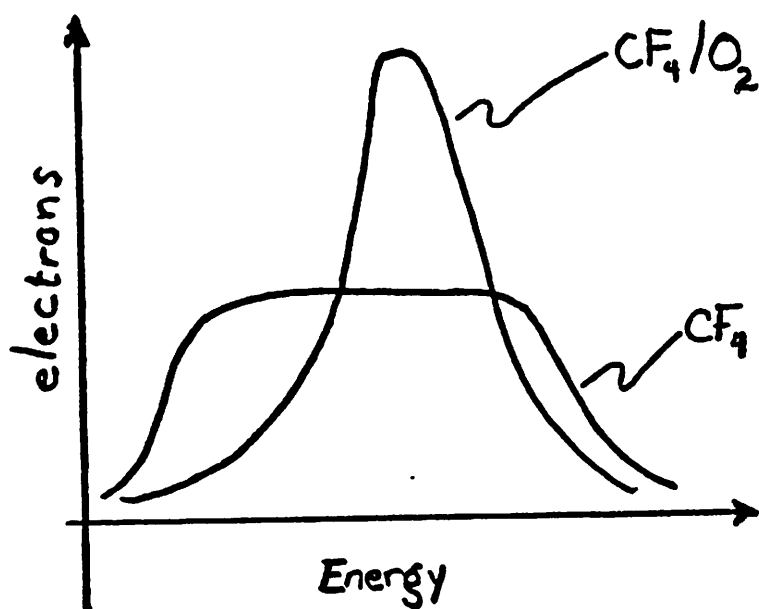


Figure 7.1
Energy distributions for electrons in CF_4 plasma and CF_4 plasma with oxygen addition.⁶

spontaneous and isotropic etching of silicon, so with the ability to monitor their relative concentration we can say something about the chemical component of etching. (This is not to say that free fluorine is the only isotropic etch species in dry etching, but it dominates the process in freon gasses.) First, the intensity of the plasma is a good indication of the power efficiency of the plasma, as well as its resistivity.

Sulfur hexafluoride has the largest rates and most characteristically isotropic etched profiles, coupled with a very high relative density (δn_F) of fluorine evolved in the plasma. The large rate makes this the most reproducible etchant as it overshadows all secondary competing effects. It shows a strong loading effect and, although the total rate does not depend on the flow rate, the isotropic portion does, showing profiles dependent on a residence time. All components of etching increase with the amount of fluorine generated, but not in a straight forward fashion, which suggests dependence on additional terms in the summation. In the anisotropic rate equation, the density of ions, n_i has a more pronounced affect than E_i in the SF_6 plasma. The voltage across the sheath also points to this independence of E_i also.

Carbon tetrafluoride mixed with oxygen generates a lesser amount of fluorine and proportionally less etching than SF_6 and oxygen. In this gas, isotropic etching demonstrates a direct dependence on the amount of fluorine present. Residence time only affects etching when it is extremely long and polymer formation on the surface becomes a consideration. The consistency of the impedance model and direct relations to profiles suggest that the CF_4 plasma process is easily qualitatively modeled. Hexafluoroethane produces a relatively small amount of fluorine and shows even less etching than for the same density of F in other gasses. There is no isotropic (or non-ion-assisted) etching until there is a sufficient amount of fluorine present. The fluorine and ion

bombardment, R_{iso} and R_{aniso} , compete with polymer formation R_{inhib} . Under conditions of few fluorine and high polymer formation, that is with long residence times, the etching process completely halts. With large amounts of fluorine, etching will even proceed without ion bombardment, that is $R_{iso} \gg R_{inhib}$. In many ways it is possible to characterize etching processes in terms of emission spectra and impedance models. For C_2F_6 a quantitative method measuring the surface inhibitors produced by the plasma is needed. A segregated anisotropic etching component depends linearly on the dc bias for other constant surface conditions.

Turning to the system dependence, these plasma properties are much more easily related to the laboratory parameters for a planar system. The plasma resistance of the equivalent circuit model is the most telling for the three different gas systems. It increases with pressure due to collisions above a certain break-point pressure. This break-point pressure depends on the number of carriers in the plasma, which vary strongly with the gasses used. Compared with argon, the fluorine-based gasses become collisional at a very low pressure. At that point, a larger voltage is dropped across the plasma, which in turn diminishes the potential drop across the sheath. SF_6 and oxygen demonstrate the most resistive plasma and the least number density of electrons.

The resistance of the plasma indicates there are about 10^{11} electrons and ions existing in the plasma, increasing by a factor of six when quadrupling the power. The electron temperature appears to be constant. About fifty percent of this ion density enters the sheath to completely cross it and hit the substrate estimating the parameter V_0 at approximately $\frac{1}{2}T_e$. The sheath circuit elements remain fairly constant for the three etch gasses. Argon's sheath capacitance is half as large and conductance twice as large for its smaller sheath due to the mass difference between the ionic species. The consistency of the sheath

plasma produces. The present models deal only in the extremes where only the first one or two of the components dominate. For example, in chlorine-based etching, where ionized species initiate the etching and the chemistry is constant, a physical model tracking the ion distribution will do. Add a complex chemistry with ions plus neutrals and then there must be more characteristics of the plasma observed to isolate the added features.

This research has successfully added two useful tools toward the complex characterization of silicon etching in fluorinated plasmas. These tools may find equal use in other operating systems. They help to bridge the information needed between etching profiles and laboratory controllables and shorten the time in developing a predictable plasma etching process for a general operating configuration.

capacitance allows us not to consider scattering and ionization in the sheath.

The dc sheath self-bias decreases substantially with pressure as the sheath path for ions becomes more mobility-limited. This potential and E_i depend linearly on the square root of the rf power when the plasma is not collisional, that is at high powers and low pressures.

For all the fluorine-based gasses that we investigated, the relative fluorine density (δn_F) increases linearly with pressure. At high pressures, when the plasma is dominated by collisions, the fluorine density saturates. Sulfur hexafluoride acts as the best source for reactive fluorine species and shows a strong power dependence. It liberates free fluorine much more effectively at higher powers. Carbon tetrafluoride does not show the same strong dependence with power for a given pressure. The direct linear dependence of etch rate on power follows from this fact. Presumably, CF_4 breaks into CF_3 and F easily, but further breakup is less favorable. C_2F_6 produces few fluorine atoms, but this amount exhibits a relatively strong power dependence.

The temperature, T_0 , at the wafer surface plays a significant role in the etching components. In this research it was neither measured or controlled. Only the electrode temperature was controlled. Calculating a temperature from a rate and an activation energy⁹ shows T_0 to be $\approx 180^\circ C$, 100° greater than the electrode temperature at 400 Watts. The temperature plays an important role since its variation can mask changes in the energies, E_s and E_i .

The models presented here show a semi-quantitative characterization of plasma etching on electrical distribution and fluorine optical emission. As more quantitative measures for the plasma itself are discovered, and as the parameters that affect the etching are better controlled, the characterization of plasma etching will converge on a universal consistent view. It is necessary to find a criteria for the amounts of etching, non-reactive and inhibiting species that the

References

1. H.F. Winters and J.W. Coburn, "The etching of silicon with XeF₂ vapor," *Applied Physics Letters*, vol. 34, no. 1, p. 70, (January 1979).
2. A.C. Adams and C.D. Capio, "Edge profiles in plasma etching of polycrystalline silicon," *Journal of the Electrochemical Society*, vol. 128, no. 2, p. 366, (February 1981).
3. J.L. Reynolds, A.R. Neureuther, and W.G. Oldham, "Simulation of dry-etched line-edge profiles," *Journal of Vacuum Science and Technology*, vol. 18, no. 6, (November/December 1979).
4. M.J. Kushner, "A kinetic study of the plasma etching process: I. A model for etching Si and SiO₂ in C₆F₆/H₂ and C₆F₆/O₂ plasmas," *Journal of Applied Physics*, vol. 53, no. 4, p. 2923, (April 1982).
5. Ch. Steinbruechel, "Langmuir probe measurements on CHF₃ and CF₄ plasmas: The role of ions in the reactive sputter etching of SiO₂ and Si," *Journal of the Electrochemical Society*, vol. 130, no. 3, p. 648, (March 1983).
6. Brian Chapman, in *Glow discharge processes - - sputtering and plasma deposition*, Wiley-Interscience, (1980).
7. S.C. Brown, *Introduction to Electrical Discharges in Gases*, Wiley, (1966).
8. J.W. Coburn, H.F. Winters, and T.J. Chuang, "Ion-surface interactions in plasma etching," *Journal of Applied Physics*, vol. 48, no. 8, p. 3532, (August 1977).
9. D.L. Flamm, C.J. Mogab, and R. Sklaver, "The reaction of fluorine atoms with silicon," *Journal of Applied Physics*, vol. 50, p. 624, (February 1979).

BIBLIOGRAPHY

- Adams, A.C. and C.D. Capiro, "Edge profiles in plasma etching of polycrystalline silicon," *Journal of the Electrochemical Society*, vol. 128, no. 2, p. 366, (February 1981).
- Arikado, T. and S. Horiuchi, "Etching mechanism of SiO₂ in CF₄/H₂ mixed gas plasma," in *Plasma Processing*, ed. R.G. Frieser & C.J. Mogab, *Proceedings of the Symposium on Plasma Etching and Deposition*, p. 66, The Electrochemical Society, (1981).
- Barber, D.J., F.C. Frank, M. Moss, J.W. Steeds, and I.S.T. Tsong, "Prediction of ion-bombarded surface topographies using Frank's kinematic theory of crystal dissolution," *Journal of Material Science*, vol. 8, p. 1030, (1973).
- Baron and Zelez, "Vacuum systems for plasma etching, deposition, and CVD," *Solid State Technology*, p. 61, (December 1978).
- Batchelder, T., "Simple Metal Lift-Off Process for 1 Micron AL/5% Cu Lines," *Solid State Technology*, vol. 25, no. 2, p. 111, (February, 1982).
- Batley, J.F., "The effects of geometry on diffusion controlled chemical reaction rates in a plasma," *Journal of the Electrochemical Society*, vol. 124, no. 3, p. 437, (March 1977).
- Bayly, A.R., "Secondary processes in the evolution of sputtering topographies," *Journal of Material Science*, vol. 7, p. 404, (1972).
- Beinvogl, W., H.R. Deppe, R. Stokan, and B. Hasler, "Plasma etching of polysilicon and silicon nitride in SF₆ with some impacts on MOS device characteristics," *IEEE-Transactions on Electron Devices*, vol. ED 28, no. 11, p. 1332, (November 1981).
- Bergendahl, A.S., S.F. Bergeron, and D.L. Harmon, "Optimization of plasma processing for silicon gate FET manufacturing applications," *IBM Journal of Research Development*, vol. 26, no. 5, p. 580, (September 1982).
- Bersin, R.L., "A survey of plasma etching processes," *Solid State Technology*, vol. 19, no. 5, p. 31, (May 1976).
- Bersin, R.L., "Chemically selective, anisotropic plasma etching," *Solid State Technology*, vol. 21, no. 3, p. 117, (April 1978).
- Blech, I.A., "Evaporated Film Profiles Over Steps in Substrates," *Thin Solid Films*, vol. 6, p. 113, (1970).
- Blech, I.A., D.B. Fraser, and S.E. Hasyko, "Optimization of Al Step Coverage Through Computer Simulation and Scanning Electron Microscopy," *Journal of Vacuum Science and Technology*, vol. 15, no. 1, p. 13019, (1978).
- Bollinger, L.D., "Ion milling for semiconductor production processes," *Solid State Technology*, vol. 20, no. 11, p. 66, (November 1977).
- Bondur, J.A., "Dry process technology," *Journal of Vacuum Science and Technology*, vol. 13, no. 5, p. 1023, (May 1976).
- Bondur, J.A. and H.A. Clark, "Plasma etching of SiO₂ profile for profile control," *Solid State Technology*, vol. 23, no. 4, p. 122, (April 1980).
- Bondur, J.A. and R.G. Frieser, "Shaping of profiles in SiO₂ by plasma etching," in *Plasma Processing*, ed. R.G. Frieser & C.J. Mogab, *Proceedings of the Symposium on Plasma Etching and Deposition*, p. 180, The Electrochemical Society, (1981).

- Boyd, H. and M. Tang, "Applications of SiF₄ in plasma etching," *Solid State Technology*, vol. 22, no. 4, p. 133, (April 1979).
- Bresnock, F.J. Consequences and control of the plasma space potential in etching tools diagnostics, M. Aktik, Y. Segui, and B. Ai, "Growth of polymer films on compound semiconductors and dry etching process." *Journal of Applied Physics*, vol. 50, no. 10, p. 8567, The Electrochemical Society, (October 1979).
- Brown, S.C., *Basic Data of Plasma Physics*, MIT press, (1959).
- Brown, S.C., *Introduction to Electrical Discharges in Gases*, Wiley, (1966).
- Bruce, R.H., "Frequency dependence of CCl₄ etching," in *Plasma Processing*, ed. R.G. Frieser & C.J. Mogab, *Proceedings of the Symposium on Plasma Etching and Deposition*, p. 243, The Electrochemical Society, (1981).
- Bruce, R.H., "Ion response to plasma excitation frequency," *Journal of Applied Physics*, vol. 52, no. 12, p. 7064, (December 1981).
- Bruce, R.H., "Anisotropy control in dry etching," *Solid State Technology*, p. 64, (October 1981).
- Bruce, R.H. and G.P. Malafsky, "High rate anisotropic aluminum etching," *Journal of the Electrochemical Society*, vol. 130, no. 6, p. 1359, (June 1983).
- Bruno, G., P. Capezzuto, F. Cramarossa, and R. d'Agostino, "Analysis of decomposition and oxidation of SF₆ under rf plasma quartz and alumina reactors," in *Plasma Processing*, ed. R.G. Frieser & C.J. Mogab, *Proceedings of the Symposium on Plasma Etching and Deposition*, p. 203, The Electrochemical Society, (1981).
- Butler, H.S. and G.S. Kino, "Plasma sheath formation by radio-frequency fields," *The Physics of Fluids*, vol. 6, no. 9, p. 1346, (September 1963).
- Cantagrel, M., "Considerations on high resolution patterns engraved by ion etching," *IEEE-Transactions on Electron Devices*, vol. ED 22, no. 7, p. 483, (July 1975).
- Carter, G., J.S. Colligon, and M.J. Nobes, "The growth of topography during sputtering of amorphous solids -IV. A generalized theory," *Journal of Material Science*, vol. 8, p. 1473, (1973).
- Carter, G., J.S. Colligon, and M.J. Nobes, "Analytical model of sputter induced surface morphology," *Radiation Effects*, vol. 31, p. 65, (1977).
- Chapman, Brian, in *Glow discharge processes - - sputtering and plasma deposition*, Wiley-Interscience, (1980).
- Chen, Frances F., *Introduction to Plasma Physics*, Plenum Press, New York, (1974).
- Chinn, J.D., I. Adesida, E.D. Wolf, and R.C. Tiberio, "Reactive ion etching for sub-micron structures," *Journal of Vacuum Science and Technology*, vol. 19, no. 4, p. 1418, (November/December 1981).
- Chung, S., "Determining a plasma etch cycle," *Solid State Technology*, vol. 20, no. 4, p. 114, (April 1978).
- Cobine, J.D., *Gaseous Conductors*, Dover, (1941).
- Coburn, J.W. and E. Kay, "Some chemical aspects of the fluorocarbon plasma etching of silicon and its compounds," *IBM Journal of Research and Development*, vol. 23, no. 1, p. 33, (January 1979).

- Coburn, J.W. and M.Chen, "Optical emission spectroscopy of reactive plasmas: a method for correlating emission intensities to reactive particle density." *Journal of Applied Physics*, vol. 51, no. 6, p. 3134, (June 1980).
- Coburn, J.W. and H.F. Winters, "Plasma etching - a discussion of mechanisms," *Journal of Vacuum Science and Technology*, vol. 16, no. 2, (March/April 1979).
- Coburn, J.W., H.F. Winters, and T.J. Chuang, "Ion-surface interactions in plasma etching," *Journal of Applied Physics*, vol. 48, no. 8, p. 3532, (August 1977).
- Crawford, F.W., "Modulated Langmuir probe characteristics," *Journal of Applied Physics*, vol. 34, no. 7, p. 1897, (July 1963).
- Crockett, A.R. and M.M. Stark, *Single wafer, in line plasma etching of silicon dioxide*. Andy, 1981
- Danner, D.A., D.L. Flamm, and J.A. Mucha, "Downstream Atomic Monitoring for absolute etch-rate determination," *Journal of the Electrochemical Society*, vol. 130, no. 4, p. 905, (April 1983).
- Doane, Daryl Ann, David B. Fraser, and Dennis W. Hess, "Semiconductor Technology," in *Proceeding of the Tutorial Symposium; Electrochemical Society*, vol. 82-5, (1982).
- Doken, M. and I. Miyata, "Etching uniformities of silicon in CF₄/4%O₂ plasma," *Journal of the Electrochemical Society*, vol. 120, no. 12, p. 2235, (December 1978).
- Donnelly, V.M., D.L. Flamm, and J.A. Mucha, "Optical emission from transient species in halocarbon and fluorosilicon plasmas," in *Plasma Processing*, ed. R.G. Frieser & C.J. Mogab, *Proceedings of the Symposium on Plasma Etching and Deposition*, p. 270, The Electrochemical Society, (1981).
- Ducommun, J.P., "Evolution of well defined surface contours," *Journal of Material Science*, vol. 10, p. 52, (1975).
- Egitto, F.D., D.N.K. Wang, and D. Maydan, "Ion-assisted plasma etching of silicon oxides in a multifacet system," *Solid State Technology*, p. 71, (December 1981).
- Eisele, K.M., "Plasma etching of silicon with nitrogen trifluoride," in *Plasma Processing*, ed. R.G. Frieser & C.J. Mogab, *Proceedings of the Symposium on Plasma Etching and Deposition*, p. 166, The Electrochemical Society, (1981).
- Ephrath, L.M., "The effect of cathode materials on reactive ion etching of silicon and silicon dioxide in a CF₄ plasma," *Journal of Electronic Materials*, vol. 7, no. 3, p. 415, (1978).
- Ephrath, L.M., "Selective etching of SiO₂ using reactive ion etching with CF₄-H₂," *Journal of the Electrochemical Society*, vol. 126, no. 8, p. 1419, (August 1979).
- Ephrath, L.M., "Reactive ion etching for VLSI," *IEEE-Transactions on Electron Devices*, vol. ED 28, no. 11, p. 1315, (November 1981).
- Ephrath, L.M. and E.J. Petrillo, "Parameter and reactor dependence of selective oxide RIE in CF₄+H₂," *Journal of the Electrochemical Society*, vol. 129, no. 10, p. 2282, (October 1982).
- Flamm, D.L., "Mechanisms of etchant production and the role of oxidants in CF₃Cl, CF₃Br and related plasma etching gasses," in *Plasma Processing*, ed. R.G. Frieser & C.J. Mogab, *Proceedings of the Symposium on Plasma Etching and Deposition*, p. 55, The Electrochemical Society, (1981).

- Flamm, D.L., "Measurements and mechanisms of etchant production during the plasma oxidation of CF₄ and C₂F₆," *Solid State Technology*, vol. 22, no. 4, p. 109, (April 1979).
- Flamm, D.L., "Mechanisms of radical production in rf discharges of CF₃Cl, CF₃BR, and certain other etchants: spectrum of transient species," *Journal of Applied Physics*, vol. 51, no. 11, p. 5688, (November 1980).
- Flamm, D.L. and V.M. Donnelly, "The design of plasma etchants," *Plasma Chemistry and Plasma processing*, vol. 1, no. 4, p. 317, (1981).
- Flamm, D.L., C.J. Mogab, and R. Sklaver, "The reaction of fluorine atoms with silicon," *Journal of Applied Physics*, vol. 50, p. 824, (February 1979).
- Flamm, D.L., D.N.K. Wang, and D. Maydan, "Multiple etchant loading effect in ClF₃ and related mixtures," *Journal of the Electrochemical Society*, vol. 129, no. 12, p. 2755, (December 1982).
- Foxe, T.T., B.D. Hunt, C. Rogers, A.W. Kleinsasser, and R.A. Buhrman, "Reactive ion etching of niobium," *Journal of Vacuum Science and Technology*, vol. 19, no. 4, p. 1394, (November/December 1981).
- Frieser, R.G. and J. Nogay, "Optical spectroscopy applied to the study of plasma etching," *Applied Spectroscopy*, vol. 34, no. 1, p. 31, (1980).
- Geis, M.W., G.A. Lincoln, N. Efremow, and W.J. Piacentini, "A novel anisotropic dry etch technique," *Journal of Vacuum Science and Technology*, vol. 19, no. 4, p. 1390, (November/December 1981).
- Gerlach, *Surface Science*, (1981).
- Gloersen, Per G., "Ion beam etching," *Journal of Vacuum Science and Technology*, vol. 12, no. 1, p. 28, (January/February 1975).
- Godyak, V.A., "Steady state, low pressure rf discharge," *Soviet Journal of Plasma Physics*, vol. 2, no. 1, p. 78, (January/February 1976).
- Hamasaki, M., "On an analytical solution for two-dimensional diffusion of silicon self-interstitials during oxidation of silicon," *Solid State Technology*, (1981).
- Harper, J.M.E., J.J. Cuomo, P.A. Leary, and G.M. Summa, "Low energy ion beam etching," in *Proceedings on the Symposium on Electron and Ion Beam Technology*, ed. Robert Bakish, vol. 80-6, p. 518, Journal of the Electrochemical Society.
- Harshbarger, W.R., "Analysis of N₂ plasma to characterize plasma etching systems," *Solid State Technology*, vol. 25, no. 4, p. 126, (April 1982).
- Harshbarger, W.R. and R.A. Porter, "A study of optical emission from a rf plasma during etching," *Applied spectroscopy (also Bell Laboratories Technical Journal)*, vol. 31, p. 201, (1977).
- Harshbarger, W.R. and R.A. Porter, "Spectroscopic analysis of RF plasmas," *Solid State Technology*, p. 99, (April 1978).
- Harshbarger, W.R., R.A. Porter, and P. Norton, "Optical detector to monitor plasma etching," *Journal of Electronic Materials*, vol. 7, no. 3, p. 429, (1978).
- Heath, B.A., "Etching SiO₂ in a reactive ion beam," *Solid State Technology*, p. 75, (October 1981).
- Heinecke, R., "Plasma reactor design for selective etching of SiO₂ on Si," *Solid State Technology*, vol. 19, p. 1039, (1976).
- Herb, G.K., R.E. Caffrey, E.T. Eckroth, and Q.T. Jarrett, "Plasma processing: Some safety, health and engineering considerations," *Solid State Technology XV 26*, no. 8, p. 185, (August 1983).

- Hirata, K., Y. Ozaki, M. Oda, and M. Kimizuka, "Dry etching technology for 1um VLSI fabrication," *IEDM*, p. 405, (December 1980).
- Hiroaka, H. and L.W. Welsh, "Negative fluorine ions in plasma etchings," in *Plasma Processing*, ed. R.G. Frieser & C.J. Mogab, *Proceedings of the Symposium on Plasma Etching and Deposition*, p. 59, The Electrochemical Society, (1981).
- Hollahan, R. and A. Bell, "Semiconductor device fabrication," in *Applications in Plasma Chemistry*, Wiley, (1974).
- Homma, Y., A. Yajima, and S. Harada,, "Feature Size Limit Analysis of Lift-Off Metallization Technology," in *1981 IEDM Technical Digest*, p. 570, (December 1981).
- Horiki, Y., M. Shibagaki, and K. Kadono, "Silicon and silicon dioxide etching characteristics by fluorocarbon ion beam," *Journal of Applied Physics*, vol. 18, no. 12, p. 2309, (1979).
- Hudson, W.R., "Ion beam texturing," *Journal of Vacuum Science and Technology*, vol. 14, no. 1, p. 286, (1977).
- Hunter, W.R., T.C. Holloway, P.K. Chatterjee, and A.F. Tasch, "New edge-defined vertical etch approaches for submicrometer MOSSFET fabrication," *IEDM*, p. 764, (December 1980).
- Ianno, N.J. and J.T. Verdeyen, "Comparison of the etching and plasma characteristics of discharges in CF₄ and NF₃," in *Plasma Processing*, ed. R.G. Frieser & C.J. Mogab, *Proceedings of the Symposium on Plasma Etching and Deposition*, p. 155, The Electrochemical Society, (1981).
- Jinno, K. and S. Inomata, *Study of plasma etching reactions and photo-resist performance in CF₄-O₂ plasmas*, Translation provided by IPC, (1978).
- Jones, A.B. and G.S. Plonski,, "Ion Milling of Thin Films for Magnetic Bubble Circuits," in *Electrochemical Society extended abstracts*, (San Francisco, 1974).
- K.Lee, Y.Sakai, and A.R.Neureuther, *Topography dependent step coverage resistance for VLSI design*, 1982 Symposium on VLSI Technology. (September 1982, Oiso, Japan).
- Kammerdiner, L., "Aluminum plasma etch considerations for VLSI production," *Solid State Technology*, p. 79, (October 1981).
- Kawata, H., "The relation between etch rate and optical emission intensity in plasma etching," *Journal of the Electrochemical Society*, vol. 129, no. 6, p. 1325, (June 1982).
- Keller, J.H. and W.B. Pennebaker, "Electrical properties of sputtering systems," *IBM Journal of Research and Development*, vol. 23, no. 1, p. 3, (January 1979).
- Keller, J.H. and R.G. Simmons, "Sputtering process model of deposition rate," *IBM Journal of Research and Development*, vol. 23, no. 1, p. 24, (January 1979).
- Kern, D.P. and C.B. Zarowin, "Computer simulation of etch front propagation," in *Plasma Processing*, ed. R.G. Frieser & C.J. Mogab, *Proceedings of the Symposium on Plasma Etching and Deposition*, p. 86, The Electrochemical Society, (1981).
- Kinoshita, H., "Anisotropic etching of Si by a gas plasma," *Journal of Applied Physics*, vol. 18, no. 2, p. 381, (1977).

- Klinger, R.E. and J.E. Green, "Glow discharge optical spectroscopy of the reactive ion etching of Si," in *Plasma Processing*, ed. R.G. Frieser & C.J. Mogab, *Proceedings of the Symposium on Plasma Etching and Deposition*, p. 257, The Electrochemical Society, (1981).
- Koenig, H.R. and L.I. Maisel, "Application of rf discharges to sputtering," *IBM Journal of Research and Development*, vol. 14, no. 3, p. 163, (March 1970).
- Komiya, H. and H. Toyoda, "Analysis of line width and undercutting during plasma etching of Si₃N₄," *7th conference on Solid State Devices*, (September 1-12, 1975).
- Kumar, R., C. Ladas, and G. Hudson, "Characterization of plasma etching for semiconductor applications," *Solid State Technology*, p. 54, (October 1976).
- Kunkel, Wulf B., *Plasma physics in theory and application*, McGraw-Hill, (1966).
- Kunkel, Wulf, *142A notes, Introduction to plasma physics*, UC Berkeley course, (Winter 1980).
- Kushner, M.J., "A kinetic study of the plasma etching process: I. A model for etching Si and SiO₂ in CnFm/H₂ and CnFm/O₂ plasmas," *Journal of Applied Physics*, vol. 53, no. 4, p. 2923, (April 1982).
- Kushner, M.J., "A kinetic study of the plasma etching process: II. Electrical properties in an rf plasma reactor," *Journal of Applied Physics*, vol. 53, no. 4, p. 2939, (April 1982).
- Lechaton, J.S. and J.L. Mauer, "A model for the etching of silicon in a Chlorine/Argon plasma," in *Plasma Processing*, ed. R.G. Frieser & C.J. Mogab, *Proceedings of the Symposium on Plasma Etching and Deposition*, p. 75, The Electrochemical Society, (1981).
- LeClare, R., "Advances in planar plasma etching equipment," *Solid State Technology*, vol. 22, no. 4, p. 139, (April 1979).
- Lee, R.E., "Microfabrication by ion-beam etching," *Journal of Vacuum Science and Technology*, vol. 16, no. 2, p. 164, (March/April 1979).
- Lehmann, H.W., E. Heeb, and K. Frick, "Plasma diagnosis by time resolved mass spectrometry," *Solid State Technology*, p. 69, (October 1981).
- Lehmann, H.W., Krausbauer, and R. Widmer, "Redeposition - a serious problem.," *Journal of Vacuum Science and Technology*, vol. 14, no. 1, p. 281, (1977).
- Lehmann, H.W. and R. Widmer, "Profile control by reactive sputter etching.," *Journal of Vacuum Science and Technology*, vol. 15, no. 2, (March/April 1978).
- Light, R.W. and H.B. Bell, "Profile control of poly-silicon lines with SF₆/O₂ plasma etch process," *Journal of the Electrochemical Society*, vol. 130, no. 7, p. 1567, (July 1983).
- Light, R.W., H.B. Bell, and H. Macro, "Plasma etching techniques for polysilicon, SiO₂, and Al/Si," *Proceedings of the Electrochemical Society*, no. Abstract no. 169, (May 1983, San Francisco).
- Lin, Jung, "Via etch in metallization," *Internal Technical Report 82-6*, Integrated Circuit Processing Laboratory, Hewlett Packard, (December 1982).
- MacCracken, G.M., "The behaviour of surfaces under ion bombardment," *Rep. Prog. Phys.*, vol. 38, p. 241, (1975).
- Maddox and Parker, "Application of reactive plasma to practical microelectric processing systems," *Solid State Technology*, p. 107, (April 1978).

- Mader, H., "Anisotropic plasma etching of polysilicon with CF₄," in *Plasma Processing*, ed. R.G. Frieser & C.J. Mogab, *Proceedings of the Symposium on Plasma Etching and Deposition*, p. 125, The Electrochemical Society, (1981).
- Mader, L. and J. Hoefner, "Ion beam etching of silicon dioxide on silicon," *Journal of the Electrochemical Society*, vol. 123, no. 12, p. 1893, (December 1976).
- Maria, D.J., L.M. Ephrath, and D.R. Young, "Radiation damage in SiO₂ films exposed to reactive ion etching," *Journal of Applied Physics*, vol. 50, no. 6, p. 4015, (1979).
- Matsuo, S., "Preferential SiO₂ etching on Si substrate by reactive sputter etching," *Journal of Applied Physics*, vol. 16, no. 1, p. 175, (1977).
- Matsuo, S., "Etching characteristics of various materials by plasma reactive sputter etching," *Journal of Applied Physics*, vol. 17, no. 1, p. 175, (1978).
- Matsuo, S., "Selective etching of SiO₂ relative to Si by plasma reactive etching," *Journal of Vacuum Science and Technology*, vol. 17, no. 2, p. 587, (1980).
- Matsuo, S., "Selective etching of Si relative to SiO₂ without undercutting by CBrF₃ plasma," *Applied Physics Letters*, vol. 36, no. 9, p. 768, (May 1980).
- Matsuo, S. and Y. Adachi, "Reactive ion beam etching using a broad beam ECR ion source," *Journal of Applied Physics*, vol. 21, no. 1, p. L4, (January 1982).
- Mayer, T.M. and R.A. Barker, "Reaction ion beam etching with CF₄: Characterization of a Kaufman ion source and details of SiO₂ etching," *Journal of the Electrochemical Society*, vol. 129, no. 3, p. 585, (March 1982).
- Mayer, T.M. and J.H. McConville, "Line-width control in anisotropic plasma etching of polycrystalline Si," *IEDM Technical Digest*, p. 44, (December 1979).
- Meliar-Smith, C.M., "Ion etching for pattern delineation," *Journal of Vacuum Science and Technology*, vol. 12, no. 5, p. 1008, (September/October 1976).
- Meliar-Smith, C.M. and C.J. Mogab, "Plasma assisted etching techniques for pattern delineation," in *Thin film processes*, ed. Vossen, Academic Press, (1978).
- Minkiewicz, J., M. Chen, J.W. Coburn, B.N. Chapman, and K. Lee, "Magnetic field control of reactive plasma etching," *Journal of Applied Physics*, vol. 35, no. 5, p. 393, (September 1, 1979).
- Mogab, C.J., "The loading effect in plasma etching," *Journal of the Electrochemical Society*, p. 1282, (August 1977).
- Mogab, C.J. and W.R. Harshbarger, "Plasma processes set to etch finer lines with less undercutting," *Electronics*, vol. 115, p. 117, (August 31, 1978).
- Mogab, C.J. and H.J. Levinstein, "Anisotropic plasma etching of polysilicon," *Journal of Vacuum Science and Technology*, vol. 17, no. 3, p. 721, (May/June 1980).
- Morgan, R.A., "The rf voltage/current characteristics and related dc negative bias properties of an Electrotech flat bed plasma etcher," *Journal of Vacuum Science and Technology*, vol. 32, no. 5, p. 297, (1952).
- Mullins, C. and Single wafer plasma etching - 2. SiO₂ etching mechanisms and characteristics, *Solid State Technology*, p. 89, (August 1952).
- Mundt, R., K.C. Patel, and K. Cowen, "Etch uniformity in a CCl₄ plasma aluminum etch," *IEDM Technical Digest*, p. 409, (December 1980).

- N.Rovedo., in *Master's Report, University of California.*, Electronics Research Laboratory, Berkeley, (1979).
- Nagel, L.W., "SPICE2: A computer program to simulate semiconductor circuits," *ERL Memo*, no. ERL M520, Electronics Research Laboratory, University of California, Berkeley, May 1975.
- Nandgaonkar, S.N., "Design of a simulator program (SAMPLE) for IC fabrication," *Master's report*, Electronics Research Laboratory, Univ of California, Berkeley, CA 94720, (June 19, 1978).
- Nerstroem, H., R. Olaison, S. Berg, and L.P. Anderson, "Application of the Langmuir probe in sputter techniques," *Journal of the Electrochemical Society*, vol. 127, no. 12, (December 1980).
- Neureuther, A.R., "Simulating VLSI wafer technology," *IEDM Technical Digest*, p. 214, (December 1980).
- Neureuther, A.R., C.H. Ting, and C.Y.Liu, "Application of line-edge profile simulation to thin film deposition processes," *IEEE-Transactions on Electron Devices*, vol. ED-27, no. 8, p. 1449, (August 1980).
- Nishizawa, J. and N. Hayasaka In situ observation in Si plasma etching diagnostics, gasses: CF₄ C₂F₆, in *Plasma Processing*, ed. R.G. Frieser & C.J. Mogab, *Proceedings of the Symposium on Plasma Etching and Deposition*, p. 278, The Electrochemical Society, (1981).
- O'Toole, M.M., "Simulation of optically formed image profiles in positive resist," *PhD thesis*, Electronics Research Laboratory, Univ of California, Berkeley, CA 94720.
- Ogura, S., P.T. Tsang, W.W. Walker, D.L. Critchlow, and J.F. Shepard, "Elimination of Hot Electron Gate Current by the Lightly Doped Drain-Source Structure," in *1981 IEDM Technical Digest*, December 1981.
- Okano, H. and Y. Horike, "The angular dependence for sputtering yield with reactive ion beam," in *Plasma Processing*, ed. R.G. Frieser & C.J. Mogab, *Proceedings of the Symposium on Plasma Etching and Deposition*, p. 199, The Electrochemical Society, (1981).
- Oldham, W.G., S.N. Nandgaonkar, A.R. Neureuther, and M.M. O'Toole, "A general simulator for VLSI lithography and etching processes: Part I application to photolithography," *IEEE-Transactions on Electron Devices*, vol. ED 26, no. 4, (April 1979).
- Oldham, W.G., A.R. Neureuther, J.L. Reynolds, C.S. Sung, and S.N. Nandgaonkar, "A general simulator for VLSI lithography and etching processes: Part II application to deposition and etching," *IEEE-Transactions on Electron Devices*, vol. ED 27, no. 8, (August 1980).
- Oni, H. and H. Tango, "A new technology for tapered windows in insulating films," *Journal of the Electrochemical Society*, vol. 126, no. 3, p. 504, (March 1979).
- Oshima, M., "A study of dry etching related contamination on Si and SiO₂," *Surface Science*, vol. 86, p. 858, (1979).
- Paraszczak, J. and M. Hatzakis, "Comparison of CF₄/O₂ and CF₂Cl₂/O₂ plasmas used for the reactive ion etching of single crystal silicon," *Journal of Vacuum Science and Technology*, vol. 19, no. 4, p. 1412, (November/December 1981).
- Parrens, P., "Anisotropic and selective reactive ion etching of polysilicon using SF₆," *Journal of Vacuum Science and Technology*, vol. 19, no. 4, p. 1403, (November/December 1981).

- Parry, P.D. and A.F. Rodde, "Anisotropic plasma etching of semiconductor materials," *Solid State Technology*, vol. 22, no. 4, p. 125, (April 1979).
- Pederson, L.A., "Structural composition of polymers relative to their plasma etch characteristics," *Journal of the Electrochemical Society*, vol. 129, no. 1, p. 205, (January 1982).
- Peterson, J.F. and Hans A. Steinherz, "Vacuum pump technology: short course on theory and operations," *Solid State Technology*, p. 82, (December 1981).
- Pogge, H.B., J.A. Bondur, and P.J. Burkhardt, "Reactive Ion Etching of silicon with Cl₂/Ar," *Journal of the Electrochemical Society*, vol. 130, no. 7, p. 1592, (July 1983).
- Poulsen, R.G., "Plasma etching in IC manufacture," *Journal of Vacuum Science and Technology*, vol. 14, no. 1, p. 266, (1977).
- Poulsen, R.G. and M. Brochu, "Importance of temperature and temperature control in plasma etching," in *Etching for Pattern Definition*, p. 143, Electrochemical Society symposium series, (1976).
- Reinberg, A.R., "Plasma etching in semiconductor manufacture," in *Etching for Pattern Definition*, Electrochemical Society symposium series, (1976).
- Revell, P.J. and G.F. Goldspink, "Reactive ion beam etching of silicon compounds with a saddle-field ion source," *Journal of Vacuum Science and Technology*, vol. 19, no. 4, p. 1398, (November/December 1981).
- Reynolds, J.L., "Computer simulation of dry-etched line-edge profiles," *Master's report*, Electronics Research Laboratory, Univ of California, Berkeley, CA 94720, (December 14, 1979).
- Reynolds, J.L., A.R. Neureuther, and W.G. Oldham, "Simulation of dry-etched line-edge profiles," *Journal of Vacuum Science and Technology*, vol. 16, no. 6, (November/December 1979).
- Robertson, D.D., "Advances in ion beam milling," *Solid State Technology*, p. 57, (December 1978).
- Romankiw, L.T., "Pattern generation in metal films using wet chemical techniques," in *Etching for Pattern Definition*, Electrochemical Society symposium series, (1976).
- Rothman, L.B., "Process for forming tapered vias in SiO₂ by RIE," in *Plasma processes*, Proceedings of the Electrochemical Society, (1981).
- Rothman, L.B., J.L. Mauer IV, G.C. Schwartz, and J.S. Logan, "Process for forming tapered vias in SiO₂ by reactive ion etching," in *Plasma Processing*, ed. R.G. Frieser & C.J. Mogab, *Proceedings of the Symposium on Plasma Etching and Deposition*, p. 193, The Electrochemical Society, (1981).
- Sakai, Y., J.L. Reynolds, and A.R. Neureuther, "Topology simulation for dry etching," *Proceedings of the Electrochemical Society*, no. Abstract 144, (May 1982, Montreal).
- Schwartz, G.C. and P.M. Schaible, "Reactive ion etching of silicon: temperature effects," in *Plasma Processing*, ed. R.G. Frieser & C.J. Mogab, *Proceedings of the Symposium on Plasma Etching and Deposition*, p. 133, The Electrochemical Society, (1981).
- Schwarz, G.C., L.B. Rothman, and T.J. Schopen, "Competing mechanisms in reactive ion etching in a CF₄ plasma," *Journal of the Electrochemical Society*, vol. 126, no. 3, p. 464, (March 1979).

- Schwarz, G.C., L.B. Zielinski, and T.J. Schopen, "Reactive ion etching," in *Etching for Pattern Definition*, Electrochemical Society symposium series, (1976).
- Shibata, T., K.Hieda, M Sato, M. Konaka, R.L.M. Dang, and H. Zizukai, "An optimally designed process for submicron MOSFETs," in *1981 IEDM Technical Digest*, p. 647, (1981).
- Shibayam, H., T. Ogawa, and K. Kobayashi, "Triode type reactive ion etching system," in *Proceedings on the Symposium on Electron and Ion Beam Technology*, ed. Robert Bakish, vol. 80-6, p. 508, Journal of the Electrochemical Society.
- Smith, D.L. and R.H. Bruce, "Silicon and aluminum etching and product detection in a plasma beam under ultrahigh vacuum," *Journal of the Electrochemical Society*, vol. 129, no. 9, p. 2045, (September 1982).
- Smith, H.I., "Ion beam etching," in *Etching for Pattern Definition*, Electrochemical Society symposium series, (1976).
- Smolinsky, G. and D.L. Flamm, "The plasma oxidation of CF₄ in a tubular-alumina fast-flow reactor," *Journal of Applied Physics*, vol. 50, no. 7, p. 4982, (July 1979).
- Smolinsky, G., T.M. Mayer, and E.A. Truesdale, "Plasma etching of silicon dioxide with hydrogen fluoride mixtures," in *Plasma Processing*, ed. R.G. Friesser & C.J. Mogab, *Proceedings of the Symposium on Plasma Etching and Deposition*, p. 120, The Electrochemical Society, (1981).
- Smolinsky, G., T.M. Mayer, and E.A. Truesdale, "Plasma etching of SiO₂ with HF mixtures," *Journal of the Electrochemical Society*, vol. 129, no. 8, p. 1770, (August 1982).
- Smolinsky, G., E.A. Truesdale, D.N.K. Wang, and D. Maydan, "RIE of silicon oxides with ammonia and trifluoromethane - the role of nitrogen," *Journal of the Electrochemical Society*, vol. 129, no. 5, p. 1036, (May 1982).
- Somekh, S., "Introduction to ion and plasma etching," *Journal of Vacuum Science and Technology*, vol. 13, no. 5, p. 1003, (1975).
- Steinbruechel, Ch., "Langmuir probe measurements on CHF₃ and CF₄ plasmas: The role of ions in the reactive sputter etching of SiO₂ and Si," *Journal of the Electrochemical Society*, vol. 130, no. 3, p. 643, (March 1983).
- Suzuki, K., "Micro wave plasma etching," *Journal of Applied Physics*, vol. 16, no. 11, p. 1979, (November 1979).
- Sze, S.M., editor, *VLSI Technology, Series in Electrical Engineering*, McGraw-Hill Book Company, (1983).
- Ting, C.Y., V.J. Vivalda, and H.G. Schaefer, "Study of Planarized Sputter-Deposited SiO₂," *Journal of Vacuum Science and Technology*, vol. 15, no. 3, p. 1105, (May/June 1978).
- Tokunaga, K. and D.W. Hess, "Aluminum etching in CCl₄ plasmas," *Journal of the Electrochemical Society*, vol. 127, no. 4, p. 923, (April 1980).
- Tonks, Lewi and Irving Langmuir, "A general theory of the plasma of an arc," *Physics Review*, vol. 34, p. 876, (1929).
- Tretola, A.R. Impedance mismatch endpoint detection method for plasma etching diagnostics, gasses CF₄/O₂, in *Plasma Processing*, ed. R.G. Friesser & C.J. Mogab, *Proceedings of the Symposium on Plasma Etching and Deposition*, p. 295, The Electrochemical Society, (1981).

- Truesdale, E.A. and G. Smolinsky, "The effect of added Hydrogen on the rf discharge chemistry of CF₄, CF₃H, C₂F₆," *Journal of Applied Physics*, vol. 50, no. 11, p. 8594, (November 1979).
- Tsui, R.T.C., "Calculation of ion bombarding energy and its distribution in rf sputtering," *Physics Review*, vol. 168, no. 1, p. 107, (April 5, 1969).
- Tsukada, T. and K. Ukai End point determination for plasma etching with a double beam optical emission spectrometer diagnostics, materials: Al, in *Plasma Processing*, ed. R.G. Frieser & C.J. Mogab, *Proceedings of the Symposium on Plasma Etching and Deposition*, p. 288, The Electrochemical Society, (1981).
- Ukai, K. and K. Hanazana, "Analysis of the imaging accuracy in reactive ion etching," *Journal of Vacuum Science and Technology*, vol. 15, no. 2, p. 338, (1978).
- Valyi, L., V. Schiller, J. Gyimesi, and J. Gyulai, "Analysis of chemical processes of plasma etching," *Thin Solid Films*, vol. 76, p. 215, (1981).
- Ven, P.G.T. van de and P.A. Zijlstra, "A critical comparison of SiF₄/O₂ and CF₄/O₂ as plasma etching gasses," in *Plasma Processing*, ed. R.G. Frieser & C.J. Mogab, *Proceedings of the Symposium on Plasma Etching and Deposition*, p. 112, The Electrochemical Society, (1981).
- Viswanathan, N.S., "Simulation of Plasma Etched Lithographic Structures," *Journal of Vacuum Science and Technology*, vol. 16, no. 2, p. 388, (Mar/Apr 1979).
- Vossen, J.L., "Glow discharge phenomena in plasma etching and plasma deposition," *Journal of the Electrochemical Society*, vol. 126, no. 2, p. 319, (February 1979).
- Watanabe, S., "SET - Stepped electrode transistor," in *Semi-conductor Silicon*, p. 992, Electrochemical Society Symposium Series, (1977).
- White, F.R., C.W. Koburger, D.L. Harmon, and H.J. Geipel, "Plasma etching of composite silicide gates electrodes," *Journal of the Electrochemical Society*, vol. 129, no. 6, p. 1330, (June 1982).
- Wilson, I.H., "The topography of sputtered semiconductors," *Radiation Effects*, vol. 18, p. 95, (1973).
- Winters, H.F., "Physical sputtering: a discussion of experiment and theory," in *Radiation Effects on Solid Surfaces*, ed. M. Kaminsky, *Advances in Chemistry Series*, (1976).
- Winters, H.F. and J.W. Coburn, "The etching of silicon with XeF₂ vapor," *Applied Physics Letters*, vol. 34, no. 1, p. 70, (January 1979).
- Winters, H.F. and J.W. Coburn, "Ion- and electron-assisted gas-surface chemistry—An important effect in plasma etching," *Journal of Applied Physics*, vol. 50, no. 5, p. 3189, (May 1979).
- Winters, H.F., J.W. Coburn, and E.Kay, "Plasma etching -- A 'pseudo-black-box' approach," *Journal of Applied Physics*, vol. 48, no. 12, p. 4973, (December 1977).
- Witcomb, M.J., "Conical topography formed on ion etched crystalline surfaces," *Journal of Applied Physics*, vol. 46, no. 11, p. 5053, (1975).
- Witcomb, M.J., "Dissolution applied to the prediction of apex angles of conical ion-bombarded structures," *Journal of Material Science*, vol. 10, p. 669, (1975).

- Youngner, D.W. and C.M. Haynes, "Modeling ion beam etching," *Journal of Vacuum Science and Technology*, vol. 21, no. 2, p. 677, (July/August 1982).
- Zarowin, C.B., "Control of plasma etch profiles with plasma sheath electric field and rf power density," *Journal of the Electrochemical Society*, vol. 129, no. 11, p. 2541, (November 1982).
- Zarowin, C.B., "Plasma etch anisotropy -- Theory and some verifying experiments relating ion transport, ion energy and etch profiles," *Journal of the Electrochemical Society*, vol. 130, no. 5, p. 1144, (May 1983).
- Zijlstra, P.A. and C.I.M. Beenakker, "Evaluation of silicon-chemiluminescence monitoring as a novel method for atomic fluorine determination and end point detection in plasma etch systems," *Applied Spectroscopy*, vol. 35, no. 4, (1981).

APPENDIX A

A. PLASMA THERM PK-12 PLASMA ETCHER & USER MANUAL

Introduction.

The plasma Therm PK-12 PE/RIE is a very flexible parallel plate plasma etching system. It has a 12 inch chamber capable of handling 6 3" wafers simultaneously. The flexibility stems from two types of pumping systems, two modes of supplying power (to the upper electrode, plasma etch mode; and to the lower electrode, reactive ion etch mode (RIE)), three mass flow controllers and 2 needle valves for gas handling, and three modes of operation (manual, pre-set and automatic). The various modes offer a wide variety of plasma etching results, from isotropic to directional. Currently the use of the system will be restricted to etching silicides with fluorine based gasses for integrity and reproducibility. The user must choose between the modes of operation, manual for very specialized processes requiring constant attention, pre-set for push-button control, and automatic which a preprogrammed microprocessor controls. This manual describes these methods. The first section describes each component that makes up the reactor and the manual mode of operation. The second section details the pre-set push-button mode and the third section, the fixed program microprocessor control for common processing steps.

MANUAL OPERATION and COMPONENT DESCRIPTION.

This section describes the components of the etching system and their control manually. They are systematically presented starting at the top of the instrument cabinet and working down and over to the reactor panel.

The rf power supply.

The power supply provides 0-500 Watts (<0.8 Watts/cm²) to the reactor plates, although it is sometimes hard to sustain a plasma at very low powers (< 50 Watts). It operates at a frequency of 13.56 MHz in the industrial application FM band.

First the power cable should be checked to see that it is connected to the proper plate. Attached to the upper plate, the system will perform what is called plasma-assisted etching which is characterized by good selectivity and a good degree of anisotropy. Connected underneath, the lower plate receives the power and will build up a large DC bias between the wafer and the plasma, resulting in more ion bombardment than the plasma etching mode. This is called reactive ion etching (RIE) and is characterized by vertical sidewalls, but less selectivity. There is a grounding stub that must be connected to the plate that is not powered.

- ∇ The power meters at the top monitor the forward and reflected power in Watts that the rf generator sees the plasma through the power cable. The automatic matching network should always reduce the reflected power to less than 10% of the forward if not zero. If the reflected power seems excessive, check to see that the automatic matching network is indeed in automatic mode (at the bottom of the reactor panel) and that there is indeed a plasma ignited in the chamber.
- The POWER on light should be on during operation to indicate the the rf generator is turned on on the reactor panel.

- The POWER OFF button should be lit in stand-by mode and indicates that the rf power can be turned on by the next button. If this light is off check special interlocks, such as maximum pressure, chamber closed and instrument panel closed.
 - The RF POWER ON button turns on the generator to the power selected either manually or pre-set by the knobs described below.
 - The Over Load (O.L.) RESET button lights once the maximum power has been exceeded. Press it to reset, then try a lower power before turning on the generator with RF ON button.
 - ⊙ The Selector and Multimeter monitors voltage and current at key points through out the rf generator. They are used primarily used for diagnosing problems with the power supply. Points 8 & 9 indicate the high voltage and rf current that the supply provides to its load.
 - The POWER knob controls the power when the power supply is in the manual mode. When the supply is set in automatic mode this knob acts as a limiter to the power that can be cranked in, so it is best to leave it completely clock-wise when in automatic mode to get the full range.
 - ! The AUTO / MANUAL switch controls whether the pre-sets or the power knob controls the amount of power respectively.
 - ! The INCIDENT / PROGRAM switch determines whether the incident power potentiometer or the pre-set potentiometers control the amount of power. It should be to the program position for push-button or microprocessor control.
 - The INCIDENT power pot controls the power when the left toggle is in the incident mode. It is a useful pre-set without disturbing the three push-button pre-sets.
 - PRESETS 1 2 3 set the power for the push-buttons below and the microprocessor. Please do not disturb them for fear of ruining a succeeding users' process.
 - VSWR TRIP sets the maximum voltage standing wave ratio that the power supply will detect.
 - ⊙ The alarm and resets tells you that the rf power supply needs your attention.
- === The POWER CONTROL switches set up the controlling source of the power. In order that the power be controlled from the instrument cabinet and the microprocessor, they should be set in LOCAL, ON, ON.

The Thermo-couple pressure gauges.

- ! Power switch.
- ∇ The pressure meter indicates the amount of pressure in $\mu\text{m Hg}$ of N_2 . This is equivalent to milliTorr, but note that the gauge is calibrated in terms of Nitrogen and will give scaled readings for other gasses.
- ! The TC1 / TC2 toggle chooses at which point the above gauge indicates the pressure, TC1 in the chamber and TC2 at the roughing valve.
- Other meters and switches to the right are useful in measuring pressure below $1 \mu\text{m Hg}$ ($< .1 \text{ mT}$). They are essentially useless without a diffusion pump attached to the chamber.

Capacitance manometer.

- ::: The digital read-out indicates the pressure in the chamber measured by the capacitance manometer. It appears in Torr with 1 milliTorr the minimum.
- + The zero screw adjusts the zero-reading of the digital display. Often the manometer drifts and should be reset. Negative pressures or far deviation from the TC1 reading indicate that the display should be re-zeroed.

Mass flow controllers

The mass flow controllers have the capability of controlling the flow-rates of 3 gasses fairly accurately. Channels 1 and 2 have a 10 - 3000 sccm capacity and channel 3 a 2 -100 sccm capacity. Typically, CF_4 (Carbon Tetrafluoride) or C_2F_6 (Freon 116) is in channel 1, SF_6 (Sulfur Hexafluoride) in channel 2, and O_2 (house oxygen) in channel 3.

- ∇ The horizontal voltage dials indicate the amount of volts and how far open each controller is opened. Zero, far left is closed, and far right is full open.
- The pot on the right beneath each dial controls the scaling factor individual to each gas. The mass flow controllers are calibrated for Nitrogen (CAL = 1) and their measurements must be scaled (according to the ratio of specific heats) for gasses other than nitrogen. The CAL factor scales the reading for easy and quick conversion of the gas flow on the digital display.
- The left pot for each gas controls the setting of the gas (either absolute or relative depending on the switch FLOW /RATIO) The number setting on the dial is related to the percentage of the full open capacity of the controller.
- The OFF / AUTO switch disables or enables the controller.
- oo The status lights indicate the condition of the controller. Green tells of some flow, red means closed completely.
- The FLOW / RATIO switch determines if the amount set by the SET pot is absolute (some % of maximum) pr relative (some % of ratio base gas).
- ⊙ The RATIO BASE selector chooses the "master" gas channel such that those channels set to RATIO will "slave" to it. MAIN is for microprocessor control. 1,2, or 3 forces one gas in manual control mode.
- ⊙ The READING selector selects the flow-rate of the gas channel to be displayed on the digital flow-meter.
- ::: The digital flow-meter indicates the flow-rate of the gas selected by READ in sccm (standard cubic cm / minute). Please be sure CAL is properly set for each gas.
- The NORM / ALL OFF switch totally disables the flow meters in the ALL OFF position.
- This CALibration potentiometer sets up an across the panel scaling factor for systematic offsets. It should be normally set to 1.0.
- | Power switch. It works better if the power is ON.

Pressure pre-set controls.

The controls operate only on the roughing valve that is located in the 1.5" pipeline to the mechanical pump. They are insignificant when the blower GATE (on the reactor panel) is open. Since they control the roughing valve they have limited minimum pressures.

- PRESSURE SET POINT potentiometers set up the pressure for the push-button and microprocessor control of the vacuum system. There is a one-to-one correspondence of the dial setting to the pre-set pressure, e.g. 5.0

=> 5.0 Torr.

- ∞ The GAIN and PHASE settings affect the feedback system that the roughing valve uses to control the pumping speed.
- ∇ The DEVIATION meter shows the deviation (+ or -) of the actual pressure from the set pressure.
- ⊙ The Full Scale D.C. set the units of the deviation meter.
- ⊙ The CONTROL MODE knob selects the mode of operation. AUTO tells the system to adjust roughing valve to achieve pre-set pressure. CLOSE closes the aperture completely. HOLD holds the aperture at its present opening and thus keeps the pumping speed constant. OPEN opens the valve fully.

Pre-set controls.

This section of the panel is a group of push buttons that control which pre-set points are selected.

Gas Control

- Purge Gas 1 operates the solenoid valve between the needle valve on the reactor panel and the chamber.
- Purge Gas 2 operates the solenoid valve between the needle valve on the reactor panel and the chamber.
- FLUSH flushed the chilled water line with N_2 You do not want to ever do that.
- The VENT button vent the chamber with nitrogen at a very slow rate.
- PROCESS opens valves which allow the pre-set mass flow controllers to operate.
- ROUGH opens the roughing valve. It duplicates the action of the button on the reactor panel. Note: the buttons on the reactor panel over ride those on the instrument cabinet.

PRESSURE SET

- The button labeled 0 (0 NOT 0 {zero}) fully opens the roughing valve. It pumps to the base pressure of the roughing pump.
- 1 tells the roughing valve to constrict (open) to achieve the pressure pre-set by the PRESSURE SET POINT pot 1.
- 2 tells the roughing valve to constrict (open) to achieve the pressure pre-set by the PRESSURE SET POINT pot 2.
- 3 tells the roughing valve to constrict (open) to achieve the pressure pre-set by the PRESSURE SET POINT pot 3.

TEMPERATURE SET

- Pressing 1 heats (cools) the lower electrode (only) to the temperature pre-set by the potentiometer on the reactor panel, provided that the selector knob there is in AUTO setting.
- Pressing 2 heats (cools) the lower electrode (only) to the temperature pre-set by the potentiometer on the reactor panel, provided that the selector knob there is in AUTO setting.
- Pressing 3 heats (cools) the lower electrode (only) to the temperature pre-set by the potentiometer on the reactor panel, provided that the selector knob there is in AUTO setting.

RF POWER

- 1 sets the power to the setting on pre-set pot 1 if the toggles above are in program and auto positions.
- 2 sets the power to the setting on pre-set pot 2 if the toggles above are in program and auto positions.
- 3 sets the power to the setting on pre-set pot 3 if the toggles above are in program and auto positions.
- ? The MANUAL / SEQUENCE key switch should be in the MANUAL position for pre-set push-button procedures and in the SEQUENCE position for microprocessor control.
- | Power switch.

The micro-processor.

The use of this instrument is described in section 4 on automatic control.

Matching Network

Make sure that this light is lit to insure the matching network is functional.

rf generator.

- The rf power switch for the instrument cabinet turn on the rf power generator and controls if power is being supplied from the reactor panel.

The Reactor Panel

- The EPO (Emergency Power Off) button is the panic button to immediately shut down all systems.
- The red VAC light shines when the chamber is under vacuum. Do not try to open the chamber when it is on.
- | The HOIST motion switch determines the motion of the chamber top, raising/opening it in the UP position, and lowering/closing it in the DOWN position. In the UP position the chamber will automatically start to open when it is no longer under vacuum.

○

Depress both yellow buttons to enact the motion of the hoist. Use both hands so that one does not get trapped in the chamber.

■

The CKTS ON button re-enables the circuits broken after an EPO or with the initial turn on line.

○

The VENETIAN BLIND throttles the Roots blower by operating a butterfly valve. It is enabled when only the ■ GATE light is on.

PUMP and VALVE control

- | Power switch. It controls better if it is on.
- The DIFFusion button is useless since there is no diffusion pump.
- The top ROUGH button turns on the roughing pump. It should be turned on after the ROUGH valve (below) is opened.
- The FOREline button is useless since there is no diffusion pump.
- The GATE button opens the 4-inch channel through to the Roots blower. There is an interlock which only allows the valve to be open when the

chamber pressure is below 2.000 Torr.

- The VENETIAN light fully opens the butterfly valve between the blower and the chamber. It disables control from the VENETIAN BLIND knob and causes the chamber to be pumped to its lowest pressure.
- The ROUGH button opens the 1.5-inch channel to the roughing pump. Note: this valve over-rides any other valve control, so it must be off to light and enable the other valves.
- The VENT opens a nitrogen venting valve.

Master Switches.

- The red-light indicates power is coming to the unit and the circuits are unbroken.
- II The VACUUM SYSTEM master switch enables power to the pumps.
- II The RF GENERATOR master switch enables power to the rf power supply.
- II The LINE master switch enables power to the other master switches. Usually it is sufficient to turn it on, since other significant master switches are left ON in stand-by mode.
- II The AUXiliary switch enables power to whatever is currently connected to the auxiliary port (nothing now).
- II The REFRIGERANT switch enables power to the refrigerant system, which this system does not possess. It does have a heat exchanging system which will cool the lower electrode to ambient.
- II The INSTRUMENT CABINET switch enables power to the controls on the instrument cabinet.
- II The HEAT EXCHANGER switch enables power to the heat exchanging system (silicon oil) that controls the temperature of the lower electrode.
- II The CONTROL master switch enables power to the reactor panel controls.

Gas meters.

- = The flow needle valve and control knob measures and sets the flow-rate of purge gas (P.G.) 2 when it is enabled from the instrument panel.
- = The flow needle valve and control knob measures and sets the flow-rate of purge gas (P.G.) 1 when it is enabled from the instrument panel.
- ∇ The five meters monitor the pressure of the gas lines coming into the reactor. If you are unable to get a gas flow check to see there is pressure to flow in.

Temperature control and pre-sets.

- The green light indicates the heat exchanger is trying to cool the lower electrode to the set temperature, the red to heat it to the set temperature.
- ::: The digital display displays the temperature of one electrode in degrees Centigrade.
- ! The UPPER / LOWER toggle switch selects the electrode which the digital display monitors.
- ⊙ The selector knob selects to which pre-set the lower electrode converges. In the AUTO position it allows control from the push-buttons on the instrument cabinet.
- PRESETS 1 2 3 set the temperature for the push-buttons on the instrument cabinet and the microprocessor. The reading on the potentiometer is one-

half that temperature (in °C) which the heat exchanger tries to achieve (roughly). 175° C is the maximum without help from a heating plasma. Please do not disturb them for fear of ruining a succeeding users' process.

| The power switch. You will get the temperature you want sooner if this is ON.

Matching network.

The matching network consists of two variable capacitors, one series and one shunt, and a series inductor. Two servo motors drive the variable capacitors to minimize the reflected power. LOADING indicates the parallel capacitor control, and TUNING the series one.

- The AUTO / MAN switch determines whether the servo motors adjust the capacitance automatically or the manual buttons below control it. The only time that it should be in manual mode is to set the capacitors to some intermediate value if they are too far out to even attempt a match.
- ::: The digital read-out indicates the number of turns of the variable capacitors (0-203). If one goes to 203 without achieving zero reflected power then a perfect match isn't possible with this system.
- x In MANUAL the left (right) button increases (decreases) the number of turns of the respective capacitor.

PRE-SET PROCEDURE

Preparation.

Before turning any power on check to see that the proper electrode is powered. There is a sign on the instrument cabinet which should be current, or if your are suspicious look to see if the power cable is to the upper or lower electrode in the rear of the reactor. Change the cable of you desire, but be sure it is tight and the grounding stub is at the other connection.

Open the appropriate gas bottles on the left of the reactor panel and check the panel meter to insure that the line is pressurized. Oxygen and Nitrogen from the in house lines behind the reactor should always be on, with N_2 less than 5 psi. Switch the LINE lever up and press CKTS ON. Make sure the RF, VACUUM, CONTROL, and INSTRUMENT CABINET levers are up, plus the HEAT EXCHANGER if you are using that to heat the lower electrode. The chamber should be under vacuum so to open vent with the two VENT buttons. Flip hoist toggle up and wait for the chamber to open. It is good to know that the top of the chamber will swing back out of the way. Load the samples; toward the outside of the plate seems to produce better uniformity. To close the chamber, flip the hoist toggle downward and depress BOTH the yellow buttons. Lower the top until it stops. If it is not centered over the chamber it will correct itself on the way down (within reason, of course).

Temperature Set.

Make sure the temperature selector knob is in the AUTO position on the reactor panel. Choose from the 3 pre-sets on the potentiometers and press the corresponding button on the instrument cabinet. The setting on the pot is roughly 1/2 the temperature (in degrees Centigrade) that the heat-exchanger will try to achieve. The red light will remain on while the lower electrode is heating and once the heat-exchanger thinks it has reached the pre-set temperature it will alternate RED-GREEN quickly.

Pump-down.

If the vacuum pumps are not off, turn them off. It is important to open the ROUGH VALVE, by pushing the green valve control button FIRST, then turn on the pumps with the green ROUGH PUMP CONTROL. If you open the roughing valve after the roots blower has started pumping it will grind to a halt and restart once the roughing pump has lowered the pressured differential sufficiently. Also these actions protect your samples from being whisked down the center by the sudden pumping motion. The vacuum red light should glow immediately, if not check to see that the top meets the chamber walls properly. Make sure that the VENTs and Purge Gasses are off and the pressure should quickly drop on the capacitance manometer. Once the pressure has dropped below 2.000T you can open the blower valve, GATE and VENETIAN, and pump lower more quickly. The capacitance manometer often drifts so see that it agrees roughly with TC1. Note that TC1 is calibrated in terms of N_2 so that the agreement is limited to nitrogen or air being pumped out. The blower should pump the system to a base pressure of 3-5 mTorr and the roughing pump, ~25mT.

Adjusting the gas flow-rate.

Check that the channel(s) that conduct the desired gasses are set to AUTO and others are OFF. If two gasses are used in ratio formation, place the master gas in FLOW position and the subordinate gas in RATIO. Set the RATIO BASE selector to the number of the channel of the master gas, then set the READ selector to

the gas whose flow-rate you want to monitor. Having set the gasses up properly, or insuring that they are set up consistent with your process, press PROCESS and set the flow with the SET potentiometer. Do not disturb the CAL pot.

Adjusting the pressure.

Now that the gas(es) are set-up the pressure can be controlled independently, (within limits). There are two ways to adjust the pressure; 1) using the blower which provides high through-put and low pressures and 2) using the roughing valve which enjoys an automatic adjust. Below is a table showing the lowest pressure possible by the two methods. If the roughing pump cannot sustain a pressure low enough to suit you, you may set it manually using the throttling valve on the Roots blower.

center box;	cB	cB	cB	c	c	Flow-rate	Rough minimum	Blower minimum
pressure	0	(base)	25mT	3-5mT	5	sccm	128mT	5mT
sccm	170mT	35mT	50	sccm	240mT	52mT	100	sccm363mT
sccm	560mT	130mT	400	sccm	1.02T	250mT		79mT
								200

Manual pressure control.

With the desired gas flow the pressure may be set to a higher value by throttling the Roots blower. The GATE (blue) button should be on and the VENETIAN (yellow) should be off to enable the butterfly valve. The Venetian knob at the upper left of the reactor panel controls the aperture of the butterfly valve. Turn that until the manometer displays the pressure that you desire. Note: do not force the knob in either extreme so not to break the screw connection.

Automatic pressure control.

Automatic pressure control is achieved through the automatic roughing valve. The GATE and VENETIAN lights should be extinguished and the ROUGH lights ON. On the instrument cabinet select a pre-set pressure, dialed in on the pre-set potentiometers, and press the corresponding blue button. The pressure should converge to that set point within the roughing pump's capacity.

Power selection.

Select a power from those pre-set on potentiometers 1,2, or 3 or flip to INCIDENT POWER CONTROL and set the INCIDENT pot to the desired power. The toggles should be in AUTO and PROGRAM positions all the time, so return them there for the next user if use choose to set the power manually during your process. If the RF OFF light is not on there is some reason that the rf generator does not want to provide power. Check that the chamber is closed, the cabinet door is closed, and the chamber is not venting. Press the RF ON button to ignite the plasma and begin timing your process. Make sure the reflected power dies away as the process continues. It it does not change check to see the servo's are set to auto on the front of the reactor panel. Hit the RF OFF to stop the process.

Shut down procedure.

Turn off the gas flow by pressing PROCESS to extinguish the light. Turn on GATE and VENETIAN to pump sufficiently low. With SF_6 , CF_4 and C_2F_6 no purge is necessary, the chamber can be vented immediately. In case a purge is desired, pres P.G. 2 and Nitrogen will flow through the reactor. Close the blower valve, off with GATE and VENETIAN. Turn off the roughing pump, the green button. Hit the VENT buttons, one or both. Flip the hoist toggle up and wait until the chamber top starts its motion upward. Hasten the upward motion by holding in the yellow

buttons. Unload your samples. Close the chamber, hoist down, depress yellow buttons. Open ROUGH valve control and turn on pumps, ROUGH. Pump to less than 2.000T (make sure the vents and purge gasses are off. Turn on GATE and VENETIAN to pump to less than 10mT. Close all valves, GATE, VENETIAN, and ROUGH. Turn off pumps, top ROUGH out. Turn off LINE and sign out. Do not forget to close the gas bottles when finished.

Default settings for pre-sets.

Here is a roster of the pre-sets as you begin use of the controls and should be left as you are finished your processing.

center box; 11. Power: Temperature:

AUTO AUTO

PROGRAM Pre-Set 1 - 15.0 (30° C)

Power Control - local, on, on Pre-Set 2 - 36.0 (65° C)

Power knob - full clockwise Pre-Set 3 - 100.0 (180° C)

Pre-Set 1 - 100 Watts

Pre-Set 2 - 250 Watts Reactor Panel Switches (II):

Pre-Set 3 - 400 Watts Vacuum System - up rf Generator - up

center box; 11. Pressure: Line - down (when not in use)

Thermocouple meter - TC1 Auxiliary - down

Set Point 1 - 300 mTorr Refrigerant - down

Set Point 2 - 500 mTorr Instrument Cabinet - up

Set Point 3 - 1.000 Torr Heat Exchanger - up

Full Scale D.C. - 1 Control - up

Control Mode - AUTO Hoist - down

center box; 11. Mass Flow Controllers:

Channel 1 (CF_4) Channel 3 (O_2)

CAL - 0.42 CAL - 1.00

Set - (20 sccm) Set - (10% of ratio base)

OFF FLOW AUTO RATIO

Channel 2 (SF_6) Ratio Base - 2

CAL - 0.28 Reading - 2

Set - 0.20 (20 sccm) NORM

AUTO FLOW CAL 1.00

The microprocessor

The microprocessor is capable of storing 4 16-step programs and executing the 16 steps sequentially. These steps includes outputs such as turn on a pre-set, wait until a condition is satisfied (including timing), and jump to another command. Inputs include time and values that can be monitored from the instrument panels, and conditions based on these values. For now, there are no standard process stored and the interested user is reference to the user manuals. The suggested standard programs will probably be the following processes:

- 1] Poly-crystalline silicon etching
- 2] Silicon Dioxide etching
- 3] Tungsten/other silicide etching
- 4] Cleaning cycle/research sequence.

APPENDIX B

COMPUTER CODE FOR CALCULATING IMPEDANCE OF PLASMA

```
# calc.z, a C shell script called with the following arguments.  
# calc.z gas power mode pressure flow-rate load input (turns)
```

```
set gas = "$1"  
while($gas == "")  
  echo -n "What gas? "  
  set gas="$<"  
end  
set power = "$2"  
while($power == "")  
  echo -n "What power (in Watts)? "  
  set power="$<"  
end  
set mode = "$3"  
while($mode == "")  
  echo -n "What mode (PE or RIE)? "  
  set mode="$<"  
end  
set pressure = "$4"  
while($pressure == "")  
  echo -n "What pressure (in milliTorr)? "  
  set pressure="$<"  
end  
set flow = "$5"  
while($flow == "")  
  echo -n "What flowrate (in sccm)? "  
  set flow="$<"  
end  
set turnl = "$6"  
while($turnl == "")  
  echo -n "How many load turns (0-201)? "  
  set turnl="$<"  
end  
set turni = "$7"  
while($turni == "")  
  echo -n "How many input turns (0-201)? "  
  set turni="$<"  
end  
echo "$gas $power Watts in $mode mode, $pressure mT and $flow sccm. " >>  
~reynolds/Data/$gas.IV.27  
# echo "CALCIMP is now called"  
~reynolds/bin/z.out $turnl $power $pressure $flow $gas $mode >>  
~reynolds/Data/$gas.IV.27  
echo "" >> ~reynolds/Data/$gas.IV.27  
bel
```

FORTRAN PROGRAM IN FILE z.out

```
cpp
c  /* Program to calculate the impedance of the plasma from */
c  /* the values of the tuning capacitors.          */
cpp
    program clcimp
c  /* clcimp calculates the impedance of a plasma from
c  /* the matching network variables.
c
    call calc
    stop
    end
cs
    subroutine calc
c  /* input variables
    character*40 cturni, cturnl
    character*40 cpower, cpres, cflow
    character*8 cgas
    character*4 cmode
    real turni, turnl
c  /* variables to be calculated.
    real csvf, cvcj, cser, cpar, trnrng, rsc, lser
    real rimp, aimimp
c  /* variables to be echoed
    real power, pres, flow
c  /* read data
c  SERIES == INPUT == CVCJ1000
c  PARALLEL == LOAD == CSVF500
    call getarg(1,cturni)
    call getarg(2,cturnl)
    call getarg(3,cpower)
    call getarg(4,cpres )
    call getarg(5,cflow )
    call getarg(6,cgas )
    call getarg(7,cmode )
    read(cturni,*)turni
    read(cturnl,*)turnl
    read(cpower,*)power
    read(cpres ,*)pres
    read(cflow ,*)flow
    turni=(turni)*(20.0/200.)
    turnl=(turnl)*(20.0/200.)
c  /* use a linear interpolation to calculate the capacitance
c  /* associated with each number of turns.
    trnrng=200.0
    trlni=13.0
    trlnl=19.0
    cvcj=terp(1000.0,0.0,14.42,turni,14.42)
    csvf=terp(500.0,0.0,20.25,turnl,20.25)
c  /* check to make sure the turns is in linear range.
    if((turni.le.trlni).and.(turnl.le.trlnl)) goto 100
c  /* do something else that will make a better approximation.
    if(turni.le.trlni) go to 90
    write(6,*)'***** input turns out of linear range'
```

```
ctmp=terp(1000.0,0.0,14.42,turnl,14.42)
cvcj=terp(ctmp,7.0,20.25,turnl,7.25)
90 continue
   if(turnl.le.turnl) goto 100
   write(6,*)'***** loading turns out of linear range'
   csvf=12.0
c
100 continue
    write(6,10)turnl,cvcj,turnl,csvf
10 format(6x,'Cseries {cvcj:',f4.1,' input} ',f6.2,' pF',
  & ' & Cpar'l {csvf:',f4.1,' load} ',f6.2,' pF')
c /* now call the routine that calculate the impedance.
cser=cvcj*1.0e-12
cpar=csvf*1.0e-12
lser=1.0*1.0e-06
rsc=50.0
rffreq=13.58e06
rimp=req(cser,cpar,rsc,lser,rffreq)
aimimp=xeq(cser,cpar,rsc,lser,rffreq)
reactc=1/(rffreq*2.0*3.1415926*aimimp)
write(6,30)rimp,aimimp,reactc,rffreq
30 format(6x,'r + ix = ',f8.4,'+',2pg10.2,' ohms {= ',
  & '1/i2*pi*',2pg9.2,'*',2pg9.2;}')
rsheah=parlr(aimimp,rimp,rffreq)
csheah=parlc(aimimp,rimp,rffreq)
rplasm=serr(aimimp,rimp,rffreq)
cshea2=parlc2(aimimp,rimp,rffreq)
write(6,40)rsheah,csheah
write(6,50)rplasm,cshea2
write(6,60)cmode,cgas,power,pres,flow,rimp,aimimp,csheah,rsheah
40 format(6x,'The // Rsheath = ',3pg10.2,
  & ' ohms & Csheath = ',1pg10.2,' F.')
50 format(1x,5(1h~),'Rplasma = ',3pg10.2,
  & ' ohms & Csheath = ',1pg10.2,' F.{for comparison}')
60 format(1x,'Z-Mode gas power pres flow r ',
  & ' x Csh Rsh',',
  & ' Z ',a4,1x,a8,f8.1,f8.1,f8.1,f10.2,f10.2,2pg10.2,2pg10.2)
return
end
cf
function req(cs,cp,rs,als,rf)
c /* func req calculate the real part of the plasma imp.
omega=rf*2.0*3.1415926
tausp=(rs*cp)
req=rs/(((omega*tausp)**2 + 1.0)
return
end
cf
function xeq(cs,cp,rs,als,rf)
c /* func xeq calculate the imaginary part of the plasma imp.
omega=rf*2.0*3.1415926
summer= (1/(omega*cs)) - omega*als
tausp=(rs*cp)
xeq=(omega*tausp*r:)/(((omega*tausp)**2+1.0) + summer
```

```
    return
  end
cf
function terp(yone,ytwo,xtwo,xtwxt,xinc)
cf
c /* func terp interpolates between y1 and y2, at xtwxt.
   terp=ytwo - ((xtwo-xtwxt)/xinc)*(ytwo-yone)
   return
   end
cffi
function parlr(x,r,rf)
cf
  omega=2.0*3.1415926*rf
  ratio=x/r
  parlr=r*(1+(ratio**2))*0.5
  return
  end
cffi
function parlc(x,r,rf)
cf
  omega=2.0*3.1415926*rf
  ratio=r/x
  parlc=(2.0/omega)/(ratio*r + x)
  return
  end
function serr(r,x,rf)
cf
  omega=2.0*3.1415926*rf
  serr=r
  return
  end
cffi
function parlc2(r,x,rf)
cf
  omega=2.0*3.1415926*rf
  parlc2=(2.0/omega)*(x)
  return
  end
```

APPENDIX C

TABLES OF PLASMA DATA FOR THE PK-12

.....
 ::: Impedance measurements with electrode spacing at 1.7 cm :::

C2F6 and CF4 data taken March 17, 1983

SF6 data taken April 6, 1983

Argon data taken April 18, 1983

RIE Mode

gas	power	pres	flow	r	x	Csh	Rsh
0.	1000.000	0.0000	180.0000				
3.000							
17.000							
C2F6-02	100.0	45.0	20.0	23.86	78.48	27.97e-11	13.45e+01
C2F6-02	100.0	50.0	20.0	25.42	76.50	27.63e-11	12.78e+01
C2F6-02	100.0	75.0	20.0	25.69	78.53	27.00e-11	13.29e+01
C2F6-02	100.0	100.0	20.0	27.07	78.46	26.74e-11	12.72e+01
C2F6-02	100.0	125.0	20.0	49.87	60.36	32.41e-11	80.97
C2F6-02	100.0	150.0	20.0	78.3	60.36	32.41e-11	80.97
C2F6-02	100.0	175.0	20.0	93.7	62.59	31.62e-11	86.05
C2F6-02	100.0	200.0	20.0	98.7	64.90	30.83e-11	91.5
C2F6-02	100.0	250.0	20.0	110.	64.90	30.83e-11	91.5
C2F6-02	100.0	300.0	20.0	119.00	64.90	30.83e-11	91.5
C2F6-02	100.0	400.0	20.0	153.00	64.90	30.83e-11	91.5
C2F6-02	100.0	500.0	20.0	200.00	64.90	30.83e-11	91.5
C2F6-02	100.0	600.0	20.0	186.00	58.19	33.19e-11	76.21
C2F6-02	100.0	700.0	20.0	188.00	50.15	36.29e-11	60.07
C2F6-02	100.0	800.0	20.0	187.00	44.70	38.48e-11	50.50
C2F6-02	100.0	900.0	20.0	159.00	36.54	41.55e-11	38.2
C2F6-02	100.0	999.0	20.0	161.00	15.75	37.84e-11	18.09
13.000							
C2F6-02	250.0	59.0	20.0	22.88	78.45	27.58e-11	14.59e+01
C2F6-02	250.0	75.0	20.0	21.05	80.33	27.34e-11	16.38e+01
C2F6-02	250.0	100.0	20.0	24.11	80.63	26.72e-11	14.69e+01
C2F6-02	250.0	125.0	20.0	24.89	80.64	26.58e-11	14.31e+01
C2F6-02	250.0	150.0	20.0	25.42	80.64	26.48e-11	14.06e+01
C2F6-02	250.0	175.0	20.0	26.79	82.75	25.68e-11	14.12e+01
C2F6-02	250.0	200.0	20.0	27.07	82.72	25.63e-11	13.99e+01
C2F6-02	250.0	250.0	20.0	64.5	62.59	31.62e-11	86.1
C2F6-02	250.0	300.0	20.0	81.6	67.27	30.05e-11	97.30
C2F6-02	250.0	400.0	20.0	100.4	74.89	27.74e-11	117.40
C2F6-02	250.0	500.0	20.0	123.	80.41	26.24e-11	133.20
C2F6-02	250.0	600.0	20.0	143.	83.32	25.50e-11	142.10
C2F6-02	250.0	700.0	20.0	162.	83.32	25.50e-11	142.10
12.000							
C2F6-02	400.0	68.0	20.0	22.41	80.51	27.06e-11	15.58e+01
C2F6-02	400.0	100.0	20.0	23.12	82.74	26.32e-11	15.96e+01
C2F6-02	400.0	125.0	20.0	23.86	82.78	26.18e-11	15.55e+01

C2F6-02	400.0	150.0	20.0	24.63	82.81	26.04e-11	15.15e+01
C2F6-02	400.0	175.0	20.0	25.15	82.81	25.95e-11	14.89e+01
C2F6-02	400.0	200.0	20.0	25.69	82.80	25.86e-11	14.63e+01
C2F6-02	400.0	250.0	20.0	27.07	84.96	25.08e-11	14.69e+01
C2F6-02	400.0	300.0	20.0	28.23	84.83	24.91e-11	14.16e+01
C2F6-02	400.0	400.0	20.0	66.5	67.27	30.05e-11	97.3
C2F6-02	400.0	500.0	20.0	99.3	80.41	26.24e-11	133.20
C2F6-02	400.0	600.0	20.0	102.1	80.41	26.24e-11	133.20
C2F6-02	400.0	700.0	20.0	116.	83.32	25.50e-11	142.10

gas	power	pres	flow	r	x	Csh	Rsh
0.	1000.000	0.0000	200.0000				
3.000							
17.000							
CF4-02	100.0	42.0	20.0	23.12	74.45	28.75e-11	13.14e+01
CF4-02	100.0	50.0	20.0	22.88	74.44	28.81e-11	13.25e+01
CF4-02	100.0	75.0	20.0	23.86	78.52	27.37e-11	14.11e+01
CF4-02	100.0	100.0	20.0	25.15	78.54	27.11e-11	13.52e+01
CF4-02	100.0	125.0	20.0	25.69	78.53	27.00e-11	13.29e+01
CF4-02	100.0	150.0	20.0	26.79	78.48	26.79e-11	12.84e+01
CF4-02	100.0	175.0	20.0	27.93	78.37	26.58e-11	12.39e+01
CF4-02	100.0	200.0	20.0	31.94	77.56	25.88e-11	11.02e+01
CF4-02	100.0	250.0	20.0	75.00	58.19	33.19e-11	76.20
CF4-02	100.0	300.0	20.0	87.60	60.36	32.41e-11	80.97
CF4-02	100.0	400.0	20.0	97.7	62.59	31.62e-11	86.05
CF4-02	100.0	500.0	20.0	122.00	64.90	30.83e-11	91.50
CF4-02	100.0	600.0	20.0	143.00	64.90	30.83e-11	91.50
CF4-02	100.0	700.0	20.0	169.00	64.90	30.83e-11	91.50
CF4-02	100.0	800.0	20.0	191.00	64.90	30.83e-11	91.50
CF4-02	100.0	900.0	20.0	222.00	64.90	30.83e-11	91.50
CF4-02	100.0	999.0	20.0	240.00	62.59	31.62e-11	86.05
15.000							
CF4-02	250.0	57.0	20.0	20.83	76.15	28.68e-11	14.96e+01
CF4-02	250.0	75.0	20.0	21.05	78.23	27.98e-11	15.59e+01
CF4-02	250.0	100.0	20.0	22.41	80.51	27.06e-11	15.58e+01
CF4-02	250.0	125.0	20.0	23.61	80.61	26.82e-11	14.94e+01
CF4-02	250.0	150.0	20.0	24.63	80.64	26.63e-11	14.43e+01
CF4-02	250.0	175.0	20.0	25.42	80.64	26.48e-11	14.06e+01
CF4-02	250.0	200.0	20.0	25.96	80.63	26.38e-11	13.82e+01
CF4-02	250.0	250.0	20.0	28.23	80.44	25.98e-11	12.87e+01
CF4-02	250.0	300.0	20.0	28.23	80.44	25.98e-11	12.87e+01
CF4-02	250.0	400.0	20.0	62.3	62.59	31.62e-11	86.05
CF4-02	250.0	500.0	20.0	90.70	72.27	28.50e-11	110.20
CF4-02	250.0	600.0	20.0	104.00	77.60	26.98e-11	125.00
CF4-02	250.0	700.0	20.0	133.00	83.32	25.50e-11	142.1
CF4-02	250.0	800.0	20.0	143.00	86.34	24.77e-11	151.5
CF4-02	250.0	900.0	20.0	160.00	86.34	24.77e-11	151.5
11.000							
CF4-02	400.0	72.0	20.0	21.27	78.26	27.93e-11	15.46e+01
CF4-02	400.0	100.0	20.0	21.72	80.43	27.20e-11	15.98e+01
CF4-02	400.0	125.0	20.0	22.64	82.70	26.41e-11	16.23e+01
CF4-02	400.0	150.0	20.0	23.37	82.76	26.27e-11	15.82e+01
CF4-02	400.0	175.0	20.0	24.37	82.80	26.09e-11	15.29e+01

CF4-02	400.0	200.0	20.0	24.89	82.81	26.00e-11	15.02e+01
CF4-02	400.0	250.0	20.0	26.79	82.75	25.68e-11	14.12e+01
CF4-02	400.0	300.0	20.0	28.52	82.56	25.40e-11	13.38e+01
CF4-02	400.0	400.0	20.0	28.82	84.75	24.83e-11	13.90e+01
CF4-02	400.0	500.0	20.0	64.00	67.27	30.05e-11	97.4
CF4-02	400.0	600.0	20.0	79.20	74.89	27.74e-11	117.40
CF4-02	400.0	700.0	20.0	160.00	86.34	24.77e-11	151.5

gas	power	pres	flow	r	x	Csh	Rsh
0.	200.000	0.0000	200.0000				
3.000							
8.000							
SF6-02	100.0	43.0	20.0	78.00	77.60	26.98e-11	125.00
SF6-02	100.0	50.0	20.0	102.00	86.34	24.77e-11	151.50
SF6-02	100.0	75.0	20.0	134.00	89.46	24.05e-11	161.70
SF6-02	100.0	100.0	20.0	163.00	89.46	24.05e-11	161.70
SF6-02	100.0	125.0	20.0	189.00	89.46	24.05e-11	161.70
SF6-02	100.0	150.0	20.0	222.00	89.46	24.05e-11	161.70
SF6-02	100.0	175.0	20.0	271.00	89.46	24.05e-11	161.70
SF6-02	100.0	200.0	20.0	353.00	92.71	23.34e-11	172.70
5.000							
SF6-02	250.0	61.0	20.0	27.93	89.55	24.03e-11	162.00
SF6-02	250.0	75.0	20.0	64.30	77.60	26.98e-11	125.
SF6-02	250.0	100.0	20.0	103.00	96.08	22.64e-11	184.5
SF6-02	250.0	125.0	20.0	136.00	103.22	21.29e-11	210.8
SF6-02	250.0	150.0	20.0	163.00	107.01	20.62e-11	225.6
2.000							
SF6-02	400.0	81.0	20.0	27.64	89.58	23.93e-11	15.90e+01
SF6-02	400.0	100.0	20.0	64.00	77.60	26.98e-11	125.

RIE Mode

gas	power	pres	r	x	Csh	Rsh
0.	1000.000	0.0000	100.0000			
3.000						
17.000						
Ar	100.0	23.0	110.00	69.73	9.65e-11	77.1
Ar	100.0	50.0	49.87	62.59	22.94e-11	64.2
Ar	100.0	75.0	49.87	64.90	22.74e-11	67.
Ar	100.0	100.0	49.87	67.27	22.52e-11	70.
Ar	100.0	125.0	49.87	69.73	22.27e-11	74.
Ar	100.0	150.0	49.87	70.99	22.14e-11	75.
Ar	100.0	175.0	49.87	72.27	22.00e-11	77.
Ar	100.0	200.0	73.00	72.27	16.10e-11	72.3
Ar	100.0	250.0	75.00	74.89	15.60e-11	74.9
Ar	100.0	300.0	78.80	74.89	14.90e-11	75.0
Ar	100.0	400.0	82.40	74.89	14.20e-11	75.2
Ar	100.0	500.0	90.10	77.60	12.90e-11	78.5
Ar	100.0	600.0	91.60	80.41	12.70e-11	81.1
Ar	100.0	700.0	93.20	80.41	12.50e-11	81.3
Ar	100.0	800.0	94.70	80.41	12.20e-11	81.5
Ar	100.0	900.0	98.00	80.41	11.70e-11	82.
Ar	100.0	999.0	103.60	80.41	13.00e-11	80.9
17.000						
Ar	250.0	40.0	98.70	77.60	11.60e-11	79.9

Ar	250.0	50.0	72.90	72.27	16.10e-11	72.3
Ar	250.0	75.0	73.60	77.60	15.90e-11	77.7
Ar	250.0	100.0	71.30	77.60	16.40e-11	77.9
Ar	250.0	125.0	71.30	80.41	16.30e-11	81.0
Ar	250.0	150.0	78.40	83.32	14.90e-11	83.5
Ar	250.0	175.0	77.40	83.32	15.10e-11	83.5
Ar	250.0	200.0	71.30	84.82	16.20e-11	86.1
Ar	250.0	250.0	70.90	86.34	16.20e-11	88.0
Ar	250.0	300.0	70.10	89.46	16.30e-11	92.1
Ar	250.0	400.0	70.10	89.46	16.30e-11	92.1
Ar	250.0	500.0	71.80	92.71	15.80e-11	95.8
Ar	250.0	600.0	75.00	92.71	15.30e-11	94.8
Ar	250.0	700.0	77.20	94.72	14.90e-11	96.7
Ar	250.0	800.0	79.80	94.72	14.50e-11	96.1
Ar	250.0	900.0	84.80	96.08	13.70e-11	96.8
Ar	250.0	999.0	83.50	96.08	13.90e-11	97.0
16.000						
Ar	400.0	62.0	96.20	83.32	12.10e-11	84.2
Ar	400.0	75.0	89.80	84.52	13.00e-11	84.7
Ar	400.0	100.0	91.60	89.46	12.80e-11	89.5
Ar	400.0	125.0	94.70	92.71	12.40e-11	92.7
Ar	400.0	150.0	94.70	96.08	12.40e-11	96.1
Ar	400.0	175.0	96.20	96.08	12.20e-11	96.1
Ar	400.0	200.0	72.70	94.38	15.60e-11	97.6
Ar	400.0	250.0	71.70	92.71	15.80e-11	95.8
Ar	400.0	300.0	71.60	96.08	15.70e-11	100.0
Ar	400.0	400.0	73.30	99.58	15.30e-11	104.0
Ar	400.0	500.0	74.40	99.58	15.10e-11	104.0
Ar	400.0	600.0	76.30	103.22	14.70e-11	108.0
Ar	400.0	700.0	76.10	103.22	14.70e-11	108.0
Ar	400.0	800.0	77.00	103.22	14.60e-11	108.0
Ar	400.0	900.0	77.70	103.22	14.50e-11	107.0
Ar	400.0	999.0	77.70	99.58	14.70e-11	103.0

.....
 ::: DC Bias and Fluorine 704 emission measurements :::
 ::: with the electrode spacing at 1.7 cm :::

C2F6 and CF4 data taken March 17, 1983

SF6 data taken April 6, 1983

Argon data taken April 16, 1983

RIE Mode

gas	power	pres	flow	DC Bias	[704] F	[704/750]
0.	1000.000	0.0000	40.0000			
3.000						
17.000						
C2F6-O2	100.0	45.0	20.0	-118.6	0.557	3.48
C2F6-O2	100.0	50.0	20.0	-110.1	0.510	3.00
C2F6-O2	100.0	75.0	20.0	-84.56	0.592	3.34
C2F6-O2	100.0	100.0	20.0	-66.8	0.678	3.90
C2F6-O2	100.0	125.0	20.0	-45.5	0.753	4.62
C2F6-O2	100.0	150.0	20.0	-29.2	0.781	4.88
C2F6-O2	100.0	175.0	20.0	-24.5	0.858	5.72

C2F6-02	100.0	200.0	20.0	-21.8	0.927	6.48
C2F6-02	100.0	250.0	20.0	-17.2	0.989	7.67
C2F6-02	100.0	300.0	20.0	-14.2	1.04	9.04
C2F6-02	100.0	400.0	20.0	-11.4	1.15	12.4
C2F6-02	100.0	500.0	20.0	-8.77	1.11	12.4
C2F6-02	100.0	600.0	20.0	-8.54	1.24	16.6
C2F6-02	100.0	700.0	20.0	-7.15	1.11	18.1
C2F6-02	100.0	800.0	20.0	-5.79	1.19	23.2
C2F6-02	100.0	900.0	20.0	-5.64	1.25	26.5
C2F6-02	100.0	999.0	20.0	-5.31	1.44	36.6
13.000						
C2F6-02	250.0	59.0	20.0	-228.3	1.87	5.57
C2F6-02	250.0	75.0	20.0	-200.0	1.86	5.83
C2F6-02	250.0	100.0	20.0	-168.9	1.85	5.84
C2F6-02	250.0	125.0	20.0	-145.9	1.91	6.10
C2F6-02	250.0	150.0	20.0	-130.0	2.04	6.73
C2F6-02	250.0	175.0	20.0	-119.2	2.17	7.46
C2F6-02	250.0	200.0	20.0	-105.3	2.29	8.36
C2F6-02	250.0	250.0	20.0	-75.26	2.38	8.59
C2F6-02	250.0	300.0	20.0	-49.04	2.41	10.04
C2F6-02	250.0	400.0	20.0	-34.46	2.78	13.0
C2F6-02	250.0	500.0	20.0	-22.83	2.90	15.4
C2F6-02	250.0	600.0	20.0	-17.65	2.95	17.5
C2F6-02	250.0	700.0	20.0	-13.53	2.92	17.80
12.000						
C2F6-02	400.0	68.0	20.0	-291.7	3.13	7.34
C2F6-02	400.0	100.0	20.0	-238.9	3.44	9.45
C2F6-02	400.0	125.0	20.0	-213.5	3.56	9.97
C2F6-02	400.0	150.0	20.0	-197.2	3.60	10.75
C2F6-02	400.0	175.0	20.0	-178.4	3.60	11.1
C2F6-02	400.0	200.0	20.0	-164.3	3.68	11.50
C2F6-02	400.0	250.0	20.0	-147.8	3.92	13.1
C2F6-02	400.0	300.0	20.0	-127.5	3.94	13.5
C2F6-02	400.0	400.0	20.0	-88.15	3.85	14.6
C2F6-02	400.0	500.0	20.0	-56.44	4.14	16.4
C2F6-02	400.0	600.0	20.0	-49.47	4.59	18.1
C2F6-02	400.0	700.0	20.0	-33.19	4.62	17.50
gas	power	pres	flow	DC Bias	[704] F	[704/750]
0.	1000.000	0.0000	400.0000			
3.000						
17.000						
CF4-02	100.0	42.0	20.0	-149.2	5.39	33.3
CF4-02	100.0	50.0	20.0	-137.2	5.74	33.8
CF4-02	100.0	75.0	20.0	-100.8	7.88	44.5
CF4-02	100.0	100.0	20.0	-86.04	8.34	47.9
CF4-02	100.0	125.0	20.0	-73.78	8.19	50.2
CF4-02	100.0	150.0	20.0	-65.32	8.22	51.4
CF4-02	100.0	175.0	20.0	-58.77	8.53	56.9
CF4-02	100.0	200.0	20.0	-50.31	8.56	59.9
CF4-02	100.0	250.0	20.0	-34.04	9.65	74.8
CF4-02	100.0	300.0	20.0	-26.85	10.62	92.3
CF4-02	100.0	400.0	20.0	-17.04	12.33	133.0
CF4-02	100.0	500.0	20.0	-12.54	13.92	155.9

CF4-02	100.0	600.0	20.0	-9.87	15.44	207.0
CF4-02	100.0	700.0	20.0	-8.10	15.60	254.0
CF4-02	100.0	800.0	20.0	-6.98	15.80	303.5
CF4-02	100.0	900.0	20.0	-5.60	16.16	342.4
CF4-02	100.0	999.0	20.0	-4.08	15.27	388.5
15.000						
CF4-02	250.0	57.0	20.0	-272.7	9.08	26.9
CF4-02	250.0	75.0	20.0	-232.5	10.98	34.4
CF4-02	250.0	100.0	20.0	-198.5	13.50	42.6
CF4-02	250.0	125.0	20.0	-172.5	14.8	47.3
CF4-02	250.0	150.0	20.0	-154.1	16.2	53.5
CF4-02	250.0	175.0	20.0	-138.5	16.9	58.1
CF4-02	250.0	200.0	20.0	-126.4	16.9	61.7
CF4-02	250.0	250.0	20.0	-108.7	16.7	60.3
CF4-02	250.0	300.0	20.0	-94.71	17.3	72.1
CF4-02	250.0	400.0	20.0	-70.18	18.6	86.9
CF4-02	250.0	500.0	20.0	-45.66	27.0	143.6
CF4-02	250.0	600.0	20.0	-27.06	32.9	194.7
CF4-02	250.0	700.0	20.0	-15.56	38.0	231.7
CF4-02	250.0	800.0	20.0	-8.79	42.6	291.8
CF4-02	250.0	900.0	20.0	-4.00	47.5	336.9
12.000						
CF4-02	400.0	72.0	20.0	-342.5	15.1	33.7
CF4-02	400.0	100.0	20.0	-285.4	18.6	51.1
CF4-02	400.0	125.0	20.0	-249.5	22.0	61.6
CF4-02	400.0	150.0	20.0	-224.1	23.5	69.5
CF4-02	400.0	175.0	20.0	-206.5	25.2	77.8
CF4-02	400.0	200.0	20.0	-189.0	27.1	84.7
CF4-02	400.0	250.0	20.0	-160.7	28.8	96.0
CF4-02	400.0	300.0	20.0	-138.3	25.7	88.0
CF4-02	400.0	400.0	20.0	-116.5	27.7	104.9
CF4-02	400.0	500.0	20.0	-96.0	32.6	128.9
CF4-02	400.0	600.0	20.0	-76.3	33.3	126.1
CF4-02	400.0	700.0	20.0	-30.9	39.8	161.1
gas	power	pres	flow	DC	Bias	[704]
0.	200.000	0.0000	100.0000			
3.000						
8.000						
SF6-02	100.0	43.0	20.0	-37.84	3.40	20.9
SF6-02	100.0	50.0	20.0	-25.58	3.80	22.4
SF6-02	100.0	75.0	20.0	-13.99	5.40	30.5
SF6-02	100.0	100.0	20.0	-12.24	8.06	46.3
SF6-02	100.0	125.0	20.0	-11.12	9.58	58.8
SF6-02	100.0	150.0	20.0	-9.62	9.62	60.1
SF6-02	100.0	175.0	20.0	-8.18	8.60	57.3
SF6-02	100.0	200.0	20.0	-7.93	10.37	72.5
5.000						
SF6-02	250.0	61.0	20.0	-134.7	11.10	33.3
SF6-02	250.0	75.0	20.0	-87.52	15.69	49.2
SF6-02	250.0	100.0	20.0	-28.96	20.2	63.7
SF6-02	250.0	125.0	20.0	-18.98	24.7	78.9
SF6-02	250.0	150.0	20.0	-13.66	28.4	93.7
2.000						
SF6-02	400.0	81.0	20.0	-195.8	20.8	48.6

F

RIE	SF6-02 Mode	400.0	100.0	20.0	-124.1	28.8	79.1
	gas	power	pres	DC	Bias	[F]	
	0.	500.000	0.0000	400.0000			
	3.000						
	17.000						
	Ar	100.0	23.0	-42.9	143.		
	Ar	100.0	50.0	-47.6	170.		
	Ar	100.0	75.0	-47.0	177.		
	Ar	100.0	100.0	-45.0	174.		
	Ar	100.0	125.0	-41.9	163.		
	Ar	100.0	150.0	-38.1	160.		
	Ar	100.0	175.0	-35.3	150.		
	Ar	100.0	200.0	-32.4	143.		
	Ar	100.0	250.0	-28.8	129.		
	Ar	100.0	300.0	-26.2	115.		
	Ar	100.0	400.0	-23.1	92.7		
	Ar	100.0	500.0	-22.0	89.3		
	Ar	100.0	600.0	-20.3	74.6		
	Ar	100.0	700.0	-19.4	61.4		
	Ar	100.0	800.0	-18.6	51.4		
	Ar	100.0	900.0	-18.4	47.2		
	Ar	100.0	999.0	-18.0	39.3		
	17.00						
	Ar	250.0	40.0	-94.3	306.		
	Ar	250.0	50.0	-88.8	345.		
	Ar	250.0	75.0	-84.4	319.		
	Ar	250.0	100.0	-79.1	317.		
	Ar	250.0	125.0	-76.1	313.		
	Ar	250.0	150.0	-73.2	303.		
	Ar	250.0	175.0	-70.6	291.		
	Ar	250.0	200.0	-67.3	274.		
	Ar	250.0	250.0	-61.5	277.		
	Ar	250.0	300.0	-57.7	240.		
	Ar	250.0	400.0	-52.7	214.		
	Ar	250.0	500.0	-48.9	188.		
	Ar	250.0	600.0	-45.9	169.		
	Ar	250.0	700.0	-44.8	164.		
	Ar	250.0	800.0	-43.4	146.		
	Ar	250.0	900.0	-41.9	141.		
	Ar	250.0	999.0	-40.0	130.		
	16.00						
	Ar	400.0	62.0	-135.4	433.		
	Ar	400.0	75.0	-127.7	449.		
	Ar	400.0	100.0	-112.7	364.		
	Ar	400.0	125.0	-106.0	357.		
	Ar	400.0	150.0	-97.9	338.		
	Ar	400.0	175.0	-91.4	324.		
	Ar	400.0	200.0	-77.2	320.		
	Ar	400.0	250.0	-73.0	300.		
	Ar	400.0	300.0	-68.5	292.		
	Ar	400.0	400.0	-62.2	264.		
	Ar	400.0	500.0	-59.9	253.		
	Ar	400.0	600.0	-58.2	264.		

Ar	400.0	700.0	-57.3	247.
Ar	400.0	800.0	-57.3	231.
Ar	400.0	900.0	-56.0	219.
Ar	400.0	999.0	-53.7	212.

Current and Voltage calculations from the rf power and impedance

C2F6 and CF4 data taken March 17, 1983

SF6 data taken April 6, 1983

Argon data taken April 16, 1983

RIE Mode

gas	power	pres	flow	r	x	I	V
0.	1000.000	0.0000	400.0000				
3.000							
17.000							
C2F6-02	100.0	45.0	45.4	23.86	76.48	2.05	164.0
C2F6-02	100.0	50.0	49.8	25.42	76.50	1.98	159.9
C2F6-02	100.0	75.0	78.4	25.69	78.53	1.97	163.0
C2F6-02	100.0	100.0	92.7	27.07	78.46	1.92	159.5
C2F6-02	100.0	125.0	65.4	49.87	60.36	1.42	110.9
C2F6-02	100.0	150.0	82.5	78.3	60.36	1.13	111.7
C2F6-02	100.0	175.0	91.9	93.7	62.59	1.03	116.4
C2F6-02	100.0	200.0	97.1	98.7	64.90	1.01	118.9
C2F6-02	100.0	250.0	104.6	110.	64.90	0.95	121.8
C2F6-02	100.0	300.0	110.1	119.00	64.90	0.92	124.3
C2F6-02	100.0	400.0	123.0	153.00	64.90	0.81	134.4
C2F6-02	100.0	500.0	139.9	200.00	64.90	0.71	148.7
C2F6-02	100.0	600.0	134.4	186.00	58.19	0.73	142.9
C2F6-02	100.0	700.0	134.8	188.00	50.15	0.73	141.9
C2F6-02	100.0	800.0	124.5	187.00	44.70	0.80	130.3
C2F6-02	100.0	900.0	123.8	159.00	36.54	0.79	129.4
C2F6-02	100.0	999.0	122.2	161.00	15.75	0.79	127.5
15.0							
C2F6-02	250.0	59.0	41.8	22.88	78.45	3.31	270.1
C2F6-02	250.0	75.0	86.2	21.05	80.33	3.45	286.2
C2F6-02	250.0	100.0	102.1	24.11	80.63	3.22	271.0
C2F6-02	250.0	125.0	121.6	24.89	80.64	3.17	267.5
C2F6-02	250.0	150.0	135.2	25.42	80.64	3.14	265.2
C2F6-02	250.0	175.0	146.5	26.79	82.75	3.05	265.7
C2F6-02	250.0	200.0	159.2	27.07	82.72	3.04	264.5
C2F6-02	250.0	250.0	101.6	64.5	62.59	1.97	176.9
C2F6-02	250.0	300.0	136.1	81.6	67.27	1.75	185.1
C2F6-02	250.0	400.0	163.2	100.4	74.89	1.58	197.7
C2F6-02	250.0	500.0	186.7	123.	80.41	1.43	209.5
C2F6-02	250.0	600.0	201.1	143.	83.32	1.32	218.8
C2F6-02	250.0	700.0	212.8	162.	83.32	1.24	226.3
12.000							
C2F6-02	400.0	68.0	61.4	22.41	80.51	4.23	353.1
C2F6-02	400.0	100.0	118.4	23.12	82.74	4.16	357.3
C2F6-02	400.0	125.0	139.2	23.86	82.78	4.09	352.7
C2F6-02	400.0	150.0	151.0	24.63	82.81	4.03	348.2
C2F6-02	400.0	175.0	166.8	25.15	82.81	3.99	345.2

C2F6-02	400.0	200.0	177.8	25.69	82.80	3.95	342.1
C2F6-02	400.0	250.0	195.0	27.07	84.96	3.84	342.8
C2F6-02	400.0	300.0	209.0	28.23	84.83	3.76	336.5
C2F6-02	400.0	400.0	143.9	66.5	67.27	2.45	232.0
C2F6-02	400.0	500.0	200.0	99.3	80.41	2.01	256.5
C2F6-02	400.0	600.0	207.7	102.1	80.41	1.98	257.2
C2F6-02	400.0	700.0	232.0	116.	83.32	1.86	265.2

Mode	gas	power	pres	flow	r	x	I	V
0.	100.0000	0.0000	400.0000					
3.000								
17.000								
CF4-02	100.0	42.0	12.9	23.12	74.45	2.08	162.1	
CF4-02	100.0	50.0	25.6	22.88	74.44	2.09	162.8	
CF4-02	100.0	75.0	67.2	23.86	78.52	2.05	168.0	
CF4-02	100.0	100.0	78.4	25.15	78.54	1.99	164.4	
CF4-02	100.0	125.0	89.2	25.69	78.53	1.97	163.0	
CF4-02	100.0	150.0	94.9	26.79	78.48	1.93	160.2	
CF4-02	100.0	175.0	98.6	27.93	78.37	1.89	157.4	
CF4-02	100.0	200.0	98.1	31.94	77.56	1.77	148.4	
CF4-02	100.0	250.0	75.6	75.00	58.19	1.15	109.6	
CF4-02	100.0	300.0	86.6	87.60	60.36	1.07	113.7	
CF4-02	100.0	400.0	100.4	97.7	62.59	1.01	117.4	
CF4-02	100.0	500.0	112.6	122.00	64.90	0.91	125.1	
CF4-02	100.0	600.0	121.4	143.00	64.90	0.84	131.3	
CF4-02	100.0	700.0	131.2	169.00	64.90	0.77	139.3	
CF4-02	100.0	800.0	139.0	191.00	64.90	0.72	146.0	
CF4-02	100.0	900.0	149.6	222.00	64.90	0.67	155.2	
CF4-02	100.0	999.0	156.0	240.00	62.59	0.65	160.1	
15.000								
CF4-02	250.0	57.0	00.8	20.83	76.15	3.46	273.5	
CF4-02	250.0	75.0	46.7	21.05	78.23	3.45	279.2	
CF4-02	250.0	100.0	80.6	22.41	80.51	3.34	279.1	
CF4-02	250.0	125.0	100.8	23.61	80.61	3.25	273.3	
CF4-02	250.0	150.0	114.5	24.63	80.64	3.19	268.6	
CF4-02	250.0	175.0	130.1	25.42	80.64	3.14	265.2	
CF4-02	250.0	200.0	136.5	25.96	80.63	3.10	262.9	
CF4-02	250.0	250.0	145.0	28.23	80.44	2.98	253.7	
CF4-02	250.0	300.0	159.0	28.23	80.44	2.98	253.7	
CF4-02	250.0	400.0	106.7	62.3	62.59	2.00	176.9	
CF4-02	250.0	500.0	146.8	90.70	72.27	1.66	192.5	
CF4-02	250.0	600.0	174.1	104.00	77.60	1.55	201.2	
CF4-02	250.0	700.0	199.6	133.00	83.32	1.37	215.2	
CF4-02	250.0	800.0	212.1	143.00	86.34	1.32	220.9	
CF4-02	250.0	900.0	223.3	160.00	86.34	1.25	227.3	
12.000								
CF4-02	400.0	72.0	9.2	21.27	78.26	4.34	351.7	
CF4-02	400.0	100.0	72.1	21.72	80.43	4.29	357.5	
CF4-02	400.0	125.0	110.9	22.64	82.70	4.20	360.4	
CF4-02	400.0	150.0	131.7	23.37	82.76	4.14	355.8	
CF4-02	400.0	175.0	143.2	24.37	82.80	4.05	349.7	
CF4-02	400.0	200.0	157.6	24.89	82.81	4.01	346.6	
CF4-02	400.0	250.0	176.1	26.79	82.75	3.84	336.1	

CF4-02	400.0	300.0	188.8	28.52	82.56	3.75	327.1
CF4-02	400.0	400.0	217.0	28.82	84.75	3.73	333.5
CF4-02	400.0	500.0	136.1	64.00	67.27	2.50	232.1
CF4-02	400.0	600.0	168.7	79.20	74.89	2.25	245.0
CF4-02	400.0	700.0	256.6	160.00	86.34	1.58	287.5

RIE

Mode	gas	power	pres	flow	r	x	I	V
0.		200.000	0.0000	300.0000				
1.000								
8.000								
SF6-02		100.0	43.0	86.8	78.00	77.60	1.13	124.6
SF6-02		100.0	50.0	106.7	102.00	86.34	0.99	132.3
SF6-02		100.0	75.0	125.2	134.00	89.46	0.86	139.2
SF6-02		100.0	100.0	133.4	163.00	89.46	0.78	145.6
SF6-02		100.0	125.0	141.0	189.00	89.46	0.73	152.1
SF6-02		100.0	150.0	151.0	222.00	89.46	0.67	160.6
SF6-02		100.0	175.0	165.2	271.00	89.46	0.61	173.4
SF6-02		100.0	200.0	186.8	353.00	92.71	0.53	194.7
5.000								
SF6-02		250.0	61.0	145.9	27.93	89.55	2.99	280.6
SF6-02		250.0	75.0	111.2	64.30	77.60	1.97	198.7
SF6-02		250.0	100.0	191.2	103.00	96.08	1.56	220.2
SF6-02		250.0	125.0	212.5	136.00	103.22	1.36	231.5
SF6-02		250.0	150.0	227.8	163.00	107.01	1.24	241.5
2.000								
SF6-02		400.0	81.0	160.8	27.64	89.58	3.80	356.6
SF6-02		400.0	100.0	127.4	64.00	77.60	2.5	251.5

RIE

Mode	gas	power	pres	r	x	I	V
0.		1000.000	0.0000	300.00			
3.000							
17.000							
Ar		100.0	23.0	110.00	69.73	0.95	124.2
Ar		100.0	50.0	49.87	62.59	1.42	113.3
Ar		100.0	75.0	49.87	64.90	1.42	115.9
Ar		100.0	100.0	49.87	67.27	1.42	118.6
Ar		100.0	125.0	49.87	69.73	1.42	121.4
Ar		100.0	150.0	49.87	70.99	1.42	122.9
Ar		100.0	175.0	49.87	72.27	1.42	124.3
Ar		100.0	200.0	73.00	72.27	1.17	120.2
Ar		100.0	250.0	75.00	74.89	1.15	122.4
Ar		100.0	300.0	78.80	74.89	1.13	122.5
Ar		100.0	400.0	82.40	74.89	1.10	122.7
Ar		100.0	500.0	90.10	77.60	1.05	125.3
Ar		100.0	600.0	91.60	80.41	1.04	127.4
Ar		100.0	700.0	93.20	80.41	1.04	127.5
Ar		100.0	800.0	94.70	80.41	1.03	127.7
Ar		100.0	900.0	98.00	80.41	1.01	128.1
Ar		100.0	999.0	103.60	80.41	0.98	128.9
17.000							
Ar		250.0	40.0	98.70	77.60	1.59	199.8
Ar		250.0	50.0	72.90	72.27	1.85	190.1

Ar	250.0	75.0	73.60	77.60	1.84	197.1
Ar	250.0	100.0	71.30	77.60	1.87	197.3
Ar	250.0	125.0	71.30	80.41	1.87	201.2
Ar	250.0	150.0	78.40	83.32	1.79	204.3
Ar	250.0	175.0	77.40	83.32	1.80	204.4
Ar	250.0	200.0	71.30	84.82	1.87	207.5
Ar	250.0	250.0	70.90	86.34	1.88	209.8
Ar	250.0	300.0	70.10	89.46	1.89	214.6
Ar	250.0	400.0	70.10	89.46	1.89	214.6
Ar	250.0	500.0	71.80	92.71	1.87	218.8
Ar	250.0	600.0	75.00	92.71	1.83	217.7
Ar	250.0	700.0	77.20	94.72	1.80	219.9
Ar	250.0	800.0	79.80	94.72	1.77	219.2
Ar	250.0	900.0	84.80	96.08	1.72	220.0
Ar	250.0	999.0	83.50	96.08	1.73	220.3
15.00						
Ar	400.0	62.0	96.20	83.32	2.04	259.5
Ar	400.0	75.0	89.80	84.52	2.11	260.3
Ar	400.0	100.0	91.60	89.46	2.09	267.6
Ar	400.0	125.0	94.70	92.71	2.06	272.4
Ar	400.0	150.0	94.70	96.08	2.06	277.3
Ar	400.0	175.0	96.20	96.08	2.04	277.2
Ar	400.0	200.0	72.70	94.38	2.35	279.5
Ar	400.0	250.0	71.70	92.71	2.36	276.8
Ar	400.0	300.0	71.60	96.08	2.36	283.2
Ar	400.0	400.0	73.30	99.58	2.34	288.9
Ar	400.0	500.0	74.40	99.58	2.32	288.2
Ar	400.0	600.0	76.30	103.22	2.29	293.9
Ar	400.0	700.0	76.10	103.22	2.29	294.0
Ar	400.0	800.0	77.00	103.22	2.28	293.5
Ar	400.0	900.0	77.70	103.22	2.27	293.1
Ar	400.0	999.0	77.70	99.58	2.27	286.6

.....
 ::: Impedance power dependence with the electrode spacing at 1.7 cm :::

RIE Mode

gas	power	pres	flow	r	x	Csh	Rsh
0.	500.000	0.0000	300.0000				
1.000							
10.000							
CF4-O2	50.0	100.0	20.0	32.26	75.43	26.31e-11	10.43e+01
CF4-O2	100.0	100.0	20.0	26.23	74.49	28.04e-11	11.89e+01
CF4-O2	150.0	100.0	20.0	24.37	76.50	27.86e-11	13.22e+01
CF4-O2	200.0	100.0	20.0	23.86	76.48	27.97e-11	13.45e+01
CF4-O2	250.0	100.0	20.0	23.12	78.47	27.52e-11	14.47e+01
CF4-O2	300.0	100.0	20.0	22.17	78.38	27.73e-11	14.96e+01
CF4-O2	350.0	100.0	20.0	22.17	80.48	27.11e-11	15.72e+01
CF4-O2	400.0	100.0	20.0	22.17	80.48	27.11e-11	15.72e+01
CF4-O2	450.0	100.0	20.0	22.17	80.48	27.11e-11	15.72e+01
CF4-O2	500.0	100.0	20.0	22.17	80.48	27.11e-11	15.72e+01

SF6-O2	50.0	100.0	100.0	315.60	96.08	2.07e-11	17.20e+01
SF6-O2	100.0	100.0	100.0	179.	96.08	5.47e-11	11.53e+01
SF6-O2	150.0	100.0	100.0	131.	96.08	8.55e-11	10.70e+01
SF6-O2	200.0	100.0	100.0	110.00	96.08	10.57e-11	96.96
SF6-O2	250.0	100.0	100.0	93.17	92.71	12.60e-11	92.71
SF6-O2	300.0	100.0	100.0	83.33	89.46	14.05e-11	89.69
SF6-O2	350.0	100.0	100.0	50.00	77.60	21.38e-11	85.22
SF6-O2	400.0	100.0	100.0	32.91	93.43	22.35e-11	14.91e+01
SF6-O2	450.0	100.0	100.0	28.52	94.47	22.77e-11	17.07e+01
SF6-O2	500.0	100.0	100.0	27.35	92.07	23.43e-11	16.86e+01

.....
:: DC Bias and Fluorine 704 emission power dependence ::
:::: with the electrode spacing at 1.7 cm ::::
.....

RIE Mode

gas	power	pres	flow	DC	bias	[F]	704nm
0.	500.00	-350.000	00.0000				
1.000							
10.000							
CF4-O2	50.0	100.0	20.0	-37.4	1.24		
CF4-O2	100.0	100.0	20.0	-94.5	5.65		
CF4-O2	150.0	100.0	20.0	-141.2	8.98		
CF4-O2	200.0	100.0	20.0	-178.0	11.98		
CF4-O2	250.0	100.0	20.0	-209.1	13.48		
CF4-O2	300.0	100.0	20.0	-241.2	15.00		
CF4-O2	350.0	100.0	20.0	-263.0	16.80		
CF4-O2	400.0	100.0	20.0	-280.7	17.40		
CF4-O2	450.0	100.0	20.0	-308.2	18.7		
CF4-O2	500.0	100.0	20.0	-326.0	19.6		
SF6-O2	50.0	100.0	100.0	-8.08	2.35		
SF6-O2	100.0	100.0	100.0	-11.52	5.68		
SF6-O2	150.0	100.0	100.0	-14.29	9.10		
SF6-O2	200.0	100.0	100.0	-19.24	13.20		
SF6-O2	250.0	100.0	100.0	-28.75	16.80		
SF6-O2	300.0	100.0	100.0	-46.51	20.60		
SF6-O2	350.0	100.0	100.0	-91.54	21.20		
SF6-O2	400.0	100.0	100.0	-129.4	23.20		
SF6-O2	450.0	100.0	100.0	-166.2	26.8		
SF6-O2	500.0	100.0	100.0	-194.7	30.2		

.....
:: Impedance measurements with electrode spacing at 2.5 cm ::
.....

RIE Mode

gas	power	pres	flow	r	x	Csh	Rsh
0.	1000.000	0.0000	150.0000				
1.000							
19.000							
CF4-O2	400.0	40.0	20.0	20.19	64.96	32.95e-11	11.46e+01

CF4-02	400.0	50.0	20.0	20.19	64.96	32.95e-11	11.46e+01
CF4-02	400.0	75.0	20.0	20.19	66.68	32.25e-11	12.02e+01
CF4-02	400.0	100.0	20.0	20.19	68.45	31.55e-11	12.61e+01
CF4-02	400.0	119.0	20.0	21.49	68.67	31.14e-11	12.04e+01
CF4-02	400.0	200.0	20.0	22.41	68.78	30.85e-11	11.68e+01
CF4-02	400.0	250.0	20.0	24.11	70.72	29.74e-11	11.57e+01
CF4-02	400.0	300.0	20.0	24.89	70.73	29.53e-11	11.30e+01
CF4-02	400.0	400.0	20.0	27.35	70.62	28.90e-11	10.48e+01
CF4-02	400.0	500.0	20.0	27.07	74.44	27.85e-11	11.59e+01
CF4-02	400.0	600.0	20.0	33.24	75.11	26.13e-11	10.15e+01
CF4-02	400.0	700.0	20.0	52.50	58.19	22.24e-11	47.62
CF4-02	400.0	800.0	20.0	55.10	60.36	21.21e-11	50.51
CF4-02	400.0	900.0	20.0	62.30	67.27	18.78e-11	57.87
CF4-02	400.0	999.0	20.0	75.80	72.27	15.47e-11	79.59
CF4-02	100.0	39.0	20.0	20.40	61.70	34.30e-11	10.35e+01
CF4-02	100.0	50.0	20.0	20.40	61.70	34.30e-11	10.35e+01
CF4-02	100.0	75.0	20.0	21.27	63.47	33.25e-11	10.54e+01
CF4-02	100.0	100.0	20.0	21.72	65.21	32.40e-11	10.88e+01
CF4-02	100.0	125.0	20.0	24.11	65.41	31.59e-11	10.08e+01
CF4-02	100.0	150.0	20.0	24.11	65.41	31.59e-11	10.08e+01
CF4-02	100.0	175.0	20.0	25.42	67.14	30.58e-11	10.14e+01
CF4-02	100.0	200.0	20.0	25.69	67.14	30.50e-11	10.06e+01
CF4-02	100.0	250.0	20.0	27.35	67.04	30.02e-11	96.
CF4-02	100.0	300.0	20.0	45.61	58.07	25.00e-11	60.
CF4-02	100.0	400.0	20.0	70.00	50.15	15.88e-11	10.32e+01
CF4-02	100.0	500.0	20.0	92.70	54.05	11.02e-11	18.27e+01
CF4-02	100.0	600.0	20.0	105.00	54.05	9.10e-11	25.06e+01
CF4-02	100.0	700.0	20.0	134.00	54.05	6.08e-11	47.88e+01
CF4-02	100.0	800.0	20.0	156.00	56.09	4.79e-11	68.14e+01
CF4-02	100.0	900.0	20.0	183.00	50.15	3.27e-11	13.10e+02
CF4-02	100.0	999.0	20.0	190.00	41.30	2.56e-11	21.06e+03
CF4-02	250.0	50.0	20.0	19.38	63.11	33.99e-11	11.25e+01
CF4-02	250.0	75.0	20.0	19.38	63.11	33.99e-11	11.25e+01
CF4-02	250.0	100.0	20.0	19.38	64.79	33.26e-11	11.80e+01
CF4-02	250.0	200.0	20.0	24.89	67.15	30.74e-11	10.30e+01
CF4-02	250.0	250.0	20.0	24.89	68.91	30.13e-11	10.79e+01
CF4-02	250.0	300.0	20.0	25.42	70.73	29.39e-11	11.11e+01
CF4-02	250.0	400.0	20.0	27.64	68.78	29.38e-11	99.
CF4-02	250.0	500.0	20.0	28.23	72.39	28.15e-11	10.69e+01
CF4-02	250.0	600.0	20.0	54.00	54.05	21.74e-11	53.95
CF4-02	250.0	700.0	20.0	67.40	62.59	13.37e-11	72.78
CF4-02	250.0	800.0	20.0	88.10	67.27	12.85e-11	11.96e+01
CF4-02	250.0	900.0	20.0	106.00	72.27	10.31e-11	16.70e+01
CF4-02	250.0	999.0	20.0	112.00	74.89	9.69e-11	18.12e+01
CF4-02	100.0	30.0	5.0	19.99	61.62	34.47e-11	10.50e+01
CF4-02	100.0	50.0	5.0	20.62	63.37	33.50e-11	10.77e+01
CF4-02	100.0	75.0	5.0	21.49	63.51	33.17e-11	10.46e+01
CF4-02	100.0	100.0	5.0	22.64	65.32	32.08e-11	10.55e+01
CF4-02	100.0	125.0	5.0	22.88	65.34	32.00e-11	10.47e+01
CF4-02	100.0	153.0	5.0	24.37	67.14	30.89e-11	10.47e+01
CF4-02	100.0	175.0	5.0	25.42	68.91	29.99e-11	10.61e+01
CF4-02	100.0	200.0	5.0	25.96	68.90	29.84e-11	10.44e+01
CF4-02	100.0	250.0	5.0	27.64	67.01	29.94e-11	95.
CF4-02	100.0	300.0	5.0	34.24	67.15	27.75e-11	83.

CF4-O2	100.0	400.0	5.0	73.30	54.05	15.30e-11	10.41e+01
CF4-O2	100.0	500.0	5.0	100.00	56.09	10.02e-11	20.89e+01
CF4-O2	100.0	600.0	5.0	115.00	56.09	8.04e-11	29.92e+01
CF4-O2	100.0	700.0	5.0	150.00	56.09	5.13e-11	61.14e+01
CF4-O2	100.0	800.0	5.0	150.00	44.70	4.28e-11	91.96e+01
CF4-O2	100.0	900.0	5.0	177.00	50.15	3.48e-11	11.91e+02
CF4-O2	100.0	999.0	5.0	163.00	44.70	3.67e-11	11.65e+02
CF4-O2	100.0	75.0	100.0	22.41	61.99	33.49e-11	97.
CF4-O2	100.0	100.0	100.0	22.88	62.03	33.31e-11	96.
CF4-O2	100.0	125.0	100.0	22.88	65.34	32.00e-11	10.47e+01
CF4-O2	100.0	150.0	100.0	23.37	65.37	31.84e-11	10.31e+01
CF4-O2	100.0	175.0	100.0	24.37	67.14	30.89e-11	10.47e+01
CF4-O2	100.0	200.0	100.0	25.42	67.14	30.58e-11	10.14e+01
CF4-O2	100.0	250.0	100.0	27.07	67.06	30.10e-11	97.
CF4-O2	100.0	300.0	100.0	31.61	66.26	28.86e-11	85.
CF4-O2	100.0	400.0	100.0	65.70	46.46	16.84e-11	98.54
CF4-O2	100.0	500.0	100.0	90.00	52.07	19.37e-11	69.83
CF4-O2	100.0	600.0	100.0	95.30	52.07	10.36e-11	20.73e+01
CF4-O2	100.0	700.0	100.0	105.00	52.07	8.90e-11	26.60e+01
CF4-O2	100.0	800.0	100.0	132.00	52.07	6.07e-11	49.01e+01
CF4-O2	100.0	900.0	100.0	142.00	44.70	4.74e-11	78.75e+01
CF4-O2	100.0	999.0	100.0	150.00	42.98	4.14e-11	98.85e+01

RIE Mode

gas	power	pres	flow	r	x	Csh	Rsh
0.	1000.000	0.0000	150.0000				
1.000							
15.000							
SF6-O2	100.0	90.0	100.0	108.00	86.34	10.60e-11	88.51
SF6-O2	100.0	125.0	100.0	152.00	86.34	20.39e-11	100.
SF6-O2	100.0	150.0	100.0	194.00	86.34	4.50e-11	116.32
SF6-O2	100.0	175.0	100.0	235.00	86.34	3.23e-11	133.4
SF6-O2	100.0	30.0	5.0	27.64	70.59	28.83e-11	10.40e+01
SF6-O2	100.0	50.0	5.0	60.50	64.90	22.74e-11	67.
SF6-O2	100.0	75.0	5.0	83.00	80.41	14.13e-11	80.45
SF6-O2	100.0	100.0	5.0	110.00	86.34	10.36e-11	88.88
SF6-O2	100.0	125.0	5.0	141.00	86.34	7.41e-11	96.93
SF6-O2	100.0	150.0	5.0	177.00	86.34	5.23e-11	109.6
SF6-O2	100.0	175.0	5.0	231.00	86.34	3.33e-11	131.6
SF6-O2	100.0	40.0	20.0	27.64	70.59	28.83e-11	10.40e+01
SF6-O2	100.0	50.0	20.0	49.87	60.36	23.11e-11	61.
SF6-O2	100.0	75.0	20.0	74.00	77.60	15.84e-11	77.69
SF6-O2	100.0	100.0	20.0	117.00	86.34	9.59e-11	90.36
SF6-O2	100.0	125.0	20.0	150.00	86.34	6.77e-11	100.5
SF6-O2	100.0	150.0	20.0	190.00	86.34	4.65e-11	114.6
SF6-O2	100.0	175.0	20.0	230.00	86.34	3.36e-11	131.2
SF6-O2	250.0	75.0	20.0	25.96	72.58	28.67e-11	11.45e+01
SF6-O2	250.0	100.0	20.0	65.70	83.32	17.37e-11	85.7
SF6-O2	250.0	125.0	20.0	76.60	92.71	15.05e-11	11.54e+01
SF6-O2	250.0	150.0	20.0	122.00	110.96	9.58e-11	11.15e+01
SF6-O2	400.0	100.0	20.0	25.89	72.59	28.74e-11	11.54e+01
SF6-O2	400.0	125.0	20.0	53.60	100.05	18.23e-11	34.49
SF6-O2	400.0	125.0	20.0	49.87	77.60	21.41e-11	85.
SF6-O2	400.0	150.0	20.0	49.87	115.07	17.17e-11	15.77e+01

RIE Mode

N2	100.0	50.0	20.0	19.78	68.36	31.68e-11	12.80e+01
N2	100.0	50.0	100.0	20.40	70.31	30.79e-11	13.13e+01
N2	100.0	100.0	20.0	21.49	68.67	31.14e-11	12.04e+01
N2	100.0	200.0	20.0	25.42	68.91	29.99e-11	10.61e+01
N2	250.0	50.0	20.0	18.60	66.32	32.81e-11	12.75e+01
N2	400.0	50.0	20.0	19.38	68.28	31.82e-11	13.00e+01

Original impedance measurements

Plasma Etching Mode.

	gas	power	pres	flow	r	x	Csh	Rsh
	0.	100.000	0.e-11	40.e-11				
	1.000							
	141.000							
CF4-02	50.0	50.0	20.0	23.12	67.08	31.28e-11	10.89e+01	
CF4-02	100.0	50.0	20.0	21.49	61.88	33.85e-11	100.	
CF4-02	100.0	100.0	20.0	23.12	65.36	31.92e-11	10.39e+01	
CF4-02	100.0	100.0	20.0	24.89	70.73	29.53e-11	11.30e+01	
CF4-02	100.0	250.0	20.0	33.24	69.33	27.53e-11	89.	
CF4-02	100.0	300.0	20.0	49.87	44.70	23.40e-11	45.	
CF4-02	150.0	100.0	20.0	24.63	74.52	28.40e-11	12.51e+01	
CF4-02	200.0	50.0	20.0	23.12	78.47	27.52e-11	14.47e+01	
CF4-02	200.0	100.0	20.0	24.11	78.53	27.32e-11	13.99e+01	
CF4-02	250.0	50.0	20.0	19.99	63.25	33.75e-11	11.01e+01	
CF4-02	250.0	50.0	20.0	23.12	78.47	27.52e-11	14.47e+01	
CF4-02	250.0	100.0	20.0	22.17	68.75	30.93e-11	11.77e+01	
CF4-02	250.0	300.0	20.0	25.69	70.72	29.32e-11	11.02e+01	
CF4-02	250.0	500.0	20.0	45.61	65.66	24.12e-11	70.	
CF4-02	250.0	525.0	20.0	49.87	56.09	23.37e-11	56.	
CF4-02	300.0	50.0	20.0	23.12	78.47	27.52e-11	14.47e+01	
CF4-02	300.0	100.0	20.0	23.86	78.52	27.37e-11	14.11e+01	
CF4-02	350.0	50.0	20.0	23.12	78.47	27.52e-11	14.47e+01	
CF4-02	350.0	100.0	20.0	23.86	80.62	26.77e-11	14.81e+01	
CF4-02	400.0	50.0	20.0	20.40	65.00	32.87e-11	11.37e+01	
CF4-02	400.0	50.0	20.0	23.12	80.57	26.92e-11	15.19e+01	
CF4-02	400.0	100.0	20.0	21.72	70.52	30.41e-11	12.53e+01	
CF4-02	400.0	100.0	20.0	23.61	78.51	27.42e-11	14.23e+01	
CF4-02	400.0	300.0	20.0	25.96	72.58	28.67e-11	11.45e+01	
CF4-02	400.0	500.0	20.0	27.35	76.39	27.24e-11	12.03e+01	
CF4-02	400.0	710.0	20.0	49.87	60.36	23.11e-11	61.	
CF4-02	450.0	50.0	20.0	23.12	80.57	26.92e-11	15.19e+01	
CF4-02	450.0	100.0	20.0	23.61	78.51	27.42e-11	14.23e+01	
SF6-02	100.0	50.0	20.0	49.87	80.41	21.08e-11	90.	
SF6-02	150.0	50.0	20.0	49.87	80.41	21.08e-11	90.	
SF6-02	200.0	50.0	20.0	49.87	80.41	21.08e-11	90.	
SF6-02	250.0	50.0	20.0	49.87	80.41	21.08e-11	90.	
SF6-02	300.0	50.0	20.0	40.35	92.08	21.39e-11	12.52e+01	
SF6-02	350.0	50.0	20.0	40.35	92.08	21.39e-11	12.52e+01	
SF6-02	400.0	50.0	20.0	40.68	89.19	21.79e-11	11.81e+01	
SF6-02	450.0	50.0	20.0	31.61	93.83	22.47e-11	15.50e+01	

RIE Mode

C2F6-02	50.0	50.0	20.0	24.89	74.52	28.34e-11	12.40e+01
C2F6-02	100.0	50.0	5.0	49.87	39.67	22.93e-11	41.
C2F6-02	100.0	50.0	20.0	24.89	76.50	27.75e-11	13.00e+01
C2F6-02	100.0	50.0	20.0	49.87	41.30	23.12e-11	42.
C2F6-02	100.0	50.0	100.0	49.87	39.67	22.93e-11	41.
C2F6-02	100.0	100.0	5.0	49.87	39.67	22.93e-11	41.
C2F6-02	100.0	100.0	20.0	49.87	39.67	22.93e-11	41.
C2F6-02	100.0	100.0	100.0	49.87	28.70	20.35e-11	33.
C2F6-02	100.0	200.0	5.0	49.87	39.67	22.93e-11	41.
C2F6-02	100.0	200.0	20.0	49.87	44.70	23.40e-11	45.
C2F6-02	100.0	200.0	100.0	49.87	-34.57-22.04e-11	37.	
C2F6-02	150.0	50.0	20.0	24.89	78.54	27.16e-11	13.64e+01
C2F6-02	200.0	50.0	20.0	24.89	80.64	26.58e-11	14.31e+01
C2F6-02	250.0	50.0	5.0	49.87	41.30	23.12e-11	42.
C2F6-02	250.0	50.0	20.0	25.15	82.81	25.95e-11	14.89e+01
C2F6-02	250.0	50.0	20.0	49.87	44.70	23.40e-11	45.
C2F6-02	250.0	50.0	100.0	49.87	1073.22	21.83e-12	11.57e+03
C2F6-02	250.0	100.0	5.0	49.87	41.30	23.12e-11	42.
C2F6-02	250.0	100.0	20.0	49.87	39.67	22.93e-11	41.
C2F6-02	250.0	100.0	100.0	49.87	41.30	23.12e-11	42.
C2F6-02	250.0	200.0	5.0	49.87	42.98	23.28e-11	43.
C2F6-02	250.0	200.0	20.0	49.87	44.70	23.40e-11	45.
C2F6-02	250.0	200.0	100.0	49.87	39.67	22.93e-11	41.
C2F6-02	300.0	50.0	20.0	25.15	85.04	25.38e-11	15.64e+01
C2F6-02	350.0	50.0	20.0	25.15	85.04	25.38e-11	15.64e+01
C2F6-02	400.0	50.0	5.0	49.87	44.70	23.40e-11	45.
C2F6-02	400.0	50.0	20.0	49.87	44.70	23.40e-11	45.
C2F6-02	400.0	50.0	100.0	49.87	1073.22	21.83e-12	11.57e+03
C2F6-02	400.0	100.0	5.0	49.87	42.98	23.28e-11	43.
C2F6-02	400.0	100.0	20.0	49.87	36.54	22.44e-11	38.
C2F6-02	400.0	100.0	100.0	49.87	44.70	23.40e-11	45.
C2F6-02	400.0	200.0	5.0	49.87	42.98	23.28e-11	43.
C2F6-02	400.0	200.0	20.0	49.87	44.70	23.40e-11	45.
C2F6-02	400.0	200.0	100.0	49.87	41.30	23.12e-11	42.
C2F6-02	450.0	50.0	20.0	25.15	85.04	25.38e-11	15.64e+01

CF4-02	100.0	50.0	5.0	49.87	39.67	22.93e-11	41.
CF4-02	100.0	50.0	20.0	21.05	72.29	29.94e-11	13.47e+01
CF4-02	100.0	50.0	20.0	49.87	38.09	22.71e-11	39.
CF4-02	100.0	50.0	100.0	49.87	28.70	20.35e-11	33.
CF4-02	100.0	100.0	5.0	49.87	41.30	23.12e-11	42.
CF4-02	100.0	100.0	20.0	25.42	78.54	27.05e-11	13.41e+01
CF4-02	100.0	100.0	20.0	49.87	36.54	22.44e-11	38.
CF4-02	100.0	100.0	100.0	49.87	36.54	22.44e-11	38.
CF4-02	100.0	150.0	20.0	45.61	63.68	24.36e-11	67.
CF4-02	100.0	200.0	5.0	49.87	41.30	23.12e-11	42.
CF4-02	100.0	200.0	20.0	49.87	38.09	22.71e-11	39.
CF4-02	100.0	200.0	20.0	49.87	58.19	23.26e-11	59.
CF4-02	100.0	200.0	100.0	49.87	36.54	22.44e-11	38.
CF4-02	250.0	50.0	5.0	41.01	59.63	26.72e-11	64.
CF4-02	250.0	50.0	20.0	19.99	72.09	30.24e-11	14.00e+01
CF4-02	250.0	50.0	20.0	49.87	42.98	23.28e-11	43.
CF4-02	250.0	50.0	100.0	49.87	1073.22	21.83e-12	11.57e+03

CF4-02	250.0	100.0	5.0	36.61	60.90	28.32e-11	69.
CF4-02	250.0	100.0	20.0	21.94	80.46	27.16e-11	15.85e+01
CF4-02	250.0	100.0	20.0	39.34	60.91	27.20e-11	67.
CF4-02	250.0	100.0	100.0	49.87	42.98	23.28e-11	43.
CF4-02	250.0	200.0	5.0	49.87	41.30	23.12e-11	42.
CF4-02	250.0	200.0	20.0	49.87	44.70	23.40e-11	45.
CF4-02	250.0	200.0	100.0	49.87	38.09	22.71e-11	39.
CF4-02	250.0	300.0	20.0	28.82	82.52	25.36e-11	13.25e+01
CF4-02	250.0	350.0	20.0	36.95	79.77	24.23e-11	10.46e+01
CF4-02	250.0	400.0	20.0	49.87	62.59	22.94e-11	64.
CF4-02	400.0	50.0	5.0	49.87	50.15	23.54e-11	50.
CF4-02	400.0	50.0	20.0	20.83	74.17	29.33e-11	14.25e+01
CF4-02	400.0	50.0	20.0	49.87	46.46	23.48e-11	47.
CF4-02	400.0	50.0	100.0	49.87	1073.22	21.83e-12	11.57e+03
CF4-02	400.0	100.0	5.0	27.64	67.01	29.94e-11	95.
CF4-02	400.0	100.0	20.0	21.27	80.36	27.30e-11	16.25e+01
CF4-02	400.0	100.0	20.0	28.52	66.90	29.69e-11	93.
CF4-02	400.0	100.0	100.0	49.87	44.70	23.40e-11	45.
CF4-02	400.0	200.0	5.0	49.87	42.98	23.28e-11	43.
CF4-02	400.0	200.0	20.0	49.87	42.98	23.28e-11	43.
CF4-02	400.0	200.0	100.0	49.87	42.98	23.28e-11	43.
CF4-02	400.0	300.0	20.0	26.79	82.75	25.68e-11	14.12e+01
CF4-02	400.0	400.0	20.0	28.52	84.79	24.87e-11	14.03e+01
CF4-02	400.0	450.0	20.0	32.91	83.76	24.28e-11	12.30e+01
CF4-02	400.0	475.0	20.0	34.58	83.14	24.07e-11	11.72e+01
CF4-02	400.0	500.0	20.0	49.87	62.59	22.94e-11	64.

SF6-02	100.0	50.0	5.0	49.87	83.32	20.74e-11	95.
SF6-02	100.0	50.0	20.0	49.87	77.60	21.41e-11	85.
SF6-02	100.0	50.0	100.0	49.87	83.32	20.74e-11	95.
SF6-02	100.0	100.0	5.0	49.87	89.46	20.02e-11	10.52e+01
SF6-02	100.0	100.0	20.0	49.87	69.73	22.27e-11	74.
SF6-02	100.0	100.0	100.0	49.87	64.90	22.74e-11	67.
SF6-02	100.0	200.0	5.0	49.87	86.34	20.39e-11	100.
SF6-02	100.0	200.0	20.0	49.87	67.27	22.52e-11	70.
SF6-02	100.0	200.0	100.0	49.87	-24.69-18.72e-11	31.	
SF6-02	250.0	50.0	5.0	24.89	111.92	19.99e-11	26.41e+01
SF6-02	250.0	50.0	20.0	26.79	87.28	24.58e-11	15.56e+01
SF6-02	250.0	50.0	100.0	49.87	1073.22	21.83e-12	11.57e+03
SF6-02	250.0	100.0	5.0	49.87	99.58	18.85e-11	12.44e+01
SF6-02	250.0	100.0	20.0	49.87	103.22	18.44e-11	13.18e+01
SF6-02	250.0	100.0	100.0	49.87	67.27	22.52e-11	70.
SF6-02	250.0	200.0	5.0	49.87	103.22	18.44e-11	13.18e+01
SF6-02	250.0	200.0	20.0	49.87	-18.05-15.06e-11	28.	
SF6-02	250.0	200.0	100.0	49.87	46.46	23.48e-11	47.
SF6-02	400.0	50.0	5.0	25.42	85.04	25.34e-11	15.50e+01
SF6-02	400.0	50.0	20.0	26.51	87.30	24.62e-11	15.70e+01
SF6-02	400.0	50.0	100.0	49.87	1073.22	21.83e-12	11.57e+03
SF6-02	400.0	100.0	5.0	49.87	69.73	22.27e-11	74.
SF6-02	400.0	100.0	20.0	49.87	72.27	22.00e-11	77.
SF6-02	400.0	100.0	100.0	49.87	72.27	22.00e-11	77.
SF6-02	400.0	200.0	5.0	49.87	1073.22	21.83e-12	11.57e+03
SF6-02	400.0	200.0	20.0	49.87	1073.22	21.83e-12	11.57e+03

SF6-02	400.0	200.0	100.0	49.87	56.09	23.37e-11	56.
C2F6-02	100.0	50.0	5.0	49.87	39.67	22.93e-11	41.
C2F6-02	100.0	50.0	20.0	49.87	41.30	23.12e-11	42.
C2F6-02	100.0	50.0	100.0	49.87	39.67	22.93e-11	41.
C2F6-02	100.0	100.0	5.0	49.87	39.67	22.93e-11	41.
C2F6-02	100.0	100.0	20.0	49.87	39.67	22.93e-11	41.
C2F6-02	100.0	100.0	100.0	49.87	28.70	20.35e-11	33.
C2F6-02	100.0	200.0	5.0	49.87	39.67	22.93e-11	41.
C2F6-02	100.0	200.0	20.0	49.87	44.70	23.40e-11	45.
C2F6-02	100.0	200.0	100.0	49.87	-34.57-22.04e-11		37.
C2F6-02	250.0	50.0	5.0	49.87	41.30	23.12e-11	42.
C2F6-02	250.0	50.0	20.0	49.87	44.70	23.40e-11	45.
C2F6-02	250.0	50.0	100.0	49.87	1073.22	21.83e-12	11.57e+03
C2F6-02	250.0	100.0	5.0	49.87	41.30	23.12e-11	42.
C2F6-02	250.0	100.0	20.0	49.87	39.67	22.93e-11	41.
C2F6-02	250.0	100.0	100.0	49.87	41.30	23.12e-11	42.
C2F6-02	250.0	200.0	5.0	49.87	42.98	23.28e-11	43.
C2F6-02	250.0	200.0	20.0	49.87	44.70	23.40e-11	45.
C2F6-02	250.0	200.0	100.0	49.87	39.67	22.93e-11	41.
C2F6-02	400.0	50.0	5.0	49.87	44.70	23.40e-11	45.
C2F6-02	400.0	50.0	20.0	49.87	44.70	23.40e-11	45.
C2F6-02	400.0	50.0	100.0	49.87	1073.22	21.83e-12	11.57e+03
C2F6-02	400.0	100.0	5.0	49.87	42.98	23.28e-11	43.
C2F6-02	400.0	100.0	20.0	49.87	36.54	22.44e-11	38.
C2F6-02	400.0	100.0	100.0	49.87	44.70	23.40e-11	45.
C2F6-02	400.0	200.0	5.0	49.87	42.98	23.28e-11	43.
C2F6-02	400.0	200.0	20.0	49.87	44.70	23.40e-11	45.
C2F6-02	400.0	200.0	100.0	49.87	41.30	23.12e-11	42.
CF4-02	100.0	50.0	5.0	49.87	39.67	22.93e-11	41.
CF4-02	100.0	50.0	20.0	49.87	38.09	22.71e-11	39.
CF4-02	100.0	50.0	100.0	49.87	28.70	20.35e-11	33.
CF4-02	100.0	100.0	5.0	49.87	41.30	23.12e-11	42.
CF4-02	100.0	100.0	20.0	49.87	36.54	22.44e-11	38.
CF4-02	100.0	100.0	100.0	49.87	36.54	22.44e-11	38.
CF4-02	100.0	200.0	5.0	49.87	41.30	23.12e-11	42.
CF4-02	100.0	200.0	20.0	49.87	38.09	22.71e-11	39.
CF4-02	100.0	200.0	100.0	49.87	36.54	22.44e-11	38.
CF4-02	250.0	50.0	5.0	41.01	59.63	26.72e-11	64.
CF4-02	250.0	50.0	20.0	49.87	42.98	23.28e-11	43.
CF4-02	250.0	50.0	100.0	49.87	1073.22	21.83e-12	11.57e+03
CF4-02	250.0	100.0	5.0	36.61	60.90	28.32e-11	69.
CF4-02	250.0	100.0	20.0	39.34	60.91	27.20e-11	67.
CF4-02	250.0	100.0	100.0	49.87	42.98	23.28e-11	43.
CF4-02	250.0	200.0	5.0	49.87	41.30	23.12e-11	42.
CF4-02	250.0	200.0	20.0	49.87	44.70	23.40e-11	45.
CF4-02	250.0	200.0	100.0	49.87	38.09	22.71e-11	39.
CF4-02	400.0	50.0	5.0	49.87	50.15	23.54e-11	50.
CF4-02	400.0	50.0	20.0	49.87	46.46	23.48e-11	47.
CF4-02	400.0	50.0	100.0	49.87	1073.22	21.83e-12	11.57e+03
CF4-02	400.0	100.0	5.0	27.64	67.01	29.94e-11	95.

CF4-02	400.0	100.0	20.0	28.52	66.90	29.69e-11	93.
CF4-02	400.0	100.0	100.0	49.87	44.70	23.40e-11	45.
CF4-02	400.0	200.0	5.0	49.87	42.98	23.28e-11	43.
CF4-02	400.0	200.0	20.0	49.87	42.98	23.28e-11	43.
CF4-02	400.0	200.0	100.0	49.87	42.98	23.28e-11	43.
SF6-02	100.0	50.0	5.0	49.87	83.32	20.74e-11	95.
SF6-02	100.0	50.0	20.0	49.87	77.60	21.41e-11	85.
SF6-02	100.0	50.0	100.0	49.87	83.32	20.74e-11	95.
SF6-02	100.0	100.0	5.0	49.87	89.46	20.02e-11	10.52e+01
SF6-02	100.0	100.0	20.0	49.87	69.73	22.27e-11	74.
SF6-02	100.0	100.0	100.0	49.87	64.90	22.74e-11	67.
SF6-02	100.0	200.0	5.0	49.87	86.34	20.39e-11	100.
SF6-02	100.0	200.0	20.0	49.87	67.27	22.52e-11	70.
SF6-02	100.0	200.0	100.0	49.87	-24.69-18.72e-11	31.	
SF6-02	250.0	50.0	5.0	24.89	111.92	19.99e-11	26.41e+01
SF6-02	250.0	50.0	20.0	26.79	87.28	24.58e-11	15.56e+01
SF6-02	250.0	50.0	100.0	49.87	1073.22	21.83e-12	11.57e+03
SF6-02	250.0	100.0	5.0	49.87	99.58	18.85e-11	12.44e+01
SF6-02	250.0	100.0	20.0	49.87	103.22	18.44e-11	13.18e+01
SF6-02	250.0	100.0	100.0	49.87	67.27	22.52e-11	70.
SF6-02	250.0	200.0	5.0	49.87	103.22	18.44e-11	13.18e+01
SF6-02	250.0	200.0	20.0	49.87	-18.05-15.06e-11	28.	
SF6-02	250.0	200.0	100.0	49.87	46.46	23.48e-11	47.
SF6-02	400.0	50.0	5.0	25.42	85.04	25.34e-11	15.50e+01
SF6-02	400.0	50.0	20.0	26.51	87.30	24.62e-11	15.70e+01
SF6-02	400.0	50.0	100.0	49.87	1073.22	21.83e-12	11.57e+03
SF6-02	400.0	100.0	5.0	49.87	69.73	22.27e-11	74.
SF6-02	400.0	100.0	20.0	49.87	72.27	22.00e-11	77.
SF6-02	400.0	100.0	100.0	49.87	72.27	22.00e-11	77.
SF6-02	400.0	200.0	5.0	49.87	1073.22	21.83e-12	11.57e+03
SF6-02	400.0	200.0	20.0	49.87	1073.22	21.83e-12	11.57e+03
SF6-02	400.0	200.0	100.0	49.87	56.09	23.37e-11	56.

APPENDIX D

D. SIMULATION INPUT FOR FIGURES (SPICE and SAMPLE)

```
.....
::: Figure 3.2 :::
.....
PLASMA RF NETWORK AND IMPEDANCE MODEL
* conditions for 50mT 250W / RIE mode CF4 plasma
* rf source
vrf 1 0 sin(0.0 300 13.56MEG )
* matching network
cpmatch 1 0 290p
esmatch 2 3 85p
lsmatch 1 2 1u
* plasma
db 3 40 didial
vdb 40 4 dc 0.0
cshb 3 41 300p
vcshb 41 4 dc 0.0
vrshb 42 4 dc 0.0
rshb 3 42 140
rplsm1 45 5 25
vrplsm 45 4 dc 0.0
dt 6 0 didial
csht 6 0 300p
rsht 3 0 140
rplsm2 6 5 25
lplsm 2 6 5 1.85u
.model didial D RS=30m IS=100u
.options acct itl5=0
.tran 5ns 16u 15u
* source across plasma center of plasma across sheath
.print tran v(1,0) v(3,0) i(vrplsm) v(5,0) i(vdb) i(vrshb) v(3,4) i(vcshb)
.plot tran v(1,0) v(3,0) i(vrplsm) v(5,0) i(vdb) i(vrshb) v(3,4) i(vcshb)
.end
```

```
.....
::: Figure 4.1 :::
.....
* Isotropic etching of SiO2 beneath McDermid 74
trial 78 1 0.0 0.5 0.0
trial 79 -3 3
trial 79 2 .80
trial 79 1 1.2
trial 79 0 6.0
trial 84 4
trial 85 7 12.0
trial 86 8.0
trial 87 1 1
```

trial 88 1 4 3
trial 89
* Substrate etching with 2 components.
trial 78 10 (0.0000 0.0000)
 (0.0 0.0)
 (0.10 0.35)
trial 94 0 4.0 4.0 1.0 2.5
trial 87 1 1
trial 84 6
trial 86 8.0
trial 88 1 5 5
trial 89

.....
:: Figure 4.2a ::
.....
* Isotropic etching of SiO₂ beneath McDermid 74
trial 78 1 0.0 0.5 0.0
trial 79 -3 3
trial 79 2 2.30
trial 79 1 1.2
trial 79 0 4.5
trial 84 4
trial 85 0.0 0.0 5.0 0.0 5.2 2.3 8.0 2.3
trial 86 8.0
trial 87 1 1
trial 88 1 4 3
trial 89
* Substrate etching with 2 components.
trial 78 10 (0.0000 0.0000)
 (0.0 0.0)
 (0.55 0.35)
trial 87 1 1
trial 84 6
trial 86 8.0
trial 88 1 5 5
trial 89

.....
:: Figure 4.2b ::
.....
* Isotropic etching of SiO₂ beneath McDermid 74
trial 78 1 0.0 0.5 0.0
trial 79 -3 3
trial 79 2 2.30
trial 79 1 1.2
trial 79 0 4.5
trial 84 4
trial 85 0.0 0.0 5.0 0.0 5.2 2.3 8.0 2.3
trial 86 8.0
trial 87 1 1
trial 88 1 4 3

trial 89

* Substrate etching with 2 components.

trial 78 7 (0.0000 0.0000)

(0.0 0.0)

(0.10 0.35)

trial 94 0 2.0 4.0 1.0 2.5

trial 87 1 1

trial 84 6

trial 86 8.0

trial 88 1 5 5

trial 89

* Isotropic etching of SiO2 beneath McDermid 74

trial 78 1 0.0 0.5 0.0

trial 79 -3 3

trial 79 2 2.30

trial 79 1 1.2

trial 79 0 4.5

trial 84 4

trial 85 0.0 0.0 5.0 0.0 5.2 2.3 8.0 2.3

trial 86 8.0

trial 87 1 1

trial 88 1 4 3

trial 89

* Substrate etching with 2 components.

trial 78 10 (0.0000 0.0000)

(0.0 0.0)

(0.55 0.35)

trial 87 1 1

trial 84 6

trial 86 8.0

trial 88 1 5 5

trial 89

.....

::: Figure 4.3a :::

.....

* Isotropic etching of SiO2 beneath McDermid 74

trial 78 1 0.0 0.5 0.0

trial 79 -3 3

trial 79 2 2.30

trial 79 1 1.2

trial 79 0 2.1

trial 84 4

trial 85 0.0 0.0 5.0 0.0 5.2 2.3 8.0 2.3

trial 86 8.0

trial 87 1 1

trial 88 1 4 3

trial 89

* Substrate etching positive deposition rate.

trial 50 4 60 .001 .01 0.0075

trial 51 1

trial 53 1 1

trial 54 8.0 8.0

trial 58 60 300 5
trial 59

.....
::: Figure 4.3b :::
.....

* Isotropic etching of SiO₂ beneath McDermid 74

trial 78 1 0.0 0.5 0.0
trial 79 -3 3
trial 79 2 2.30
trial 79 1 3.6
trial 79 0 2.1
trial 84 4
trial 85 0.0 0.0 5.0 0.0 5.2 2.3 8.0 2.3
trial 86 8.0
trial 87 1 1
trial 88 1 4 3
trial 89

* Substrate etching positive deposition rate.

trial 50 4 60 .001 .01 0.0075
trial 51 1
trial 53 1 1
trial 54 8.0 8.0
trial 58 60 300 5
trial 59

.....
::: Figure 5.2 :::
.....

* Poly Slide Etching Simulation-d13

trial 78 10 0.00 0.01 0.0 0.1 0.0 0.0
trial 79 -3 3
trial 79 2 1.0
trial 79 1 0.2
trial 79 0 1.8
trial 84 8
trial 85 (0.0,1.0) (0.5,1.0) (0.51,0.0) (1.499 0.0) (1.5,1.0) (2.0,1.0)
trial 86 2.0
trial 87 1 1
trial 88 20 120,6
trial 89

* Isotropic Etching

trial 78 1 0.01 0.1 0.0
trial 79 -3 3
trial 79 2 1.0
trial 79 1 0.2
trial 79 0 1.8
trial 84 8
trial 86 2.0
trial 87 1 1
trial 88 60 300,5
trial 89

***Multistep Etching Simulation Example: file name~depo3.in**

***Step 1: Poly-Si Deposition**

trial 78 2 -0.003

trial 79 -4 3

trial 79 2 0.7

trial 79 1 0.5

trial 79 0 0.8

trial 84 10

trial 85 6

trial 86 2.0

trial 87 1 1

trial 88 4000

trial 89

***Step 2: Anisotropic Etching of Poly-Si**

trial 78 10 0.0 0.1 0.0 0.1 0.0 0.0

trial 84 10

trial 86 2.0

trial 87 1 1

trial 88 30 120,4

trial 96

trial 89

***Step 3: Isotropic Etching of Poly-Si Residue**

trial 78 10 0.1 0.0 0.1 0.0 0.0 0.0

trial 84 14

trial 86 2.0

trial 87 1 1

trial 88 30 120,4

trial 96

trial 89

.....
:: Figure 5.6 ::
.....

***Contact Hole Anisotropic-Etching Simulation**

***decs.1-without postbaking**

trial 78 10 0.00 0.0125 0.0 0.05 0.0 0.01

trial 79 -4 3

trial 79 2 2.5

trial 79 1 1.0

trial 79 0 1.0

trial 84 8

trial 85 (0.0 1.4) (1.15 1.4) (1.3 2.5) (2.85 2.5) (3.0 1.4) (4.5 1.4)

trial 86 4.5

trial 87 1 1

trial 88 240 1920,8

trial 89

***ASH**

trial 78 1 0.1 0.0 0.0

trial 84 8

trial 86 4.5

trial 87

trial 88 660

trial 89

***AL Sputtering**

trial 50 3 -90.0 90.0 -0.001
trial 51
trial 53 2 1
trial 54 4.5 4.5
trial 58 200 1000,5
trial 59

***Contact Hole Anisotropic-Etching Simulation**

***decs.1-without postbaking**

trial 78 10 0.00 0.0125 0.0 0.05 0.0 0.01
trial 79 -4 3
trial 79 2 2.5
trial 79 1 1.0
trial 79 0 1.0
trial 84 8
trial 85 (0.0 1.4) (1.15 1.4) (1.3 2.5) (2.85 2.5) (3.0 1.4) (4.5 1.4)
trial 86 4.5
trial 87 1 1
trial 88 240 1920,8
trial 89

***ASH**

trial 78 1 0.1 0.0 0.0
trial 84 8
trial 86 4.5
trial 87
trial 88 660
trial 89

***AL Sputtering**

trial 50 3 -90.0 90.0 -0.001
trial 51
trial 53 2 1
trial 54 4.5 4.5
trial 58 200 1000,5
trial 59

***Contact Hole Anisotropic-Etching Simulation**

***decs.2-with postbaking**

trial 78 10 0.00 0.008 0.0 0.05 0.0 0.01
trial 79 -4 3
trial 79 2 2.5
trial 79 1 1.0
trial 79 0 1.0
trial 84 8
trial 85 (0.0 1.8) (1.4 2.5) (3.3 2.5) (4.5 1.9)
trial 86 4.5
trial 87 1 1
trial 88 120 1200,10
trial 89

***ASH**

trial 78 1 0.1 0.0 0.0
trial 84 8
trial 86 4.5
trial 87
trial 88 420
trial 89
*Al Sputtering
trial 50 3 -90.0 90.0 -0.001
trial 51
trial 53 2 1
trial 54 4.5 4.5
trial 58 200 1000,5
trial 59

.....
:: Figure 5.8 ::
.....

***Multistep Etching Simulation-d5-p5**

***Oxide Deposition (I)**

trial 78 2 -0.003
trial 79 -4 3
trial 79 2 0.6
trial 79 1 0.3
trial 79 0 0.1
trial 84 10
trial 85 0.0 0.6 0.5 0.6 0.5001 0.9 2.0 0.9
trial 86 2.0
trial 87 1 1
trial 88 4000
trial 89

***Anisotropic Etching (I)**

trial 78 9 0.0 0.1 0.0 0.1 0.0 0.0
trial 84 10
trial 86 2.0
trial 87 1 1
trial 88 120
trial 89

***Oxide Depo(II)**

trial 78 2 -0.003
trial 84 10
trial 86 2.0
trial 87 1 1
trial 88 4000
trial 89

***Anisotropic Etching (II)**

trial 78 9 0.0 0.1 0.0 0.1 0.0 0.0
trial 84 10
trial 86 2.0
trial 87 1 1
trial 88 120
trial 89

***Oxide Depo(III)**

trial 78 2 -0.003

trial 84 10
trial 86 2.0
trial 87 1 1
trial 88 4000
trial 89
*Anisotropic Etching(III)
trial 78 9 0.0 0.1 0.0 0.1 0.0 0.0
trial 84 10
trial 86 2.0
trial 87 1 1
trial 88 120
trial 89
*Oxide Depo(IV)
trial 78 2 -0.003
trial 84 10
trial 86 2.0
trial 87 1 1
trial 88 4000
trial 89
*Anisotropic Etching(IV)
trial 78 9 0.0 0.1 0.0 0.1 0.0 0.0
trial 84 10
trial 86 2.0
trial 87 1 1
trial 88 120
trial 89
*Oxide Depo(V)
trial 78 2 -0.003
trial 84 10
trial 86 2.0
trial 87 1 1
trial 88 4000
trial 89
*Anisotropic Etching(V)
trial 78 9 0.0 0.1 0.0 0.1 0.0 0.0
trial 84 10
trial 86 2.0
trial 87 1 1
trial 88 120
trial 89

.....
:: Figure 5.9 ::
.....

* Simulation of Planarization Process, file:/etch-2/decs3.1
*Isotropic Oxide Deposition
trial 78 2 -0.03
trial 79 -4 3
trial 79 2 1.5
trial 79 1 1.0
trial 79 0 0.5
trial 84 8
trial 85 (0.0,1.5) (1.0,1.5) (1.0,2.5) (2.0,2.5) (2.0,1.5) (3.0,1.5)

trial 86 3.0
trial 87 1 1
trial 88 500 2000,4
trial 89
*Anisotropic Etching
trial 78 10 0.0 0.5 0.0 0.5 0.0 0.0
trial 84 8
trial 86 3.0
trial 87 1 1
trial 88 30 120,4
trial 96
trial 89

* Simulation of Planarization Process, file: /etch-2/decs3.15
*Isotropic Oxide Deposition
trial 78 2 -0.03
trial 79 -4 3
trial 79 2 1.5
trial 79 1 1.0
trial 79 0 0.5
trial 84 8
trial 85 (0.0,1.5) (0.75,1.5) (0.75,2.5) (2.25,2.5) (2.25,1.5) (3.0,1.5)
trial 86 3.0
trial 87 1 1
trial 88 500 2000,4
trial 89
*Anisotropic Etching
trial 78 10 0.0 0.5 0.0 0.5 0.0 0.0
trial 84 8
trial 86 3.0
trial 87 1 1
trial 88 30 120,4
trial 96
trial 89

* Simulation of Planarization Process, file: /etch-2/decs3.2
*Isotropic Oxide Deposition
trial 78 2 -0.03
trial 79 -4 3
trial 79 2 1.5
trial 79 1 1.0
trial 79 0 0.5
trial 84 8
trial 85 (0.0,1.5) (0.5,1.5) (0.5,2.5) (2.5,2.5) (2.5,1.5) (3.0,1.5)
trial 86 3.0
trial 87 1 1
trial 88 500 2000,4
trial 89
*Anisotropic Etching
trial 78 10 0.0 0.5 0.0 0.5 0.0 0.0

trial 84 8
trial 86 3.0
trial 87 1 1
trial 88 30 120,4
trial 96
trial 89

.....
:: Figure 6.3 ::
.....

* Directional etching with isotropic undercut.

trial 78 10 0.0003 0.00 0.0097 0.00 0.0 0.0
trial 79 -3 3
trial 79 2 1.2
trial 79 1 0.7
trial 79 0 0.1
trial 84 8
trial 85 3 75
trial 86 4.0
trial 87 1 1
trial 88 36 108 3
trial 94 1 2.0 8.0 1.4
trial 89

.....
:: Figure 6.4 ::
.....

* Directional etching with loading effect.

trial 78 7 0.0003 0.00 0.0033 0.0065 0.0 0.0
trial 79 -3 3
trial 79 2 1.2
trial 79 1 0.7
trial 79 0 0.1
trial 84 8
trial 85 3 75
trial 86 4.0
trial 87 1 1
trial 88 36 108 3
trial 94 1 2.0 8.0 1.4
trial 89

.....
:: Figure 6.5 ::
.....

* Directional etching with photo resist erosion.

trial 78 10 0.0033 0.00 0.0033 0.0065 0.0 0.0
trial 79 -3 3
trial 79 2 1.2
trial 79 1 0.7
trial 79 0 0.1
trial 84 8

trial 85 3 75
trial 86 4.0
trial 87 1 1
trial 88 36 108 3
trial 89

.....
::: Figure 6.7 :::
.....

* Directional etching with surface diffusion later.

trial 78 7 0.0003 0.00 0.0033 0.0065 0.0 0.0
trial 79 -3 3
trial 79 2 1.2
trial 79 1 0.7
trial 79 0 0.1
trial 84 8
trial 85 3 75
trial 86 4.0
trial 87 1 1
trial 88 36 108 3
trial 94 1 1.0 0.4 1.4
trial 89